

**TOWARD A RELIABLE PREDICTION
OF SHOCKS IN HYPERSONIC FLOW:
RESOLVING CARBUNCLES WITH
ENTROPY AND VORTICITY
CONTROL**

by
Farzad Ismail

A dissertation submitted in partial fulfillment
of the requirements for the degree of
Doctor of Philosophy
(Aerospace Engineering and Scientific Computing)
in The University of Michigan
2006

Doctoral Committee:

Professor Philip L. Roe, Chair
Professor Robert Krasny
Professor Kenneth G. Powell
Professor Bram Van Leer

INFORMATION TO USERS

The quality of this reproduction is dependent upon the quality of the copy submitted. Broken or indistinct print, colored or poor quality illustrations and photographs, print bleed-through, substandard margins, and improper alignment can adversely affect reproduction.

In the unlikely event that the author did not send a complete manuscript and there are missing pages, these will be noted. Also, if unauthorized copyright material had to be removed, a note will indicate the deletion.



UMI Microform 3208472

Copyright 2006 by ProQuest Information and Learning Company.
All rights reserved. This microform edition is protected against
unauthorized copying under Title 17, United States Code.

ProQuest Information and Learning Company
300 North Zeeb Road
P.O. Box 1346
Ann Arbor, MI 48106-1346

© Farzad Ismail 2006
All Rights Reserved

This thesis is dedicated to my granduncle, Anas Maarof for being relentless in
emphasizing the importance of education in our family.

ACKNOWLEDGEMENTS

My deepest gratitude to my wife, Zaireeni for her love and unwavering support throughout my entire graduate education, particularly toward the end. Her presence was the source of strength and inspiration for me to complete this thesis in which I will be eternally grateful. I am also thankful to my daughter Maira for her tears and laughter, which provided me a soothing comfort after those long hard days at work. Of course, I would like to thank my parents Ismail Mohamed and Kasmini Kassim, for their ever-lasting warmth, love and encouragements and for believing in me whenever I had self-doubt. Not to forget, my in-laws Azmi Ahmad and Raja Zainab Raja Ibrahim for their patience and understanding.

I owe a huge amount of gratitude to my committee members, especially to Professor Roe for sharing with me his knowledge, craftsmanship and wisdom in conducting scientific research. He taught me a lot of things but there is one that I will always remember, that is, science is not mainly about facts, but it is about the methods of discovering the facts. In addition, he also showed me the essentials of effective oral and written scientific presentations. It has been a privilege to be his student.

Professor van Leer was instrumental in my formative years in Michigan, both as an undergraduate and graduate student. As my undergraduate advisor, he was the person who introduced me to fluid dynamics, and coincidentally, in my first year at graduate school, he illuminated me with the fascinating field of Computational Fluid Dynamics (CFD). I am indebted to him for this and for always having his door

open whenever I encountered any difficulties. Special thanks to Professor Powell and Professor Krasny for serving in the committee and for their valuable inputs on the thesis.

Many thanks to all my friends and colleagues, whom I am unable to mention all of their names because the list will simply be too long. However, I would like to acknowledge several of them. Firstly, I would like to thank Dr. Hiroaki Nishikawa for being a friend and mentor in CFD and research in general. I am also grateful to Chad Ohlandt, Yoshifumi Suzuki, Hseng-Ji (Sam) Huang, Norhal El-Halwagy, Paul Kominsky and Edmund Wierzbicki for their support and lively conversations. Particular thanks to Dr. Greg Burton for his advise on managing research and for providing the latex template for the nomenclature section. Last but not least, special debts of gratitude to Max and Kerry Zain, Norzaimi Nordin and Rafizan Baharum for their unconditional friendship and assistance.

Finally, great appreciation must be extended to the University Science of Malaysia, the Department of Aerospace Engineering, University of Michigan and NASA's Space Vehicle Technology Institute (SVETI) for providing the financial means for my graduate education. Without their generous support, this thesis would have never been written.

TABLE OF CONTENTS

DEDICATION	ii
ACKNOWLEDGEMENTS	iii
LIST OF FIGURES	viii
LIST OF TABLES	xx
LIST OF APPENDICES	xxi
NOMENCLATURE	xxii
CHAPTER	
I. INTRODUCTION	1
1.1 A Brief History of Numerical Inviscid Flow Algorithms	4
1.2 “Carbuncles”	8
1.3 Numerical Vorticity Control	12
1.4 Numerical Entropy Control	16
1.5 Thesis Outline	18
II. THE CARBUNCLE PHENOMENON	20
2.1 Introduction	20
2.2 The 1 1/2 Dimensional “Carbuncle”	26
2.2.1 Initial Set Up	26
2.2.2 The Stages of “Carbuncle”	28
2.2.3 Improved Set Up	32
2.2.4 Analysis of “Bleeding” Stage	35
2.2.5 Analysis of “Pimple” Stage	42
2.3 The 1 Dimensional “Carbuncle”	43
2.3.1 Initial Set Up	43
2.3.2 The Profile of a One Dimensional Carbuncle	44
2.3.3 Analysis of 1 Dimensional Shock Instability	46
2.4 Concluding Remarks	53

III. VORTICITY PRESERVATION IN LINEAR WAVE EQUATIONS	56
3.1 Preserving Vorticity For Two Dimensional Acoustic Equations: The Rotated Richtmyer Scheme	62
3.1.1 On Two Dimensional Cartesian Grids	63
3.1.2 Including Limiters	68
3.2 Preserving Vorticity For Two Dimensional Linear Wave Equations	72
3.2.1 Including Constant Advection	72
3.2.2 Preserving Vorticity With Limiters	75
3.3 Introducing a Vorticity Correction Algorithm	81
3.4 The Modified Rotated Richtmyer Scheme	85
3.5 Numerical Results	86
IV. VORTICITY CONTROL IN EULER EQUATIONS	95
4.1 A New Flux Function That Controls Curl of Momentum in Two Dimensions	98
4.2 Independent Estimate of Inviscid Vorticity	101
4.2.1 Two-Dimensional Case	103
4.3 An Independent Discrete Vorticity Estimate in Two Dimensions	104
4.3.1 First Order Method	104
4.3.2 Second Order Method	105
4.4 Algorithm	107
4.5 Modelling Travelling Vortex	108
4.5.1 Exact Solution	109
4.5.2 Numerical Results	110
4.6 A New Method of Controlling the Carbuncle I: Controlling Vorticity	113
4.6.1 The 1 1/2 Dimensional Carbuncle	114
V. ENTROPY CONSERVATION IN BURGERS EQUATION	118
5.1 Discrete Inviscid Burgers Equation	120
5.2 Non Entropy-Conservative Fluxes	121
5.3 Entropy Conservation For Inviscid Burgers Equation	123
5.4 Including Entropy Production	125
5.4.1 Entropy Production For the Symmetric Flux	126
5.4.2 Entropy Production For the Asymmetric Flux	126
5.5 Including Entropy Fix to Ensure Entropy Consistency	127
5.5.1 Achieving Entropy Consistency from the ‘Jump’ Condition	127
5.5.2 Achieving Entropy Consistency from $\bar{f} - f_C$	129

5.6	Numerical Examples	131
5.6.1	Test 1: Modelling Rarefaction with Stationary Shock	131
5.6.2	Test 2: Modelling Rarefaction with Moving Shock .	135
5.6.3	Test 3: Modelling Compression Waves I	137
5.6.4	Test 4: Modelling Compression Waves II	141
5.6.5	Test 5: Modelling Two Dimensional Problem	143
VI. ENTROPY CONSERVATION IN EULER EQUATIONS . .		150
6.1	One Dimensional Entropy Conservation For Euler Equations .	152
6.2	Discrete Entropy Conserving Fluxes For Euler Equations . . .	154
6.2.1	Tadmor's Entropy Conserving Flux Function	156
6.2.2	Barth's Entropy Conserving Flux Function	157
6.2.3	Roe's Entropy Conserving Flux Functions	158
6.3	Including Dissipative Flux	160
6.3.1	Enforcing Entropy Stability	162
6.3.2	Determining Averaged State	164
6.3.3	Enforcing Entropy Consistency	165
6.4	Extension to More Dimensions	168
6.5	One Dimensional Gas Dynamics Problems	170
6.5.1	Modelling Stationary Contact Discontinuity	171
6.5.2	Omitting Rarefaction Shocks	173
6.5.3	Modelling Stationary Shock	174
6.5.4	Sod's Shock Tube Problem	176
6.5.5	Woodward and Collela's Double Blast Problem	179
6.6	A New Method of Controlling the Carbuncle II: Controlling Entropy	182
6.6.1	The 1 dimensional carbuncle	182
6.6.2	The 1 1/2 dimensional carbuncle	183
6.6.3	The 2 dimensional carbuncle	184
VII. CONCLUSION AND FUTURE WORK		202
7.1	Conclusion	202
7.2	Future Work On Vorticity Capturing	206
7.2.1	Vorticity Corrections in Three Dimensions	207
7.2.2	The Independent Inviscid Vorticity Estimate in Three Dimensions	211
7.3	Future Work On the Entropy-Consistent Flux	212
APPENDICES		213
BIBLIOGRAPHY		233

LIST OF FIGURES

1.1	Physical solution of a cylinder subjected to $M=20$ flow.	9
1.2	The carbuncle phenomenon which depicts a pair of oblique shocks replacing the bow shock around the stagnation region.	9
1.3	Zooming into the stagnation region of the Mach contours. Note how there is a circulation region behind the oblique shock which represents spurious vorticity. More importantly, observe that the stagnation point (depicted by the concentrated circular blue contours) is way off.	9
1.4	Navier-Stokes solution for cylinder subjected to $M=20$ flow for various Reynolds numbers: $10^4, 5 \times 10^4, 10^5$ and 10^6 (with permission from [75].)	11
1.5	Initial vorticity solution with 80×80 cells.	14
1.6	Exact vorticity contour solution at $T=480$ on 80×80 cells.	15
1.7	Vorticity contour solution of the first order Roe-flux at $T=480$ on 80×80 cells.	15
2.1	Shock captured by the Roe-method for hypersonic flow ($M=20.0$) past a cylinder. Instead of having a smooth bow shock for the U-velocity profile, there exists a pair of oblique shocks near the stagnation region. Behind these oblique shocks, negative velocities exist indicating a recirculation zone.	22
2.2	The quadrilateral structured grids with 80 cells in the radial direction and 160 cells in the angular direction.	22
2.3	Zooming into the stagnation region of Fig. 2.1. Note how there is a circulation region behind the oblique shock which represents spurious vorticity.	23
2.4	The residual (in absolute value) plot for the Roe flux for Mach 20 flow past a two-dimensional cylinder. By the time the solution goes to steady-state, it would have produced a spurious but weakly consistent solution of the Euler equations.	24
2.5	The initial condition for the $1\frac{1}{2}$ dimensional carbuncle with $M_0 = 3.0$. This a Mach number contour plot with upstream conditions on the left side of the shock.	27

2.6	The corresponding vorticity plot. From now on, we will include the Mach contours on the left figures and the vorticity contours on the right.	27
2.7	The first (pimples) stage represent initial shock instability seeded by a small perturbation to one cell upstream of the shock.	28
2.8	Note spurious vorticity is generated along the shock.	28
2.9	The second (bleeding) stage depicts streaks forming or bleeding downstream of the shock.	29
2.10	The spurious vortex blobs from first stage become spurious vortex sheets and are advected downstream.	29
2.11	The third stage (the converged solution in this case) is when the full carbuncle has developed.	30
2.12	The size and magnitude of the vortex sheets are now much larger.	30
2.13	Residual plot for the 1 1/2 dimensional carbuncle. Note that oscillations represent shock instability which eventually decays. Even though the residual decreases to $O(10^{-6})$ for this case, the solution has converged to the ‘wrong’ steady state. However, this ‘wrong’ steady state value is consistent with a weak solution of the Euler equations.	31
2.14	Initial Mach profile with $M_0 = 8.0$ of the improved set up.	33
2.15	Stationary shock solution for AUSM flux at T=10000. Except that the shock profile is slightly smeared, the solution looks ‘good’ (at least for now).	33
2.16	Shock solution for the AUSM flux at T=25000. Notice that we now have a stage 1 instability with long waves instead of short waves as depicted earlier.	34
2.17	Shock solution for AUSM+ u flux at T=30000 with stage 1 instability (short waves).	34
2.18	Shock solution for AUSM flux at T=75000 in which the shock is sloshing left and right repeatedly. This suggest that there is still an inherent instability which can be implied from the residual history.	35
2.19	Shock solution for AUSM+ u flux at T=100000. The shock is also sloshing left and right repeatedly here.	35
2.20	Residual plot for the pure AUSM flux. The growth of residual indicates the growth of shock instability. Note that the residual is relatively high even after 100000 time steps which implies that the inherent instability does not go away.	36
2.21	Residual plot for the pure AUSM+u flux.	36
2.22	Vorticity contour plot for the AUSM+u flux at T=30000. Notice that spurious vorticity is produced along the shock.	37

2.23	Enstrophy plot for the AUSM+u flux solving 1 1/2 dimensional carbuncle with $M_0 = 8.0$. Note that the generation of spurious vorticity generation peaks at approximately the time that the shock instability occur ($T=25000$).	37
2.24	L2-norm of velocity divergence squared downstream of the shock.	41
2.25	L2-norm of enstrophy (vorticity squared) downstream of the shock.	41
2.26	Initial condition for the stationary shock with $M_0 = 8$ and $\epsilon = 0.7$ using Roe solver.	44
2.27	Solution at $T=1000$	44
2.28	Stationary shock at $T=1700$. Note that the solution returned to its initial values.	45
2.29	Stationary shock at $T=3400$. The intermediate cell moves again and the cycle repeats itself indefinitely Note that this process is repeatable with other γ and other sufficiently high upstream Mach numbers.	45
2.30	Residual plot for the one dimensional carbuncle. Clearly, there is an inherent instability hence the solution does not converge.	45
2.31	This is a steady state solution of a mono atomic gas $\gamma = 5/3$ with upstream Mach number $M_0 = 6.0$. Note the shock structure exhibit kinks instead of a smooth profile along the shock. This is because the shock has adjusted itself to achieve local stability (courtesy of Roe et. al [86]).	49
2.32	Critical Mach Number versus γ for the Roe flux. For $\gamma = 1.4$, $M_{crit} = 6.5$ in one dimension and 2.0 in two dimensions. The results in one dimension agrees with Barth's but slightly higher than Robinet et. al's in two dimension. Perhaps the difference is we did not include the case as unstable unless it reaches Stage 2.	50
2.33	The converged AUSM and AUSM+u solution for the one dimensional carbuncle test with $M_0 = 8.0$ and $\epsilon = 0.7$. Note that both fluxes do not suffer from carbuncle for any ϵ , γ and M_0	54
2.34	Notice how fast the residual decays to zero.	54
3.1	Grid Representation	63
3.2	Flux Interface Requirements for Preserving Vorticity. Note that the interface pressures must must be evaluated as averaged quantities at the vertices (denoted by pairs of arrow).	64
3.3	The Rotated Richtmyer Scheme. Dash lines indicate half-step whereas solid lines indicate full-step.	67
3.4	Limiting procedure. First, compute the slopes at the vertices via compact differencing using values at four surrounding cells (line with arrows). Then perform limiting on these slopes based on adjacent vertices (L,R) and (B,T) to the middle vertex M dimension by dimension (thick solid lines) before performing half step.	71

3.5	Vorticity Preserving Requirements	73
3.6	Domain D with subdomain bounded by vertex 1,2,3 and 4 defined by D_s . To preserve vorticity at cell O, all ν must be identical at vertices surrounding the cell.	79
3.7	Vorticity correction by changing cell velocities. Assume we have a clockwise spurious vorticity $\Delta\omega$ at a vertex, we introduce a counter-clockwise correctional vorticity. Although this leads to solving an a Poisson problem but it ensures vorticity is preserved locally.	82
3.8	Pressure contours (RR scheme) at T=1.	89
3.9	3D View.	89
3.10	U-velocity contours (RR scheme) at T=1.	89
3.11	3D View.	89
3.12	Vorticity contours (RR scheme) at T=1.	89
3.13	3D View. Note irrotationality.	89
3.14	Pressure contours (RR-S scheme) at T=1.	90
3.15	3D View.	90
3.16	U-velocity contours (RR-S scheme) at T=1.	90
3.17	3D View.	90
3.18	Vorticity contours (RR-S scheme) at T=1.	90
3.19	3D View. Note generation of spurious vorticity when a limiter is applied.	90
3.20	Pressure contours (RR-S-VP scheme) at T=1.	91
3.21	3D View.	91
3.22	U-velocity contours (RR-S-VP scheme) at T=1.	91
3.23	3D View.	91
3.24	Vorticity contours (RR-S-VP scheme) at T=1.	91
3.25	3D View. Note with the flux-correction, irrotationality is preserved.	91
3.26	Pressure contours (RR scheme) at T=100.	92
3.27	3D View.	92
3.28	U-velocity contours (RR scheme) at T=100.	92
3.29	3D View.	92
3.30	Vorticity contours (RR scheme) at T=1.	92
3.31	3D View. Irrotationality is maintained.	92
3.32	Pressure contours (RR-S scheme) at T=100.	93
3.33	3D View.	93
3.34	U-velocity contours (RR-S scheme) at T=100.	93
3.35	3D View.	93
3.36	Spurious Vorticity contours (RR-S scheme) at T=100.	93

3.37	3D View. We have spurious vorticity of $O(0.01)$	93
3.38	Pressure contours (RR-S-VP scheme) at T=100.	94
3.39	3D View.	94
3.40	U-velocity contours (RR-S-VP scheme) at T=100.	94
3.41	3D View.	94
3.42	Vorticity contours (RR-S-VP scheme) at T=100.	94
3.43	Note with flux-corrections, we have preserved vorticity even after T=100.	94
4.1	Grid Representation	98
4.2	Removing spurious vorticity with flux-correction. Assume we have a clockwise spurious vorticity $\Delta\Omega^{n+1}$ at a vertex, we introduce a counter-clockwise correction altering the momenta. Note that this correction does not change the discrete divergence of momentum within the vertex control volume.	101
4.3	Control volume for vorticity is marked by dashed-lines. For a particular CV with centroid C, the momentum divergence at the vorticity interface is an averaged-differencing utilizing vertices [C,E] for interface (1,4); [C,N] for interface (1,2); [C,W] for interface (2,3); [C,S] for interface (3,4). For vorticity advection, each interface is governed by pairs for upwinding, also denoted as [C,E], [C,N], [C,W] and [C,S]. The interface velocities are just the averaged of velocities at (1,4), (1,2), (2,3) and (3,4).	106
4.4	Vorticity at T=0 with 80 x 80 cells	109
4.5	Exact Vorticity at T=180	109
4.6	First order Hancock-Roe at T=180	110
4.7	First order Hancock-Roe-VC1 at T=180	110
4.8	Second order Hancock-Roe-Superbee at T=180	111
4.9	Second order Hancock-Roe-Superbee-VC2 at T=180	111
4.10	Normalized Enstrophy for various schemes using 80 x 80 cells. Note that the exact enstrophy is unity and the error of VC2 scheme is less than 2 percent after T=450 unlike the first order Hancock (85 percent).	112
4.11	Normalized L2-Norm of ω (80 x 80) for second order schemes at various sub-iteration steps. There is only about 1-2 percent difference when applying 50, 100 or 2000 sub-iterations using the VC2 scheme.	112
4.12	L2-norm of pressure (slope 1.7) and u-velocity (slope=1.87) at T=60. This implies that the correctional step in VC2 does not reduce much of its second order accuracy.	113
4.13	L2-norm of ω at T=60. Note that VC2 is twice more accurate than conventional second order Hancock-Roe-Superbee when predicting vorticity.	113

4.14	Mach profile for first order Roe at T=1000	114
4.15	First order Hancock-VC at T=10000. Note that there is first stage instability.	114
4.16	Vorticity contours for first order Hancock-Roe) at T=1000	115
4.17	Vorticity contours for first order Hancock-VC at T=10000. Even though we have instability within the shock, however, we no longer have spurious vorticity.	115
4.18	Residual and enstrophy plot for the 1 1/2 dimensional carbuncle using Hancock-VC scheme. Note that the residual grows to $O(0.1)$ and remains oscillatory for a while and then decays. The enstrophy remains machine zero.	116
4.19	Sub-iterations versus time-step plot for the 1 1/2 dimensional carbuncle using Hancock-VC scheme.	117
5.1	Dual interpretations of the updated scheme. The solid line represents residual distribution scheme. The dashed line represent finite volume scheme	121
5.2	The Riemann Problem for Burgers equation. The left flux solution means the interface is biased (upwinded) to the left flux. Likewise, right flux solution means biased to the right flux. The line that splits quadrant 2 into two regions represents a stationary shock region whereas the sonic point rarefaction region is denoted by broken lines and is omitted for Roe-solver.	122
5.3	Test 1-IC Stationary Shock	132
5.4	Test 2-IC Moving Shock	132
5.5	Test 1-Exact Riemann solver	133
5.6	Test 1-Roe solver	133
5.7	Test 1-EC-R solver	133
5.8	Test 1- EC-R solver with entropy fix 1	133
5.9	2nd order EC-R solver using harmonic limiter (Test 1) with spurious over/undershoots present.	134
5.10	2nd order EC-R solver (with entropy fix 1) using harmonic limiter for Test 1.	134
5.11	EC-R solver with entropy fix 2 (Test 1). Note that the rarefaction region is slightly smoother than the one produced with entropy fix 1.	134
5.12	2nd order EC-R solver (with entropy fix 2) using harmonic limiter for Test 1.	134
5.13	Test 2-Exact Riemann solver	135
5.14	Test 2-Roe solver	135
5.15	Test 2-EC-R solver	135
5.16	Test 2-EC-R solver with entropy fix	135

5.17	2nd Order EC-R flux with harmonic limiter for Test 2. Note that there are small spurious over/undershoots even with a limiter being applied.	136
5.18	2nd order EC-R solver (with entropy fix) using harmonic limiter	136
5.19	Test 3-T=0	138
5.20	Test 3-Compression and Expansion waves at T=1.	138
5.21	Test3-Compression and Expansion waves at T=2.	138
5.22	Slope of Compression begins to steepen at T=4 but there is only small differences between the 3 methods.	138
5.23	Test3-Shock forms at T=6. Note that there is spurious overshoot for the flux function without entropy fix.	139
5.24	Test3-Decaying of shock T=20. There is still spurious overshoot for the flux function without entropy fix.	139
5.25	Test 3-The normalized difference between numerical velocities predicted with and without entropy fix at T=1.	140
5.26	Test 3-The normalized difference between numerical velocities predicted with and without entropy fix at T=2.	140
5.27	Test 3-The normalized difference between numerical velocities predicted with and without entropy fix at T=4.	140
5.28	Test 3-The normalized difference between numerical velocities predicted with and without entropy fix at T=5 just before shock forms. Note there is at most 5-6 percent difference.	140
5.29	The second order results for Test 3 using the EC-R flux with harmonic limiter. Note that even with the limiter being applied, there are spurious overshoot and undershoots if the entropy fix is not used.	141
5.30	Test 4- $u_0 = 0.0$ at T=0	142
5.31	Test 4- $u_0 = 0.0$ at T=2.	142
5.32	Test 4- $u_0 = 0.0$ at T=6.	142
5.33	Test 4- $u_0 = 0.0$ at T=10.	142
5.34	Test 4- $u_0 = 1.0$ at T=0	145
5.35	Test 4- $u_0 = 1.0$ at T=4	145
5.36	Test 4- $u_0 = 1.0$ at T=9.	145
5.37	Test 4- $u_0 = 1.0$ at T=20.	145
5.38	Test 4- $u_0 = 5.0$ at T=0	146
5.39	Test 4- $u_0 = 5.0$ at T=8	146
5.40	Test 4- $u_0 = 5.0$ at T=20.	146
5.41	Test 4- $u_0 = 5.0$ at T=50.	146
5.42	Test 5-Results for 1st order Roe and EC1-R (with entropy fix) fluxes.	147
5.43	Test 5-EC1-R flux (no entropy fix) solution. Not much difference with the above contour plots.	147

5.44	The cross sectional cut for Roe and EC1-R (fix) fluxes across the shock.	148
5.45	The EC1-R (no fix) flux across the shock. The solution is not monotone.	148
5.46	The cross sectional cut for Roe and EC1-R (fix) fluxes across the compression waves.	148
5.47	The EC1-R (no fix) flux across the compression waves.	148
5.48	The second order EC-R (fix) flux with the Superbee limiter.	149
5.49	The cross sectional cut across the shock for the EC-R (fix) with Superbee.	149
5.50	The cross sectional cut across the compression wave for the EC-R (fix) with Superbee.	149
6.1	Dual interpretations of the updated scheme. The solid line represents residual distribution scheme. The dashed line represent finite volume scheme	154
6.2	Two adjacent cells separated by a common interface with normal direction \vec{n}_{LR}	169
6.3	EC1-RV1 scheme (Roe averaging) at T=1000.	171
6.4	A-R and EC1-RV2 schemes at T=1000.	171
6.5	A-R scheme at T=1000.	172
6.6	EC1-RV2 at T=17.	172
6.7	EC1-RV2 with entropy fix at T=17.	172
6.8	2nd Order EC1-RV2 (Harmonic) at T=17.	172
6.9	EC1-RV2 for $M_0 = 1.5$. Note there are spurious overshoot and undershoot near the shock.	175
6.10	EC1-RV2 (with entropy fix) at $M_0 = 1.5$	175
6.11	EC1-RV2 at $M_0 = 2.0$	175
6.12	EC1-RV2 (with entropy fix) at $M_0 = 2.0$	175
6.13	EC1-RV2 at $M_0 = 4.0$	176
6.14	EC1-RV2 (with entropy fix) at $M_0 = 4.0$	176
6.15	EC1-RV2 for $M_0 = 8$. Note there is a small undershoot downstream of the shock.	176
6.16	EC1-RV2 (with entropy fix) at $M_0 = 8.0$. Shock is slightly smeared.	176
6.17	EC1-RV2 at $M_0 = 16.0$	177
6.18	EC1-RV2 (with entropy fix) at $M_0 = 16.0$	177
6.19	EC1-RV2 at $M_0 = 20.0$	177
6.20	EC1-RV2 (with entropy fix) at $M_0 = 20.0$. The shock is more diffused when compared with no entropy fix. The smearing can be improved using a second order scheme.	177

6.21	Second order EC1-RV2 (fix) at $M_0 = 20.0$ using Minmod limiter.	178
6.22	Second order EC1-RV2 (fix) at $M_0 = 20.0$ using Harmonic limiter. The shock profile is much 'tighter'.	178
6.23	Density plot of Sod's problem for A-R flux.	180
6.24	EC1-RV2 flux with fix. Note how its solution is comparable to A-R's.	180
6.25	Second order A-R flux with harmonic limiter. The contact is now captured with only 4 intermediate cells.	180
6.26	Second order EC1-RV2 flux (fix) with harmonic limiter. Almost identical to the second order A-R flux.	180
6.27	Density plot for A-R flux before collision of the waves with solid lines representing exact solution.	181
6.28	Density plot of the EC1-RV2 (fix) before collision of the waves.	181
6.29	Density plot for A-R flux after the collision of the waves.	181
6.30	EC1-RV2 flux with fix. Although the solution is not as sharp as the exact solution, it is comparable to A-R's.	181
6.31	Mach profile of 1D carbuncle using A-R flux at $T=10000$	187
6.32	Mach profile of EC1-RV2 flux at $T=10000$	187
6.33	Density profile of A-R flux at $T=10000$	187
6.34	Density profile of EC1-RV2 flux at $T=10000$	187
6.35	Residual plot of A-R flux.	187
6.36	Residual plot of EC1-RV2.	187
6.37	A-R flux Mach contours of the 1 1/2 dimensional carbuncle ($M_0 =$ 8.0) at $T=10000$	188
6.38	EC1-RV2 flux Mach contours at $M_0 = 8.0$. Note the cross-sectional solution are identical to Fig. 6.32.	188
6.39	A-R flux density contours at $T=10000$ with $M_0 = 8.0$	188
6.40	EC1-RV2 flux density contours with $M_0 = 8.0$	188
6.41	Residual plot of A-R flux.	188
6.42	Residual plot of EC1-RV2.	188
6.43	EC1-RV2 flux with entropy fix Mach contours with $M_0 = 8.0$	189
6.44	The cross-sectional solution of EC1-RV2 (fix) flux in which mono- tonicity is achieved.	189
6.45	Density contours of the EC1-RV2 flux with entropy fix.	189
6.46	The cross-sectional density solution of EC1-RV2 (fix).	189
6.47	2nd order EC1-RV2 (fix) with Minmod at $M_0 = 8.0$	190
6.48	The cross-sectional solution of 2nd order EC1-RV2 (fix) having a tighter shock.	190
6.49	2nd order EC1-RV2 (fix) with Minmod at $M_0 = 20.0$	190
6.50	The cross-sectional 2nd order solution at $M_0 = 20.0$	190

6.51	The total enstrophy (vorticity squared) within the computational domain for each time-step for the EC1-RV2 flux when solving the 1 1/2 dimensional carbuncle. Since total enstrophy is machine zero, we can conclude that by controlling entropy we have prevented the generation of spurious vorticity and shock instability all together.	191
6.52	A-R flux at $M_0 = 20.0$. A typical carbuncle profile.	192
6.53	The quadrilateral 80 x 160 cells.	192
6.54	EC1-RV2 flux at $M_0 = 20.0$ with no carbuncle.	192
6.55	EC1-RV2 captures shock with only 3 intermediate cells.	192
6.56	Mach profile along $y = 0$ (stagnation region) for A-R flux. Note how the shock profile exhibit violent spurious oscillations in the stagnation region.	193
6.57	EC1-RV2 flux without entropy fix. A much better shock profile, with 3 intermediate cells but the solution is not monotone.	193
6.58	Density profile along $y = 0$ (stagnation region) for A-R flux. The solution is completely off.	193
6.59	EC1-RV2 flux without entropy fix. A much better solution compared to A-R flux but spurious overshoots are present.	193
6.60	U profile along $y = 0$ (stagnation region) for A-R flux. The negative velocity represents reverse flow within the stagnation region.	194
6.61	EC1-RV2 flux without entropy fix. By far, a much better solution at the stagnation region in which the velocity drops rapidly after crossing the shock and slowly decreases to zero as the fluid approaches the stagnation point	194
6.62	Pressusre profile along $y = 0$ (stagnation region) for A-R flux. The solution is completely off.	194
6.63	EC1-RV2 flux without entropy fix. A much more reasonable solution although not monotone.	194
6.64	The residual (in absolute value) plot for the A-R flux for Mach 20 flow past a two-dimensional cylinder. Note the oscillations depict shock instability. By the time the solution goes to steady-state, it would have produced a spurious but weakly consistent solution of the Euler equations.	195
6.65	The residual (in absolute value) plot for the new flux function EC1-RV2 predicting the Mach 20 flow past a two dimensional cylinder. The residual goes to machine zero smoothly for the most part.	195
6.66	EC1-RV2 flux with entropy fix at $M_0 = 20.0$ with no carbuncle.	196
6.67	Stagnation point predicted by AR flux at $M_0 = 20.0$. Note how its location is completely off.	196
6.68	Stagnation point predicted by EC1-RV2 flux with entropy fix at $M_0 = 20.0$	196

6.69	The Mach profile of EC1-RV2 flux with entropy fix at $M_0 = 20.0$. Monotonicity is achieved.	197
6.70	Density profile along $y = 0$ (stagnation region) for EC1-RV (fix) flux at $M_0 = 20.0$. A much improved solution compared to solution without entropy fix.	197
6.71	U-velocity profile for EC1-RV2 flux with entropy fix at $M_0 = 20.0$. . .	197
6.72	Pressure profile for EC1-RV2 flux with entropy fix at $M_0 = 20.0$. . .	197
6.73	EC1-RV2 flux with entropy fix at $M_0 = 30.0$ with no carbuncle. . .	198
6.74	Stagnation point predicted by EC1-RV2 flux with entropy fix at $M_0 = 30.0$	198
6.75	The Mach profile of EC1-RV2 flux with entropy fix at $M_0 = 30.0$. Monotonicity is still achieved but the shock profile is slightly broader than those produced with $M_0 = 20.0$	199
6.76	Density profile along $y = 0$ (stagnation region) for EC1-RV (fix) flux at $M_0 = 30.0$	199
6.77	U-velocity profile for EC1-RV2 flux with entropy fix at $M_0 = 30.0$. .	199
6.78	Pressure profile for EC1-RV2 flux with entropy fix at $M_0 = 30.0$. .	199
6.79	The normalized stagnation pressures (P_s/p_0) at the cylinder surface ($y=0$) for various upstream Mach numbers M_0 . Note the AR flux produces stagnation pressure that deviates more than 50 percent than the exact stagnation pressure. The EC1-RV2 flux only produces at most 2 percent error.	200
6.80	The normalized stagnation temperatures (T_s/t_0) at the cylinder sur- face ($y=0$) for various upstream Mach numbers M_0 . The EC1-RV2 flux only produces about 2 percent error compared to the exact stag- nation temperature as opposed to 20 percent error produced by the AR flux.	200
6.81	EC1-RV2 (fix) with 20×200 cells.	201
6.82	Zooming into the mesh of 20×200 cells.	201
6.83	EC1-RV2 (fix) with 20×400 cells.	201
6.84	Zooming into the mesh of 20×400 cells.	201
6.85	EC1-RV2 (fix) with 20×600 cells.	201
6.86	Zooming into mesh of 20×600 cells.	201
7.1	A three dimensional cell with vorticity location and flux corrections. .	207
7.2	A planar view of computing vorticity using four neighboring cells. .	211
C.1	A sample arbitrary cell with normal and tangential velocities (q, r) w.r.t to a particular interface.	222
G.1	Product of two operators on cells and vertices	231

H.1	A sample control volume with a right running shock. Assume that the shock has thickness $\rightarrow 0$.	232
-----	--	-----

LIST OF TABLES

3.1	L2-Norms of the three schemes at T=1.	87
3.2	L2-Norms of the three schemes at T=5.	88
3.3	L2-Norms of the three schemes at T=10.	88
3.4	L2-Norms of the three schemes at T=100.	88
6.1	Stability limit for various upstream conditions.	174

LIST OF APPENDICES

A.	Scaling Matrix for the Dissipative Flux	214
B.	Two Dimensional Hancock Scheme	218
C.	Two Dimensional Finite Volume Discretization of the EC1-RV2 Flux .	221
D.	Two Dimensional Finite Volume Discretization of the Roe Flux . . .	226
E.	The Logarithmic Mean	227
F.	Entropy Fix for EC1-RV2 Flux: Generating the "Correct" Sign of Entropy Production	228
G.	Discrete Operators	230
H.	Jump Conditions	232

NOMENCLATURE

<u>Symbol</u>	<u>Description</u>
u	Conservative variables-vector
V	Characteristic variables-vector
v	Entropy variables-vector
w	Primitive variables-vector
<i>S</i>	Physical entropy = $\ln(p) - \gamma \ln \rho$
<i>U</i>	Entropy-function = $\frac{-\rho S}{\gamma-1}$
<i>F</i>	Entropy-flux = $\frac{\rho u S}{\gamma-1}$
(f , g)	Conservative flux vectors
(\tilde{f} , \tilde{g})	Modified conservative flux vectors
R	Right eigenvector matrix
L	Left eigenvector matrix = \mathbf{R}^{-1}
S	Diagonal scaling matrix
C _x	Flux-correctional vector in x-direction
C _y	Flux-correctional vector in y-direction
<i>L</i> _{ω}	Discrete curl Operator
<i>a</i>	Speed of sound
Δt	Time step
<i>h</i>	Uniform mesh size

Greek

ω	Curl of velocity = $\nabla \times \vec{u}$
Ω	Curl of momentum = $\nabla \times (\rho \vec{u})$
Φ	Divergence of momentum = $\nabla \cdot (\rho \vec{u})$
γ	Fluids specific heats
λ	Fluids wave speeds
Λ	Shock speed
$\boldsymbol{\Lambda}$	Diagonal eigenvalue matrix
$\tilde{\boldsymbol{\Lambda}}$	Modified diagonal eigenvalue matrix = $\boldsymbol{\Lambda} \mathbf{S}$
$\mu_{x/y}$	Discrete averaging operator in x/y direction
$\delta_{x/y}$	Discrete differencing operator in x/y direction
$\mu_x \delta_x$	Central differencing in x-direction
$\mu_y \delta_y$	Central differencing in y-direction
$\mu_y \delta_x$	Compact differencing in x-direction
$\mu_x \delta_y$	Compact differencing in y-direction
$\Delta\omega$	Curl of velocity discrepancy
$\Delta\Omega$	Curl of momentum discrepancy

Subscripts

(i, j)	(x,y) cell coordinates
$(i \pm \frac{1}{2}, j)$	(x,y) coordinates of vertical cell-interface
$(i, j \pm \frac{1}{2})$	(x,y) coordinates of horizontal cell-interface
$(i \pm \frac{1}{2}, j \pm \frac{1}{2})$	(x,y) vertex coordinates
L	Left cell interface

R	Right cell interface
B	Bottom cell interface
T	Top cell interface

Superscripts

n	Discrete time level
k	Subiteration time level
lim	limiter being applied
-	arithmetic mean
ln	logarithmic mean

CHAPTER I

INTRODUCTION

From the first flight made by the Wright brothers, the field of aviation has been driven by the desire to fly faster and higher [3]. The 20th century marks an exponential growth in aircraft development both in speed and altitude [3], beginning in 1903 with the Wrights flying at 35 mph at sea level [32], progressing to 400 mph fighter planes at 30,000 feet in World War II [34], advancing to supersonic aircraft flying at 1200 mph (Mach 2) and cruising at 60,000 feet in the 60's [33] and finally topped by the space shuttle flying at Mach 25 from a 200-mile low earth orbit [35].

During the same period, the advent of high-speed missiles and spacecraft also took place [3], starting from the V2 rocket flying at over 5000 mph at an altitude of over 200 miles in 1949 [34], continuing to the Mach 25 intercontinental ballistic missiles and the developments of the spacecrafts Mercury, Gemini and Vostok in the 50's and 60's [35] before reaching the historic Mach 36 Apollo spacecraft taking men to moon and back in 1969 [2]. Either in the case of aircrafts, spacecrafts or missiles, flying at these extremely high-speeds is known as hypersonic flight.

During a lecture at the von Karman Institute, Belgium in 1970, P.L. Roe made a remark,

"Almost everyone has their own definition of the term hypersonic. If we were to conduct a public opinion poll among those present, and asked

everyone to name a Mach number above which the flow of the gas should properly be described as hypersonic, there would be a majority of answers round about five or six, but it would be quite possible for someone to advocate and defend, numbers as small as three, or as high as 12.”

Addressing his graduate class in gas dynamics at Rice University in 1962, H.K Beckmann said, “*Mach number is like an aborigine counting: one, two, three, four, many. Once you reach many, the flow is hypersonic.*”[11].

There is no precise Mach number limit in which the flow is deemed hypersonic but we will loosely refer to hypersonic flow if the flow Mach number is much greater than one¹. It is not crucial to determine hypersonic flow by its Mach number because hypersonic flow is best defined as that regime where certain physical flow phenomena which are neglected in supersonic speeds or lower become important [3], [11].

The most notable feature of hypersonic flow is the *high temperature* on the body surface [3], [11], [36]. At the free-stream conditions, the fluid has extremely high kinetic energy due to its extremely high velocity. The fluid will be decelerated to almost zero once it reaches the body and there will be an enormous transform of kinetic to internal energy. As a result, the temperature at the surface will rise giving tremendous heat transfer at the body. For a Mach 36 flow like the Apollo rocket, the body temperature may rise up 11,000 degrees Celsius² [3]. At this temperature, fluid molecules will dissociate and even ionize and chemical reactions may occur. Usually a hypersonic vehicle is protected by an ablative heat shield which is of a complex hydrocarbon nature and will chemically react at these high temperatures [3]. In other words, hypersonic flights are also characterized by *chemically reacting*

¹ $M = \frac{u}{a} \gg 1$ where u and a are the local fluid velocity and speed of sound.

²This is about twice the surface temperature of the sun.

flows [11],[37] which are often absent in supersonic or subsonic³ aerodynamics.

Another feature of hypersonic flow is *viscous interaction* [3]. As the high velocity hypersonic flow is slowed down by viscous effects within the boundary layer, by the same process described previously, there will be an enormous temperature rise increasing the viscosity coefficient⁴. This by itself will make the boundary layer thicker, displacing the inviscid flow⁵ outside the boundary layer causing a given body shape to appear thicker than it really is. As a result, the outer inviscid flow configuration is changed which will in turn, feed back to alter the growth of the boundary layer. It must be stressed that accurate predictions of both layers are critical to determine lift, drag and stability of hypersonic vehicles [37].

When a body is subjected to hypersonic flow, the shock forms much closer to the body as compared to those that are formed in supersonic flow, hence the term *thin shock layer* [3]. Across a shockwave, the density of the fluid increases and becomes progressively larger as the Mach number increases. By conservation of mass, the high density fluid will flow through smaller areas behind the shock which means that the distance between the shock and body is small. Near the stagnation region, it is of the same length scale with the boundary layer thickness. This implies that there will be shock-boundary layer interactions [36] which are usually ignored in most other aerospace problems.

³Subsonic flow is when $M = \frac{u}{a} \leq 0.8$, transonic is when $0.8 < M \leq 1.2$ and supersonic flow is in between transonic and hypersonic flows.

⁴For most fluid dynamics application, viscosity is assumed constant because for temperatures of 3000 degrees Celsius and below, its temperature dependence is almost negligible [11].

⁵For body subjected to a high Reynolds number flow, viscous (shearing) forces are confined to a very small region along the body. This region is called the boundary layer and its thickness is inversely proportional to the square root of the Reynolds number. Outside this region, we have the inviscid layer where inviscid forces (pressure and flow velocity) are dominant compared to viscous forces. The ratio of these two forces is the Reynolds number.

All of the above-mentioned hypersonic flow features are difficult to match and very costly to accommodate in ground-test facilities [11]. Roe [82] once said,

“The computer is attractive as a replacement for experiments that are difficult, dangerous or expensive, and as an alternative to experiments that are impossible”.

In other words, we can predict hypersonic flow through numerical simulations⁶.

Due to the extremely complex nature of hypersonic flow, its simulation is very challenging compared to predicting subsonic or supersonic flow [37]. For example, accurate simulation of heat transfer along the body of hypersonic vehicles requires accurate prediction of the boundary layer which in turn, is dependent on the inviscid layer. The inviscid layer, particularly at the stagnation region behind the shock is dependent on entropy being propagated along the streamlines⁷ across the shock. Any anomalies in the captured shock will create irregularities in entropy carried along streamlines from the shock. Presently, most numerical methods for predicting shocks in hypersonic flow are incapable of producing truly dependable shock solutions [36], [37]. In this thesis, our goal is to faithfully capture shocks in inviscid hypersonic flow. But before we proceed to do so, we need to understand the limitations and shortcomings of current numerical methods in inviscid flow.

1.1 A Brief History of Numerical Inviscid Flow Algorithms

Despite the complexity of fluid dynamics in general, most successful schemes in Computational Fluid Dynamics (CFD) are developed based on simple model

⁶This is the field of computational aerothermodynamics which is computational fluid dynamics added with high temperature gas effects on pressure, skin friction and heat transfer [37].

⁷A streamline is defined as the path line which is tangent to the local fluid velocity vector.

problems in one dimension. The simplest model is the linear advection equation $u_t + au_x = 0$, modelling fluid being advected or propagated constantly in some particular direction⁸. Although it is a very simple model, early attempts to solve it numerically beginning in the 50's had not been simple [70], [23], [51], [52], [54].

At that time, the schemes that had been developed to solve the linear advection equation had trouble with both diffusion and dispersion errors. First order schemes would propagate excessively diffused discontinuities whereas second order methods produced spurious oscillations around them [70], [53], [79], [66], [52], [22]. Furthermore, all of the schemes would have either lagging or leading phase errors compared to the true solution [53], [79].

There are many reasons for these drawbacks but the fundamental reason is due to the shortcomings of discretizing a continuous model. When we discretize, not all of the fluids physics are retained [84]. In CFD, we commonly choose a few physical properties of importance, then discretize the model in a way that will faithfully represent the selected physics and hope that most of the other properties will be retained or be reasonably accurate. Back in the early days of CFD, it was not all that clear which physical properties were important and should be chosen as the underlying physical mechanisms behind the algorithm, although there were a few candidates.

One strong candidate would be upwinding [23], which enforces information to travel in a correct physical direction and this can be done by including the physics of wave-characteristics. Conservation [52] is also important because it ensures that the fluid's mass, momentum and energy are neither unphysically created nor de-

⁸An example of fluid advection would be putting a dye in a streaming river and let it be transported by the river.

stroyed. It is natural to wonder if both of these attributes are attainable when fluid is discretized.

One way to combine them is via a finite-volume (FV) discretization⁹ of the fluid [38], [82], [106]. It is a one dimensional Eulerian approach where we define a control volume (CV) or a cell enclosing the fluid and let the fluid interact with other cells only through the cell-interfaces (boundaries). Hence, conservation is automatically satisfied. It must be emphasized that the FV concept is universal in any number of dimensions [20]. In one dimension, the cell interface is a point; in two dimensions it is an edge; in three dimension it is a face. However, the FV method requires explicit knowledge of fluxes at the interface in which upwinding can be implemented. Consequently, families of flux functions were born [38], [13], [54], [66], [89], [105] [82], [74].

There are the Lax-Wendroff family [54], [66], Flux Corrected Transport (FCT) [13] and the Flux Vector Splitting (FVS) [89], [105] just to name a few. These flux functions are based on mostly physical propagation normal to the interface [106]. However, as long as the fluids within the cells interact mostly normal to the cell interface, these flux functions are accurate enough for predicting most engineering problems in a fairly economical manner [24], [56]. In practice, the FV method is commonly used to solve not only simple one dimensional fluid dynamic problems but also complex multi dimensional problems with reasonable success [58], [18], [109].

The most famous flux function is perhaps the Godunov flux [38], [74], [82], [28]

⁹The FV technique is a discrete integral form of the fluids PDE's. This integral formulation is mathematically valid across discontinuities unlike the differential formulation or its discrete version, the finite difference (FD) method. This makes the FV technique superior than FD methods when computing flows with shocks. However, the FV technique has 'weak' or non-unique solutions of the PDE's so extra fluid conditions are required to narrow down the possible choices. The common practice is to include some form of entropy condition.

due to its apparently strong physical basis. The Godunov flux (or method) requires solving a Riemann problem at the cell interface¹⁰. Solving the Riemann problem exactly proved to be computationally expensive hence a class of approximate (or linearized) Riemann solvers were developed [74], [82], [28]. Roe's approximate Riemann solver [82] is arguably the most successful of these because it implements upwinding with minimal numerical dissipation, on account of successfully recognizing isolated discontinuities. This is a highly desirable trait in capturing contact discontinuities and shocks. One drawback is that it also captures the unphysical rarefaction shock but this can be remedied with Harten's entropy fix [43].

In spite of their huge impact on CFD, the original upwinded FV schemes were unable to circumvent Godunov's barrier theorem [38]. The theorem states that schemes that are linear when applied to linear problems, and that produce solutions free from spurious oscillations will be only at most first order accurate. This lead to the developments of nonlinear upwinded FV (or high resolution) schemes which deploy the concept of modifying the data through limiting before updating the scheme [13], [104], [43], [91].

Among the earliest to introduce limiting was van Leer [100], [101], [102], [103], [104] in the 70's in his series of paper regarding MUSCL type schemes. His concept was based on geometric considerations in one dimension. The idea is to allow data to be reconstructed as accurately as possible when there is no danger of spurious oscillations while clipping the data to first order accurate when there is a danger.

The concept of FV discretization coupled with upwinding and limiting proved

¹⁰A Riemann problem is defined as semi-infinite states of fluid separated by an interface. In the FV context, the two neighboring cells contain two fluid states separated by a common flux-interface of which solution of the fluid is given by the solution of the corresponding Riemann problem, at least for small times. At large times, information would arrive from other interfaces.

to be monumental because it greatly improved capturing of discontinuities and also tremendously lessened phase errors when solving the linear advection [83]. Moreover, these ideas were readily transported not only to nonlinear advection equation but also to almost any system of nonlinear hyperbolic PDE's¹¹ [21], [31], [109], [60].

These high resolution schemes however, were introduced mainly for predicting transonic flows in aerodynamics where only weak shocks are encountered [81]. Nevertheless, these schemes have been extensively used to predict moderately strong, steady shocks in supersonic flows and astrophysical problems with considerable success [58], [60]. It is therefore unsurprising that these schemes are also known as shock capturing methods¹². The shock capturing terminology is somewhat an overstatement, because the truth is, most shock capturing methods fall short when predicting strong shocks in hypersonic flows [76], [78], [75], [25], [36] which is a crucial element in designing reusable spacecraft and re-entry vehicles. Unfortunately, except for a few notoriously dissipative shock capturing methods, most other methods seem unable to capture strong shocks without producing numerical artifacts [78], [75], [25], [48], [36], [37]. The most infamous of these artifacts is the “*carbuncle*” phenomenon.

1.2 “Carbuncles”

Many authors have reported the presence of “carbuncles” when computing high speed flow past blunt bodies using shock capturing methods [76], [78], [75], [25], [48], [86], [27]. The earliest report was made by Peery and Imlay [76] when computing

¹¹Some examples include the system of traffic equations, the shallow water equations, the Euler equations, the Navier-Stokes Equations, Elastodynamics, Electromagnetics and the Magnetohydrodynamics (MHD) equations.

¹²This is as opposed to shock fitting methods [87] where knowledge of the shock location is known before hand to fit a suitable discontinuous function to represent the shock profile. This is not easy for complex problems even in one dimension let alone in multi dimensions.

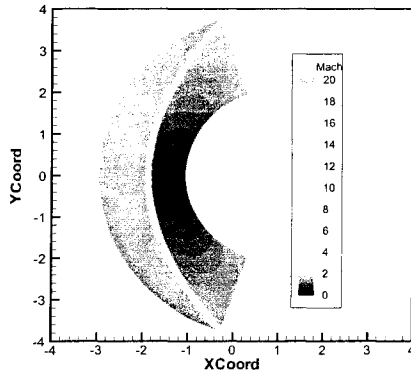


Figure 1.1: Physical solution of a cylinder subjected to $M=20$ flow.

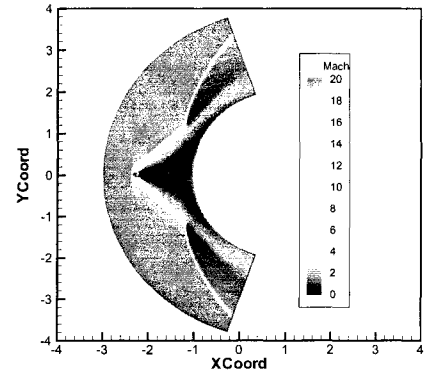


Figure 1.2: The carbuncle phenomenon which depicts a pair of oblique shocks replacing the bow shock around the stagnation region.

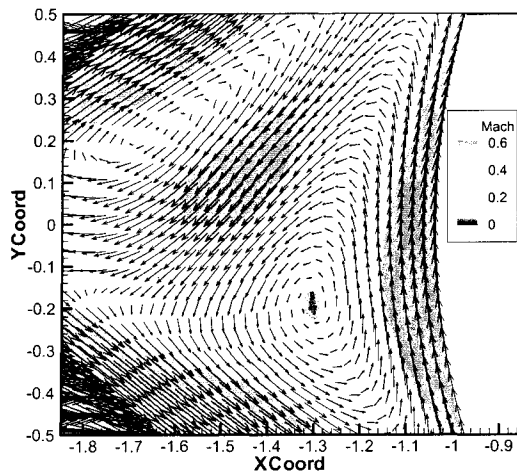


Figure 1.3: Zooming into the stagnation region of the Mach contours. Note how there is a circulation region behind the oblique shock which represents spurious vorticity. More importantly, observe that the stagnation point (depicted by the concentrated circular blue contours) is way off.

high supersonic or hypersonic flow past a circular cylinder. They observed that there were anomalies downstream of the bow shock around the stagnation region as depicted in Fig (1.2). These anomalies are usually in the form of two counter rotating *spurious vortices* (Fig 1.3). In other words, the code solves the problem as if there was a needle or spike protruding from the cylinder's stagnation point¹³. Instead of having a smooth bow shock, we have a pair of oblique shocks near the stagnation region [99]. These oblique shocks are weaker compared to the bow shock compromising the jump conditions. As a result, the stagnation conditions which are important to predict heat transfer in hypersonic flow are highly inaccurate. In fact, Fig 1.3 indicates the position of the stagnation point is not even on the body of the cylinder.

Many have proposed explanation and cures to the carbuncle problem [76], [75], [59], [62], [48], [25], [88] but none have been universally accepted [86]. The one proposed by Liou [62] is perhaps until now, the most commonly applied and was adopted in [48]. He hypothesized that in order to remove the carbuncles, the mass flux or momentum at the interface must be independent of the pressure difference. This is disturbingly unphysical. Moreover, the cures proposed in [62], [48], [88], [59] include artificial dissipation in the direction parallel to the captured shock. If this would be the way to cure the carbuncle, we should anticipate serious problems in computing shock-boundary-layer interactions [86]. Moreover, nobody has proposed how to include this adaptive dissipation on unstructured grids which is the most natural and efficient grid generation technique for curvilinear bodies. Of course, very dissipative flux functions like the Steger-Warming [89] and Harten-Lax-van Leer [60]

¹³This can be simulated experimentally [12].

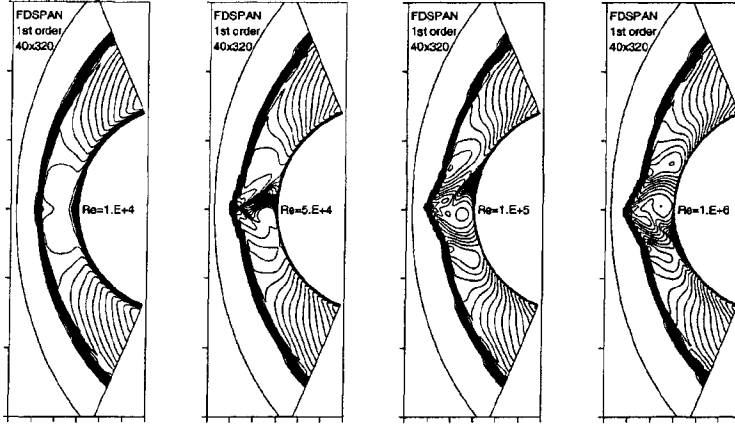


Figure 1.4: Navier-Stokes solution for cylinder subjected to $M=20$ flow for various Reynolds numbers: $10^4, 5 \times 10^4, 10^5$ and 10^6 (with permission from [75].)

fluxes may not produce carbuncles but they cannot capture contact discontinuities and tremendously diffuse boundary layers¹⁴. If the physical viscosity is included as in the Navier-Stokes equations, the tendency to form a carbuncle is reduced, but it disappears only at very low Reynolds number (Fig 1.4) [75]. Nor does it help to include the real gas¹⁵ effects that would accompany very strong shocks in the real world [27], [36], [37].

We will seek a more fundamental approach to cure the carbuncle. We see that there are shock distortions in the carbuncle problem but we do not know the root of this problem. *Could it just be poor vorticity handling? Or maybe it is due to*

¹⁴There are also schemes which adopt a hybrid of very dissipative and less dissipative fluxes, deploying the former near the shock and the latter away from shock but the basis of switch is somewhat ad hoc. Furthermore, it is unclear on how the switch would work for complex problems like shock-boundary layer interactions or shock-contact interactions.

¹⁵Real gas effects include fluid particles dissociations, ionizations and chemistry. These are crucial in high Mach number flow where high temperature gradients exist. In short, the fluid's specific heat constant γ is no longer a constant but a function of thermodynamic variables. For most fluid dynamics problem, we usually regard γ is constant (ideal gas) without losing too much accuracy.

imprecise control of entropy¹⁶? Or could there be more than one culprit involved here? In this thesis we will answer these questions.

It must be emphasized that for even for inviscid hypersonic flow, we need to include the physics of chemistry and real gas effects in order for the numerical simulation to be truly valid. However, we will not do so in this thesis. We leave it to future research to incorporate these effects, once the fundamental mechanisms are exposed.

1.3 Numerical Vorticity Control

One way to control vorticity is to use vorticity capturing methods which in compressible CFD, are still for the most part unresolved [85]¹⁷. As mentioned before, most schemes in compressible CFD are based on one dimensional physics. However, vorticity, which is the angular velocity of the fluid, is a multi dimensional feature.

In three dimensions, there are three components to the vector representing vorticity [8]. Two of them represent shear flow, which can be recognized by upwinding. The third is helicity or the dot product of vorticity-velocity and has no one dimensional analogue. It is hard to create helicity likewise is equally hard to destroy it once created. Helicity propagates over large distances and physically it is conserved along a streamline in inviscid flow. The contrails of vortices behind an aircraft are

¹⁶Current FV schemes solve directly for mass, momentum and energy but 'loosely' enforce physics of entropy or the second law of thermodynamics. The word 'loosely' here means that entropy may still be generated by truncation errors instead of solely by physical mechanisms. A good scheme or code usually produce spurious entropy within some 'reasonable' tolerance. The question is what is 'reasonable'?

¹⁷The vortex method or vortex blob approach enjoys more success when dealing with vorticity but at an extreme expense of computational cost [61]. These methods compute time accurate solution of the vorticity transport equation at the particle level. However, these computational methods are not conservative.

examples of propagated helicity.

There are a few issues concerning vorticity capturing [85], [47]. One is viscous vorticity generation or diffusion which is due to shearing effects of the fluid. Then there is the inviscid phenomenon of baroclinic generation. We also have inviscid vorticity propagation which includes vorticity advection, vortex stretchings and dilatational effects. Vorticity advection represents vorticity purely propagating with the fluid. On the other hand, the baroclinic contribution occurs when the fluid's density gradients are not parallel to its pressure gradients. When this happens, the fluid element's center of gravity does not coincide with its geometric center hence any pressure acting on the fluid element will cause it to spin¹⁸. An example for this would be non-isentropic flow. The vortex stretching effects are driven by the velocity changes along the direction of vortex lines. This effect accelerates vorticity when the vortex line is stretched and decelerates when it is compressed. Normally, vortex stretching is the term that dominates the evolution of small scale structure in turbulent flow [98]. The dilatation is due to fluid-compressibility effects. It is often neglected because most vorticity analysis has been done in the context of incompressible flow [8].

The viscous vorticity generation and the inviscid vorticity propagation components are all part of the vorticity transport equations [8]. However, we will not consider the viscous effects in this thesis. This is because accurate prediction of the viscous effects can be obtained by grid refinement but the numerical inviscid propagation may take place over large distances without the benefit of refinement. In other words, the inviscid components may produce spurious vorticity.

Morton and Roe [69] showed that almost all schemes would produce spurious

¹⁸If the density and pressure gradients are parallel, we would have no baroclinic contributions and it can be shown that this implies $\nabla p \times \nabla \rho = 0$

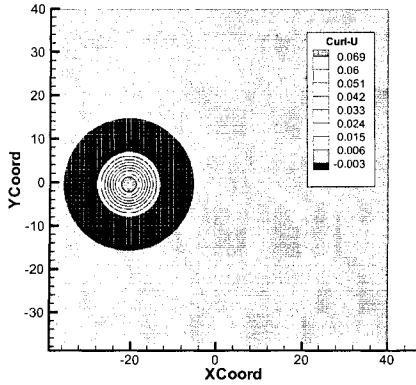


Figure 1.5: Initial vorticity solution with 80×80 cells.

vorticity out of truncation errors in the discretized *inviscid* momentum equations. They are about an order of magnitude smaller than the accuracy of the scheme but may become significant by accumulation over time. This implies that for irrotational flow, spurious vorticity may be generated (as demonstrated by the carbuncle problem) while for rotational flow, the schemes could artificially dissipate vorticity [47]. This suggests that we should focus our efforts on inviscid flow so that genuine vorticity capturing methods can be developed.

One possible approach is to use high order schemes to reduce generation of spurious vorticity¹⁹. These schemes however, require larger stencils and hence are computationally expensive and generally are not robust [44]. Using a compact but more complicated scheme such as the Discontinuous Galerkin (DG) method requires smaller stencils but needs storage for higher order moments, thus extensive memory space is still needed [64]. Also, it is unclear how to incorporate the physics of diffusion (viscous effects) to DG methods although a beginning has been made [108].

¹⁹Some examples of high order schemes are ENO, WENO and residual distribution schemes. There are also schemes from the finite element (FE) context which includes Galerkin and Discontinuous Galerkin methods.

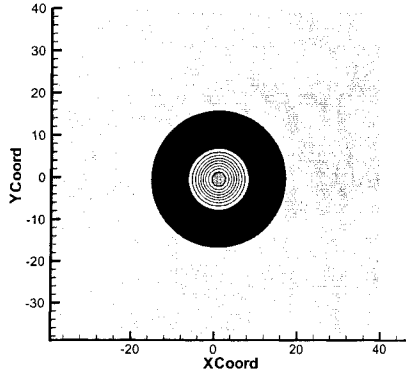


Figure 1.6: Exact vorticity contour solution at $T=480$ on 80×80 cells.

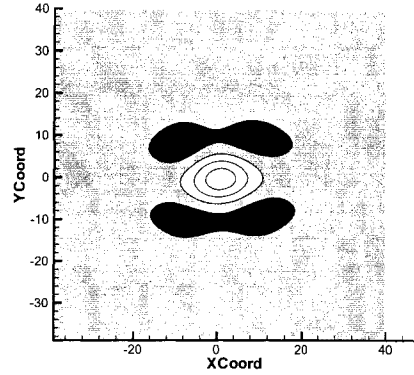


Figure 1.7: Vorticity contour solution of the first order Roe-flux at $T=480$ on 80×80 cells.

An alternative is to modify the existing low-order but robust finite volume schemes to satisfy the vorticity transport equations. The first attempt was done by Morton and Roe [69] for the linear wave equations. A similar approach was made by [30] but still in the context of linear equations²⁰. In this thesis, we will present a novel approach of controlling vorticity (or vorticity capturing) for nonlinear equations.

It must be emphasized that the application of accurate vorticity capturing is not only limited to predicting strong shocks or curing the carbuncle. In aerospace engineering, there are many problems requiring accurate prediction of vorticity, such as helicopter analysis, high-lift systems and unsteady flight [85], [90] [72], [20]. In helicopter analysis or VTOL (Vertical Take-Off and Landing) flight, there is the blade-vortex interaction (BVI). BVI occurs when a helicopter performs a descending maneuver and its rotor-blades interact with the trailing vortices shed by the blades themselves. This interaction causes sudden changes in aerodynamic loading, leading

²⁰For the record, there are other techniques for predicting vorticity which include vorticity confinement, vortex methods, hybrid and finite element methods [85], [1], [90], [61].

to blade vibration and aerodynamic instability and consequently the undesirable chopping noise.

In high lift systems and unsteady flight, the study of trailing vortices are important. An example of the former would be a multi-element airfoil in which vorticity is generated from each element and these vortex systems will interact. The propagation and interaction of these vortices contribute to the overall lift and drag coefficients of the airfoil. In the latter, vortices are shed by the motion of pitch and roll of the aircraft at high angles of attack. The amount of vorticity being shed during aircraft maneuvers has a direct influence on the forces produced [72].

All of these problems will benefit from ‘good’ vorticity capturing methods.

1.4 Numerical Entropy Control

The physics of entropy or the second law of thermodynamics is very important in supersonic and hypersonic flow²¹. Yet, current schemes still do not enforce entropy condition in a precise manner [81]. For example, when solving the Euler equations with any finite volume method, we have conservation of the main variables (mass, momentum and energy) and we assume entropy is discretely conserved along the streamlines until a shock appears. However, there is no explicit mechanism within a common finite volume scheme to discretely preserve entropy. A test of a good scheme is that this condition be met within some reasonable error tolerance.

We also assume that by capturing only physical shocks, the second law of thermodynamics is not violated [56]. In the context of finite volume formulation, an entropy condition is deployed to some schemes to destabilize discontinuous rarefac-

²¹Entropy by definition is a measure of a systems state of chaos. The second law of thermodynamics states that entropy is preserved unless the flow is irreversible [4]. An example would be when the flow encounters a shock.

tion shocks into continuous profiles. The mechanism to enforce this, however, is a form of imprecise artificial dissipation.

Without an accurate and proper control of entropy, it is likely that entropy is spuriously created within the flow and it may be shown that this actually happens. For some schemes, improper handling of entropy may result an incorrect entropy production across a shock²². As a result, the second law of thermodynamics is locally unsatisfied. We suspect that the imprecise enforcement of the second law of thermodynamics is one of the reasons contributing to the failure of accurately capturing strong shocks.

It is possible that by including the concept of entropy more directly we can improve the current technology of capturing strong shocks. This can be achieved by insisting entropy conservation for smooth data and entropy consistency when a shock is encountered during the flux discretization process. The earliest known approach was done by Tadmor [92] in the 80's at semi-discrete level in one dimension. His flux function conserves entropy exactly for smooth data. However, the fluxes are computationally expensive and are unstable as soon as a shock forms. Roe [81] developed a more practical entropy conserving flux to present some hope of enforcing a precise entropy condition.

To overcome shock instability, we need to produce entropy across a shock²³. Schemes that satisfy this property are classified as entropy-stable schemes. Roe devised an entropy-stable flux function [81] in which requires some form of averaging which is relatively simple but incomplete. We will present a complete entropy-stable

²²We will witness that this happens for the original Roe-flux when capturing a strong stationary shock in chapter 2.

²³Stability proofs are usually given in terms of mathematical entropy, which is negative of the physical entropy S , can be defined as positive and always decreases.

flux function in this thesis.

However, an entropy-stable scheme still does not generate the precise entropy production across a shock. Schemes that produce ‘enough’ entropy across shocks such that the solution is monotone and conserves entropy elsewhere are defined as entropy-consistent schemes. We will formulate an entropy-consistent flux function and elaborate and validate all of these ideas more rigorously in this thesis, which will be organized as follows.

1.5 Thesis Outline

In chapter 2, we will re-introduce the carbuncle phenomenon in a more detailed fashion. We will begin with some review both analytically and numerically. We will also introduce the simplified carbuncle problems both in 1 1/2 and 1 dimensions and how these simplified versions assist our investigation and improve our understandings on the subject.

We will introduce the concept of vorticity preservation in two dimensions in chapter 3. We will begin with the linear wave equations specifically starting from the work of Morton and Roe. We will continue their work by including a process of limiting and discuss the shortcomings of their elegant idea. The methodology of vorticity correction will be introduced here.

One of the goals of this research is to develop a second order vorticity capturing scheme solving the Euler equations in three dimensions. However, we will introduce the concept first in two dimensions and this will be the subject of chapter 4. The scheme will reduce to the implemented finite volume method in one dimension, but in higher dimensions will also locally satisfy discrete vorticity transport equations. This will be the new ideology of vorticity capturing. For applications, we will use

the scheme to model a travelling vortex and compare its quality with conventional finite volume method based on Roe-solver. We will then utilize the scheme to attack the carbuncle problem.

In chapter 5, we will introduce the concept of entropy conservation law for a scalar equation, specifically, the inviscid Burgers equation. In a general mathematical context, entropy is defined as a convex function that satisfies certain properties. For the Burgers equation, there are many choices of such function but we will select the one that is the most mathematically convenient and at the same time bears some physical interpretation. Once entropy is defined, we will thoroughly discuss the concepts of entropy stability and consistency. Then, we will derive an entropy consistent scheme for the Burgers equation. Finally, we will include some numerical examples to demonstrate the quality of the scheme.

In chapter 6, we will discuss the concept of entropy conservation law applied to the system of Euler equations. We will begin with its history and the current state of the technology, discussing the limitations and shortcomings in more detail. Then we will introduce Roe's entropy conserving flux function as a practical approach to conserve entropy and enforce stability. We will extend his work by including entropy consistency and present the complete averaged states for entropy stability. Finally, we will apply the scheme to the carbuncle problem in 1, 1 1/2 and 2 dimensions.

Chapter 7 will draw a conclusion to this thesis and will discuss some possible extension of the current work.

CHAPTER II

THE CARBUNCLE PHENOMENON

2.1 Introduction

Numerical shock prediction is a very important aspect of computing aerodynamic flows. Earlier attempts were made in the shock fitting context [68], [87] which requires the knowledge of the shock location before-hand in order to place a suitable discontinuous function to represent the shock. Although this idea works well in one dimension however, it becomes restrictively complex in multi dimensions [57]. An alternative to this idea would be shock capturing where the code would naturally recognize shocks that are forming, or those which are already present. We have briefly discussed shock capturing methods in the previous chapter and will not delve further into details of this idea but would refer the interested reader to some references [38], [82], [106], [43], [56]. In short, shock capturing methods are more successful than the shock fitting methods and have become the foundation of aerodynamic computations. However, there are still limitations to the shock capturing techniques particularly when dealing with strong shocks.

The mathematical principle of shock capturing is based on the Lax-Wendroff Theorem [54] stating that conservation plus stability yield convergence to a *weak solution*. Conservation is satisfied with a finite volume method while stability can

be obtained by some form of upwinding of the numerical fluxes. The question is whether all of the converged weak solutions are truly the ones that we desire¹?

The finite volume method represents the fluid by its mean value within a control volume which interacts with another control volume only through the flux-interface. This requires implementation of discrete flux functions at the interfaces. The most famous is perhaps the Godunov flux which requires a solution of the Riemann problem at the interface. In spite of its strong physical basis, the Godunov flux is unable to capture strong shocks without incurring numerical artifacts. This is also true for most shock-capturing methods except for a few extremely dissipative ones [75],[25],[78]. The most commonly observed artifact is the carbuncle phenomenon².

The first to report the carbuncles were Peery and Imlay [76] for a flow past a circular cylinder using shock capturing methods. They observed that there seem to be anomalies downstream of the bow shock rather than a smooth configuration. This was also confirmed by several other authors [25], [88], [78]. Quirk [78] introduced a simpler version of the carbuncle in which a perturbed one-dimensional shock is propagated in a two dimensional setting. The shock perturbation is done by utilizing non-uniform grids. He observed that the shock would break up and behave similarly to carbuncles demonstrated in the flow past a cylinder. He hypothesized that this is a form of numerical instability.

There were attempts to examine the carbuncle problem from an analytical standpoint, in particular from the perspective provided by the mathematical instability of

¹As mentioned in chapter 1, usually some form of entropy condition is used to limit our choices but is this good enough?

²By definition of dictionary.com, a carbuncle is a painful localized bacterial infection of the skin and subcutaneous tissue that usually has several openings through which pus is discharged. In layman's view, this just acne hence in our context carbuncle is a numerical acne.

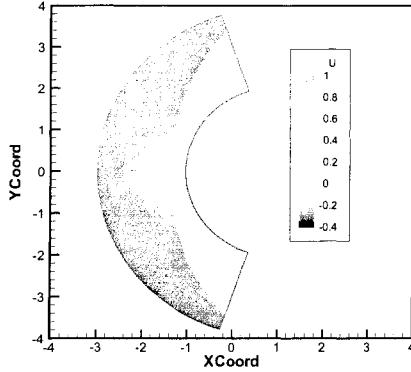


Figure 2.1: Shock captured by the Roe-method for hypersonic flow ($M=20.0$) past a cylinder. Instead of having a smooth bow shock for the U-velocity profile, there exists a pair of oblique shocks near the stagnation region. Behind these oblique shocks, negative velocities exist indicating a re-circulation zone.

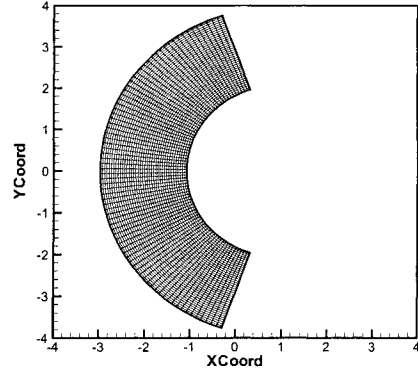


Figure 2.2: The quadrilateral structured grids with 80 cells in the radial direction and 160 cells in the angular direction.

an ideally narrow shockwave. This classical instability problem was first studied by Dyakov [26] and later presented by Landau and Lifschitz [49] and extended by Robinet et. al [80] in the context of the carbuncle. The idea is to use a linearized model of the fluid³ and find normal modes for subsonic flow downstream of the stationary normal shock. It is assumed that along the shock a sinusoidal perturbation is present while normal to it, a form of exponential perturbation exists. We will briefly present and discuss some of their results later in this chapter. The most important result that we want to highlight now is that the shock stability or instability depends only on the jump conditions imposed by the shock, which in turn depend on the equation

³In this case, it is the linearized Euler equations.

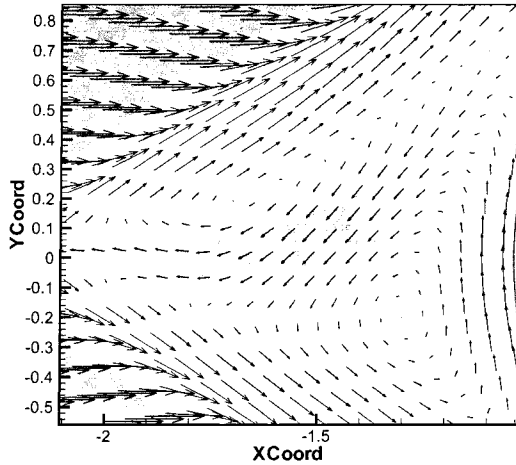


Figure 2.3: Zooming into the stagnation region of Fig. 2.1. Note how there is a circulation region behind the oblique shock which represents spurious vorticity.

of state. For an ideal gas, all shocks are stable [49], [80]. This further supports Quirk's [78] theory that the carbuncle is purely a numerical artifact.

Dumbser et. al [25] converted the discrete shock instability problem to a numerical eigenvalue problem. However, besides confirming that most shock capturing methods are susceptible to the carbuncle problem, they offer little insight into its mechanism. They nevertheless gathered extensive numerical data on the carbuncle. Pandolfi and d'Ambrosio [75] collected extensive numerical data for the supersonic flow past a cylinder⁴ in which carbuncle may or may not happen. They too concurred that most shock capturing methods are carbuncle prone.

Although there are no unstable perturbations to the downstream flow that are compatible with any displacement of an ideally narrow shock, it is possible that they

⁴They also included the effects of physical viscosity and observed that there is carbuncle even for relatively low Reynolds number ($O(10^4)$) which further supports the argument that carbuncle phenomenon is a pure numerical artifact.

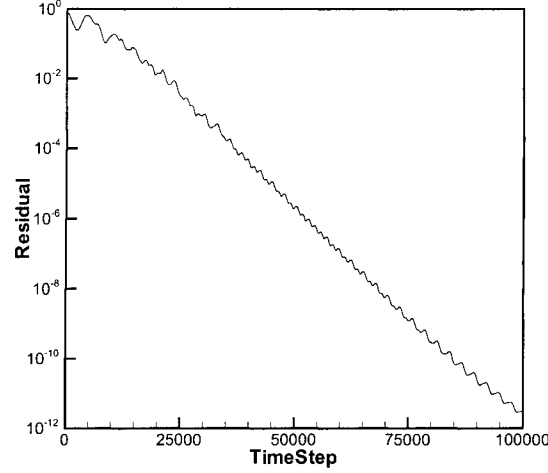


Figure 2.4: The residual (in absolute value) plot for the Roe flux for Mach 20 flow past a two-dimensional cylinder. By the time the solution goes to steady-state, it would have produced a spurious but weakly consistent solution of the Euler equations.

could be compatible with the displacement of a captured shock, having a numerical structure [6], [80]. In most of these carbuncle incidents, authors [75], [76],[78] have reported that the carbuncle satisfies all tests for weak solutions of the Euler equations. This includes entropy satisfying discontinuities⁵ and shocks that satisfy the correct jump conditions. However, instead of producing a smooth bow shock, these solutions mimic shock profiles of two dimensional or axisymmetric blunt bodies with a thin spike protruding from its stagnation point subjected to high Mach number flows [12].

It is unfortunate that the carbuncle phenomenon occurs in shock capturing methods that deploy flux functions which are designed to capture discontinuities with minimal smearing. In order to cure the carbuncle, Liou proposed that the momentum or mass flux across the cell interface has to be independent of the pressure differ-

⁵Although the definition of entropy here is not precise.

ence [62]. This led to the development of the AUSM (Advecting Upstream Splitting Method) flux and other flux functions that have this property ([62], [63], [48]). Although these flux functions are consistent with an Euler solution, this underlying principle is nonphysical. More importantly, we will witness later in this chapter that *the AUSM and AUSM+u fluxes still suffer from the 1 1/2 dimensional carbuncle phenomenon.*

To be truly carbuncle-free, most schemes require some form of artificial dissipation to those interface normal to the captured shock [86]. We suspect that even the AUSM flux-family requires this form of artificial dissipation to remove shock instabilities. This was also the strategy employed by Lin [59] and Sanders et. al [88]. In short, this strategy requires knowledge of the shocks whereabouts to deploy dissipation. It may be fairly easily implemented on Cartesian or structured grids but it is unclear how to extend this to unstructured grids. More importantly, should this strategy be accepted as cure for the carbuncle, predictions for shock-boundary layers interactions would be severely inaccurate [86]. This is because the dissipation would damp out velocity gradients parallel to the shocks compromising velocity profile within the boundary layer. We believe that we can offer a better cure for the carbuncle phenomenon.

So far, we have highlighted the history and developments of the carbuncle problem hence forth the rest of the chapter will be organized as follows. First, we will introduce simpler versions of the carbuncle phenomenon which are essentially perturbed normal stationary shocks albeit in 1 1/2⁶ or 1 dimensions. Then we will apply the Roe flux⁷ [82], the original AUSM and the more recent AUSM+u flux

⁶The 1 1/2 dimensional carbuncle are essentially vertical stacks of the 1 dimensional carbuncle. In other words, most of the physics of the former will be in the horizontal direction although we allow it to propagate in the vertical direction as well.

⁷The flux formulation is included in appendix D

functions [63] to these simplified carbuncles to observe the phenomenon based on first hand experience. Some analytical and numerical results will be included to support these observations. Finally, based on all of these findings, we will formulate a hypothesis on how to cure the carbuncle.

2.2 The 1 1/2 Dimensional “Carbuncle”

2.2.1 Initial Set Up

This simplified carbuncle problem was designed first by Quirk [78] and improved by Dumbser et. al [25] which can be described by a steady one dimensional shock wave computed on two-dimensional uniform Cartesian grids. Basically, this is solving the two dimensional Euler equations to (hopefully) produce a one dimensional solution. Our initial and boundary conditions are identical to theirs [25], except that we assumed the outflow (right) to leave the domain by setting zero slopes in all ghost cells on the right and that our top and bottom boundaries are solid walls. This carbuncle problem may be driven by small perturbations to the variables upstream of the shock, or it may arise spontaneously without being provoked⁸. We introduced very small perturbations, of order 10^{-14} as seedings to instability. We used 25 x 25 uniform Cartesian grids with Courant number $\nu = 0.8$. The shock profile satisfies the Rankine-Hugoniot⁹ jump conditions with the following description.

Assuming M_0 is the upstream Mach number with the ratio of specific heats or

⁸Sometimes, all it takes is just rounding errors.

⁹The Rankine-Hugoniot condition represents the physical condition of the fluids mass, momentum and energy across a shock.

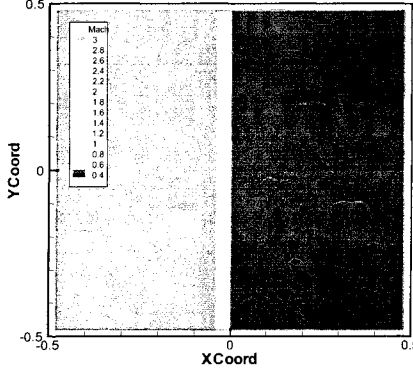


Figure 2.5: The initial condition for the 1 1/2 dimensional carbuncle with $M_0 = 3.0$. This a Mach number contour plot with upstream conditions on the left side of the shock.

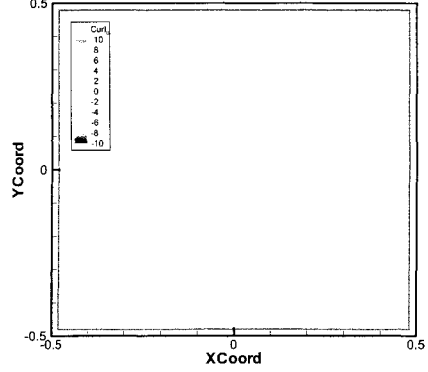


Figure 2.6: The corresponding vorticity plot. From now on, we will include the Mach contours on the left figures and the vorticity contours on the right.

air $\gamma = 1.4$, the normalized upstream and downstream conditions are given by

$$\begin{aligned} \mathbf{u}_0 &= \left[1 \quad 1 \quad 0 \quad \frac{1}{\gamma(\gamma-1)M_0^2} + \frac{1}{2} \right] \\ \mathbf{u}_1 &= \left[f(M_0) \quad 1 \quad 0 \quad \frac{g(M_0)}{\gamma(\gamma-1)M_0^2} + \frac{1}{2f(M_0)} \right] \end{aligned} \quad (2.1)$$

where $f(M_0)$ and $g(M_0)$ follow from the jump conditions of density and pressure across the shock denoted by

$$\begin{aligned} f(M_0) &= \left(\frac{2}{(\gamma+1)M_0^2} + \frac{\gamma-1}{\gamma+1} \right)^{-1} \\ g(M_0) &= \frac{2\gamma M_0^2}{(\gamma+1)} - \frac{\gamma-1}{\gamma+1} \end{aligned} \quad (2.2)$$

We applied the first order FV method with Roe-solver on this simplified carbuncle problem for various combinations of Mach numbers and grid configurations. Quite surprisingly, we observe that there is a universal pattern to the evolution of the planar shockwave instability. This was also reported by Roe, Nishikawa, Ismail and Scalabrin [86] in which they also included tests on different schemes.

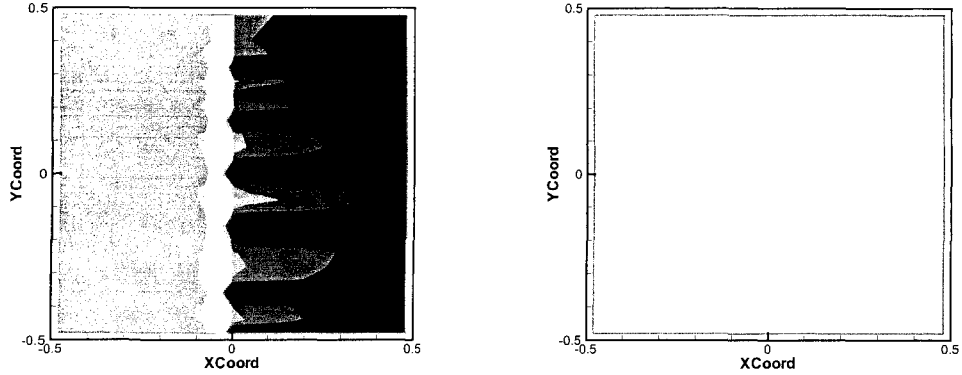


Figure 2.7: The first (pimples) stage represent initial shock instability seeded by a small perturbation to one cell upstream of the shock.

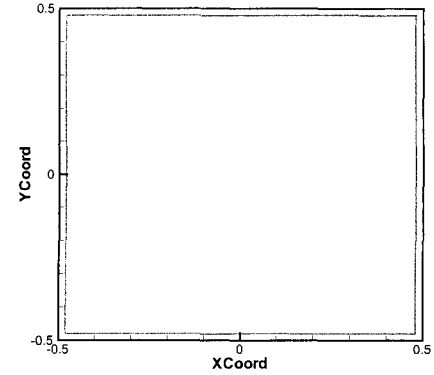


Figure 2.8: Note spurious vorticity is generated along the shock.

2.2.2 The Stages of “Carbuncle”

Based on our observations, the carbuncle consistently developed in three stages. We will use notations and definitions developed by Roe, Nishikawa, Ismail and Scalabrin [86] to describe each stage. In addition, we will include vorticity contour plots to demonstrate strong correlations between spurious vorticity generation and shock instability. The *Mach profiles* will be on the *left* whereas *vorticity contours* will be on the *right*. Although we have only included results for initial data with $M_0 = 3.0$ and $\gamma = 1.4$, *the pattern is similar with other fluid specific heat ratios γ for sufficiently large upstream Mach numbers*. An estimate for ‘sufficiently’ large Mach number can be seen in Figure 2.32. It is striking that *the carbuncle pattern is broadly independent of grid size and the choice of Courant number*.

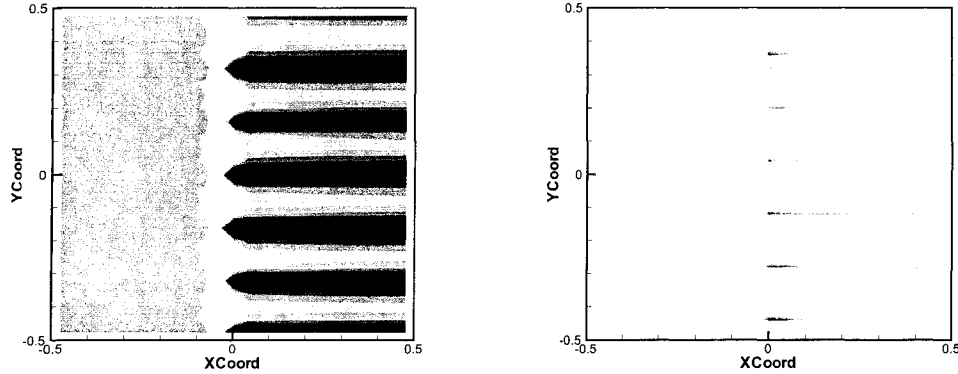


Figure 2.9: The second (bleeding) stage depicts streaks forming or bleeding downstream of the shock.

Figure 2.10: The spurious vortex blobs from first stage become spurious vortex sheets and are advected downstream.

Stage 1: “Pimples”

In the first stage, the instabilities are in the form of spots contained within the shock profile. These spots are “wavelike”, travelling back and forth parallel to the shock and this is true for all conservative and primitive variables. However, the exact structure of these waves are dependent on the type of seedings in the initial data. These waves may be sinusoidal and their amplitudes and periodicity in the y-direction of the waves can be different. More importantly, now we start to see blobs of spurious vorticity being produced along the shock.

Stage 2: “Bleeding”

Depending on the upstream Mach number, the first stage or pimples may not last long. The pimples will bleed downstream of the shock forming a series of a parallel alternating jets. These are not so obvious within the pressure contour but are most visible in the Mach number, velocity and vorticity contours. The alternating jets are

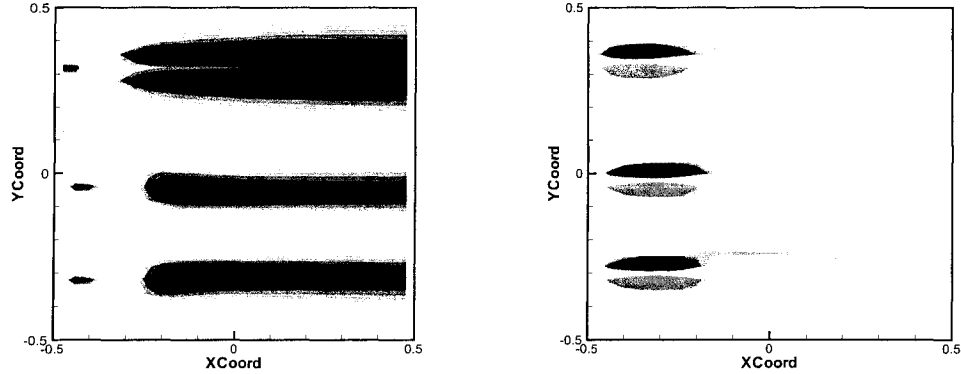


Figure 2.11: The third stage (the converged solution in this case) is when the full carbuncle has developed.

Figure 2.12: The size and magnitude of the vortex sheets are now much larger.

in the form of converging and diverging jets. The former have fast velocity which can become supersonic whereas the latter possess slow subsonic velocity. These velocity disturbances will progressively grow until the slow jets are virtually stagnant causing flow imbalance at the shock. Eventually the flow will go into reverse penetrating upstream of the shock.

Stage 3: “Carbuncles”

Once reverse flow occurs, the normal shock breaks down into several self-similar regions featuring oblique shocks. These oblique shocks encapsulate wedge-shaped regions downstream of the shock in which the core of each region consists of fluid that is almost stagnant. Behind each oblique shock, there exists a pair of vortex sheets of roughly the same magnitude (at least for this case) but rotating in opposite direction to each other. In general, the strength of the two counter rotating vortices may not be equivalent and the two are not necessarily symmetric. However, it must be noted that the angle in which these oblique shocks make are almost identical from

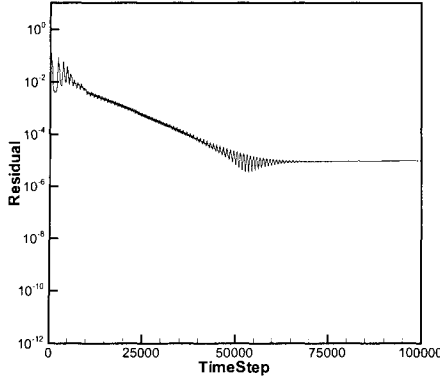


Figure 2.13: Residual plot for the 1 1/2 dimensional carbuncle. Note that oscillations represent shock instability which eventually decays. Even though the residual decreases to $O(10^{-6})$ for this case, the solution has converged to the 'wrong' steady state. However, this 'wrong' steady state value is consistent with a weak solution of the Euler equations.

run to run. This is also true for initial data with various seedings. When we vary the upstream Mach numbers, the oblique shock angles are slightly different but the overall pattern remains the same.

Sometimes, the shock may drift to the left or to the right because once instability has developed, the boundary conditions are not capable of fixing the shock to a particular location. In other words, the shock itself is adjusting to find its most 'comfortable' location.¹⁰ At other times, the shock remains in the middle for quite a long time and the carbuncle might disappear only to be replaced by others.

Dumbser et. al [25] observed the same behavior of the carbuncles. Moreover, [86] reported that their multidimensional fluctuation-splitting scheme produced similar carbuncle results to our finite volume method results. This further support our hypothesis that the carbuncle phenomenon are of similar patterns and indeed universal.

¹⁰From a more physical perspective, the shock is moving along the Rankine-Hugoniot curve searching for its most compatible spot.

Once you have seen a carbuncle, it is fair to say that you have seen all of them.

2.2.3 Improved Set Up

The normal shock location in the 1 1/2 dimensional carbuncle may drift within the computational domain. This is not like the behavior of the 2 dimensional carbuncle where we have the shock fixed upstream of the cylinder. To achieve a fixed normal shock location for the 1 1/2 dimensional carbuncle, we need to alter the boundary conditions.

We intend to prescribe the proper boundary conditions at the inflow and outflow boundaries. The inflow is purely supersonic so we can prescribe the inflow ghost cells with the initial upstream Rankine-Hugoniot conditions. These are the inflow conditions of the initial set up and were also adopted by Dumbser et. al [25]. The outflow boundary however, is a subsonic outflow hence we can prescribe a condition here that will ensure that the shock is fixed¹¹. We chose to prescribe a constant mass flux at the outflow boundary so that the total mass within the system remains the same hence the normal shock has to remain stationary¹². In other words, the new 1 1/2 dimensional carbuncle problem has the exact set up as before except that *we now fix the mass flux to be unity at the outflow boundary*. By doing so, the 1 1/2 dimensional carbuncle is consistent with and a truly 1 1/2 dimensional version¹³ of the 1 dimensional carbuncle set up (will be explained in section 2.3.1). From now on,

¹¹By fixing the shock location, we have removed another degree of freedom for the carbuncle

¹²To see this, let us sum all the mass in each cell upstream and downstream of the normal shock. If the shock moves, then the total mass in the system is no longer the same because we have different mass contributions from the upstream and downstream portions. If we fix the total mass, the normal shock cannot move since no mass entering or leaving the system.

¹³The 1 1/2 dimensional carbuncle problem are stacks in the y-direction of the 1 dimensional carbuncle problem.

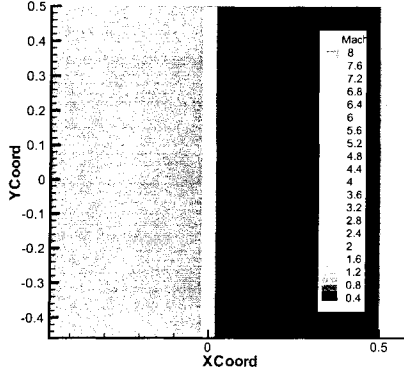


Figure 2.14: Initial Mach profile with $M_0 = 8.0$ of the improved set up.

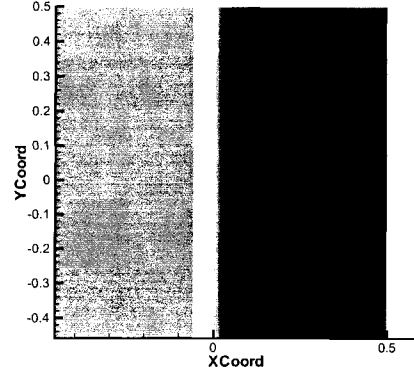


Figure 2.15: Stationary shock solution for AUSM flux at $T=10000$. Except that the shock profile is slightly smeared, the solution looks ‘good’ (at least for now).

the 1 1/2 dimensional carbuncle problem will be referred to the new set up instead of the initial set up.

Results of the original Roe-flux are similar to those before hence will be omitted for brevity. It is clear that for the shock location predicted by the Roe-flux has moved although there is an explanation for this. We have fixed the total mass in the system to ensure the *normal* shock does not move. However, in the 1 1/2 dimensional carbuncle, if the instabilities go all the way to the carbuncle stage, the normal shock structure is broken down to several oblique shocks which are weaker in strength. For the system to compensate for these weaker ‘jumps’ across the discontinuities and still maintain the total mass, the oblique shock has to move. If the instabilities are just pimples, we expect the normal shock to remain almost stationary as we will see with the AUSM fluxes.

Results of the AUSM fluxes solving the 1 1/2 dimensional carbuncle are pre-

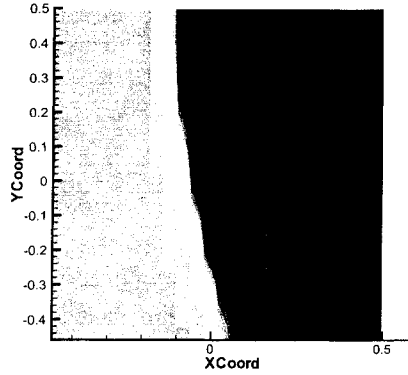


Figure 2.16: Shock solution for the AUSM flux at $T=25000$. Notice that we now have a stage 1 instability with long waves instead of short waves as depicted earlier.

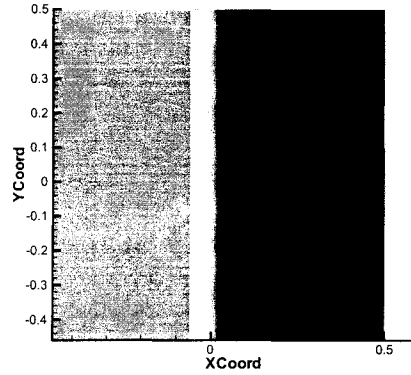


Figure 2.17: Shock solution for AUSM+ u flux at $T=30000$ with stage 1 instability (short waves).

sented (Figs. 2.15-2.23). *Clearly, the original AUSM and AUSM+ u flux functions also suffer from shock instabilities.* These instabilities are “pimples” which are usually eliminated [59] with some form of artificial dissipation parallel to the shock. As mentioned before, this form of artificial dissipation will compromise shock-boundary layer prediction. Moreover, it requires shock curvature detection which may be easily performed on a structured Cartesian mesh solving 1 1/2 dimensional carbuncle problem. However, it is not clear how to implement such dissipation on an unstructured mesh solving a more complicated problem.

To summarize, we have found that the AUSM family of fluxes also experience an anomalous shock instability, but typically at a larger wavelength. Also, it takes a much longer time to set in, and goes through a stage during which it appears to converge and stable.

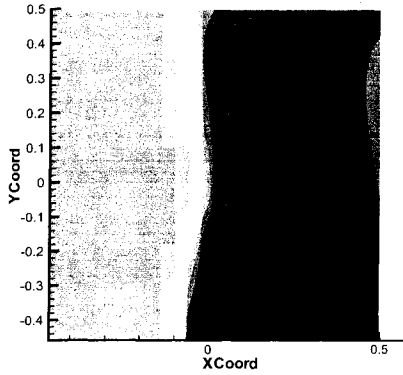


Figure 2.18: Shock solution for AUSM flux at $T=75000$ in which the shock is sloshing left and right repeatedly. This suggest that there is still an inherent instability which can be implied from the residual history.

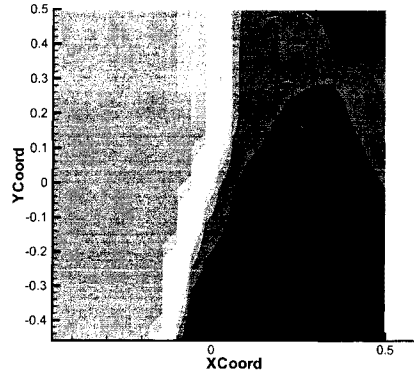


Figure 2.19: Shock solution for AUSM+ u flux at $T=100000$. The shock is also sloshing left and right repeatedly here.

2.2.4 Analysis of “Bleeding” Stage

As mentioned before, the fully developed carbuncle (or stage 3) is a ‘weak’ but consistent solution to the non-linear Euler equations, therefore it is almost impossible to perform a simple mathematical analysis here. Our best hope to perform such analysis is either in the first stage where instability is weak or the second stage where some parts of the flow can be linearized.

Note that for the first two stages, the anomalies are located within and downstream of the shock. However, we will first focus our analysis downstream of the shock by linearizing this subsonic region. This approach is similar to the classical shockwave stability analysis performed by Dyakov [26] and Landau and Lifschitz [49]. We begin by considering possible perturbations downstream of the shock in

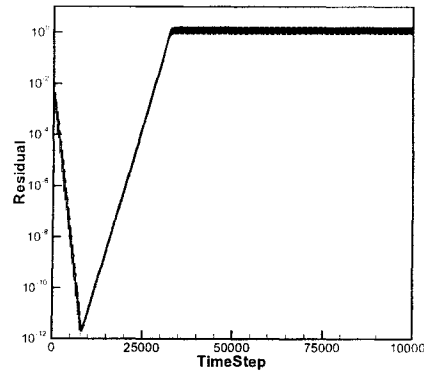


Figure 2.20: Residual plot for the pure AUSM flux. The growth of residual indicates the growth of shock instability. Note that the residual is relatively high even after 100000 time steps which implies that the inherent instability does not go away.

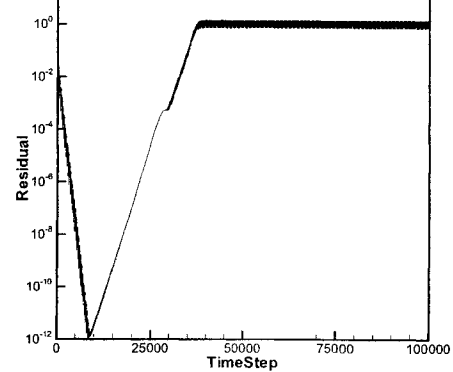


Figure 2.21: Residual plot for the pure AUSM+u flux.

which instability may occur. Before we start our analysis we will derive the linearized Euler equations. Recall that the two-dimensional isentropic Euler equations can be written as

$$\partial_t \rho + u \partial_x \rho + \rho \partial_x u + v \partial_y \rho + \rho \partial_y v = 0 \quad (2.3)$$

$$\partial_t u + u \partial_x u + v \partial_y u + \frac{1}{\rho} \partial_x p = 0 \quad (2.4)$$

$$\partial_t v + u \partial_x v + v \partial_y v + \frac{1}{\rho} \partial_y p = 0 \quad (2.5)$$

$$\partial_t S + u \partial_x S + v \partial_y S = 0 \quad (2.6)$$

where (ρ, u, v, S) are the fluids density, velocities and entropy. For isentropic flow,

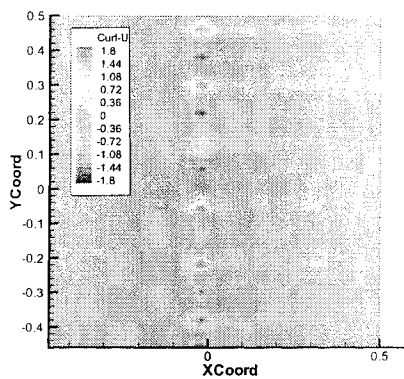


Figure 2.22: Vorticity contour plot for the AUSM+u flux at $T=30000$. Notice that spurious vorticity is produced along the shock.

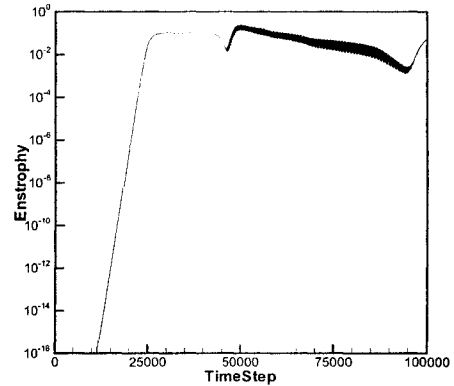


Figure 2.23: Enstrophy plot for the AUSM+u flux solving 1 1/2 dimensional carbuncle with $M_0 = 8.0$. Note that the generation of spurious vorticity generation peaks at approximately the time that the shock instability occur ($T=25000$).

the speed of sound is given as $a^2 = \frac{\partial p}{\partial \rho}$, so that

$$\partial_t p + u \partial_x p + v \partial_y p = a^2 (\partial_t \rho + u \partial_x \rho + v \partial_y \rho)$$

The mass equation can be replaced by a pressure relation hence

$$\partial_t p + u \partial_x p + v \partial_y p + \rho a^2 (\partial_x u + \partial_y v) = 0 \quad (2.7)$$

$$\partial_t u + u \partial_x u + v \partial_y u + \frac{1}{\rho} \partial_x p = 0 \quad (2.8)$$

$$\partial_t v + u \partial_x v + v \partial_y v + \frac{1}{\rho} \partial_y p = 0 \quad (2.9)$$

$$\partial_t S + u \partial_x S + v \partial_y S = 0 \quad (2.10)$$

We will now perform linearization with respect to the mean flow denoted by hat

variables such that

$$p = \hat{p} + p' \quad (2.11)$$

$$u = \hat{u} + u' \quad (2.12)$$

$$v = \hat{v} + v' \quad (2.13)$$

$$S = \hat{S} + S' \quad (2.14)$$

$$\rho = \hat{\rho} + \rho' \quad (2.15)$$

$$a = \hat{a} + a' \quad (2.16)$$

Assuming that perturbation products are negligible, our system becomes

$$\partial_t p' + \hat{u} \partial_x p' + \hat{v} \partial_y p' + \hat{\rho} \hat{a}^2 (\partial_x u' + \partial_y v') = 0 \quad (2.17)$$

$$\partial_t u' + \hat{u} \partial_x u' + \hat{v} \partial_y u' + \frac{1}{\hat{\rho}} \partial_x p' = 0 \quad (2.18)$$

$$\partial_t v' + \hat{u} \partial_x v' + \hat{v} \partial_y v' + \frac{1}{\hat{\rho}} \partial_y p' = 0 \quad (2.19)$$

$$\partial_t S' + \hat{u} \partial_x S' + \hat{v} \partial_y S' = 0 \quad (2.20)$$

We are almost ready to perform our analysis. For small perturbations to the 1 1/2 dimensional stationary shock, we will assume the mean flow M is purely normal to the shock implying that there is no advection component in the y -direction. If we let the mean flow density and speed of sound to be unity and that define the mean flow to be $M = \frac{\hat{u}}{a}$, thus

$$\partial_t p' + M \partial_x p' + \partial_x u' + \partial_y v' = 0 \quad (2.21)$$

$$\partial_t u' + M \partial_x u' + \partial_x p' = 0 \quad (2.22)$$

$$\partial_t v' + M \partial_x v' + \partial_y p' = 0 \quad (2.23)$$

$$\partial_t S' + M \partial_x S' = 0 \quad (2.24)$$

Hence the linearized 1 1/2 dimensional Euler equations written in vector form are given by

$$\partial_t \mathbf{w} + A \partial_x \mathbf{w} + B \partial_y \mathbf{w} = 0 \quad (2.25)$$

where $\mathbf{w} = [p', u', v', S']^T$ and the matrices A and B are

$$A = \begin{bmatrix} M & 1 & 0 & 0 \\ 1 & M & 0 & 0 \\ 0 & 0 & M & 0 \\ 0 & 0 & 0 & M \end{bmatrix}, \quad B = \begin{bmatrix} 0 & 0 & 1 & 0 \\ 0 & 0 & 0 & 0 \\ 1 & 0 & 0 & 0 \\ 0 & 0 & 0 & 0 \end{bmatrix} \quad (2.26)$$

Now we use the method of normal modes where an arbitrary disturbance may be resolved into independent modes of the form

$$\mathbf{w} = \exp[\xi x - \theta t + iky] \mathbf{r}_{ij} \quad (2.27)$$

where (ξ, k, θ) are wave numbers in the x,y-directions and frequency with \mathbf{r}_{ij} being columns of right eigenvectors to be determined. Applying equation (2.27) into equation (2.25), we have the following.

$$\begin{bmatrix} M\xi - \theta & \xi & ik & 0 \\ \xi & M\xi - \theta & 0 & 0 \\ ik & 0 & M\xi - \theta & 0 \\ 0 & 0 & 0 & M\xi - \theta \end{bmatrix} \mathbf{w} = \mathbf{0} \quad (2.28)$$

For nontrivial solutions, we require that

$$\det \begin{bmatrix} M\xi - \theta & \xi & ik & 0 \\ \xi & M\xi - \theta & 0 & 0 \\ ik & 0 & M\xi - \theta & 0 \\ 0 & 0 & 0 & M\xi - \theta \end{bmatrix} = (M\xi - \theta)^2[(M\xi - \theta)^2 - (\xi^2 - k^2)] = 0 \quad (2.29)$$

in which the roots of θ are $[M\xi - (\xi^2 - k^2)^{\frac{1}{2}}, M\xi, M\xi, M\xi + (\xi^2 - k^2)^{\frac{1}{2}}]$. The repeated roots correspond to shear (or vorticity) and entropy disturbances while the other two represent acoustic disturbances. After performing some algebra, we can determine the corresponding eigenvectors in the order of the eigenvalues above.

$$\mathbf{r}_{ij} = \begin{bmatrix} \sqrt{\xi^2 - k^2} & 0 & 0 & -\sqrt{\xi^2 - k^2} \\ \xi & -ik & 0 & \xi \\ ik & \xi & 0 & ik \\ 0 & 0 & 1 & 0 \end{bmatrix} \quad (2.30)$$

Hence the solutions of the perturbed quantities are

$$\mathbf{w} = \exp[\xi x - \theta_i t + iky] \mathbf{r}_{ij} \quad (2.31)$$

in which θ_i are the eigenvalues of the system with their corresponding eigenvectors \mathbf{r}_{ij} . These eigenvectors decompose the solutions into their acoustic, shear and entropy components.

To find out if these disturbances are linearly independent, we form $\det(\mathbf{r}_{ij}) = -2(\xi^2 - k^2)^{\frac{3}{2}} = 0$. This vanishes if $k = \xi$, when the shear and acoustic disturbances are indistinguishable because their eigenvectors and eigenvalues are identical. This is a dependent mode in the form of resonance which may give birth to growth and consequently instability¹⁴. Thus, the unstable modes are in the form of

$$\mathbf{w} = \exp[k(x - Mt) + iky] \begin{bmatrix} 0 & 0 & 0 & 0 \\ k & -ik & 0 & k \\ ik & k & 0 & ik \\ 0 & 0 & 1 & 0 \end{bmatrix} \quad (2.32)$$

¹⁴If we perform more analysis of the case $k = \epsilon$, that is by obtaining the generalized eigenvectors, we will have an unstable vortical mode [26]

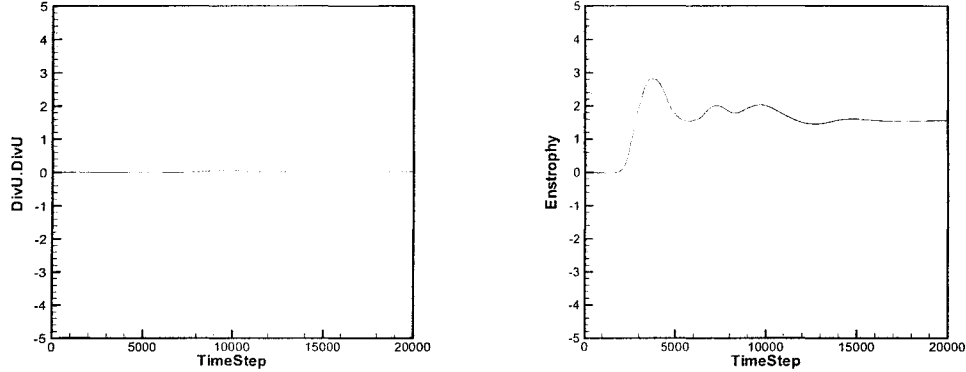


Figure 2.24: L2-norm of velocity divergence squared downstream of the shock.

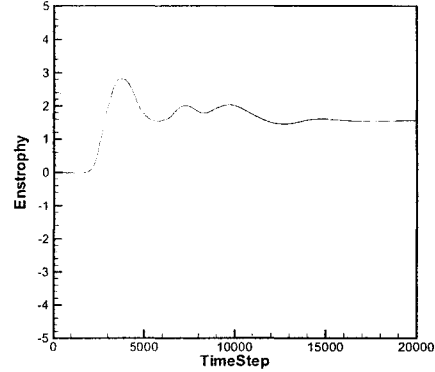


Figure 2.25: L2-norm of enstrophy (vorticity squared) downstream of the shock.

with k being a real-positive wave number. These modes convect with the flow along the $x - Mt$ characteristics and are divergence free since $u_x + v_y = \exp[k(x - Mt) + iky][(k^2 - ik^2 + k^2) + (-k^2 + ik^2 - k^2)] = 0$. These modes were intuitively mentioned but rejected by [115] as an explanation to why carbuncles occur because he believes that a parallel plane flow should always be stable. However, we will not discard these unstable modes as one of the sources of carbuncle.

The prediction for zero velocity divergence is demonstrated in our second stage computations. Even though the solution is violently changing, the norm of velocity divergence remains virtually zero the whole time (Fig (2.24)). However, Fig. (2.25) show that spurious vorticity grows rapidly with the onset of second stage and reach its peak once stage three sets in. This suggests that inadequate vorticity control could be the reason that the bleeding stage develops into a carbuncle.

2.2.5 Analysis of “Pimple” Stage

Now we need to determine whether the unstable modes are compatible with the boundary conditions of a physical shock. The boundary conditions that connects the subsonic region and the shock are given by the Rankine-Hugoniot relations. For any two dimensional small disturbances in an infinite homogeneous domain with an arbitrary equation of state, Dyakov [26] proved that the shock is unstable when either one of the inequalities below is satisfied.

$$\begin{aligned} j^2 \left(\frac{\partial \bar{V}}{\partial \bar{p}} \right)_H &< -1 \\ j^2 \left(\frac{\partial \bar{V}}{\partial \bar{p}} \right)_H &\geq 1 + 2M_1 \end{aligned} \quad (2.33)$$

where M_1 is the downstream Mach number, \bar{V} is the mean specific volume, $j^2 = \frac{\bar{p}_1 - p_0}{\bar{V}_1 - V_0}$ is the slope of the Rayleigh line and $(\frac{\partial \bar{V}}{\partial \bar{p}})_H$ is the slope of the Hugoniot curve in the pressure-volume plane.

Assuming M_0 is the upstream Mach number, Robinet et. al [83] showed that for an ideal gas,

$$j^2 \left(\frac{\partial \bar{V}}{\partial \bar{p}} \right)_H = -\frac{1}{M_0} \quad (2.34)$$

We can deduce that for any ideal gas, the instability condition (Eqn. (2.33)) can never be satisfied which implies that the unstable modes are incompatible with a physical shock.

However, Barth [6] indicated that these unstable modes are compatible with the boundary conditions imposed by a numerically captured shock. His analysis was based on a one-dimensional computation of a stationary shock.

2.3 The 1 Dimensional “Carbuncle”

2.3.1 Initial Set Up

This is a steady one dimensional problem in which an intermediate cell within a shock is introduced and perturbed to induce shock instability. The initial conditions are given by the same normalized upstream and downstream states in the 1 1/2 dimensional but are dimensionally reduced.

$$\begin{aligned}\mathbf{u}_L &= \left[1 \quad 1 \quad \frac{1}{\gamma(\gamma-1)M_0^2} + \frac{1}{2} \right] \\ \mathbf{u}_R &= \left[f(M_0) \quad 1 \quad \frac{g(M_0)}{\gamma(\gamma-1)M_0^2} + \frac{1}{2f(M_0)} \right]\end{aligned}\quad (2.35)$$

where $f(M_0)$ and $g(M_0)$ follow from the jump conditions of density and pressure across the shock given by

$$\begin{aligned}f(M_0) &= \left(\frac{2}{(\gamma+1)M_0^2} + \frac{\gamma-1}{\gamma+1} \right)^{-1} \\ g(M_0) &= \frac{2\gamma M_0^2}{(\gamma+1)} - \frac{\gamma-1}{\gamma+1}\end{aligned}\quad (2.36)$$

where M_0 and γ are the upstream Mach number and the gas specific heats ratio. The boundary conditions are identical to the *improved* 1 1/2 dimensional carbuncle but in one dimension. This includes the fix mass flux at the outflow boundary $\rho u = 1.0$.

The intermediate states within the shock are defined as

$$\mathbf{u}_C = \epsilon \mathbf{u}_L + (1-\epsilon) \mathbf{u}_R \quad (2.37)$$

where $\epsilon = 0.0, \dots, 1.0$ is a discrete weighting average. This is to perturb the intermediate state away from the Hugoniot curve and investigate if the state suffers from instability. A good numerical flux function should be stable for all of the prescribed states but apparently not for the Roe-flux.

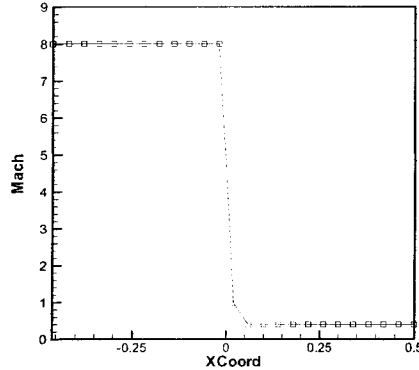


Figure 2.26: Initial condition for the stationary shock with $M_0 = 8$ and $\epsilon = 0.7$ using Roe solver.

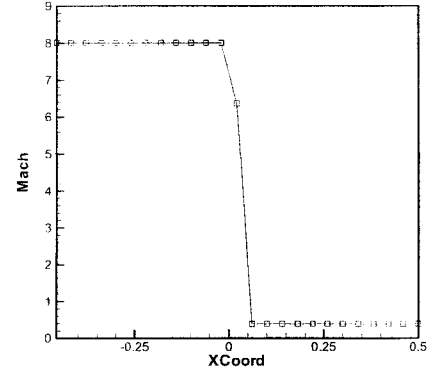


Figure 2.27: Solution at $T=1000$.

2.3.2 The Profile of a One Dimensional Carbuncle

Figures (2.26)-(2.29) indicate the nature of one dimensional carbuncle¹⁵. The shock structure has an intermediate state that is bounded by the left and right primitive variables but the conservative variables such as momentum may not be bounded. While the solution is trying to converge to equilibrium, the intermediate states may oscillate inside the shock in order to find their most compatible spot along the Rankine Hugoniot curve forming a *limit-cycle*. This is a form of intrinsic instability since the solution fails to converge to steady state even after $T=100000$. (Fig (2.30)). The results of this one dimensional carbuncle is repeatable for Mach numbers above some critical value and for any grid size. Before we determine this critical Mach number, we will first present the work of Barth [6].

¹⁵For certain choices perturbation to the intermediate state, $\epsilon = 0.0, 0.1, 0.9, 1.0$, the Roe-flux maintained sharp, monotone and stable shock profiles. However, for other choices of ϵ , the Roe-flux suffers from shock instabilities.

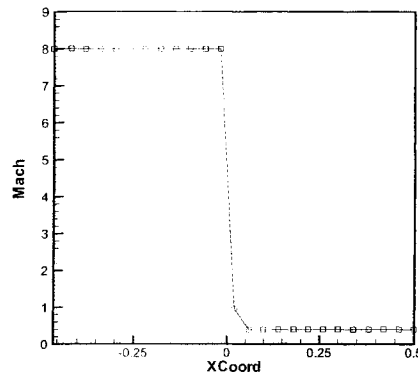


Figure 2.28: Stationary shock at $T=1700$. Note that the solution returned to its initial values.

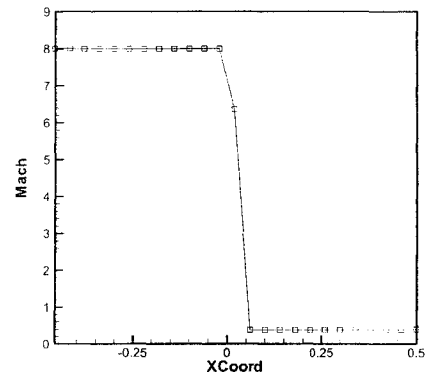


Figure 2.29: Stationary shock at $T=3400$. The intermediate cell moves again and the cycle repeats itself indefinitely. Note that this process is repeatable with other γ and other sufficiently high upstream Mach numbers.

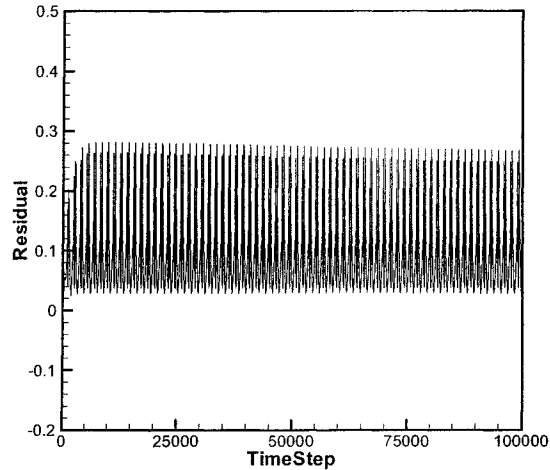


Figure 2.30: Residual plot for the one dimensional carbuncle. Clearly, there is an inherent instability hence the solution does not converge.

2.3.3 Analysis of 1 Dimensional Shock Instability Equilibrium Configuration

Consider the one dimensional Euler equations written in conservative form.

$$\partial_t \mathbf{u} + \partial_x \mathbf{f}(\mathbf{u}) = 0 \quad (2.38)$$

where $\mathbf{u} = [\rho, \rho u, \rho E]^T$ and $\mathbf{f}(\mathbf{u}) = [\rho u, \rho u^2 + p, \rho u H]^T$ ¹⁶. We will discretize the equations semi-discretely for a control volume $x_{j-\frac{1}{2}} \leq x \leq x_{j+\frac{1}{2}}$ such that

$$h \partial_t \mathbf{u}_j = \mathbf{f}_{j-\frac{1}{2}} - \mathbf{f}_{j+\frac{1}{2}} \quad (2.39)$$

where \mathbf{u}_j and $\mathbf{f}_{j\pm\frac{1}{2}}$ are the discrete cell values of \mathbf{u} and numerical flux functions evaluated at cell interfaces. Note that h is the cell-grid size.

The conservative variables are assumed to be mean values within each cell and interactions with other cells only take place at the interfaces via the numerical flux functions. The solution will be a sequence of cells, all in left state \mathbf{u}_L followed by another sequence of cells in the right state \mathbf{u}_R . The left and right states are separated by a shock satisfying the Rankine-Hugoniot jump conditions. Since the flow is in equilibrium, we have $\mathbf{f}(\mathbf{u}_L) = \mathbf{f}(\mathbf{u}_R)$. For the data to be continuous, we must consider intermediate cells within the shock. The simplest case is when we have just one intermediate cell which can be achieved via Godunov-type flux. For the Godunov-type flux, there will be an internal state \mathbf{u}_C within the shock such that all the states $(\mathbf{u}_L, \dots, \mathbf{u}_L, \mathbf{u}_C, \mathbf{u}_R, \dots, \mathbf{u}_R)$ are in equilibrium. This implies that

$$\mathbf{f}(\mathbf{u}_L) = \mathbf{f}^*(\mathbf{u}_L, \mathbf{u}_C) = \mathbf{f}^*(\mathbf{u}_C, \mathbf{u}_R) = \mathbf{f}(\mathbf{u}_R) \quad (2.40)$$

¹⁶ $E = \frac{u^2}{2} + e$ is the total energy of the system with e as the fluids internal energy. $H = E + p$ is the total enthalpy and $e = \frac{p}{\rho(\gamma-1)}$ is the equation of state for closure. Again, γ is the fluid specific heats.

which means the equilibrium jump conditions¹⁷

$$\mathbf{f}^*(\mathbf{u}_L, \mathbf{u}_C) - \mathbf{f}(\mathbf{u}_L) = \mathbf{f}^*(\mathbf{u}_C, \mathbf{u}_R) - \mathbf{f}^*(\mathbf{u}_L, \mathbf{u}_C) = \mathbf{f}(u)_R - \mathbf{f}^*(\mathbf{u}_C, \mathbf{u}_R) = 0 \quad (2.41)$$

must be simultaneously satisfied¹⁸. Based on the fact that there are always exactly two states \mathbf{u} that corresponds to a given \mathbf{f}^* , these are satisfied only if \mathbf{u}_{CR} and \mathbf{u}_{CL} take on either the left or right state values [6]. More precisely, the intermediate solutions must be restricted to¹⁹

$$\mathbf{u}_{CL} = \mathbf{u}_L \quad \mathbf{u}_{CR} = \mathbf{u}_R \quad (2.42)$$

Based on the direction of shock propagation combined with the jump conditions, Barth showed that conditions (2.42) are satisfied for the Godunov type flux if the following constraints are met.

$$\rho_L \leq \rho_C \leq \rho_R$$

$$p_L \leq p_C \leq p_R$$

$$u_L \geq u_C \geq u_R \quad (2.43)$$

Stability of Equilibrium

Barth [6] indicates that the wave structure of the Godunov-type flux identifies a single degree of freedom (DOF) when a stationary one dimensional discontinuity is present. For example, given any pair of states $(\mathbf{u}_L, \mathbf{u}_R)$ satisfying $\mathbf{f}(\mathbf{u}_L) = \mathbf{f}(\mathbf{u}_R)$,

¹⁷The jump conditions express conservation of the fluid across a stationary or moving discontinuity. For a scalar problem in one dimension, the discontinuity is bounded by left and right states of the fluid in which the following condition $\frac{[f(u)]}{[u]} = \frac{f(u)_R - f(u)_L}{u_R - u_L} = \Lambda$ is satisfied. Note that Λ is the speed of discontinuity and the derivation of this formula is included in appendix H.

¹⁸ \mathbf{f}^* denotes flux at a cell interface.

¹⁹ \mathbf{u}_{CL} refers to the intermediate state values at its left cell interface and likewise. \mathbf{u}_{CR} is at its right cell interface.

there is a one parameter family of states \mathbf{u}_C satisfying 2.43 such that the flux residual

$$\mathbf{r}(\mathbf{u}_C; \mathbf{u}_L, \mathbf{u}_R) = \mathbf{f}^*(\mathbf{u}_C, \mathbf{u}_R) - \mathbf{f}^*(\mathbf{u}_L, \mathbf{u}_C) \quad (2.44)$$

has a singular Jacobian matrix²⁰. To understand the implication of this, consider solving a system of one intermediate cell, \mathbf{u}_C with boundary data \mathbf{u}_L and \mathbf{u}_R

$$\partial_t \mathbf{u}_C + \mathbf{r}(\mathbf{u}_C; \mathbf{u}_L, \mathbf{u}_R) = 0 \quad (2.45)$$

We can linearize the system near a stationary solution $\bar{\mathbf{u}}$ since $\mathbf{r}(\mathbf{u}_C; \mathbf{u}_L, \mathbf{u}_R) = 0$.

Define the solution error $\mathbf{e} = \mathbf{u}_C - \bar{\mathbf{u}}$ satisfying

$$\partial_t \mathbf{e} + \partial_{\mathbf{u}_C} \mathbf{r}(\bar{\mathbf{u}}) = 0 \quad (2.46)$$

in which its solution is in the form of

$$\mathbf{e}(t) = \sum_{i=1}^3 (k_i \mathbf{r}_i \exp(-\lambda_i t)) \quad (2.47)$$

with λ_i and \mathbf{r}_i as the i th eigenvalues and eigenvectors of $\partial_{\mathbf{u}_C} \mathbf{r}(\bar{\mathbf{u}})$ and k_i as the solution coefficients. Barth showed that only 3 computational cells with fixed boundary data \mathbf{u}_L and \mathbf{u}_R need to be considered when solving this numerical eigenvalue problem. For the system to be stable, all of the eigenvalues must be nonnegative but that is not the case (refer [6] for details). For an arbitrary perturbation to the data, he discovered that not all of these equilibria are stable.

In other words, instability depends on where the shock sits relative to a grid. This somewhat explains why the shock shifts in the 1 1/2 carbuncle and perhaps the jagged shock appearance when solving the two-dimensional flow past a cylinder, (Fig (2.31)) even if the shock is stable [89].

²⁰Mathematically, this means that the system has a zero eigenvalue. Refer to [6] for proof and details



Figure 2.31: This is a steady state solution of a mono atomic gas $\gamma = 5/3$ with upstream Mach number $M_0 = 6.0$. Note the shock structure exhibit kinks instead of a smooth profile along the shock. This is because the shock has adjusted itself to achieve local stability (courtesy of Roe et. al [89]).

Barth also found that for a particular value of γ , the instability only occurs for Mach numbers higher than some critical value. We conducted a numerical experiment using Roe-flux to verify this in which our one-dimensional results are consistent with his (Fig. (2.32)). [89] fitted a function to this Mach number versus γ and found out the critical Mach number in one dimension is given by

$$M_{crit} = \frac{3 - \gamma}{\frac{5}{3} - \gamma} \quad (2.48)$$

which implies that for $\gamma = \frac{5}{3}$ or mono-atomic fluids are carbuncle-free! However, Roe et. al numerically verified carbuncles still occur in cylinder flows even for $\gamma = \frac{5}{3}$ so there is still much to be explored in curing the carbuncle.

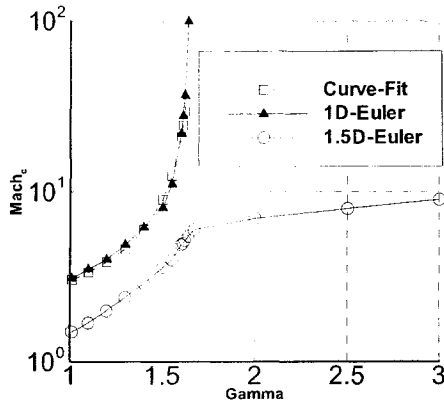


Figure 2.32: Critical Mach Number versus γ for the Roe flux. For $\gamma = 1.4$, $M_{crit} = 6.5$ in one dimension and 2.0 in two dimensions. The results in one dimension agrees with Barth's but slightly higher than Robinet et. al.'s in two dimension. Perhaps the difference is we did not include the case as unstable unless it reaches Stage 2.

Entropy Stability of Equilibrium

Strictly speaking, an inviscid fluid must satisfy the system of conservation laws (equation 2.38) and also the following inequality

$$\partial_t U + \partial_x F \leq 0 \quad (2.49)$$

where $U = -\rho g(S)$ is the entropy function and $F = -\rho u g(S)$ is the entropy flux. The variable $g(S)$ is some convex function of the physical entropy $S = \ln p + \gamma \ln \rho$. For smooth flows, 2.49 is an equality and is known as the entropy conservation law. When shocks are present, entropy is produced in the flow and to account for this, we need the inequality²¹. This is known as the entropy stability condition. We will see that the numerical prediction of the system conservation laws does not necessarily satisfy the entropy stability condition.

²¹Stability proofs are usually given in terms of mathematical entropy, which is negative of the physical entropy S , can be defined as positive and always decreases.

First, let us precisely define the entropy function and its flux [84].

$$U = \frac{-\rho S}{\gamma - 1}, \quad F = \frac{-\rho u S}{\gamma - 1} \quad (2.50)$$

We have chosen this entropy function because it is the only entropy function that can be used for the Navier-Stokes equation [49] and also because it gives a fairly simple form of the entropy variables defined as

$$\mathbf{v} = \frac{\partial U}{\partial \mathbf{u}} = [\frac{\gamma - S}{\gamma - 1} - \frac{1}{2} \frac{\rho}{p} (u^2), \frac{\rho u}{p}, -\frac{\rho}{p}]^T \quad (2.51)$$

Assuming $[a] = a_R - a_L$ is the difference between the left and right states to the interface, the numerical flux function at the interface * can be written as

$$\mathbf{f}^* = \bar{\mathbf{f}} - \frac{1}{2} \mathbf{D}[\mathbf{u}] \quad (2.52)$$

where D is the dissipative matrix. For the original Roe-flux, $D_{Roe} = \mathbf{R}|\Lambda|\mathbf{L}$ in which the dissipative matrix is decomposed into the eigenvalues and the right and left eigenvectors of the system satisfying equation 2.38. For the system of Euler equations, these eigenvalues and eigenvectors are defined in appendix A.

Barth [7] had shown that for the numerical flux to be entropy stable, the following condition has to be satisfied.

$$[\mathbf{v}]^T |\mathbf{D}| [\mathbf{u}] \geq 0 \quad (2.53)$$

We will offer a counter example to show that this condition is not satisfied by the original Roe-flux. Appealing to the test case and data presented by Barth, in which a stationary shock (with $M_0 = 8.0$ and $\gamma = 1.4$) with an intermediate cell C, is

perturbed²² away from the left state and have the following values.

$$\begin{bmatrix} \rho_C \\ u_C \\ p_C \end{bmatrix} = \begin{bmatrix} 1.00182 \\ 7.99621 \\ 0.72240 \end{bmatrix}, \quad \begin{bmatrix} \rho_R \\ u_R \\ p_R \end{bmatrix} = \begin{bmatrix} 5.56522 \\ 1.43750 \\ 53.21429 \end{bmatrix} \quad (2.54)$$

By numerical computation,

$$[\mathbf{v}]^T |\mathbf{D}_{Roe}| [\mathbf{u}] = -0.1355392 \quad (2.55)$$

which implies that the Roe-flux does *not* satisfy the entropy-stability condition and hence violating the Second Law of Thermodynamics. *Based on all of the results of the perturbed one dimensional shock and the discussions that have been presented, we propose a conjecture that the shock instabilities are caused by imprecise enforcement of entropy conditions or the second law of thermodynamics.*

Some Remarks on Conventional Entropy Conditions

Recall that the second law of thermodynamics states that the fluids physical entropy, $S = \ln p - \gamma \ln \rho$ is an increasing function, which can be enforced analytically if one of the three entropy conditions below are satisfied [60]. This is because from an analytical standpoint, all of these conditions coincide.

Entropy Condition I

The fluids entropy should remain constant along a particle path for smooth flow and will only increase when a shock is encountered.

Entropy Condition II

This basically restricts the left and right characteristic speeds with respect to the

²²In practice, the perturbation can be in the form of round-off errors.

speed of discontinuity Λ i.e.

$$\lambda_L \geq \Lambda \geq \lambda_R \quad (2.56)$$

Entropy Condition III

\mathbf{u} is a valid entropy solution, if it is a solution of the PDE with vanishing viscosity.

$$\partial_t \mathbf{u} + \partial_x \mathbf{f} = \partial_x(\alpha \partial_x \mathbf{u}) \quad (2.57)$$

as $\alpha \rightarrow 0$ from above. This implies that a discontinuity has zero thickness. Due to the nature of finite discretization, satisfying this condition is impossible. However, it is customary that the quality of a numerical scheme is judged based on how much a captured discontinuity is smeared in which less is better.

Numerically speaking, we normally choose one of these conditions and hope the other two will be satisfied to within some error tolerance. Usually condition II or something similar is used to enforce the second law of thermodynamics mainly because it is the simplest and relate directly to the computed variables. In this context, the second law of thermodynamics is enforced only by allowing physical shocks to be captured and not the unphysical rarefaction shocks [46]. This method of enforcing the entropy condition is also known as the entropy fix to destabilize rarefaction shocks. In this thesis, we will include the second law of thermodynamics more than just being able to distinguish physical or unphysical shocks, by directly including the entropy conservation law in the numerical flux function. This will be discussed in chapters 5 and 6.

2.4 Concluding Remarks

In short, the carbuncle phenomenon is a numerical shock instability problem which depends on the choice of numerical scheme predicting the shock. It is known

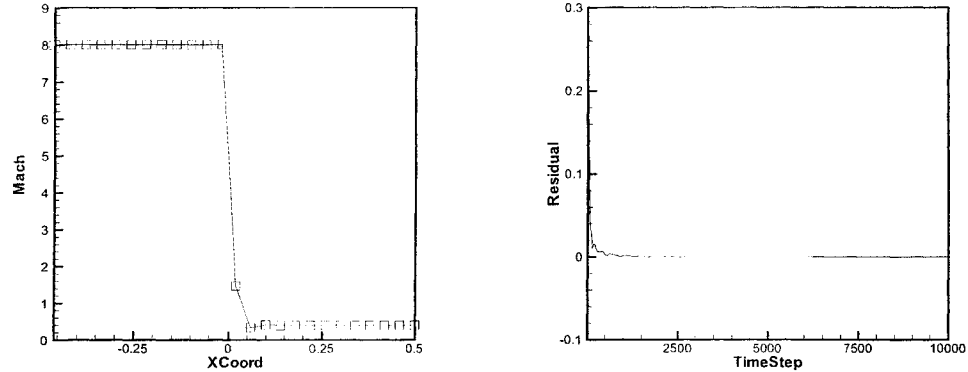


Figure 2.33: The converged AUSM and AUSM+u solution for the one dimensional carbuncle test with $M_0 = 8.0$ and $\epsilon = 0.7$. Note that both fluxes do not suffer from carbuncle for any ϵ , γ and M_0 .

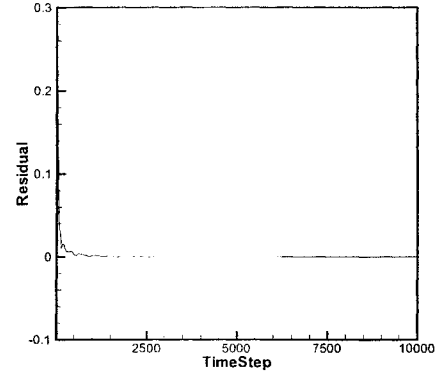


Figure 2.34: Notice how fast the residual decays to zero.

that schemes which have the least numerical dissipations are more susceptible to the symptoms of carbuncle. There has been extensive research conducted both theoretically and numerically, on the carbuncle phenomenon and many have tried to determine its roots to provide possible explanations to the problem but met only with some success. There are also others who have proposed cures to the problem but none of them are universally accepted. Until now, the most commonly applied cure is based on Liou's hypothesis which claims that the mass flux of a numerical flux function must be independent of the pressure difference. This is one of the underlying principles for the design of later members of the AUSM family.

We have included the one dimensional carbuncle results for the original AUSM flux and the more recent AUSM+u flux (Figures. 2.33-2.34). Both flux functions do not produce shock instability for any configuration of the intermediate state hence

are free from the one dimensional carbuncle. However, they still suffer from the 1/2 dimensional shock instabilities (Fig 2.16-2.17) which implies that the AUSM flux functions may require some form of artificial dissipation parallel to the normal shock in order to remove the instabilities. Overall, this suggests that the general idea of the AUSM flux is not the way to prevent the carbuncle.

In this chapter, we have conducted systematic numerical experiments to understand the nature of the carbuncle problem in which can be categorized into three distinct stages: pimples or the initial shock instability; bleeding, in which the instability is propagated downstream of the shock and third stage, the full carbuncle. It will be unwise to cure the carbuncle at the third stage because its solution is another weak-consistent solution of the Euler equations [81],[25],[78]. The goal is to prevent the carbuncle from reaching the third stage, hence any form of cure to carbuncle has to begin from either the pimples or bleeding stage. In this thesis, we aim to prevent the carbuncle before reaching the pimples stage.

We have demonstrated that the carbuncle is a spurious solution of the Euler equations attributed to possibly more than one factor. One factor is attributed to imprecise entropy conditions while another strong candidate would be poor vorticity handling. The two can be related using Crocco's Theorem²³. Unfortunately, it is not clear which of the two is the root or main culprit. However, results of the AUSM scheme indicate that perhaps the cure to the carbuncle is of a multi dimensional nature. Hence we will first attempt to prevent the carbuncle by controlling vorticity, which will be the subject of the next two chapters.

²³The theorem relates the production of vorticity to the change of entropy along the streamlines [8].

CHAPTER III

VORTICITY PRESERVATION IN LINEAR WAVE EQUATIONS

Most aerospace problems contain strong vortical flows yet until now, capturing these flows without resorting to vortex methods or vortex blob approach¹ remains elusive [88]. The underlying numerical difficulty lies in discretely solving a nonlinear system of equations with differential constraints. There is much experience in computing conservation laws under differential constraints. For example, in incompressible fluid dynamics there is the velocity divergence constraint $\nabla \cdot \vec{u} = 0$, and in Magnetohydrodynamics (MHD) we have constraints on the magnetic field $\nabla \cdot \vec{B} = 0$. In both contexts, there have been substantial success in predicting such flows which include many techniques but essentially can be divided into three general ideas [98].

The first idea utilizes source terms in the conservation laws to remove discrepancies within the cells which are conflicting with the differential constraints [14], [80], [42], [99]. In the MHD framework, an example would be Powell's method [80] which has been used to efficiently compute MHD problems with considerable success. This method is relatively cheap and does not require any subiteration or constraints on the

¹As mentioned in the first chapter, these methods are much more expensive numerical method compared to continuum CFD [65] and are not conservative.

variables or staggered grid formulations. Unfortunately, this method compromises conservation and may not be suitable for flows with strong discontinuities [98].

The second idea is the 'projection' or 'clean-up' method [14], [9], [19]. In short, this idea includes a sub-iteration within a time-step solving a Poisson-type equation forcing the solution to obey some differential constraints. This methodology satisfies conservation and also does not require any constraints on the variables. However, it requires sub-iterations within a time-step which may be costly [98].

The third idea is referred to as the constrained-transport formulation which preserve the differential constraints in a specific discretization [32], [5]. Schemes which are based on this idea usually require staggered grid formulations. At every time-step, the scheme will preserve the differential constraints within the computational domain (at particular grid locations) as long as the boundary conditions are compatible with the constraints. Except for some restrictions on the variables and the use of staggered grids, the scheme does not require any subiterations and can be designed to be conservative.

Before we begin our journey in preserving vorticity, we need to address a few issues. One is the fundamental difference between preserving vorticity and preserving magnetic field divergence. The former comes from nonlinear equations whereas the latter is of linear origins². Also, preserving the divergence of magnetic fields requires only $\nabla \cdot \vec{B} = 0$ to be satisfied at all times but unless the flow remains irrotational, preserving or conserving vorticity requires unsteady-nonlinear predictions of velocity-curl.

²By definition, vorticity is curl of velocity and velocity is computed from the nonlinear momentum equations. Although the fluid dynamics equations in MHD are nonlinear, magnetic fields satisfy the linear advection equations.

Two, we need to distinguish the notion of vorticity preserving and vorticity control (or capturing) in general. The latter refers to prediction of vorticity, either rotational or irrotational, which satisfies the vorticity transport equations. The inviscid version of these equations are another form of the Euler equations and govern the complete physics of inviscid³ vorticity which includes advection, dilatation, vortex stretchings and baroclinic terms. In short, these equations must also be satisfied when solving the discretized Euler equations. If we assume initially irrotational flow and that there are no physical mechanisms to generate vorticity then the flow should remain irrotational. In this case we say that the vorticity is preserved. We will only focus on irrotational flow in this chapter hence the term vorticity preserving is appropriate.

Three, is the issue of discretizing vorticity, which is a derivative function of the main variables. To compute discrete vorticity, we need inputs from more than one cell. Hence it is not straightforward how and where to enforce vorticity control. One guideline is to define and preserve discrete vorticity in a way that produces the least spurious modes (odd-even decoupling). The only option is then to compute compact vorticity (appendix G) as opposed to regular central differencing. Using the compact method, we use cell values as input but the output lies at the vertex. Throughout this thesis, we will *compute discrete vorticity only at the vertices*.

Morton and Roe [73] developed the vorticity preserving schemes for the linear wave equations based on the constrained-transport ideology [32], [5], [98]. These schemes are members of the Lax-Wendroff family. Similar methods have also been developed by Toroillon and Fey [33] but *all* of these schemes preserve vorticity only for linear wave equations. Moreover, none of these schemes address limiting which

³We will not include viscous effects in this thesis for the reasons that were mentioned in chapter 1.

is essential to circumvent Godunov's Theorem when computing compressible fluid dynamics with high order schemes. In this chapter, we will present a method which includes limiting and at the same time, preserving vorticity.

First, we will start from the simple vorticity preserving Rotated Richtmyer scheme developed by Morton and Roe [73]. We will re-derive the scheme and then prove that this elegant idea breaks down when nonlinear limiters are included even for linear systems. We will then formulate a new methodology to preserve vorticity in order to include limiters when solving the linear wave equations. This idea is easily extendable to solving system of nonlinear equations in particular, the Euler equations.

In general, vorticity is a three dimensional problem and our ultimate goal is to produce a vorticity capturing scheme for the three dimensional system of Euler equations. However, for the purpose of preliminary research we will restrict ourselves to two dimensions and start from the system of linear wave equations. The system of wave equations is chosen instead of the scalar wave-equation⁴ because of two reasons. One, the scalar version implies vanishing vorticity whereas the latter is what we want to study. Two, the system of wave equations describes the simplest interaction of wave propagation and vorticity which must be examined and understood before we can control vorticity in the Euler equations⁵.

We will now derive the system of linear wave equations from the Euler equations. Starting from the two-dimensional conservative Euler equations, we have

⁴ $\partial_{tt}u - \partial_{xx}u - \partial_{yy}u = 0$

⁵As mentioned before, the physics of vorticity within the context of Euler include advection, dilatation, vortex stretchings and baroclinic effects which are nonlinear. However, for the system of wave equations, vorticity depends only linearized advection and acoustic propagation.

$$\partial_t \rho + \partial_x(\rho U) + \partial_y(\rho V) = 0 \quad (3.1)$$

$$\partial_t(\rho U) + \partial_x(\rho U^2 + P) + \partial_y(\rho UV) = 0 \quad (3.2)$$

$$\partial_t(\rho V) + \partial_x(\rho UV) + \partial_y(\rho V^2 + P) = 0 \quad (3.3)$$

$$\partial_t(\rho E) + \partial_x(\rho UH) + \partial_y(\rho VH) = 0 \quad (3.4)$$

representing conservation of mass, momentum and energy⁶. We shall assume *isothermal conditions*, so the last equation drops out. We will perform linearization with respect to the mean properties of the flow denoted by hat quantities. By ignoring the products of perturbation quantities (denoted by prime values), the linearized variables are

$$\rho = \hat{\rho} + \rho' \quad (3.5)$$

$$\begin{aligned} \rho u &= (\hat{\rho} + \rho')(\hat{u} + u') \\ &\approx \hat{\rho}\hat{u} + \hat{\rho}u' + \hat{u}\rho' \end{aligned} \quad (3.6)$$

$$\rho v \approx \hat{\rho}\hat{v} + \hat{\rho}v' + \hat{v}\rho' \quad (3.7)$$

$$\begin{aligned} \rho u^2 &= (\hat{\rho} + \rho')(\hat{u} + u')^2 \\ &\approx \hat{\rho}\hat{u}^2 + 2\hat{\rho}\hat{u}u' + \hat{u}^2\rho' \end{aligned} \quad (3.8)$$

$$\rho v^2 \approx \hat{\rho}\hat{v}^2 + 2\hat{\rho}\hat{v}v' + \hat{v}^2\rho' \quad (3.9)$$

$$P = \hat{p} + p' \quad (3.10)$$

We shall insert these results into the mass and momentum equations. After performing

⁶The total energy is the sum of internal and kinetic energy of the fluid given by $E = e + \frac{1}{2}(U^2 + V^2)$. The total enthalphy is $H = E + \frac{P}{\rho}$. To obtain closure, the equation of state $P = c\rho(\gamma - 1)$ is utilized where γ is assumed constant and depends on the type of fluid ($\gamma_{air} = 1.4$).

ing some simplification, the linearized isothermal Euler equations can be written as

$$\partial_t \rho' + \hat{u} \partial_x \rho' + \hat{\rho} \partial_x u' + \hat{v} \partial_y \rho' + \hat{\rho} \partial_y v' = 0 \quad (3.11)$$

$$\partial_t u' + \hat{u} \partial_x u' + \frac{1}{\hat{\rho}} \partial_x p' + \hat{v} \partial_y u' = 0 \quad (3.12)$$

$$\partial_t v' + \hat{u} \partial_x v' + \hat{v} \partial_y v' + \frac{1}{\hat{\rho}} \partial_y p' = 0 \quad (3.13)$$

Recall that for isothermal Euler equations, the ideal gas law is given by $P = \rho a_o^2$ where a_o is the constant speed of sound. From the linearized pressure term we get

$$P = \hat{p} + p' = (\hat{\rho} + \rho') a_o^2 \quad (3.14)$$

This implies that $\hat{p} \approx \hat{\rho} a_o^2$ and more importantly $p' \approx \rho' a_o^2$. Applying these relations in the linearized isothermal Euler and making a few manipulations we have

$$\partial_t \left(\frac{p'}{\hat{\rho} a_o^2} \right) + a_o \left(\frac{\hat{u}}{a_o} \right) \partial_x \left(\frac{p'}{\hat{\rho} a_o^2} \right) + a_o \left(\frac{\hat{v}}{a_o} \right) \partial_y \left(\frac{p'}{\hat{\rho} a_o^2} \right) + a_o \left(\partial_x \left(\frac{u'}{a_o} \right) + \partial_y \left(\frac{v'}{a_o} \right) \right) = 0 \quad (3.15)$$

$$\partial_t \left(\frac{u'}{a_o} \right) + a_o \left(\frac{\hat{u}}{a_o} \right) \partial_x \left(\frac{u'}{a_o} \right) + a_o \left(\frac{\hat{v}}{a_o} \right) \partial_y \left(\frac{u'}{a_o} \right) + a_o \partial_x \left(\frac{p'}{\hat{\rho} a_o^2} \right) = 0 \quad (3.16)$$

$$\partial_t \left(\frac{v'}{a_o} \right) + a_o \left(\frac{\hat{u}}{a_o} \right) \partial_x \left(\frac{v'}{a_o} \right) + a_o \left(\frac{\hat{v}}{a_o} \right) \partial_y \left(\frac{v'}{a_o} \right) + a_o \partial_y \left(\frac{p'}{\hat{\rho} a_o^2} \right) = 0 \quad (3.17)$$

which alters the mass equation into a pressure relation. Introduce non-dimensionalized variables such that

$$p = \frac{p'}{\hat{\rho} a_o^2} \quad (3.18)$$

$$u = \frac{u'}{a_o} \quad (3.19)$$

$$M_x = \frac{\hat{u}}{a_o} \quad (3.20)$$

$$M_y = \frac{\hat{v}}{a_o} \quad (3.21)$$

Inserting these notations into the linearized isothermal Euler we get

$$\partial_t p + a_o(M_x \partial_x p + M_y \partial_y p + \partial_x u + \partial_y v) = 0 \quad (3.22)$$

$$\partial_t u + a_o(M_x \partial_x u + M_y \partial_y u + \partial_x p) = 0 \quad (3.23)$$

$$\partial_t v + a_o(M_x \partial_x v + M_y \partial_y v + \partial_y p) = 0 \quad (3.24)$$

which is the system of linear wave equations. If we let $\mathbf{u} = [p, u, v]^T$ as the non-dimensionalized variables, we can write the system in compact advection form

$$\partial_t \mathbf{u} + a_o T \mathbf{u} = 0 \quad (3.25)$$

where the differential operator is

$$T = \begin{bmatrix} M_x \partial_x + M_y \partial_y & \partial_x & \partial_y \\ \partial_x & M_x \partial_x + M_y \partial_y & 0 \\ \partial_y & 0 & M_x \partial_x + M_y \partial_y \end{bmatrix} \quad (3.26)$$

This set of equations can be further simplified by assuming no advection which becomes the linear acoustic problem. We will begin from there.

3.1 Preserving Vorticity For Two Dimensional Acoustic Equations: The Rotated Richtmyer Scheme

Let the non-dimensionalized variables $\mathbf{u} = [p, u, v]^T$ satisfy the following system of acoustic equations.

$$\partial_t p + a_o(\partial_x u + \partial_y v) = 0 \quad (3.27)$$

$$\partial_t u + a_o \partial_x p = 0 \quad (3.28)$$

$$\partial_t v + a_o \partial_y p = 0 \quad (3.29)$$

We will discretize the above equations to preserve vorticity on uniform Cartesian grids.

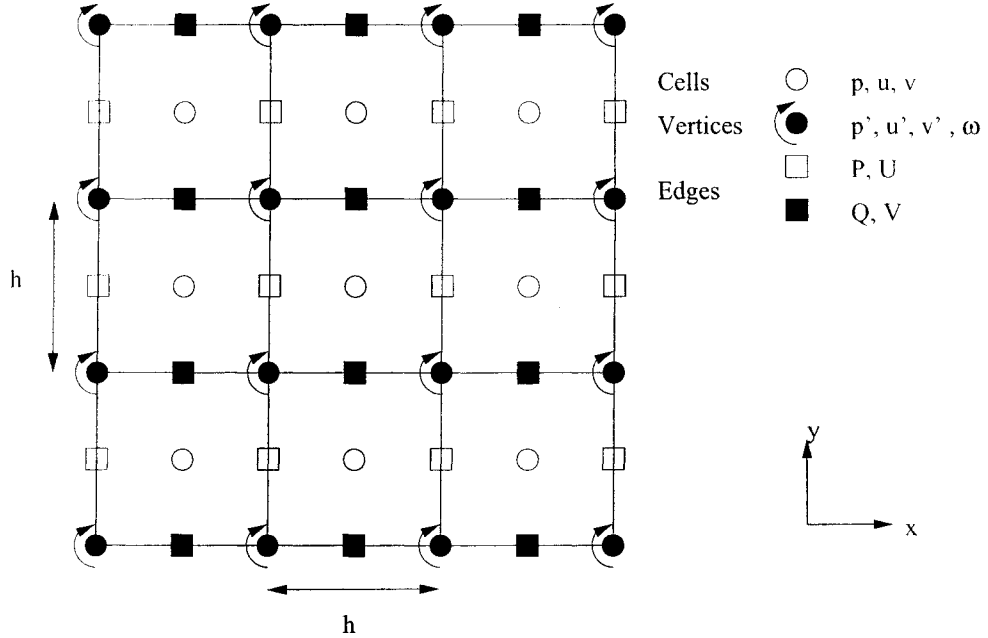


Figure 3.1: Grid Representation

3.1.1 On Two Dimensional Cartesian Grids

Before we attempt to discretize the equations, we shall introduce the grid representation. As mentioned before, vorticity preservation depends on the choice of discretization. We choose a configuration such that the *main variables are conserved within the cell and vorticity is preserved at the vertices*. Note that cell coordinates are denoted by (i, j) whereas vertex coordinates are given by $(i \pm \frac{1}{2}, j \pm \frac{1}{2})$. We will use some notations developed by Morton and Roe [73] and introduce new notations to extend their work. To ensure discrete conservation, we draw a control volume around a point of interest and write the point update as an integral around this volume. To achieve discrete conservation, we will discretize the acoustic equations as a cell-centered finite volume method defined as

$$(\mathbf{u}^{n+1} - \mathbf{u}^n)h^2 + (\delta_x \mathbf{f}^* + \delta_y \mathbf{g}^*)h\Delta t = 0 \quad (3.30)$$

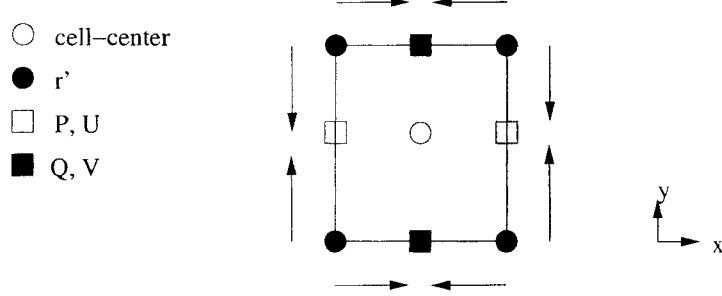


Figure 3.2: Flux Interface Requirements for Preserving Vorticity. Note that the interface pressures must be evaluated as averaged quantities at the vertices (denoted by pairs of arrow).

where $(\mathbf{f}^*, \mathbf{g}^*)$ are the numerical fluxes in (x, y) directions to be determined under a certain constraint. Let the Courant number be $\nu = a_o \frac{\Delta t}{h}$, then our formulation becomes

$$p^{n+1} = p^n - \nu(\delta_x U + \delta_y V) \quad (3.31)$$

$$u^{n+1} = u^n - \nu \delta_x P \quad (3.32)$$

$$v^{n+1} = v^n - \nu \delta_y Q \quad (3.33)$$

Define compact vorticity⁷ as

$$\omega = \mu_y \delta_x v - \mu_x \delta_y u = L_\omega(\mathbf{u}) \quad (3.34)$$

Preserving vorticity requires

$$\begin{aligned} 0 &= \omega^{n+1} - \omega^n \\ &= L_\omega(\mathbf{u}^{n+1} - \mathbf{u}^n) \\ &= -\nu[0, -\mu_x \delta_y, \mu_y \delta_x][(\delta_x U + \delta_y V), \delta_x P, \delta_y Q]^T \\ &= -\nu \delta_x \delta_y (\mu_x P - \mu_y Q) \end{aligned} \quad (3.35)$$

⁷This is as opposed to central differencing $\omega = \mu_x \delta_x v - \mu_y \delta_y u$ and note that the definition of discrete operators are included in appendix G

In order to remove spurious vorticity due to pressure terms, Morton and Roe require that

$$\mu_x P = \mu_y Q \quad (3.36)$$

Rewrite the edge values P, Q in terms of cell values p, u, v and define r' to be some quantity defined at vertices satisfying

$$P = \mu_y r' \quad (3.37)$$

$$Q = \mu_x r' \quad (3.38)$$

Hence we have

$$\mu_x P = \mu_x \mu_y r' \quad (3.39)$$

$$\mu_y Q = \mu_x \mu_y r' \quad (3.40)$$

and 3.36 is satisfied. To obtain a second order accuracy on a 9-point stencil, we need

$$\begin{aligned} r' &= \mu_x \mu_y p + \frac{dt}{2} \frac{\partial p}{\partial t} + \dots \\ &= \mu_x \mu_y p - \frac{dt}{2} (\partial_x u + \partial_y v) \\ &= \mu_x \mu_y p - \frac{\nu}{2} (\mu_y \delta_x u + \mu_x \delta_y v) \end{aligned} \quad (3.41)$$

which relates vertex quantities to cell center quantities. This value of r' will be used to determine pressure at the edges (P, Q) in order to update the discrete velocities hence

$$u^{n+1} = u^n - \nu \mu_y \delta_x r' \quad (3.42)$$

$$v^{n+1} = v^n - \nu \mu_x \delta_y r' \quad (3.43)$$

Construction of Evolution Matrix

We are now almost ready to construct an evolution scheme for \mathbf{u} based on a matrix operator K that will update the solution

$$\mathbf{u}^{n+1} = \mathbf{u}^n - K\mathbf{u}^n \quad (3.44)$$

where from our analysis so far we have

$$K = \begin{bmatrix} ?? & ?? & ?? \\ \nu\mu_x\mu_y^2\delta_x & \frac{1}{2}\nu^2\mu_y^2\delta_x^2 & \frac{1}{2}\nu^2\mu_x\mu_y\delta_x\delta_y \\ \nu\mu_x^2\mu_y\delta_y & \frac{1}{2}\nu^2\mu_x\mu_y\delta_x\delta_y & \frac{1}{2}\nu^2\mu_x^2\delta_y^2 \end{bmatrix} \quad (3.45)$$

The discrete adjoint property of matrix K requires it to be symmetric [73], hence $K_{12} = K_{21}$ and $K_{13} = K_{31}$. We now have every component for matrix K except for the first component. Before we attempt to find this component, note that the flux or edge velocity U is

$$\begin{aligned} U &= \mu_x\mu_y^2 u \\ &= \mu_y(\mu_x\mu_y u) \\ &= \mu_y u' \end{aligned} \quad (3.46)$$

where $u' = \mu_x\mu_y u$ is an average of cell velocities evaluated at the vertices. We want to write the horizontal velocity $U = \mu_y u'$ in terms of cell velocity u on a 9-point stencil with second order accuracy thus

$$\begin{aligned} u' &= \mu_x\mu_y u + \frac{dt}{2} \frac{\partial u}{\partial t} + \dots \\ &= \mu_x\mu_y p - \frac{dt}{2} \partial_x p \\ &= \mu_x\mu_y p - \frac{\nu}{2} \mu_y \delta_x p \end{aligned} \quad (3.47)$$

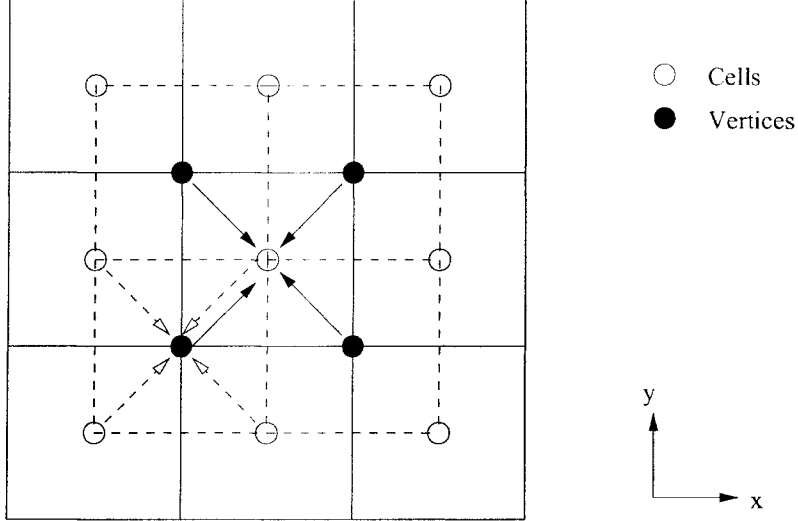


Figure 3.3: The Rotated Richtmyer Scheme. Dash lines indicate half-step whereas solid lines indicate full-step.

We can rewrite the edge velocity $U = \mu_x \mu_y^2 p - \frac{\nu}{2} \mu_y^2 \delta_x p$ and by similar arguments $V = \mu_x^2 \mu_y p - \frac{\nu}{2} \mu_x^2 \delta_y p$. Insert these results into our evolution matrix so that

$$K = \begin{bmatrix} \frac{1}{2} \nu^2 (\mu_y^2 \delta_x^2 + \mu_x^2 \delta_y^2) & \nu \mu_x \mu_y^2 \delta_x & \nu \mu_x^2 \mu_y \delta_y \\ \nu \mu_x \mu_y^2 \delta_x & \frac{1}{2} \nu^2 \mu_y^2 \delta_x^2 & \frac{1}{2} \nu^2 \mu_x \mu_y \delta_x \delta_y \\ \nu \mu_x^2 \mu_y \delta_y & \frac{1}{2} \nu^2 \mu_x \mu_y \delta_x \delta_y & \frac{1}{2} \nu^2 \mu_x^2 \delta_y^2 \end{bmatrix} \quad (3.48)$$

Morton and Roe [73] noted that this can be written as

$$K = \nu T_{\delta A} [\mu_x \mu_y I - \frac{1}{2} \nu T_{\delta a}] \quad (3.49)$$

where $T_{\delta A}$ is a discrete version of equation (3.26) (omitting the advection terms) denoted by

$$T_{\delta A} = \begin{bmatrix} 0 & \mu_y \delta_x & \mu_x \delta_y \\ \mu_y \delta_x & 0 & 0 \\ \mu_x \delta_y & 0 & 0 \end{bmatrix} \quad (3.50)$$

Hence we can write the evolution as a two-step scheme with

$$\mathbf{u}' = [\mu_x \mu_y I - \frac{\nu}{2} T_{\delta A}] \mathbf{u}^n \quad (3.51)$$

will serve as a half-step providing provisional solution at vertices. The full step

$$\mathbf{u}^{n+1} = \mathbf{u}^n - \nu T_{\delta A} \mathbf{u}' \quad (3.52)$$

uses half-step solutions to update the cells. This is the Rotated Richtmyer scheme and has properties of second order accuracy with conservation⁸, symmetry of operators and most importantly vorticity preservation.

3.1.2 Including Limiters

We attempt to include a limiting procedure at the half-step. Since vorticity is a multi dimensional physical problem, perhaps it is best to utilize multi dimensional limiting. However, much of multi dimensional limiting are uncharted territories, and to begin working on the vorticity preserving scheme using this approach is an arduous task. Thus, we will be content with limiting based on one-dimensional considerations. There are many ways to construct one dimensional limiting in solving system of equations [94], [109], [107], [13]. To name a few, there are the Flux-Correctional Transport (FCT) [13], MUSCL-type reconstruction [107] and the Flux-Limiting schemes [94]. In this chapter, we will embrace the Flux-Limiting ideology. Before we begin constructing the limiters, consider the following.

Lemma 1 *For $r' = f(x, y, t)$ defined at a vertex, where f is an arbitrary function, vorticity is preserved at the vertices for the Rotated Richtmyer scheme solving the two-dimensional acoustic equations.*

⁸This is a finite volume method in which the interface flux is determined by the quantities at the two vertices that define the interface unlike many finite volume method where the interface flux is computed using neighboring cell values sharing a common interface. The flux therefore depends on six cell values. It is easy to see that if it only depends on two values, the condition of 3.36 cannot be met.

Proof

Let P and Q to be pressures located at the vertical and horizontal interface as defined before. Assume $f(x, y, t)$ to be any function defined at the vertices so that

$$\begin{aligned} P &= \mu_y r' = \mu_y f(x, y, t) \\ Q &= \mu_x r' = \mu_x f(x, y, t) \end{aligned} \quad (3.53)$$

Appealing to commutative property of the discrete averaging operator we have

$$\mu_x \mu_y f(x, y, t) = \mu_y \mu_x f(x, y, t) \quad (3.54)$$

This is equivalent to

$$\mu_x P = \mu_y Q \quad (3.55)$$

which is our vorticity preserving requirement. This implies that the only requirement for vorticity preservation is that pressure at the flux interface (edge) must come from the vertices.

Corollary 1 *The Rotated Richtmyer scheme is vorticity preserving when solving the two-dimensional acoustic equations if a one-dimensional type of limiter is used for all variables.*

Now we are ready to construct a limiting procedure for the Rotated Richtmyer scheme. Recall that the slope of vertex variables in the x-direction can be computed via compact differencing using four cell values surrounding the vertex. Define Δ_x and Δ_y as the discrete slopes at the vertices hence

$$\Delta_x \mathbf{u}' = \mu_y \delta_x \mathbf{u} \quad (3.56)$$

Referring to Fig 3.4, in order to limit the slopes of any variable at vertex M , we require that

$$\Delta_x^{lim} \mathbf{u}'_M = \phi(\phi(\Delta_x \mathbf{u}'_M, \Delta_x \mathbf{u}'_L), \phi(\Delta_x \mathbf{u}'_R, \Delta_x \mathbf{u}'_M)) \quad (3.57)$$

will give the limited slope in the x-direction. The slope limiting function $\phi(a, b)$ is based on one dimensional geometric principles [107], [94]. Similarly,

$$\Delta_y^{lim} \mathbf{u}'_M = \phi(\phi(\Delta_y \mathbf{u}'_M, \Delta_y \mathbf{u}'_B), \phi(\Delta_y \mathbf{u}'_T, \Delta_y \mathbf{u}'_M)) \quad (3.58)$$

will give limited slope in y-direction. The limited compact differencings can be written as

$$\mu_y \delta_x^{lim} \mathbf{u} = \Delta_x^{lim} \mathbf{u}' \quad (3.59)$$

$$\mu_x \delta_y^{lim} \mathbf{u} = \Delta_y^{lim} \mathbf{u}' \quad (3.60)$$

Thus the limited half-step operator is given

$$T_{\delta A}^{lim} = \begin{bmatrix} 0 & \mu_y \delta_x^{lim} & \mu_x \delta_y^{lim} \\ \mu_y \delta_x^{lim} & 0 & 0 \\ \mu_x \delta_y^{lim} & 0 & 0 \end{bmatrix} \quad (3.61)$$

The Rotated Richtmyer scheme is then written as

$$\mathbf{u}' = [\mu_x \mu_y I - \frac{\nu}{2} T_{\delta A}^{lim}] \mathbf{u}^n \quad (3.62)$$

as the limited half-step. The full step

$$\mathbf{u}^{n+1} = \mathbf{u}^n - \nu T_{\delta A} \mathbf{u}' \quad (3.63)$$

is the same as before. The limiting function $\phi(a, b)$ can be any of the usual one-dimensional limiters⁹.

⁹These include but are not limited to the Minmod, Harmonic, van Albada and Superbee limiters[94].

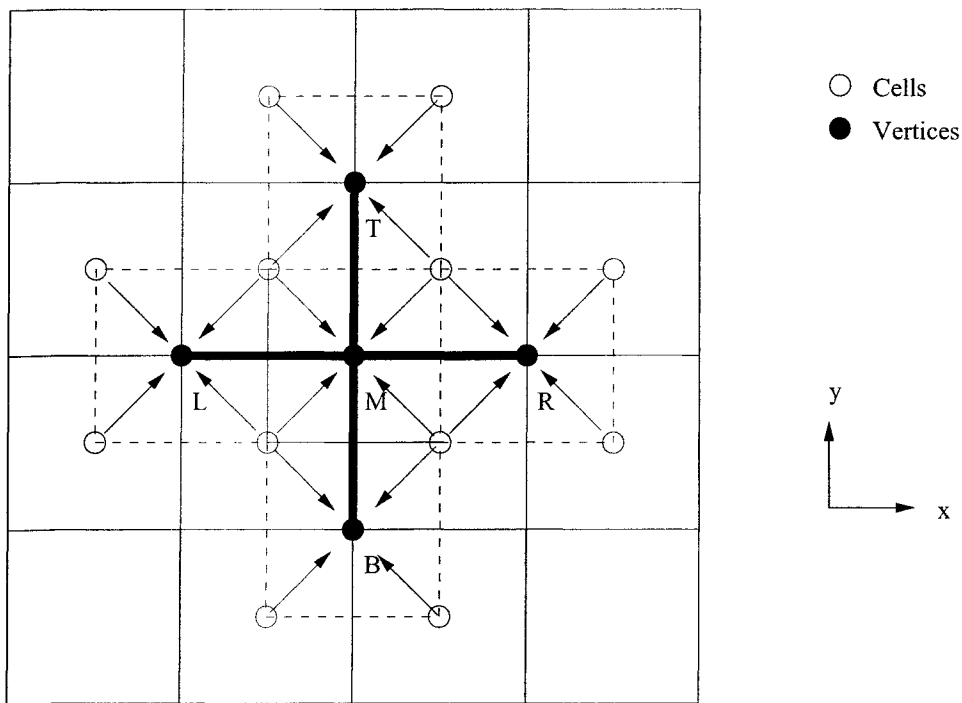


Figure 3.4: Limiting procedure. First, compute the slopes at the vertices via compact differencing using values at four surrounding cells (line with arrows). Then perform limiting on these slopes based on adjacent vertices (L,R) and (B,T) to the middle vertex M dimension by dimension (thick solid lines) before performing half step.

3.2 Preserving Vorticity For Two Dimensional Linear Wave Equations

We will now include advection and investigate how that will effect the Rotated Richtmyer vorticity preserving scheme. We will also explore the possibilities of inserting limiters.

3.2.1 Including Constant Advection

Let $[p, u, v]^T$ satisfy the following system of wave equations with non-dimensionalized constant advection (M_x, M_y) .

$$\partial_t p + a_o(M_x \partial_x p + M_y \partial_y p + \partial_x u + \partial_y v) = 0 \quad (3.64)$$

$$\partial_t u + a_o(M_x \partial_x u + M_y \partial_y u + \partial_x p) = 0 \quad (3.65)$$

$$\partial_t v + a_o(M_x \partial_x v + M_y \partial_y v + \partial_y p) = 0 \quad (3.66)$$

Using same description for P and Q and introducing horizontal and vertical edge velocities, we have the following discretization.

$$p^{n+1} = p^n - \nu(M_x \delta_x P + M_y \delta_y Q + \delta_x U + \delta_y V) \quad (3.67)$$

$$u^{n+1} = u^n - \nu(M_x \delta_x U_1 + M_y \delta_y U_2 + \delta_x P) \quad (3.68)$$

$$v^{n+1} = v^n - \nu(M_x \delta_x V_1 + M_y \delta_y V_2 + \delta_y Q) \quad (3.69)$$

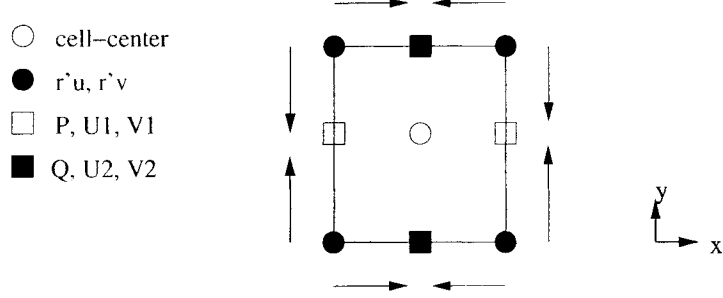


Figure 3.5: Vorticity Preserving Requirements

Preserving vorticity requires

$$\begin{aligned}
 \omega^{n+1} - \omega^n &= L_\omega[\mathbf{u}^{n+1} - \mathbf{u}^n] \\
 &= -L_\omega\nu \begin{bmatrix} \delta_x(M_xP + U_1) + \delta_y(M_yQ + V_2) \\ \delta_x(M_xU_1 + P) + \delta_y(M_yU_2) \\ \delta_x(M_xV_1) + \delta_y(M_yV_2 + Q) \end{bmatrix} \\
 &= \nu[\mu_x\delta_y[\delta_x(M_xU_1 + P) + \delta_y(M_yU_1)] - \mu_y\delta_x[\delta_x(M_xV_1) + \delta_y(M_yV_2 + Q)]] \\
 &= \nu[\delta_x\delta_y(\mu_xP - \mu_yQ) + \mu_x\delta_y(\delta_x(M_xU_1) + \delta_y(M_yU_2)) - \mu_y\delta_x(\delta_x(M_xV_1) + \delta_y(M_yV_2))] \\
 &= \nu[\delta_x\delta_y(\mu_xP - \mu_yQ) - \delta_xM_x(\mu_y\delta_xV_1 - \mu_x\delta_yU_1) - \delta_yM_y(\mu_y\delta_xV_2 - \mu_x\delta_yU_2)]
 \end{aligned} \tag{3.70}$$

We have introduced separate edge velocities (see Fig 3.5). Let U_1 and V_1 be the u and v velocities advected at the vertical edges while U_2 and V_2 be its u and v velocities advected at the horizontal edges. Let us relate the edge velocities to vertex quantities. Define

$$U_1 = \mu_y r'_u \tag{3.71}$$

$$V_1 = \mu_y r'_v \tag{3.72}$$

$$U_2 = \mu_x r'_u \tag{3.73}$$

$$V_2 = \mu_x r'_v \tag{3.74}$$

We want a compact 9-point stencil for cell velocities and the only way to achieve this is by setting

$$r'_u = \mu_x \mu_y u \quad (3.75)$$

As before, to obtain second order accuracy we require

$$\begin{aligned} r'_u &= \mu_x \mu_y u + \frac{dt}{2} \frac{\partial u}{\partial t} + \dots \\ &= \mu_x \mu_y u - \frac{\nu}{2} (M_x \mu_y \delta_x u + M_y \mu_x \delta_y u + \mu_y \delta_x p) \\ &= \mu_x \mu_y u - \frac{\nu}{2} (\mu_y \delta_x (M_x u + p) + \mu_x \delta_y (M_y u)) \end{aligned} \quad (3.76)$$

Similarly we need

$$\begin{aligned} r'_v &= \mu_x \mu_y v + \frac{dt}{2} \frac{\partial v}{\partial t} + \dots \\ &= \mu_x \mu_y v - \frac{\nu}{2} (M_x \mu_y \delta_x v + M_y \mu_x \delta_y v + \mu_x \delta_y p) \\ &= \mu_x \mu_y v - \frac{\nu}{2} (\mu_y \delta_x (M_x v) + \mu_x \delta_y (M_y v + p)) \end{aligned} \quad (3.77)$$

Applying results of r'_u and r'_v , U_1 , U_2 , V_1 and V_2 becomes

$$U_{(.)} = \mu_{(.)} (\mu_x \mu_y u - \frac{\nu}{2} (\mu_y \delta_x (M_x p + u) + \mu_x \delta_y (M_y u))) \quad (3.78)$$

$$V_{(.)} = \mu_{(.)} (\mu_x \mu_y v - \frac{\nu}{2} (\mu_y \delta_x (M_x v) + \mu_x \delta_y (M_y p + v))) \quad (3.79)$$

$$(.) = 1 \text{ or } 2 \quad (3.80)$$

$$(..) = x \text{ or } y \quad (3.81)$$

Note that r'_u and r'_v are exactly the half-step u and v velocities computed at the vertices based on cell values derived by Morton and Roe [73]. In order to remove spurious vorticity due to pressure terms, we have similar requirements as before in the pure acoustic problem i.e,

$$P = \mu_y r' \quad (3.82)$$

$$Q = \mu_x r' \quad (3.83)$$

where

$$r' = \mu_x \mu_y p - \frac{\nu}{2} (\mu_y \delta_x (M_x p + u) + \mu_x \delta_y (M_y p + v)) \quad (3.84)$$

Inserting the values of P, Q, U_1, U_2, V_1, V_2 into the vorticity evolution equation, we have

$$\begin{aligned} \omega^{n+1} - \omega^n &= \nu [\delta_x \delta_y (\mu_x P - \mu_y Q) - \delta_x M_x (\mu_y \delta_x \mu_y r'_v - \mu_x \delta_y \mu_y r'_u) - \delta_y M_y (\mu_y \delta_x \mu_x r'_v - \mu_x \delta_y \mu_x r'_u)] \\ &= -\nu (M_x \mu_y \delta_x + M_y \mu_x \delta_y) [\mu_y \delta_x r'_v - \mu_x \delta_y r'_u] \end{aligned} \quad (3.85)$$

This implies that numerical vorticity evolution is *dependent only on the half-step velocities*. This is consistent with the inviscid vorticity transport equation in two dimensions where vorticity is purely advected if there are no baroclinic effects. Our results imply that any form of limiting on the half-step pressure will not create spurious vorticity for the Rotated Richtmyer scheme. However this is not true for half-step velocities where some restrictions are required. We will determine what are the restrictions next.

3.2.2 Preserving Vorticity With Limiters

We can introduce limiters by directly limiting the gradient of the fluxes in the linear wave equations. Another interpretation of this would be to limit the flux components by varying the Courant numbers that are multiplied to each component of the flux-gradients. We shall see that there are severe restrictions for the flux components when we insist on preserving vorticity. Recall that we want to preserve vorticity at the vertices. We can write its evolution equation as

$$\omega^{n+1} - \omega^n = -\nu \tilde{Q} \omega' \quad (3.86)$$

where

$$\tilde{Q} = [M_x \mu_y \delta_x + M_y \mu_x \delta_y] \quad (3.87)$$

is the advection operator and

$$\omega' = \mu_y \delta_x v' + \mu_x \delta_y u' \quad (3.88)$$

is the *cell vorticity based on vertex velocities*. We want the numerical vorticity evolution equation to be consistent with its analytical transport equation. Assuming constant advection with zero pressure gradients, the two-dimensional vorticity transport equation is

$$\frac{\partial \omega}{\partial t} + M_x \frac{\partial \omega}{\partial x} + M_y \frac{\partial \omega}{\partial y} = 0 \quad (3.89)$$

Morton and Roe [73] have shown two things about the Rotated Richtmyer scheme when solving the system of linear wave equations. One, the initial vorticity distribution is preserved if we have pure acoustic equations and it obeys the discrete vorticity transport equation when the flow advection is constant. Two, there are no inconsistencies between the vorticity predicted by its transport equation and vorticity deduced from the velocities.

We would like to include limiting and by doing so, we will see that the scheme does not preserve vorticity even for irrotational flow. Irrotationality implies that our numerical vorticity evolution is

$$\omega^n = 0 \quad (3.90)$$

for all times. Since vorticity is a scalar quantity in two dimensions, equation (3.86) reduces to

$$\omega' = 0 \quad (3.91)$$

This imposes a restriction for the half-step velocities located at the vertices. These

velocities are computed from cell quantities and written as

$$u' = \mu_x \mu_y u - \nu_{\tilde{Q}} \tilde{Q} u - \nu_P \mu_y \delta_x p \quad (3.92)$$

$$v' = \mu_x \mu_y v - \nu_{\tilde{Q}} \tilde{Q} v - \nu_P \mu_x \delta_y p \quad (3.93)$$

where we have defined Courant numbers with respect to advection $\nu_{\tilde{Q}}$ and pressure ν_P components. Thus

$$\begin{aligned} \omega' &= \mu_x \mu_y (\mu_y \delta_x v - \mu_x \delta_y u) \\ &- \frac{1}{2} [\mu_y \delta_x (\nu_{\tilde{Q}} \tilde{Q} v) - \mu_x \delta_y (\nu_{\tilde{Q}} \tilde{Q} u)] \\ &+ \mu_y \delta_x (\nu_P \mu_x \delta_y p) - \mu_x \delta_y (\nu_P \mu_y \delta_x p) \end{aligned} \quad (3.94)$$

The first line of this equation is the initial vorticity and is zero for discretely irrotational flow. The second line is the discrete advection component which may contain spurious vorticity. The last line corresponds to spurious vorticity due to pressure gradients denoted by ω'_P . Before we hypothesize any restrictions to preserve vorticity, we will introduce product rules for the operators ¹⁰.

$$\mu_x(ab) = \mu_x(a)\mu_x(b) + \frac{1}{4}\delta_x(a)\delta_x(b) \quad (3.95)$$

$$\mu_y(ab) = \mu_y(a)\mu_y(b) + \frac{1}{4}\delta_y(a)\delta_y(b) \quad (3.96)$$

$$\delta_x(ab) = \mu_x(a)\delta_x(b) + \mu_x(b)\delta_x(a) \quad (3.97)$$

$$\delta_y(ab) = \mu_y(a)\delta_y(b) + \mu_y(b)\delta_y(a) \quad (3.98)$$

Hence contributions of spurious vorticity from pressure gradients (last line of equation

¹⁰These can be proven by direct computations.

3.94) become

$$\begin{aligned}
\omega'_P &= \mu_y \delta_x (\nu_P \mu_x \delta_y p) + \mu_x \delta_y (\nu_P \mu_y \delta_x p) \\
&= \mu_y [\mu_x \nu_P \delta_x (\mu_x \delta_x p) + \mu_x (\mu_x \delta_y p) \delta_x \nu_P] - \mu_x [\mu_y \nu_P \delta_y (\mu_y \delta_x p) + \mu_y (\mu_y \delta_x p) \delta_y \nu_P] \\
&= (\mu_y \mu_x \nu_P) (\mu_x \mu_y \delta_x \delta_y p) + \frac{1}{4} (\mu_x \delta_y \nu_P) (\mu_x \delta_x \delta_y^2 p) + (\mu_x^2 \mu_y \delta_y p) (\mu_y \delta_x \nu_P) + \frac{1}{4} (\mu_x^2 \delta_y^2 p) (\delta_x \delta_y \nu_P) \\
&- (\mu_y \mu_x \nu_P) (\mu_x \mu_y \delta_x \delta_y p) - \frac{1}{4} (\mu_y \delta_x \nu_P) (\mu_y \delta_x^2 \delta_y p) - (\mu_x \mu_y^2 \delta_x p) (\mu_x \delta_y \nu_P) - \frac{1}{4} (\mu_y^2 \delta_x^2 p) (\delta_x \delta_y \nu_P) \\
&= \frac{1}{4} (\delta_x \delta_y \nu_P) (\mu_x^2 \delta_y^2 - \mu_y^2 \delta_x^2) p + (\mu_y \delta_x \nu_P) (\mu_x^2 \mu_y \delta_y - \frac{1}{4} \mu_y \delta_x^2 \delta_y) p \\
&- (\mu_x \delta_y \nu_P) (\mu_x \mu_y^2 \delta_x - \frac{1}{4} \mu_x \delta_x \delta_y^2) p
\end{aligned}$$

Using the identities

$$\delta_x^2 = 4(\mu_x^2 - 1), \quad \delta_y^2 = 4(\mu_y^2 - 1) \quad (3.99)$$

we get

$$\begin{aligned}
\omega'_P &= (\delta_x \delta_y \nu_P) [\mu_x^2 (\mu_y^2 - 1) - \mu_y^2 (\mu_x^2 - 1)] p \\
&+ (\mu_y \delta_x \nu_P) [\mu_x^2 \mu_y \delta_y - (\mu_x^2 - 1)(\mu_y \delta_y)] p \\
&- (\mu_x \delta_y \nu_P) [\mu_x \mu_y^2 \delta_x - (\mu_y^2 - 1)(\mu_x \delta_x)] p
\end{aligned}$$

Appealing to the product rules again we have

$$\omega'_P = \delta_y (\mu_y p \delta_x \nu_P) - \delta_x (\mu_x p \delta_y \nu_P) \quad (3.100)$$

Lemma 2 $\omega'_P = 0 \Leftrightarrow \nu_P = k$ at each vertex, where k is a constant.

Proof \Rightarrow

Assume $\omega'_P = 0$ everywhere in a discretized computational domain $D \in [-0.25, 0.25] \times [-0.25, 0.25]$. Define a subset of the domain D_s as cells and vertices as shown in Fig

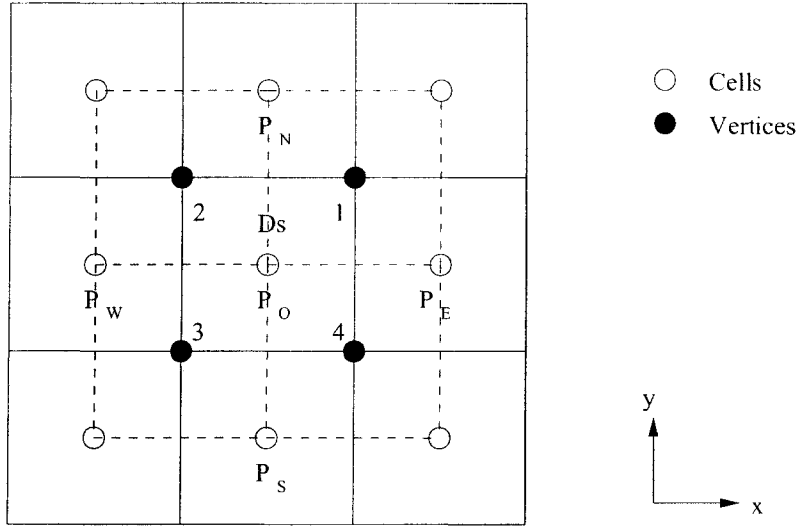


Figure 3.6: Domain D with subdomain bounded by vertex 1,2,3 and 4 defined by D_s . To preserve vorticity at cell O , all ν must be identical at vertices surrounding the cell.

(3.6). Define a non-trivial pressure $p = \cos(\pi x)\cos(\pi y)$ and its discretized form in D_s and assume non-identical ν_P . But in D_s

$$\begin{aligned}\omega'_P &= (p_O + p_N)(\nu_1 - \nu_2) - (p_O + p_S)(\nu_4 - \nu_3) - (p_O + p_E)(\nu_1 - \nu_4) + (p_O + p_W)(\nu_2 - \nu_3) \\ &= 0\end{aligned}$$

only if $\nu_1 = \nu_2 = \nu_3 = \nu_4$ which is a contradiction.

Proof \Leftarrow

If $\nu_1 = \nu_2 = \nu_3 = \nu_4$, hence

$$\begin{aligned}\omega'_P &= (\nu_4 - \nu_1)p_E + (\nu_1 - \nu_2)p_N + (\nu_2 - \nu_3)p_W + (\nu_3 - \nu_4)p_S \\ &= 0\end{aligned}$$

Corollary 2 *It is a necessary condition to have ν_P identical at each vertex for the Rotated Richtmyer scheme to be vorticity preserving.*

Now we shall look at the effects of advection located in the second line of equation

(3.94). By applying product rules we have

$$\begin{aligned}
\omega'_{\tilde{Q}} &= \mu_y \delta_x (\nu_{\tilde{Q}} \tilde{Q} v) - \mu_x \delta_y (\nu_{\tilde{Q}} \tilde{Q} u) \\
&= \mu_x [(\mu_y \nu_{\tilde{Q}}) (\delta_y \tilde{Q} u) + (\mu_y \tilde{Q} u) (\delta_y \nu_{\tilde{Q}})] - \mu_y [(\mu_x \nu_{\tilde{Q}}) (\delta_x \tilde{Q} v) + (\mu_x \tilde{Q} v) (\delta_x \nu_{\tilde{Q}})] \\
&= (\mu_x \mu_y \nu_{\tilde{Q}}) (\mu_x \delta_y \tilde{Q} u) + \frac{1}{4} (\mu_y \delta_x \nu_{\tilde{Q}}) (\delta_x \delta_y \tilde{Q} u) + (\mu_x \mu_y \tilde{Q} u) (\mu_x \delta_y \nu_{\tilde{Q}}) + \frac{1}{4} (\mu_y \delta_x \tilde{Q} u) (\delta_x \delta_y \nu_{\tilde{Q}}) \\
&- (\mu_x \mu_y \nu_{\tilde{Q}}) (\mu_y \delta_x \tilde{Q} v) + \frac{1}{4} (\mu_x \delta_y \nu_{\tilde{Q}}) (\delta_x \delta_y \tilde{Q} v) - (\mu_x \mu_y \tilde{Q} v) (\mu_y \delta_x \nu_{\tilde{Q}}) + \frac{1}{4} (\mu_x \delta_y \tilde{Q} v) (\delta_x \delta_y \nu_{\tilde{Q}})
\end{aligned}$$

After simplifying we get

$$\begin{aligned}
\omega'_{\tilde{Q}} &= (\mu_x \mu_y \nu_{\tilde{Q}}) \tilde{Q} (\mu_x \delta_y u - \mu_y \delta_x v) \\
&+ \frac{1}{4} (\delta_x \delta_y \nu_{\tilde{Q}}) \tilde{Q} (\mu_x \delta_y u - \mu_y \delta_x v) \\
&+ (\mu_x \delta_y \nu_{\tilde{Q}}) \tilde{Q} (\mu_x \mu_y v - \frac{1}{4} \delta_x \delta_y v) - (\mu_y \delta_x \nu_{\tilde{Q}}) \tilde{Q} (\mu_x \mu_y u - \frac{1}{4} \delta_x \delta_y u) \quad (3.101)
\end{aligned}$$

Appealing to irrotationality of the data, $\omega'_{\tilde{Q}}$ reduces to

$$\omega'_{\tilde{Q}} = (\mu_x \delta_y \nu_{\tilde{Q}}) \tilde{Q} (\mu_x \mu_y v - \frac{1}{4} \delta_x \delta_y v) - (\mu_y \delta_x \nu_{\tilde{Q}}) \tilde{Q} (\mu_x \mu_y u - \frac{1}{4} \delta_x \delta_y u) \quad (3.102)$$

We are ready to claim another Lemma.

Lemma 3 $\omega'_{\tilde{Q}} = 0 \Leftrightarrow \nu_{\tilde{Q}} = k$ at each vertex, where k is a constant.

The proof is included in appendix G.

Corollary 3 It is also a necessary condition to have $\nu_{\tilde{Q}}$ identical at each vertex for the Rotated Richtmyer scheme to be vorticity preserving.

We have explained earlier in this section that we could introduce limiting locally if we vary the Courant number locally. From our analytical results it is clear that unless any limiter used is global, the Rotated Richtmyer scheme will not be vorticity preserving when solving the system of linear wave equations. The only global choice that gives second order accuracy is $\nu_{\tilde{Q}} = \nu$, which is not monotone.

This is not surprising since the Rotated Richtmyer scheme is designed using a specific linear averaging such that it will preserve vorticity for linear wave equations, hence may not preserve vorticity when nonlinearity is included. The scheme is also designed to preserve vorticity from a local standpoint but since it does not preserve vorticity for nonlinear settings, we will have to give up this local property and settle for a global mechanism. This will be the subject of the next section.

3.3 Introducing a Vorticity Correction Algorithm

We have learnt that the Rotated Richtmyer scheme is not vorticity preserving unless global limiters are used to limit the fluxes that govern cell velocities. We therefore abandon any analogy with constrained transport, and turn to a correction method. We implement this similarly to Brandt's two-step method [15] for solving incompressible flow problems where in one of the steps, zero velocity divergence is enforced without altering the curl of velocities. Here we want to bring about some required curl of velocity without altering velocity divergence. We will perform the vorticity correction as follows. Let

$$\Delta\omega = \omega_{IND} - (\mu_y \delta_x v - \mu_x \delta_y u) \quad (3.103)$$

be defined as the vertex vorticity discrepancy where ω_{IND} is an independent estimate of vorticity. For the linear wave equations, this would be the initial vorticity. If we have spurious clockwise vorticity at a vertex, a counter-clockwise correction is performed by altering the surrounding cell velocities and vice-versa. Note that each cell velocity is dependant on its 4 neighboring vertices. We will perform corrections on the cell velocities as (see Fig 3.7)

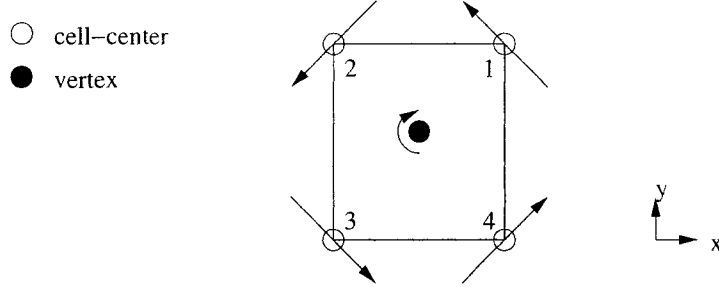


Figure 3.7: Vorticity correction by changing cell velocities. Assume we have a clockwise spurious vorticity $\Delta\omega$ at a vertex, we introduce a counter-clockwise correctional vorticity. Although this leads to solving an a Poisson problem but it ensures vorticity is preserved locally.

$$u_1 \rightarrow u_1 - k\Delta\omega \quad v_1 \rightarrow v_1 + k\Delta\omega$$

$$u_2 \rightarrow u_2 - k\Delta\omega \quad v_2 \rightarrow v_2 - k\Delta\omega$$

$$u_3 \rightarrow u_3 + k\Delta\omega \quad v_3 \rightarrow v_3 - k\Delta\omega$$

$$u_4 \rightarrow u_4 + k\Delta\omega \quad v_4 \rightarrow v_4 + k\Delta\omega$$

where k is a nonzero constant. This correction does not alter the estimated divergence of the flow, $\text{div}u = \mu_y\delta_x u + \mu_x\delta_y v$, but it will change the velocity at neighboring vertices, and we need to iterate to convergence. This makes the method global. By including four neighboring vertices, the velocity corrections can be written as

$$\begin{aligned} u &\rightarrow u - k\mu_x\delta_y\Delta\omega \\ v &\rightarrow v + k\mu_y\delta_x\Delta\omega \end{aligned} \tag{3.104}$$

We want to include the vorticity correction as a part of updating the full step and this has to be done in a conservative manner. One way to do this is to modify the edge (or cell interface) values before updating the full step. Let the discrete linear

wave equation operator be defined as

$$T_\delta = \begin{bmatrix} M_x\mu_y\delta_x + M_y\mu_x\delta_y & \mu_y\delta_x & \mu_x\delta_y \\ \mu_y\delta_x & M_x\mu_y\delta_x + M_y\mu_x\delta_y & 0 \\ \mu_x\delta_y & 0 & M_x\mu_y\delta_x + M_y\mu_x\delta_y \end{bmatrix} \quad (3.105)$$

so that the modified full step will be

$$\mathbf{u}^{n+1} = \mathbf{u}^n - \nu T_\delta \mathbf{u}' + \frac{\Delta t}{h} (\delta_x \mathbf{C}_x + \delta_y \mathbf{C}_y) \quad (3.106)$$

where the correctional vectors in the x and y-directions are defined as

$$\begin{aligned} \mathbf{C}_x &= [0, 0, c_x]^T \\ \mathbf{C}_y &= [0, c_y, 0]^T \end{aligned} \quad (3.107)$$

To preserve vorticity, we alter the x-velocity by a small correction in the y-direction c_y and likewise the y-momentum by c_x in the x-direction. Taking the discrete curl of the full step, we get a relation between the corrected and uncorrected vorticities given by

$$\tilde{\omega}^{n+1} = \omega^{n+1} + \frac{\Delta t}{h^2} [\mu_y \delta_x^2 c_x - \mu_x \delta_y^2 c_y]^n \quad (3.108)$$

We insist that the corrected vorticity is identical to some independent estimate of vorticity

$$\tilde{\omega}^{n+1} = \omega_{IND}^{n+1} \quad (3.109)$$

and to achieve this we will use subiterations within the timestep. Although this independent vorticity estimate is zero for irrotational flow, it will generally be nontrivial and will serve as a numerical link to include physical vorticity information. Denote conditions after the k th subiteration by $(\cdot)^k$ and conditions after the subiterations

have converged by $(\cdot)^\infty$. The problem that we wish to solve is

$$\omega^\infty = \omega_{IND}^{n+1} = \omega^{n+1} + \frac{\Delta t}{h^2} [\mu_y \delta_x^2 c_x^\infty - \mu_x \delta_y^2 c_y^\infty] \quad (3.110)$$

where c_x^∞, c_y^∞ are the corrections that need to be determined. The sub-iterations that bring this about are

$$\omega^{k+1} = \omega^k + \frac{\Delta t}{h^2} [\mu_y \delta_x^2 (c_x^{k+1} - c_x^k) - \mu_x \delta_y^2 (c_y^{k+1} - c_y^k)] \quad (3.111)$$

where we assume ω^{n+1} as the initial values for the subiterations. The particular choices

$$\begin{aligned} c_x^{k+1} - c_x^k &= \zeta \mu_y (\omega^k - \omega_{IND}^{n+1}) \\ c_y^{k+1} - c_y^k &= -\zeta \mu_x (\omega^k - \omega_{IND}^{n+1}) \end{aligned} \quad (3.112)$$

with ζ as a parameter that restricts the relaxation factor will lead to the discrete Laplacian operator

$$\omega^{k+1} = \omega^k + \kappa [\mu_y^2 \delta_x^2 (\omega^k - \omega_{IND}^{n+1}) + \mu_x^2 \delta_y^2 (\omega^k - \omega_{IND}^{n+1})] \quad (3.113)$$

where $\kappa = \zeta \frac{\Delta t}{h^2}$ is the relaxation. Define vorticity discrepancy as

$$\Delta \omega^k = \omega^k - \omega_{IND}^{n+1} \quad (3.114)$$

so that

$$\Delta \omega^{k+1} = \Delta \omega^k + \kappa [\mu_y^2 \delta_x^2 + \mu_x^2 \delta_y^2] \Delta \omega^k \quad (3.115)$$

which is a relaxation for $\Delta \omega$. Clearly this problem has no intrinsic interest because its steady solution is identically zero. It is however, the mechanism by which c_x and c_y are generated in equation (3.110).

Note that this discrete Laplacian of the vorticity uses a bad stencil, the rotated $\mu_y^2 \delta_x^2 + \mu_x^2 \delta_y^2$ rather than the standard five point $\delta_x^2 + \delta_y^2$. This introduces odd-even

decoupling into the vorticity, but when this is averaged to give c_x and c_x the spurious mode disappears.

3.4 The Modified Rotated Richtmyer Scheme

Assume we perform the same method of limiting for the half-step described in section 3.2 and at the same time, we also include discrete advection. Let

$$T_{\delta}^{lim} = \begin{bmatrix} M_x \mu_y \delta_x^{lim} + M_y \mu_x \delta_y^{lim} & \mu_y \delta_x^{lim} & \mu_x \delta_y^{lim} \\ \mu_y \delta_x^{lim} & M_x \mu_y \delta_x^{lim} + M_y \mu_x \delta_y^{lim} & 0 \\ \mu_x \delta_y^{lim} & 0 & M_x \mu_y \delta_x^{lim} + M_y \mu_x \delta_y^{lim} \end{bmatrix} \quad (3.116)$$

be a limited discrete version of equation (3.26) where $\mu_y \delta_x^{lim}$ and $\mu_x \delta_y^{lim}$ are the limited compact differencing providing limited slopes of vertex variables. Then the limited half-step Rotated Richtmyer scheme will be

$$\mathbf{u}' = [\mu_x \mu_y I - \frac{\nu}{2} T_{\delta}^{lim}] \mathbf{u}^n \quad (3.117)$$

providing temporal solution at the vertices. The modified full step is then

$$\mathbf{u}^{n+1} = \mathbf{u}^n - \nu T_{\delta} \mathbf{u}' + \frac{\Delta t}{h} (\delta_x \mathbf{C}_x + \delta_y \mathbf{C}_y) \quad (3.118)$$

where the correctional vectors are defined in the previous section. The overall algorithm is independent of the scheme employed and can be summed as below.

- Compute the wave equations using the limited Rotated Richtmyer scheme or any other 'good'¹¹ scheme. Solve for the provisional vorticity ω^{n+1} and
 1. Compute initial vorticity discrepancy, $\Delta\omega^0 = \omega^{n+1} - \omega_{IND}^{n+1}$ at each vertex with initial $c_x = c_y = 0$ and $\omega^0 = \omega^{n+1}$.

¹¹We certainly do not want the pure central scheme because it is an unstable scheme.

2. Solve the Poisson equation for $\Delta\omega^{k+1}$ using a relaxation scheme with $\Delta\Omega = 0$ at the boundaries for one sub-iteration step.
 3. Perform correction on c_x and c_y at each cell-interface based on the updated values $\Delta\omega^{k+1}$ using equation (3.110).
 4. Compute the updated vorticity discrepancy, if $\Delta\omega^{k+1} <$ error tolerance, stop the iteration and compute the overall fluxes at each interface and update the full step. Else go back to step 2.
- Compute compact vorticity at time $n+1$. To compute the next time-level, start again with the new solution as data.

Since we only deal with irrotational flow in this chapter, we set $\omega_{IND}^{n+1} = 0$.

3.5 Numerical Results

Define a two dimensional computational domain as $D \in [-2.0, 2.0] \times [-2.0, 2.0]$ with the following initial value problem.

$$p = -\sqrt{2}\sin\left(\frac{\pi}{2}x\right)\sin\left(\frac{\pi}{2}y\right) \quad (3.119)$$

$$u = 0.0 \quad (3.120)$$

$$v = 0.0 \quad (3.121)$$

We will include a uniform constant advection with $|M| = \sqrt{2}$ at an angle of 45 degrees (counter-clockwise) relative to the x-axis. We have chosen a Courant number $\nu = 0.5$ and imposed a periodic boundary conditions. Our objective is to predict time-accurate solutions of the linear wave equations with constant advection. This is a problem where there will be linear interactions between the pressure and velocity but nevertheless, the solution should remain irrotational for all times.

We have included results for three schemes: the pure Rotated-Richtmyer scheme (RR), the Rotated-Richtmyer scheme with Superbee limiter (RR-S) and the Modified Rotated-Richtmyer scheme with Superbee limiter (RR-S-VP). The results are shown in Fig. 3.8-3.43. In short, all the three schemes produce almost identical pressure and velocity results¹². However, only the RR and RR-S-VP schemes preserve irrotationality. When applying the Superbee limiter¹³, the Rotated-Richtmyer scheme no longer preserves vorticity (Figs. 3.18, 3.36). This is consistent with our theoretical results in section 3.2.2. By including the vorticity correctional algorithm, we are able to remove the spurious vorticity (Figs. 3.24, 3.42) and preserve irrotationality to $O(10^{-8})$ ¹⁴.

Moreover, the vorticity correctional algorithm does not alter the velocity divergence¹⁵ (Table 3.1-3.4). This is also consistent with our condition that when the velocity curl is modified, the velocity divergence should remain unchanged. Also, note that for the RR-S scheme, the production of spurious vorticity grows with time, which makes its time-accurate vorticity solution to be unreliable.

Scheme	RR	RR-S	RR-S-VP
curl-u	1.5359e-16	4.6871e-5	9.3451e-9
div-u	-2.7912e-19	8.8878e-18	4.3214e-18

Table 3.1: L2-Norms of the three schemes at T=1.

As mentioned before, for this chapter it was sufficient to set $\omega_{IND}^{n+1} = 0$. However,

¹²Our objective is not to show accurate predictions of pressure and velocity but to provide a numerical example to demonstrate that the RR-S scheme is not vorticity preserving unless a vorticity correctional algorithm is included.

¹³Or any limiter when solving the linear wave equations with constant advection.

¹⁴This is the prescribed vorticity error tolerance. We can prescribe a smaller error tolerance but this comes with the price of more sub-iterations required per time step.

¹⁵We have also defined a compact velocity divergence, located at the vertices.

Scheme	RR	RR-S	RR-S-VP
curl-u	2.3842e-16	2.1071e-4	8.7254e-9
div-u	-9.2378e-18	6.9085e-18	5.2131e-18

Table 3.2: L2-Norms of the three schemes at T=5.

Scheme	RR	RR-S	RR-S-VP
curl-u	2.3842e-16	5.0231e-4	8.2734e-9
div-u	-9.2378e-18	6.9085e-18	5.2131e-18

Table 3.3: L2-Norms of the three schemes at T=10.

Scheme	RR	RR-S	RR-S-VP
curl-u	2.3423e-16	9.0234e-2	8.8231e-9
div-u	-7.8654e-18	-5.5512e-18	5.6678e-18

Table 3.4: L2-Norms of the three schemes at T=100.

we can extend the idea to a general vortical flow by incorporating the discretized vorticity transport equations which is necessary for computing general vortical flows. In addition, although the modified Rotated Richtmyer scheme is monotonicity and vorticity preserving, it does not have upwinding which is vital in computing supersonic flows. The idea of including information from the discrete vorticity transport equation and upwinding will be presented and discussed in the next chapter.

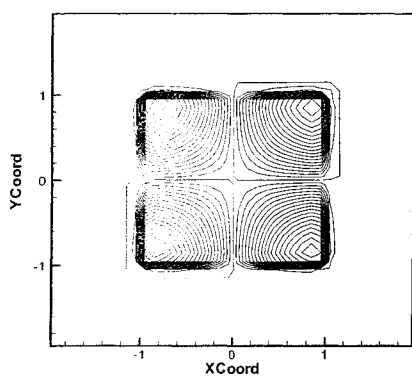


Figure 3.8: Pressure contours (RR scheme) at $T=1$.

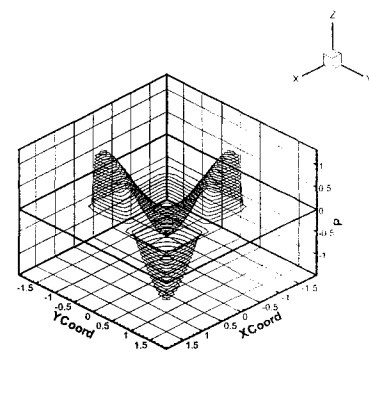


Figure 3.9: 3D View.

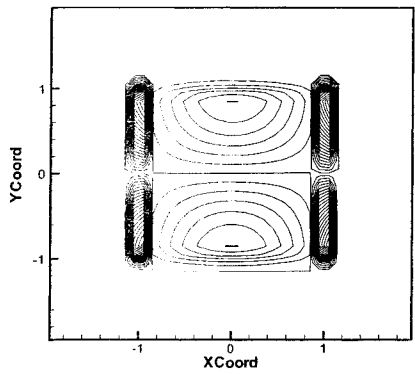


Figure 3.10: U-velocity contours (RR scheme) at $T=1$.

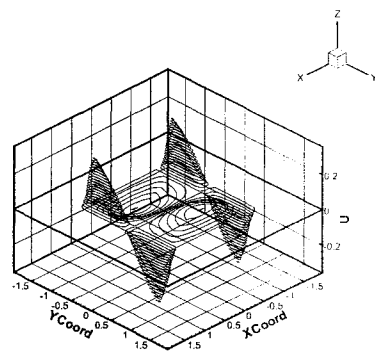


Figure 3.11: 3D View.

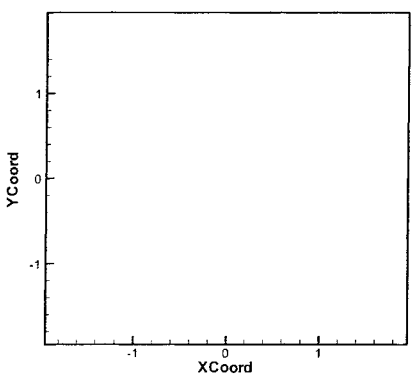


Figure 3.12: Vorticity contours (RR scheme) at $T=1$.

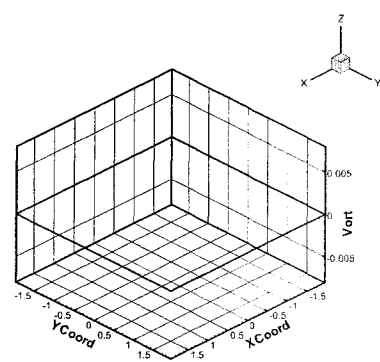


Figure 3.13: 3D View. Note irrotationality.

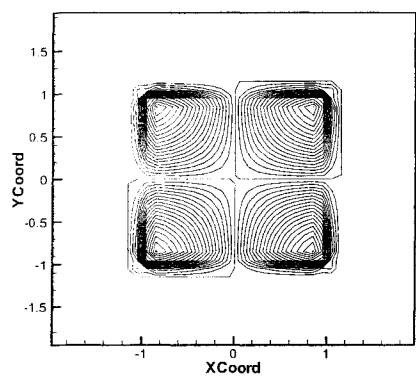


Figure 3.14: Pressure contours (RR-S scheme) at $T=1$.

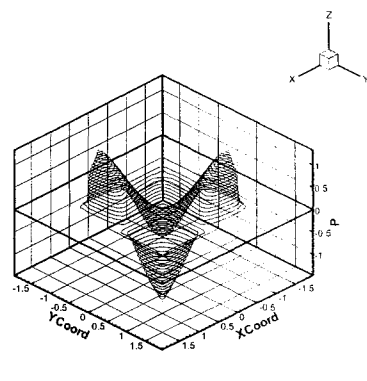


Figure 3.15: 3D View.

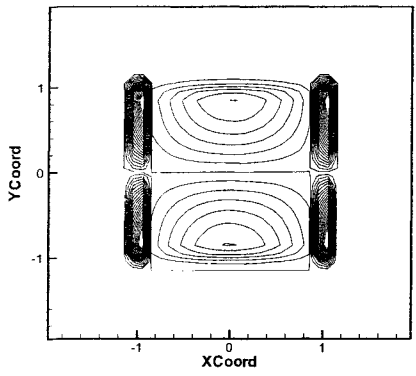


Figure 3.16: U-velocity contours (RR-S scheme) at $T=1$.

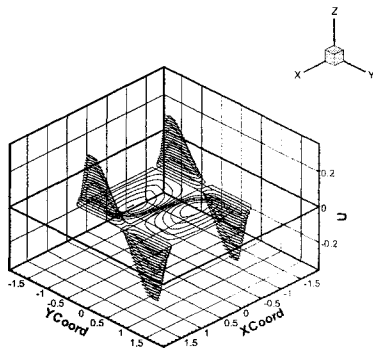


Figure 3.17: 3D View.

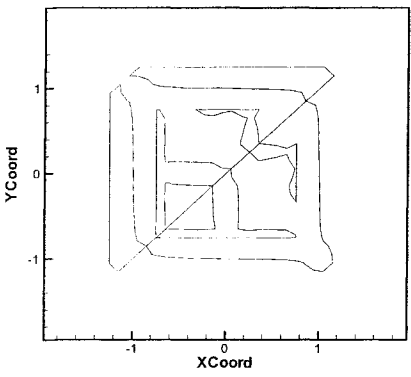


Figure 3.18: Vorticity contours (RR-S scheme) at $T=1$.

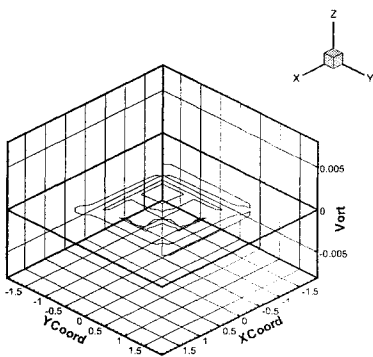


Figure 3.19: 3D View. Note generation of spurious vorticity when a limiter is applied.

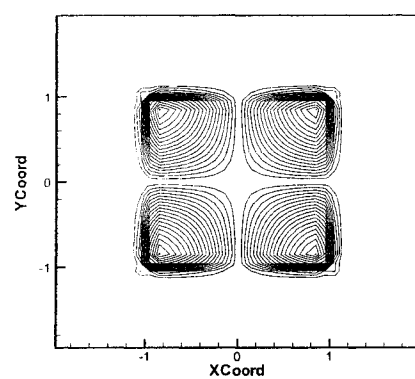


Figure 3.20: Pressure contours (RR-S-VP scheme) at $T=1$.

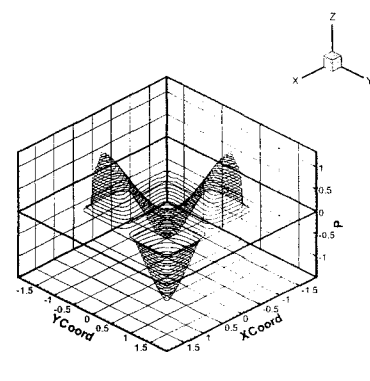


Figure 3.21: 3D View.

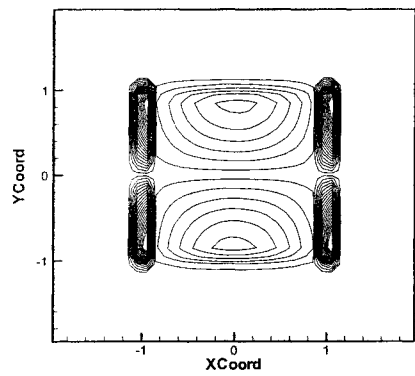


Figure 3.22: U-velocity contours (RR-S-VP scheme) at $T=1$.

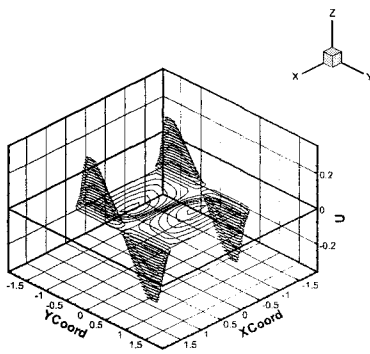


Figure 3.23: 3D View.

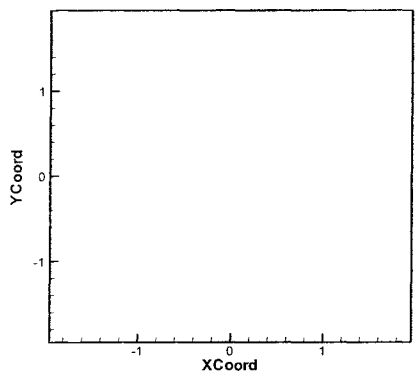


Figure 3.24: Vorticity contours (RR-S-VP scheme) at $T=1$.

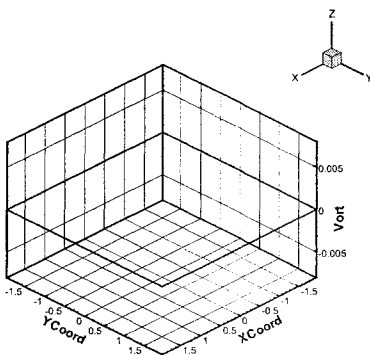


Figure 3.25: 3D View. Note with the flux-correction, irrotationality is preserved.

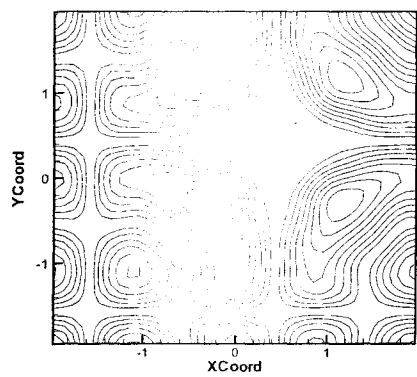


Figure 3.26: Pressure contours (RR scheme) at $T=100$.

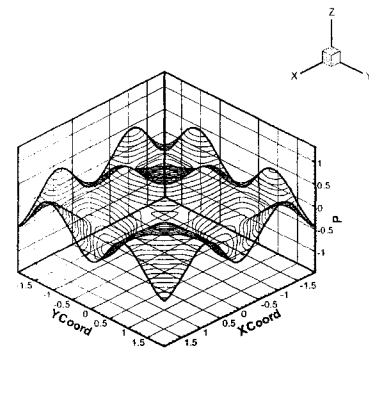


Figure 3.27: 3D View.

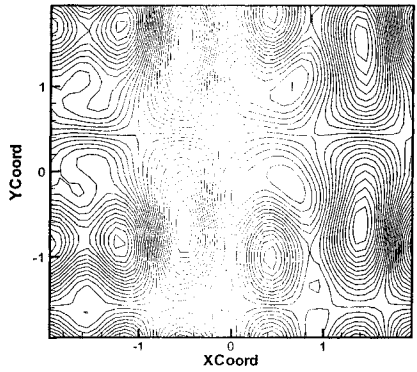


Figure 3.28: U-velocity contours (RR scheme) at $T=100$.

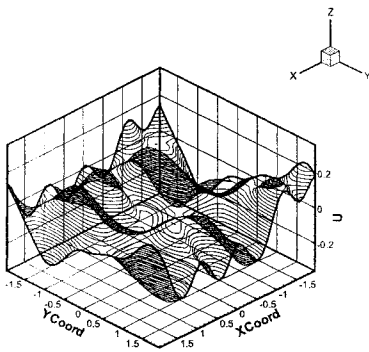


Figure 3.29: 3D View.

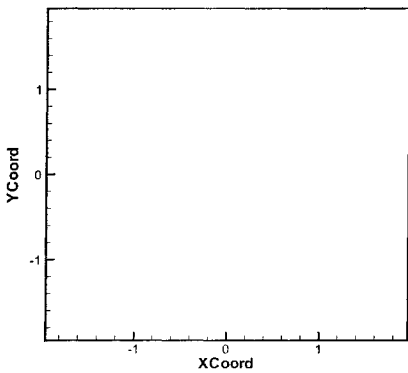


Figure 3.30: Vorticity contours (RR scheme) at $T=1$.

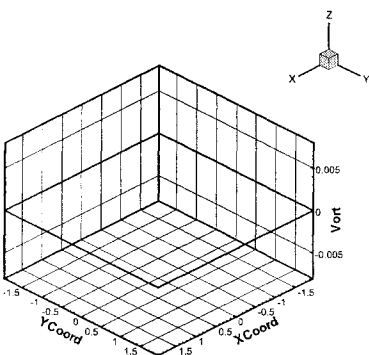


Figure 3.31: 3D View. Irrotationality is maintained.

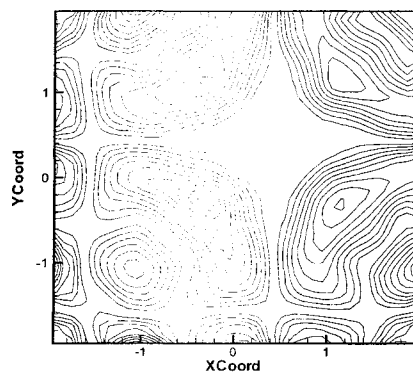


Figure 3.32: Pressure contours (RR-S scheme) at $T=100$.

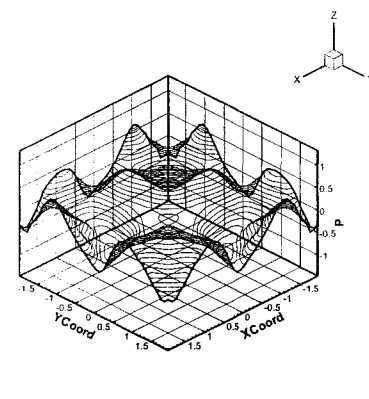


Figure 3.33: 3D View.

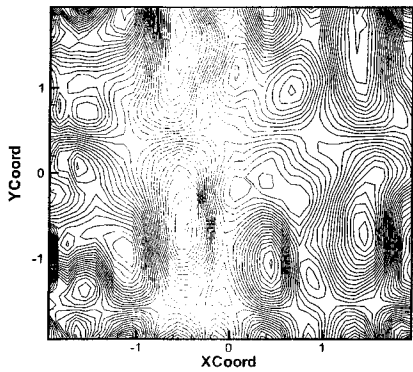


Figure 3.34: U-velocity contours (RR-S scheme) at $T=100$.

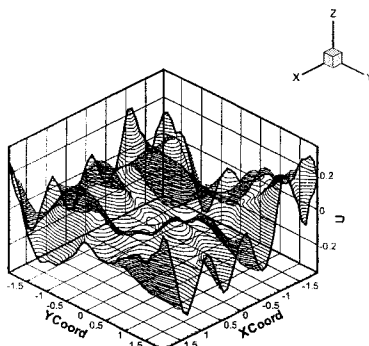


Figure 3.35: 3D View.

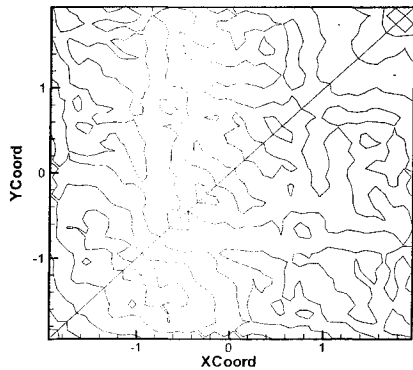


Figure 3.36: Spurious Vorticity contours (RR-S scheme) at $T=100$.

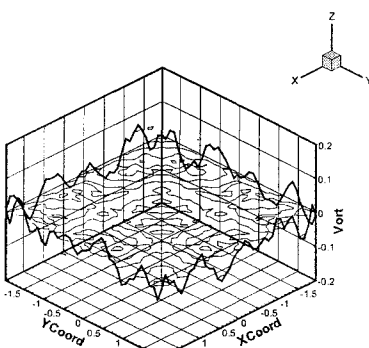


Figure 3.37: 3D View. We have spurious vorticity of $O(0.01)$.

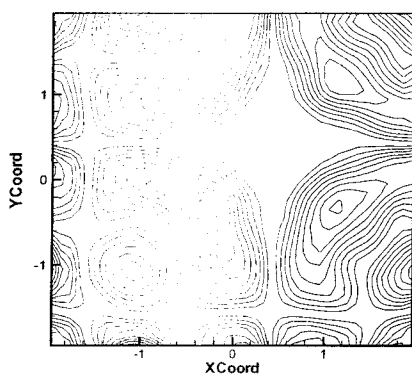


Figure 3.38: Pressure contours (RR-S-VP scheme) at $T=100$.

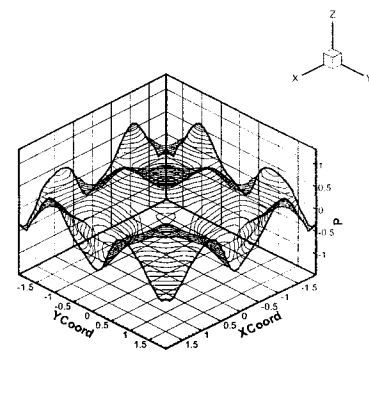


Figure 3.39: 3D View.

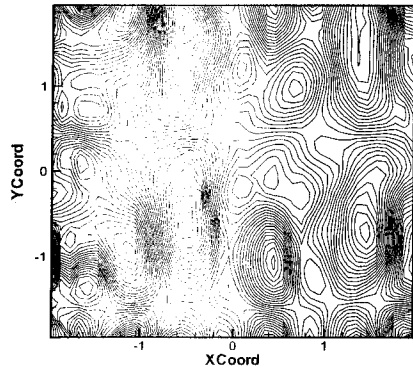


Figure 3.40: U-velocity contours (RR-S-VP scheme) at $T=100$.

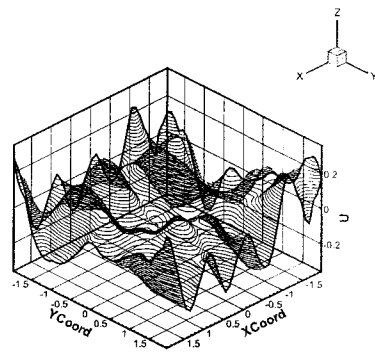


Figure 3.41: 3D View.

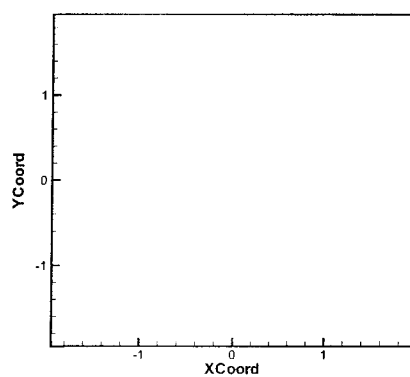


Figure 3.42: Vorticity contours (RR-S-VP scheme) at $T=100$.

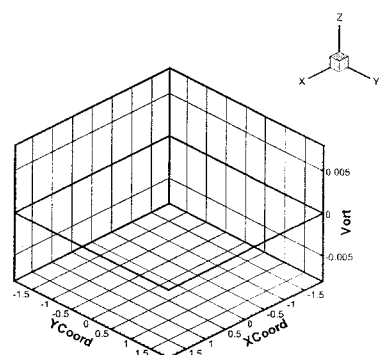


Figure 3.43: Note with flux-corrections, we have preserved vorticity even after $T=100$.

CHAPTER IV

VORTICITY CONTROL IN EULER EQUATIONS

Finite volume schemes based on Riemann solvers are the most popular and practical methods in solving compressible fluid dynamic problems. These schemes are conservative and upwinded based on wave characteristics hence have the strongest physical basis for modelling the fluid¹. They are also relatively cheap, robust and easily extended to multi dimensions. However, finite volume schemes based on one-dimensional Riemann solvers cannot be vorticity preserving² [73].

Based on what we have learnt from the previous chapter, we will introduce a method that modifies the numerical fluxes of the momentum equations to capture vorticity to within an error tolerance. Strictly, it is the curl of the momentum that is captured, because that objective makes it easier to retain conservation in the conventional sense and since we merely want to control some aspect of rotational flow. Because there seems to be no generally-accepted term for this quantity, we frequently refer to it loosely as ‘vorticity’; when we need to stress the distinction we

¹However, this does not mean that the Roe-flux is perfect. We have witnessed in chapter 2 how the flux suffers from instabilities in a perturbed stationary shock problem.

²Refer to footnote in page 67.

call it ‘pseudo-vorticity’. The method can be used with any good flux function but we want to use a flux function which has the least numerical dissipation hence Roe’s flux solver [86] fits well. In short, the algorithm utilizes a conventional Roe solver with extra terms to remove spurious vorticity. It is assumed that an independent, and more accurate prediction of vorticity is available, that is obtained from a solution of the vorticity transport equation. Because the underlying scheme is consistent with the Euler equations, the vorticity that it predicts must be, at each time step, close to the true vorticity, and so the corrections that are made must be small. They preserve the formal accuracy of the basic scheme, but prevent the small errors from accumulating into major discrepancies.

The numerical fluxes for the momentum equations are conservatively augmented by small artificial terms before each full step. These terms are obtained by solving a Poisson problem, driven by the discrepancy between the vorticity that would be predicted without any correction, and the vorticity obtained independently from the (pseudo) vorticity transport equation. The Hancock scheme³ [110], [97] is chosen for time-integration although the algorithm could be utilized with any other time integration method⁴.

To demonstrate the concept we will utilize a finite volume scheme with Roe-flux differencing[85] on a uniform two-dimensional Cartesian grid. All the conservative and primitive variables are stored in the cell center except for pseudo-vorticity which is defined from the cell quantities as

$$\Omega = L_\omega \mathbf{u} = \frac{1}{h} [\mu_y \delta_x(\rho v) - \mu_x \delta_y(\rho u)] \quad (4.1)$$

³This scheme is included in appendix B

⁴An example would be a Runge-Kutta method.

and therefore located at the cell vertex (Fig 4.1). Before we begin with the vorticity control analysis, recall that the two-dimensional Euler equations can be written as

$$\partial_t \mathbf{u} + \partial_x \mathbf{f}(\mathbf{u}) + \partial_y \mathbf{g}(\mathbf{u}) = 0 \quad (4.2)$$

where $\mathbf{u} = \mathbf{u}(x, y, t), \mathbf{f}(\mathbf{u}), \mathbf{g}(\mathbf{u})$ are the conservative variables and the corresponding fluxes defined as

$$\mathbf{u} = [\rho, \rho u, \rho v, \rho E]^T \quad (4.3)$$

$$\mathbf{f}(\mathbf{u}) = [\rho u, \rho u^2 + p, \rho uv, \rho uH]^T \quad (4.4)$$

$$\mathbf{g}(\mathbf{u}) = [\rho v, \rho uv, \rho v^2 + p, \rho vH]^T \quad (4.5)$$

from the fluid density ρ , velocity in x and y-direction u and v , the total energy $E = e + \frac{u^2+v^2}{2}$ and the total enthalpy $H = E + \frac{p}{\rho}$. The pressure is determined from the equation of state, $e = \frac{p(\gamma-1)}{\rho}$ which is assumed to be with an ideal gas constant γ . We also define the non-conservative (or primitive) variables as $\mathbf{w} = [\rho, u, v, p]^T$.

Our analysis is presented in two dimensions as a foundation to extend to three dimensions. We will start with controlling vorticity in the numerical flux, introducing correctional vectors. Then, we will derive the general vorticity transport equations for inviscid compressible flow. This is followed by discretizing the vorticity transport equations and the overall vorticity capturing algorithm. We will simulate a travelling vortex as a numerical example to illustrate the superiority of the vorticity capturing schemes as compared to conventional finite volume schemes. Finally, we will attempt to cure the 1 1/2 dimensional carbuncle problem.

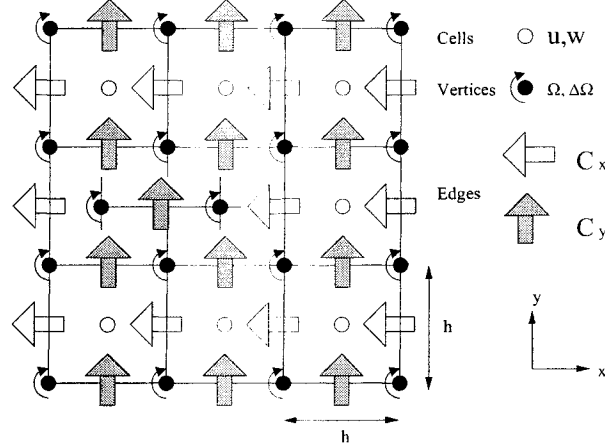


Figure 4.1: Grid Representation

4.1 A New Flux Function That Controls Curl of Momentum in Two Dimensions

We intend to alter only the momentum equations since vorticity is hidden in them and leave the mass and energy equations untouched. This is done by adding variable coefficients (or flux corrections) \mathbf{C}_x and \mathbf{C}_y to the numerical fluxes of the momentum equations. Since the order of magnitude of spurious vorticity is smaller than the scheme's order of accuracy, we will introduce small corrections to the momentum equations.

To preserve vorticity, we proceed by analogy with section 3.3, by altering the x-momentum by a small correction in the y-direction c_x and likewise the y-momentum by c_y in the x-direction. Our modified flux functions at the interface will have the following form.

$$\tilde{\mathbf{f}}_I = \mathbf{f}(\mathbf{u}_L, \mathbf{u}_R) - \mathbf{C}_x \quad (4.6)$$

$$\tilde{\mathbf{g}}_I = \mathbf{g}(\mathbf{u}_B, \mathbf{u}_T) - \mathbf{C}_y \quad (4.7)$$

and we will choose $(\mathbf{f}, \mathbf{g}) = (\mathbf{f}_{Roe}, \mathbf{g}_{Roe})$ as the numerical flux function⁵ in which the original Roe flux in the x and y directions [85] which can be obtained in appendix D. Note that we have introduced the interface flux corrections \mathbf{C}_x and \mathbf{C}_y only to the momentum equations given by

$$\begin{aligned}\mathbf{C}_x &= [0, 0, c_x, 0]^T \\ \mathbf{C}_y &= [0, c_y, 0, 0]^T\end{aligned}\quad (4.8)$$

Hence we shall discretize the two-dimensional Euler equations using the standard and modified fluxes i.e.

$$\mathbf{u}_{i,j}^{n+1} = \mathbf{u}_{i,j}^n - \frac{\Delta t}{h} [\mathbf{f}_{i+\frac{1}{2},j}^n - \mathbf{f}_{i-\frac{1}{2},j}^n + \mathbf{g}_{i,j+\frac{1}{2}}^n - \mathbf{g}_{i,j-\frac{1}{2}}^n] \quad (4.9)$$

$$\tilde{\mathbf{u}}_{i,j}^{n+1} = \tilde{\mathbf{u}}_{i,j}^n - \frac{\Delta t}{h} [\tilde{\mathbf{f}}_{i+\frac{1}{2},j}^n - \tilde{\mathbf{f}}_{i-\frac{1}{2},j}^n + \tilde{\mathbf{g}}_{i,j+\frac{1}{2}}^n - \tilde{\mathbf{g}}_{i,j-\frac{1}{2}}^n] \quad (4.10)$$

where $\mathbf{u}_{i,j}^n$ and $\tilde{\mathbf{u}}_{i,j}^n$ are the standard and modified cell averages of the conservative variables at coordinate (i,j) and time level n. We define pseudo-vorticity Ω at a vertex through the compact difference of four neighboring cell-center momenta ($\rho\vec{u}$) that surround the vertex, as in (4.1).

Controlling this particular discretization of the vorticity allows the checkerboard mode of the momenta in the cells, although not in the fluxes. There are other ways to define discrete vorticity using larger stencils but these come with even more spurious modes [73]. We will follow the same analysis in previous chapter except that now we want to control vorticity based on curl of momentum Ω instead of curl of velocity ω . We begin by defining the relations of corrected and uncorrected vorticities

$$\tilde{\Omega}^{n+1} = \Omega^{n+1} + \frac{\Delta t}{h^2} [\mu_y \delta_x^2 c_x - \mu_x \delta_y^2 c_y]^n \quad (4.11)$$

⁵Any other ‘good’ flux function can also be used.

We will insist that the corrected vorticity is identical to some independent estimate that will be discussed in the following section,

$$\tilde{\Omega}^{n+1} = \Omega_{IND}^{n+1} \quad (4.12)$$

and to achieve this we will use subiterations within the timestep. Denote conditions after the k th subiteration by $(\cdot)^k$ and conditions after the subiterations have converged by $(\cdot)^\infty$. The problem that we wish to solve is

$$\Omega^\infty = \Omega_{IND}^{n+1} = \Omega^{n+1} + \frac{\Delta t}{h^2} [\mu_y \delta_x^2 c_x^\infty - \mu_x \delta_y^2 c_y^\infty] \quad (4.13)$$

where c_x^∞, c_y^∞ are the corrections that need to be determined. The sub-iterations that bring this about are

$$\Omega^{k+1} = \Omega^k + \frac{\Delta t}{h^2} [\mu_y \delta_x^2 (c_x^{k+1} - c_x^k) - \mu_x \delta_y^2 (c_y^{k+1} - c_y^k)] \quad (4.14)$$

where we assume Ω^{n+1} as the initial values for the subiterations. The particular choices

$$\begin{aligned} c_x^{k+1} - c_x^k &= \zeta \mu_y (\Omega^k - \Omega_{IND}^{n+1}) \\ c_y^{k+1} - c_y^k &= -\zeta \mu_x (\Omega^k - \Omega_{IND}^{n+1}) \end{aligned} \quad (4.15)$$

with ζ as a parameter that restricts the relaxation factor will lead to the discrete Laplacian operator

$$\Omega^{k+1} = \Omega^k + \kappa [\mu_y^2 \delta_x^2 (\Omega^k - \Omega_{IND}^{n+1}) + \mu_x^2 \delta_y^2 (\Omega^k - \Omega_{IND}^{n+1})] \quad (4.16)$$

where $\kappa = \zeta \frac{\Delta t}{h^2}$ is the relaxation. Define vorticity discrepancy as

$$\Delta \Omega^k = \Omega^k - \Omega_{IND}^{n+1} \quad (4.17)$$

so that

$$\Delta \Omega^{k+1} = \Delta \Omega^k + \kappa [\mu_y^2 \delta_x^2 + \mu_x^2 \delta_y^2] \Delta \Omega^k \quad (4.18)$$

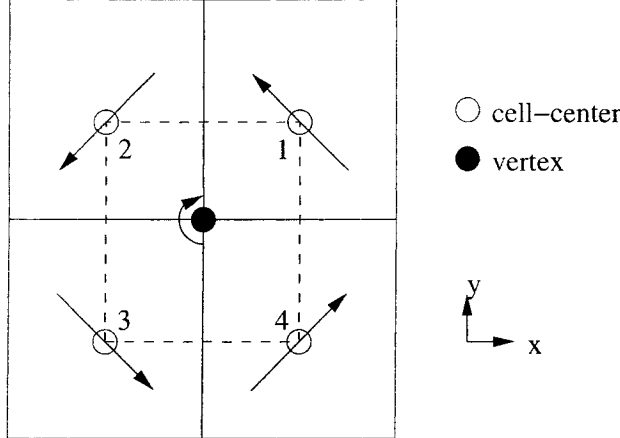


Figure 4.2: Removing spurious vorticity with flux-correction. Assume we have a clockwise spurious vorticity $\Delta\Omega^{n+1}$ at a vertex, we introduce a counter-clockwise correction altering the momenta. Note that this correction does not change the discrete divergence of momentum within the vertex control volume.

which is a relaxation for $\Delta\Omega$. This problem will be the mechanism by which c_x and c_x are generated in equation (4.15). Note that incorporating these flux corrections maintains conservation of momentum, but redistributes it so as to be compatible with the independent vorticity calculation.

4.2 Independent Estimate of Inviscid Vorticity

We shall derive an integral form of the inviscid vorticity transport equations by taking the curl of the momentum equations. For an arbitrary control volume dV with surface S , the inviscid momentum equations can be written in the following form

$$\frac{\partial}{\partial t} \iiint_V \rho \vec{U} dV + \oint_S (\rho \vec{U} \cdot d\vec{S}) \vec{U} + \oint_S P d\vec{S} = 0 \quad (4.19)$$

Appealing to the Divergence Theorem, we can rewrite the last two terms as

$$\oint_S (\rho \vec{U} \cdot d\vec{S}) \vec{U} = \iiint_V \nabla \cdot (\rho \vec{U} \vec{U}) dV \quad (4.20)$$

$$\oint_S P d\vec{S} = \iiint_V \nabla P dV \quad (4.21)$$

We define vorticity as $\vec{\Omega} = \nabla \times \rho \vec{U}$, and applying the curl operator on the momentum equations we get

$$\frac{\partial}{\partial t} \iiint_V \vec{\Omega} dV + \iiint_V \nabla \times [\nabla \cdot (\rho \vec{U} \vec{U})] dV = 0 \quad (4.22)$$

since the $\nabla \times \nabla$ operator is zero. Recall that the dyadic tensor is defined as

$$\vec{U} \vec{U} = \vec{U} \circ \vec{U} = \begin{bmatrix} u^2 & uv & uw \\ vu & v^2 & vw \\ wu & wv & w^2 \end{bmatrix}$$

Note that $\rho \vec{U} \circ \vec{U} = \vec{U} \circ \rho \vec{U}$. Also, recall the following vector identities.

$$\nabla \cdot (\vec{A} \circ \vec{B}) = \vec{B} \circ \nabla \vec{A} + \vec{A} (\nabla \cdot \vec{B}) \quad (4.23)$$

$$\vec{A} \times \nabla \times \vec{B} = \frac{1}{2} \nabla (\vec{A} \cdot \vec{B}) - \vec{B} \circ \nabla \vec{A} \quad (4.24)$$

$$\nabla \times \vec{A} \times \vec{B} = \vec{A} \nabla \cdot \vec{B} - \vec{B} \nabla \cdot \vec{A} + (\vec{B} \cdot \nabla) \vec{A} - (\vec{A} \cdot \nabla) \vec{B} \quad (4.25)$$

Using the first identity we expand the divergence term as

$$\nabla \cdot (\vec{U} \circ \rho \vec{U}) = \rho \vec{U} \circ \nabla \vec{U} + \vec{U} (\nabla \cdot \rho \vec{U}) \quad (4.26)$$

Using the second vector identity we write the first term of the previous equation as

$$\rho \vec{U} \circ \nabla \vec{U} = \frac{1}{2} \nabla (\vec{U} \cdot \rho \vec{U}) - \vec{U} \times \nabla \times \rho \vec{U} \quad (4.27)$$

The curl of this equation is

$$\begin{aligned}
\nabla \times [\vec{U} \circ \nabla \rho \vec{U}] &= \nabla \times [\frac{1}{2} \nabla (\rho \vec{U} \cdot \vec{U})] - \nabla \times [\vec{U} \times \nabla \times \rho \vec{U}] \\
&= -\nabla \times [\vec{U} \times \vec{\Omega}] \\
&= (\vec{U} \cdot \nabla) \vec{\Omega} + \vec{\Omega} \nabla \cdot \vec{U} - (\vec{\Omega} \cdot \nabla) \vec{U} \\
&= \nabla \cdot (\vec{\Omega} \circ \vec{U}) - (\vec{\Omega} \cdot \nabla) \vec{U}
\end{aligned} \tag{4.28}$$

after using the third vector identity and that $\nabla \cdot \nabla \times$ is trivial. All together, the curl of momentum for an arbitrary control volume V can be written as

$$\iiint_V [\frac{\partial \vec{\Omega}}{\partial t} + \nabla \cdot (\vec{\Omega} \circ \vec{U}) - (\vec{\Omega} \cdot \nabla) \vec{U} + \nabla \times [\vec{U}(\Phi)]] dV = 0 \tag{4.29}$$

The first three terms correspond to unsteady vorticity, vorticity advection and vortex stretching. The last term represents compressibility effects. Note for incompressible flow, we can rewrite the equation as

$$\iiint_V [\frac{\partial \vec{\omega}}{\partial t} + \nabla \cdot (\vec{\omega} \circ \vec{U}) - (\vec{\omega} \cdot \nabla) \vec{U}] dV = 0 \tag{4.30}$$

recovering the conventional inviscid vorticity transport equations given in [8].

4.2.1 Two-Dimensional Case

In two-dimensions, $\vec{\Omega} = [0, 0, \Omega_z]^T$ hence the vortex stretching term drops out and

$$\nabla \cdot (\vec{\Omega} \circ \vec{U}) = \frac{\partial(u\Omega_z)}{\partial x} + \frac{\partial(v\Omega_z)}{\partial y} \tag{4.31}$$

$$\nabla \times [\vec{U}(\Phi)] = \frac{\partial(v\Phi)}{\partial x} - \frac{\partial(u\Phi)}{\partial y} \tag{4.32}$$

Define normal velocity vectors $\vec{U}_n = [v, -u]^T$ thus vorticity transport equation becomes

$$\iint_S [\frac{\partial \Omega_z}{\partial t} + \nabla \cdot (\vec{U}\Omega_z + \vec{U}_n\Phi)] dS = 0 \tag{4.33}$$

This equation is in conservation form⁶. Applying the Divergence Theorem we get

$$\iint_S \frac{\partial \Omega_z}{\partial t} dS + \oint_l (\vec{U} \Omega_z + \vec{U}_n \Phi) \cdot d\vec{l} = 0 \quad (4.34)$$

where S is an arbitrary area closed by a line l . For brevity, we will assume from now on that $\Omega_z = \Omega$. In three dimensions, conservation form is lost due to the stretching term.

4.3 An Independent Discrete Vorticity Estimate in Two Dimensions

4.3.1 First Order Method

Discrete conservation is ensured by drawing a control volume around the point of interest (in this case it is the vertex) and perform the update as an integral around the control volume. Appealing to a uniform Cartesian grid, with fluxes F, G in the (x,y) -directions, respectively, the vorticity at the vertices are discretized as

$$h^2[\Omega^{n+1} - \Omega^n] + h\Delta t[\delta_x f_* + \delta_y g_*] = 0 \quad (4.35)$$

where f_*, g_* are numerical fluxes evaluated from some formula to be determined. We shall employ the staggered grid formulation defined in Fig. 4.3. The primitive variables are located in the cell-center but vorticity is located at the vertices. We need the velocities (both normal and tangential velocities) at the interface of the control volume that defines vorticity. We have the primitive values at the cell-centers which encloses the control volume of vorticity. At any interface, the primitive values are the average of two primitive cell-centered values. In two dimensions there are two terms in the equation for vorticity evolution: the gradients of pseudo-vorticity and

⁶This does not mean that pseudo-vorticity is a conserved quantity, unless it also obeys suitable jump conditions

momentum divergence. We chose to treat the former as an advection term to be upwinded. The latter is discretized using a central scheme since it is a divergence of a gradient quantity and is diffusion-like. We will evaluate the interface fluxes as the following.

$$f_* = [uf_{up}(\Omega_L, \Omega_R) + v\frac{1}{2}((\Phi)_L + (\Phi)_R)] \quad (4.36)$$

$$g_* = [vf_{up}(\Omega_B, \Omega_T) - u\frac{1}{2}((\Phi)_B + (\Phi)_T)] \quad (4.37)$$

where u, v indicate interface velocities and Φ is the momentum divergence located at the vertices evaluated via compact divergence utilizing cell-centered velocities.

$$\Phi = \frac{1}{h}[\mu_y \delta_x(\rho u) + \mu_x \delta_y(\rho v)] \quad (4.38)$$

The one-dimensional upwinded horizontal flux function is evaluated as

$$f_{up}(\Omega_L, \Omega_R) = \Omega_L(u > 0) \quad (4.39)$$

$$f_{up}(\Omega_L, \Omega_R) = \Omega_R(u < 0) \quad (4.40)$$

Note if the interface velocity is zero, the flux will be an average of the two states. The vertical fluxes are evaluated by a similar process. With first order forward Euler time integration method, the independent estimate for vorticity is updated as

$$\Omega_{IND}^{n+1} = \Omega_{IND}^n - \frac{\Delta t}{h}[\delta_x f_* + \delta_y g_*] \quad (4.41)$$

We combine this with the Hancock scheme and get the first order vorticity capturing scheme (VC1).

4.3.2 Second Order Method

We will now construct a second order scheme for the vorticity transport equation. The time-integration will be second order Runge-Kutta with advection components

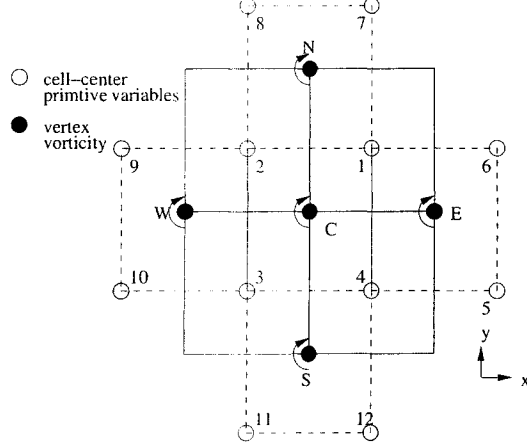


Figure 4.3: Control volume for vorticity is marked by dashed-lines. For a particular CV with centroid C, the momentum divergence at the vorticity interface is an averaged-differencing utilizing vertices [C,E] for interface (1,4); [C,N] for for interface (1,2); [C,W] for interface (2,3); [C,S] for for interface (3,4). For vorticity advection, each interface is governed by pairs for upwinding, also denoted as [C,E], [C,N], [C,W] and [C,S]. The interface velocities are just the averaged of velocities at (1,4), (1,2), (2,3) and (3,4).

of the numerical fluxes being linearly reconstructed. To avoid spurious overshoots, we will limit these fluxes. The divergence of momentum will still be discretized as a central scheme. This will be a two-step scheme in which we have two options. One option is to limit only the half-step and the other is where limiter is applied to both half and full-steps (VC2). The slope limiting is based on one-dimensional considerations hence any conventional one-dimensional limiter can be used, and we have chosen the Superbee limiter. Since our grids are uniform, we can define the limited slopes of vorticity in x and y-directions centered at the vertices as

$$\delta\Omega_{i,j}^x = \text{lim}(\Omega_{i,j} - \Omega_{i-1,j}, \Omega_{i+1,j} - \Omega_{i,j}) \quad (4.42)$$

$$\delta\Omega_{i,j}^y = \text{lim}(\Omega_{i,j} - \Omega_{i,j-1}, \Omega_{i,j+1} - \Omega_{i,j}) \quad (4.43)$$

To obtain second order spatial accuracy, we shall use these limited slopes to reconstruct the left and right states of the cell-vertex scheme.

$$\tilde{\Omega}_L = \Omega_L + \frac{1}{2}\delta\Omega_L^x \quad (4.44)$$

$$\tilde{\Omega}_R = \Omega_R - \frac{1}{2}\delta\Omega_R^x \quad (4.45)$$

In the vertical direction, a similar method is used. These values will be used in the upwinded function defined on the previous section thus the limited fluxes are evaluated as

$$\tilde{f}_* = [uf_{up}(\tilde{\Omega}_L, \tilde{\Omega}_R) + v\frac{1}{2}((\Phi)_L + (\Phi)_R)] \quad (4.46)$$

$$\tilde{g}_* = [vf_{up}(\tilde{\Omega}_B, \tilde{\Omega}_T) - u\frac{1}{2}((\Phi)_B + (\Phi)_T)] \quad (4.47)$$

The half and full-steps of the vorticity capturing scheme are written as

$$\begin{aligned} \Omega_{IND}^{n+\frac{1}{2}} &= \Omega_{IND}^n - \frac{\Delta t}{2h}[\delta_x \tilde{f}_*^n + \delta_y \tilde{g}_*^n] \\ \Omega_{IND}^{n+1} &= \Omega_{IND}^n - \frac{\Delta t}{h}[\delta_x f_*^{n+\frac{1}{2}} + \delta_y g_*^{n+\frac{1}{2}}] \end{aligned} \quad (4.48)$$

where the full-step fluxes are identical to fluxes derived in the previous section.

For VC2 scheme, we also update the full-step with limited and linearly reconstructed fluxes. This will be our second order vorticity capturing scheme.

4.4 Algorithm

There will be two distinct numerical processes, one solving the Euler equations while the other solves the vorticity transport equation. The former is computed via Hancock scheme with Superbee limiter while the latter will be evaluated using the discretized scheme discussed in the previous section. Both will be coupled and run concurrently with each other. The algorithm below describes the steps involved.

- Compute vorticity estimate at time level $n+1$ (Ω_{IND}^{n+1}) using equation (4.48) with variables at time n .
- Compute the Euler equations using Hancock scheme. Solve the conventional one dimensional Riemann problem using a Roe-solver providing a provisional solution, with provisional vorticity Ω^{n+1} and
 1. Compute initial vorticity discrepancy, $\Delta\Omega^0 = \Omega^{n+1} - \Omega_{IND}^{n+1}$ at each vertex with initial $c_x = c_y = 0$ and $\Omega^0 = \Omega^{n+1}$.
 2. Solve the Poisson equation for $\Delta\Omega^{k+1}$ using a relaxation scheme with $\Delta\Omega = 0$ at the boundaries for one sub-iteration step.
 3. Perform correction on c_x and c_y at each cell-interface based on the updated values $\Delta\Omega^{k+1}$ using equation (4.15).
 4. Compute the updated vorticity discrepancy, if $\Delta\Omega^{k+1} < \text{error tolerance}$, stop the iteration and compute the overall fluxes at each interface and update the conservative variables at time level $n+1$. Else go back to step 2.
- Compute other variables such as primitive variables and compact vorticity at time $n+1$. To compute the next time-level, start again from the beginning.

4.5 Modelling Travelling Vortex

In general, vorticity is produced by both viscous and inviscid mechanisms. We want to check whether its subsequent transport by an inviscid flow will be correct and for the reasons explained in chapter 1, we will ignore the viscous part. For rotational flow, we came up with a test problem that features vorticity advected in a square

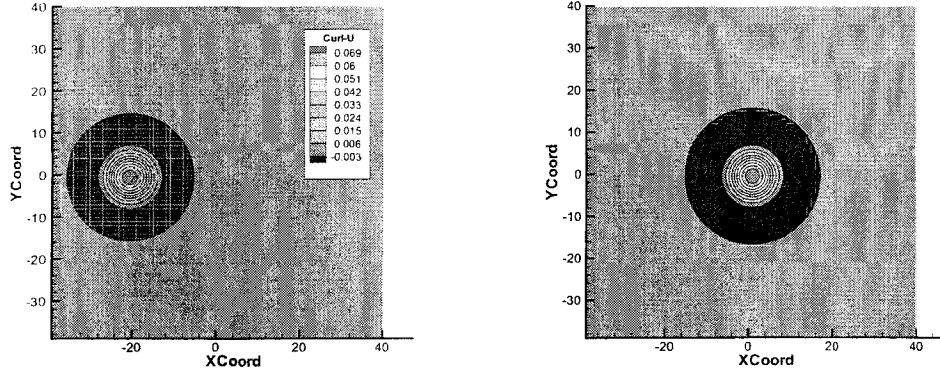


Figure 4.4: Vorticity at $T=0$ with 80×80 cells

Figure 4.5: Exact Vorticity at $T=180$

domain with periodic boundary conditions. We will set Courant number $\nu = 0.45$ with $\kappa = 0.6$. To solve the Poisson problem given by equation (4.18), we have used the Gauss-Seidel method. The Gauss-Seidel method is not the most efficient technique of solving the Poisson problem [113], [100]; utilizing a better relaxation scheme such as multigrid [16] should speed up the method considerably.

4.5.1 Exact Solution

This is to simulate a simple vorticity advection problem that satisfies the Euler equations with periodic boundary conditions. We derived a simple exact solution by assuming steady flow with a Gaussian pressure disturbance. Then we found a divergence-free velocity field satisfying $\frac{\partial p}{\partial r} = \frac{\rho \vec{U}^2}{r}$, and finally superposed a uniform advection speed. The solution is

$$\begin{aligned} u &= q \cos \alpha + c_1[y - y_o - qt \sin \alpha] \exp[-c_2([x - x_o - qt \cos \alpha]^2 + [y - y_o - qt \sin \alpha]^2)] \\ v &= q \sin \alpha - c_1[x - x_o - qt \cos \alpha] \exp[-c_2([x - x_o - qt \cos \alpha]^2 + [y - y_o - qt \sin \alpha]^2)] \\ P &= P_b - 0.25\rho \frac{c_1^2}{c_2} (\exp[-2c_2([x - x_o - qt \cos \alpha]^2 + [y - y_o - qt \sin \alpha]^2)] - 1) \end{aligned} \quad (4.49)$$

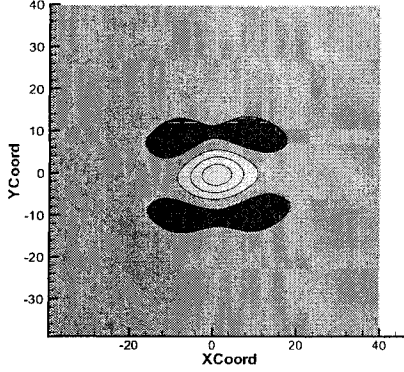


Figure 4.6: First order Hancock-Roe at
T=180

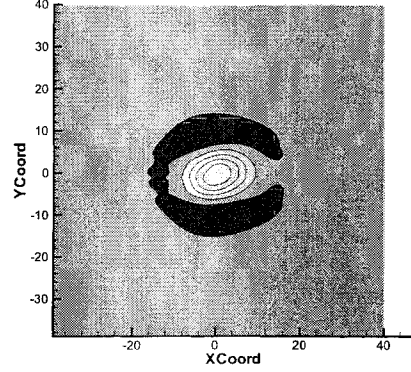


Figure 4.7: First order Hancock-Roe-
VC1 at T=180

where q , α and p_b are the background flow velocity ($q = 0.5$), flow angle ($\alpha = 0$) and pressure ($p_b = 1.0$) with perturbation coefficients $(c_1, c_2) = (-0.04, 0.02)$. The reference coordinates are chosen to be $(x_o, y_o) = (-20, 0)$. For simplicity, we set density to be a constant ($\rho = 1.4$). We could have utilized the isentropic relations $\frac{p}{\rho^\gamma} = k$ but did not do so in this example.

4.5.2 Numerical Results

Our results demonstrate that the VC2 scheme is superior to any other schemes (Fig 4.9) preserving enstrophy⁷ closest to the exact solution even after 450 time-steps. The first order Hancock is the worst, diffusing 85 percent of enstrophy after over 400 time-steps (Fig. 4.10)⁸. The second order Hancock scheme with Superbee limiter does not diffuse enstrophy due to its nature of steepening slopes when there is no danger of overshoot. This works well with shocks, however, for this case the steep-

⁷Enstrophy is defined as the dot product of vorticity with itself.

⁸Note that the enstrophy plot is normalized to unity, representing the enstrophy of the exact solution in which other schemes are compared to.

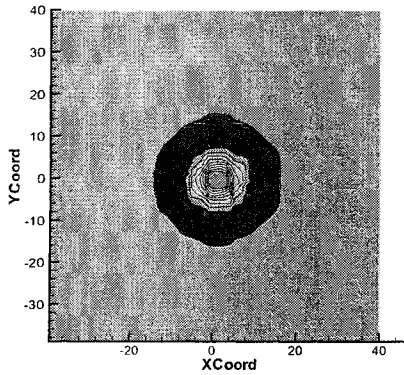


Figure 4.8: Second order Hancock-Roe-Superbee at $T=180$

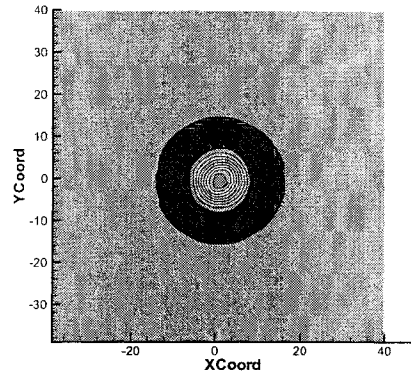


Figure 4.9: Second order Hancock-Roe-Superbee-VC2 at $T=180$

ening generates spurious enstrophy (approximately 20 percent after 400 timesteps) with time.

The VC2 scheme also uses Superbee to limit its Euler and vorticity fluxes but it only produces 2 percent of spurious enstrophy relative to the exact solution. This is attributed to vorticity physics being incorporated to the scheme in addition to conventional upwinding. The performance of the VC1 scheme lies in between the first order upwind and the Superbee method. This is quite unsurprising since vorticity accuracy depends strongly on the discretization of its independent estimate. When solving the vorticity transport equation, VC1 is only a first order method. This contributes to excess diffusion of enstrophy. In addition, Fig (4.11) illustrates that for this simple case, *solving the Poisson equation with 50 or 2000 iterations yields about 1 percent error for the VC2 scheme*. For the record the VC2 scheme needs about 50 sub-iterations per time step to achieve $O(10^{-8})$ error tolerance. This can be improved considerably if we use a more efficient Poisson solver like the multigrid.

It must be emphasized that the accuracy of the second order Hancock scheme is

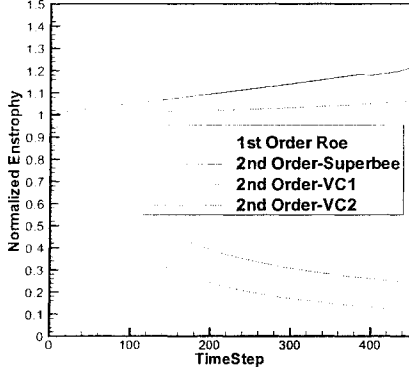


Figure 4.10: Normalized Enstrophy for various schemes using 80×80 cells. Note that the exact enstrophy is unity and the error of VC2 scheme is less than 2 percent after $T=450$ unlike the first order Hancock (85 percent).

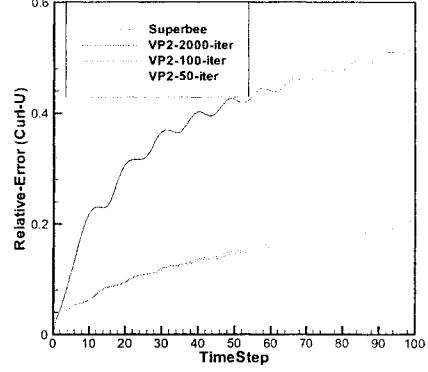


Figure 4.11: Normalized L2-Norm of ω (80×80) for second order schemes at various sub-iteration steps. There is only about 1-2 percent difference when applying 50, 100 or 2000 sub-iterations using the VC2 scheme.

not compromised when the vorticity correctional algorithm is included (Fig 4.12). In fact, the order of accuracy of predicting vorticity is twice more accurate for the VC2 scheme compared to the original Roe-flux (Fig 4.13).

In summary, we have established an accurate vorticity capturing method for predicting unsteady rotational flow in two dimensions. Our next quest is to use this vorticity capturing method in a much simpler vortical problem, that is to preserve irrotationality for a steady $1\frac{1}{2}$ dimensional shock with a hope to eliminate the carbuncle phenomenon. We will present the work in the next section.

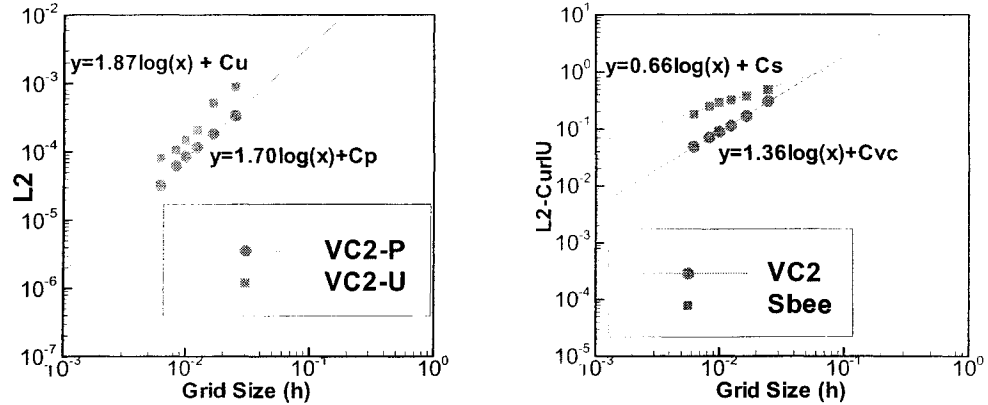


Figure 4.12: L₂-norm of pressure (slope 1.7) and u-velocity (slope=1.87) at T=60. This implies that the correctional step in VC2 does not reduce much of its second order accuracy.

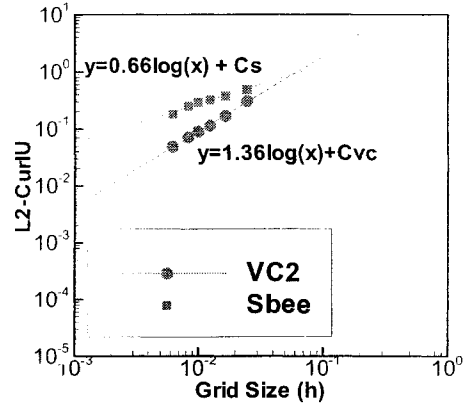


Figure 4.13: L₂-norm of ω at T=60. Note that VC2 is twice more accurate than conventional second order Hancock-Roe-Superbee when predicting vorticity.

4.6 A New Method of Controlling the Carbuncle I: Controlling Vorticity

Our philosophy is to prevent the carbuncle without compromising profiles of contact discontinuities and shear layers. Our first method deploys a first order Godunov method with Roe's solver that includes vorticity correctional step to remove spurious vorticity. The Godunov-type fluxes arguably have the strongest physical basis in finite volume methods so we expect our scheme to have minimal numerical dissipation. Since this method is a two-dimensional cure, we will not attempt to solve the one dimensional carbuncle but only the 1 1/2 dimensional carbuncle. *The scheme does not require predictions from any independent vorticity computation since the problem is purely an irrotational flow.* The vorticity correction algorithm will assume the independent vorticity estimate $\Omega_{IND}^{n+1} = 0$ at all times. Coupled with the Hancock

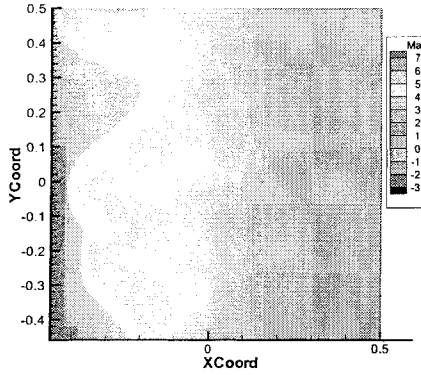


Figure 4.14: Mach profile for first order Roe at $T=1000$

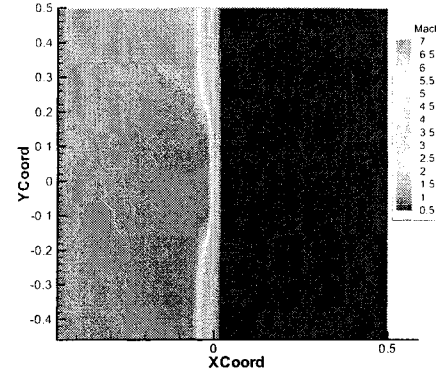


Figure 4.15: First order Hancock-VC at $T=10000$. Note that there is first stage instability.

scheme and Roe-solver, it will be defined as Hancock-VC scheme. Also, we will again use a Gauss-Seidel method to perform the sub-iterations within each time step with $\kappa = 0.6$. However, we will enforce a tighter error vorticity tolerance ($O(10^{-14})$) to eliminate the contribution of spurious vorticity to the carbuncle.

4.6.1 The 1 1/2 Dimensional Carbuncle

This is a test problem which produces shock instabilities and spurious vorticity. The configuration and parameters of this numerical experiment are described in chapter 2 and note that we chose $\nu = 0.4$ and $\gamma = 1.4$.

Our results indicate that for a Mach 7 flow, the vorticity capturing Hancock scheme (Hancock-VC) preserves irrotationality even after $T=10000$ (Fig 4.17) unlike the pure Roe-method(Fig 4.16). However the VC scheme requires 1000 sub-iterations⁹ per time step. For some problems, the VC scheme also needed a larger value for κ to suppress the instability while for other problems, the scheme is not

⁹This is the maximum number of sub-iterations we have allowed in one time step.

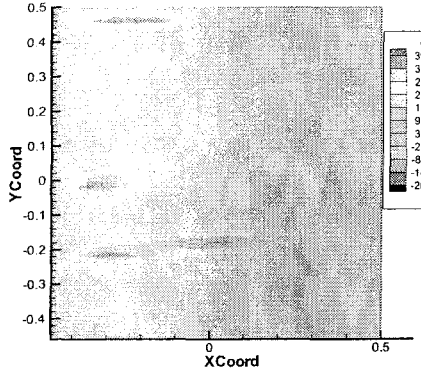


Figure 4.16: Vorticity contours for first order Hancock-Roe) at $T=1000$

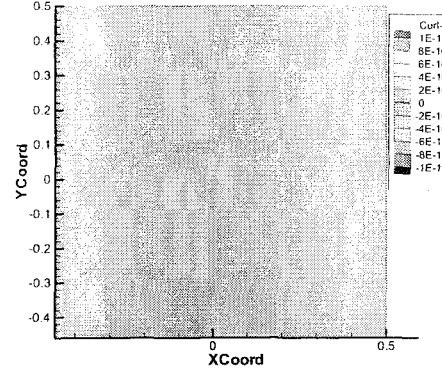


Figure 4.17: Vorticity contours for first order Hancock-VC at $T=10000$. Even though we have instability within the shock, however, we no longer have spurious vorticity.

able to contain the instability at all.

For this Mach 7 flow, preserving vorticity is not enough to prevent the shock instabilities as seen in Fig 4.15¹⁰. We still observe the ‘pimples’ stage only without spurious vorticity. In Fig 4.18, we see that the residual increases quite rapidly to $O(0.1)$ yet the enstrophy within the system remains machine-zero.

It is clear now that vorticity is not the root of the carbuncle. We now strongly believe that spurious vorticity generation is more of an effect rather than a cause of the carbuncle. *This implies that controlling vorticity is not the solution to cure the carbuncle.* We suspect that the instability is driven by a very strong mechanism which is of a one dimensional nature.

¹⁰Our results are not inconsistent with the results in [51] because they had a slightly different set-up. In particular, they assume periodic top-bottom boundaries and used a smaller seeding $O(10^{-16})$

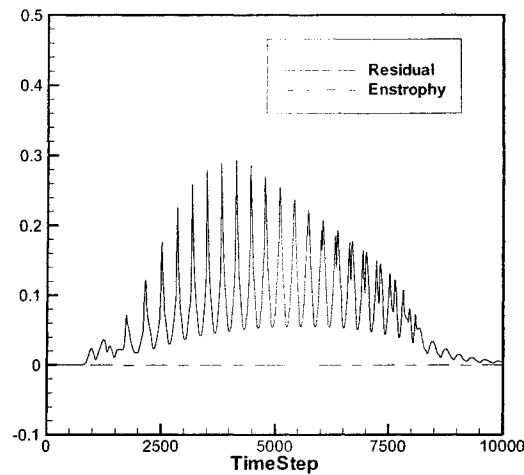


Figure 4.18: Residual and enstrophy plot for the 1 1/2 dimensional carbuncle using Hancock-VC scheme. Note that the residual grows to $O(0.1)$ and remains oscillatory for a while and then decays. The enstrophy remains machine zero.

Having said that, we seek a different methodology of preventing the carbuncle, specifically by directly controlling discrete entropy. This will be the subject of the next two chapters.

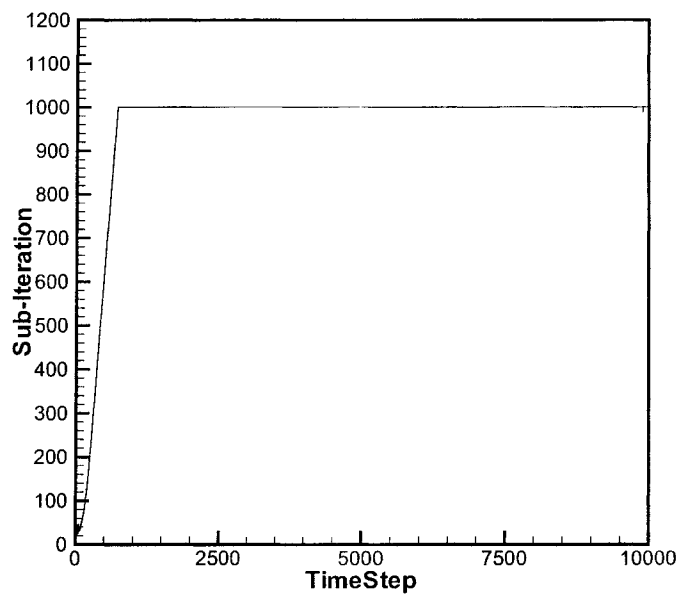


Figure 4.19: Sub-iterations versus time-step plot for the 1 1/2 dimensional carbuncle using Hancock-VC scheme.

CHAPTER V

ENTROPY CONSERVATION IN BURGERS EQUATION

We have seen in chapter 2 that the entropy condition based on equation 2.43¹ is not sufficient to enforce the second law of thermodynamics when numerically solving a steady stationary strong shock in one dimension. Another approach to impose the second law of thermodynamics is to define an entropy function² $U(\mathbf{u})$ for which an additional conservation law holds for smooth solutions. There is an inequality however, for discontinuous data. This chapter is intended to introduce the concept of implementing discrete entropy conservation law directly into a numerical flux function.

In theory, discretely controlling entropy is an easier task than controlling vorticity. In a system of conservation laws, conserving entropy is only an algebraic constraint on the main variables³ whereas conserving vorticity⁴ is a differential constraint. Moreover, entropy remains a scalar quantity even in three dimensions but

¹This is for a right moving shock. For a left moving shock, the inequality signs are flipped over.

²This entropy function has to be convex.

³Usually density, velocity and pressure are defined as main variables.

⁴Vorticity is conserved only in two dimensions as we have witnessed in the previous chapter.

vorticity is a vector with three components. The entropy conservation equation is a hyperbolic scalar conservation law similar to the conservation of mass equation. These equations can be predicted quite accurately based on one dimensional physics. However, the same thing cannot be said for vorticity. As seen and discussed in the previous two chapters, controlling vorticity requires corrections of multi dimensional nature.

There are benefits of modelling and predicting a fluid based on one dimensional grounds. If the physics remain mostly one dimensional, the technology extension to multi dimension is straight-forward. Appealing to a finite volume formulation, we can predict the fluid in a cells of a Cartesian mesh based on computing the fluxes at each interface dimension by dimension.

In a more general context, we only need a flux-solution (flux function) at the normal interface of adjacent control volumes which contain two states of fluid⁵. This is a very simple yet elegant idea which can be used in arbitrary-shaped control volumes particularly in unstructured grids, the most natural grid technique on curvilinear bodies or complex configurations. The computational cost of one dimensional techniques is also usually cheaper than those of multi dimensional methods.

Should including entropy conservation be the cure to the carbuncle phenomenon, we can expect that the formulation will go a long way making its mark in the CFD community. Our goal is to include entropy conservation directly into the numerical method when solving the systems of Euler equations. However, we intend to introduce the concept and underlying principles of entropy conservation in a scalar problem which is much simpler than those from a nonlinear system like the Euler

⁵Recall that this is a finite volume method.

equations. The scalar problem in mind will be the Burgers equation. Once we have understood entropy conservation for Burgers equation, we will present the idea in the context of Euler equations.

5.1 Discrete Inviscid Burgers Equation

The original one dimensional Burgers equation is written as

$$\partial_t u + u \partial_x u = \alpha \partial_{xx} u \quad (5.1)$$

If we take the limit $\alpha \rightarrow 0$, we get the inviscid Burgers equation which can be written as a scalar hyperbolic conservation law

$$\partial_t u + \partial_x f = 0 \quad (5.2)$$

where $f = \frac{u^2}{2}$ is the conservative flux. The wave speed is $\lambda = \frac{\partial f}{\partial u} = u$ and the shock speed is $\Lambda_s = \frac{[f]}{[u]} = \frac{(u_R^2 - u_L^2)}{2(u_R - u_L)} = \frac{1}{2}(u_L + u_R)$.

We will follow closely Roe's discretization technique in one dimension [84]. Assume that we have two adjacent states (L, R) with dual cell area (h_L, h_R) , we discretize the Burgers equation semi-discretely as

$$\begin{aligned} h_L \partial_t u_L &= f_L - f^* \\ h_R \partial_t u_R &= f^* - f_R \end{aligned} \quad (5.3)$$

where $f^* = f_{sym}^* - \psi$ is a numerical flux at $*$ decomposed into symmetric f_{sym}^* and asymmetric parts ψ yet to be determined. The update has two kind of interpretations. One, the left and right states are point values at vertices that surround a linear element centered at $*$. This is a residual distribution scheme where the residual $(f_L - f_R)$ is split as $(f_L - f^*) + (f^* - f_R)$ and distributed to the left and right

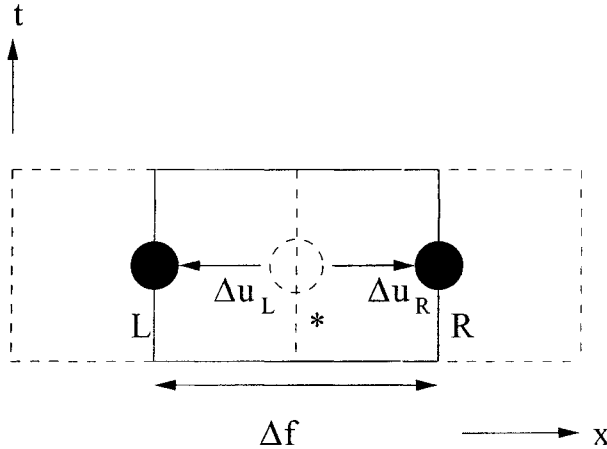


Figure 5.1: Dual interpretations of the updated scheme. The solid line represents residual distribution scheme. The dashed line represent finite volume scheme

states respectively. The other is finite volume interpretation where the left and right states are cell-averaged values separated by a flux-interface *.

First, we will revisit the non-entropy conservative Godunov-type fluxes to obtain the asymmetric part ψ . Then, we will construct an entropy conservative symmetric flux based on a chosen entropy variable. Finally, we will determine the entropy fix for an accurate entropy production across a shock.

5.2 Non Entropy-Conservative Fluxes

A finite volume flux discretization via Godunov type flux can be written as

$$f_I = f_{sym}^* - \psi \quad (5.4)$$

where ψ is an asymmetric flux dissipation to stabilize the symmetric part f_{sym}^* . The interface flux f_I is solved by a Riemann problem. For Burgers equation the exact

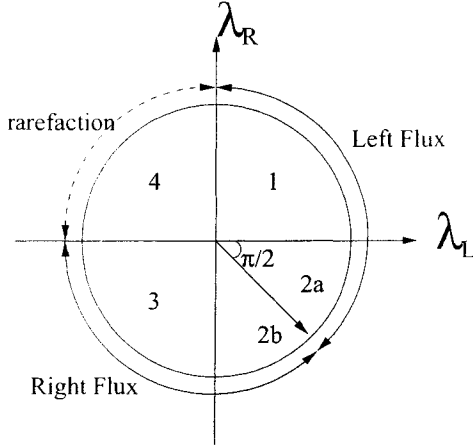


Figure 5.2: The Riemann Problem for Burgers equation. The left flux solution means the interface is biased (upwinded) to the left flux. Likewise, right flux solution means biased to the right flux. The line that splits quadrant 2 into two regions represents a stationary shock region whereas the sonic point rarefaction region is denoted by broken lines and is omitted for Roe-solver.

Riemann solver has the following fluxes at the interface.

$$f_I = \begin{cases} 0 & \text{if } \lambda_L < 0 < \lambda_R \text{ implying sonic point rarefaction,} \\ f_L & \text{elseif } \lambda_L + \lambda_R \geq 0 \text{ implying left state solution,} \\ f_R & \text{else } \lambda_L + \lambda_R < 0 \text{ implying right state solution.} \end{cases} \quad (5.5)$$

The Roe-solver for the Burgers equation has the same solution except that it does not recognize sonic point rarefactions (omit the first line of the above solution). To include the solutions of the Riemann problem, set $\psi = \frac{1}{2}\lambda^*[u]$ where $[u] = u_R - u_L$, hence we will re-write the flux at the interface as

$$f_I = \bar{f} - \frac{1}{2}\lambda^*[u] \quad (5.6)$$

where we assume central differencing $f_{sym}^* = \bar{f} = \frac{f_R + f_L}{2}$ for the symmetric part. The asymmetric part is in terms of the interface wave speed λ^* and the velocity difference

of left and right states. The wave speeds for the exact and Roe solvers are

$$\lambda^*_{Exact} = \begin{cases} \frac{u_R^2 + u_L^2}{2(u_R - u_L)} & \text{if } \lambda_L < 0 < \lambda_R, \\ \frac{u_R + u_L}{2} & \text{elseif } \lambda_L + \lambda_R \geq 0, \\ -\frac{u_R + u_L}{2} & \text{else } \lambda_L + \lambda_R < 0. \end{cases} \quad (5.7)$$

$$\lambda^*_{Roe} = \begin{cases} \frac{u_R + u_L}{2} & \text{elseif } \lambda_L + \lambda_R \geq 0, \\ -\frac{u_R + u_L}{2} & \text{elseif } \lambda_L + \lambda_R < 0. \end{cases} \quad (5.8)$$

Note that for Burgers equation, the wave speed is also the actual fluid velocity. Note that $\lambda^* = 0$ for stationary shocks. More importantly, except for cases that include sonic point rarefactions, the exact and Roe solver solutions are identical. Although this flux function enforces upwinding, however, it does not have any mechanism to ensure that entropy is conserved for smooth flow. We shall next introduce the concept of entropy conservation law.

5.3 Entropy Conservation For Inviscid Burgers Equation

For most aerospace engineers, entropy is a representation of the second law of thermodynamics and is precisely defined as $S = \ln p - \gamma \ln \rho$. In a more general perspective, entropy is defined as a scalar convex function U such that a system of equations like the hyperbolic conservation laws $\partial_t \mathbf{u} + \partial_x \mathbf{f} = 0$ can be uniquely mapped into the scalar one dimensional entropy conservation law

$$\partial_t U + \partial_x F = 0 \quad (5.9)$$

via the entropy variables $\mathbf{v} = \frac{\partial U}{\partial \mathbf{u}}$ [96], [7]. However, the choice of entropy variables is not unique even for the scalar Burgers equation. But nevertheless, we will choose a simple yet physically relevant quantity to represent entropy for the Burgers equation.

Define a convex entropy function $U = u^2$ so that the entropy variable is $v = \frac{\partial U}{\partial u} = 2u$. We insist that $\frac{\partial F}{\partial U} = \frac{\partial f}{\partial u}$ which implies that the entropy flux is $F = \frac{2}{3}U^{\frac{3}{2}} = \frac{2}{3}u^3$. Note that the selected entropy variable is twice the kinetic energy of the system.

We intend to include the discrete entropy conservation law in our numerical flux function while at the same time, keeping the usual discrete conservation of fluid velocity in the inviscid Burgers equation. In other words, we want to include another constraint to the numerical flux function so that it satisfies entropy conservation law.

Consider the same semi-discrete update proposed by Roe [84]. We want entropy conservation in the symmetric part so we will drop the asymmetric part in this analysis. Hence

$$\begin{aligned} h_L \partial_t u_L &= f_L - f_{sym}^* \\ h_R \partial_t u_R &= f_{sym}^* - f_R \end{aligned} \quad (5.10)$$

An entropy update will be

$$\begin{aligned} h_L \partial_t U_L &= v_L (f_L - f_{sym}^*) \\ h_R \partial_t U_R &= v_R (f_{sym}^* - f_R) \end{aligned} \quad (5.11)$$

with the total element update computed as the sum of the two nodes given by

$$\partial_t (h_L U_L + h_R U_R) = -[vf] + [v] f_{sym}^* \quad (5.12)$$

Next, we will directly include the discrete entropy conservation law to the numerical flux of the Burgers equation. To ensure proper entropy update, we need the semi discrete flux function to satisfy the semi discrete entropy conservation law, $\partial_t (h_L U_L + h_R U_R) = -[F]$ which requires $[vf] - [v] f_{sym}^* = [F]$ so that

$$(u_R^3 - u_L^3) - 2(u_R - u_L)f_{sym}^* = \frac{2}{3}(u_R^3 - u_L^3) \quad (5.13)$$

Solve for the entropy conservative fluxes

$$f_{sym}^* = \frac{1}{6}(u_R^2 + u_R u_L + u_L^2) = f_C \quad (5.14)$$

Of course, this entropy conserving flux is not applicable across a shock since entropy is not conserved across one.

5.4 Including Entropy Production

For smooth solutions, we want entropy to satisfy a hyperbolic conservation law. However, when a solution is discontinuous, entropy should be produced across the discontinuity. For Burgers equation, the shock is the only the form of physical discontinuity⁶. For entropy variable $U = u^2$, it decreases across a shock. All of these can be achieved if our scheme is entropy stable. Mathematically, an entropy stable scheme satisfies the following inequality [96], [7].

$$\partial_t U + \partial_x F \leq 0 \quad (5.15)$$

We now include a proper entropy production so that the updated scheme is entropy stable. It suffices for now that it ensures the correct sign of entropy production rather than the correct quantity of production. A semi-discrete entropy update of the two points are

$$\begin{aligned} h_L \partial_t U_L &= v_L(f_L - f_{sym}^*) + v_L \psi \\ h_R \partial_t U_R &= v_R(f_{sym}^* - f_R) - v_R \psi \end{aligned} \quad (5.16)$$

giving total entropy update as

$$\partial_t(h_L U_L + h_R U_R) = -[v f] + [v] f_{sym}^* - [v] \psi \quad (5.17)$$

⁶For the Euler equations, we have a contact discontinuity across which entropy is conserved.

5.4.1 Entropy Production For the Symmetric Flux

First, let us assume no contribution from the asymmetric part $\psi = 0$. To achieve entropy conservation, we need (as before) $[v]f - [v]f_{sym}^* = [F]$ in which $f_{sym}^* = f_C$. But now, we are interested in the entropy production of f_{sym}^* . Let the difference between any flux f_{sym}^* and the entropy conservative flux F be the entropy production

$$P = [v]f_{sym}^* - [v]f + [F] \quad (5.18)$$

The total entropy update computed directly from the entropy conservation law is

$$\partial_t(h_L U_L + h_R U_R) + [F] = P \quad (5.19)$$

in which we require $P \leq 0$ for entropy stability. For the Burgers equation, the general symmetric flux function can be written as ⁷

$$f_{sym}^* = \frac{\alpha}{4}(u_L^2 + u_R^2) + \frac{1-\alpha}{2}u_L u_R = \frac{1}{4}(u_L^2 + u_R^2) - \frac{1}{4}(1-\alpha)[u]^2 \quad (5.20)$$

Hence the entropy production satisfies the following relation [84], [75]

$$P = \frac{1}{2}(\alpha - \frac{2}{3})[u]^3 \quad (5.21)$$

We need to take $\alpha > \frac{2}{3}$ for compressive regions $[u] < 0$ and $\alpha < \frac{2}{3}$ for expansive regions to ensure entropy stability. For the choice of $\alpha = \frac{2}{3}$, we retain the entropy conserving flux $f_{sym}^* = f_C$ with zero entropy production, and assign the task of entropy production in the asymmetric part.

5.4.2 Entropy Production For the Asymmetric Flux

Ideally, we would like the symmetric flux to be purely an entropy conserving flux so that the job of producing entropy will be done by the asymmetric (dissipative)

⁷Note if $\alpha = 1$, we have the pure central difference scheme.

flux. Assume that now we apply dissipative flux in the form of $\psi = \frac{1}{2}\lambda^*[u]$, where λ^* can be either from exact or Roe method described in section 5.1. If we choose $f_{sym}^* = f_C$, 5.17 becomes

$$\partial_t(h_L U_L + h_R U_R) + [F] = -[v]\frac{1}{2}\lambda^*[u] \quad (5.22)$$

which implies that entropy production would come only from the dissipative flux. Note that λ^* is always greater than zero which means that $[v]\frac{1}{2}\lambda^*[u] = [u]\lambda^*[u] \geq 0$. Thus we have entropy stability. But achieving entropy stability means that we merely have obtained the correct sign of entropy production and not the correct amount. To understand this further, we will introduce the term entropy consistency.

5.5 Including Entropy Fix to Ensure Entropy Consistency

Our intention is to include accurate entropy production across shocks. If not enough entropy is produced across shocks, we may get unstable solutions or spurious oscillations being generated. But producing too much entropy will create a diffused shock profile. We will loosely define an accurate or consistent entropy production as the precise amount of entropy needed to produce monotone solution when the fluid goes through a shock without compromising much of the shock profile.

Ideally, there should be a balance between achieving monotone solutions and a crisp shock profile. However, it is difficult to gauge exactly how much entropy needs to be produced to obtain this especially in the context of solving the Euler equations. Fortunately for the Burgers equation, there is a simple approach.

5.5.1 Achieving Entropy Consistency from the ‘Jump’ Condition

One way to determine consistent entropy production is by looking from the perspective of the fluids jump condition. Note that the jump condition enforces conser-

vation across discontinuities and can be written as (refer to appendix H)

$$[f] = \Lambda[u] \quad (5.23)$$

where Λ is the speed of discontinuity and $[u] = u_R - u_L$. It must be stressed that entropy is not conserved across shocks. We assume that the entropy jump condition will be enhanced by a production term across a shock⁸. Assuming U and F are entropy functions and fluxes, entropy will satisfy the following condition

$$[F] = \Lambda[U] + P \quad (5.24)$$

where P denotes production term⁹. From section (5.3), to ensure we semi-discretely satisfy entropy conservation, we require

$$[v]f^* - [vf] + [F] = 0 \quad (5.25)$$

To satisfy entropy-consistency, we insist that

$$[v]f^* - [vf] + [F] = P = [F] - \Lambda[U] \quad (5.26)$$

Hence

$$[v]f^* = ([vf] - [F]) + ([F] - \Lambda[U]) \quad (5.27)$$

Note that on the RHS, quantities in the first parenthesis represent entropy-conserving part. Quantities in the second parenthesis denote the consistent entropy-production. The former can be viewed as the symmetric part of the flux. The latter should be a

⁸This is also included in appendix H.

⁹To be precise, we actually have to include sum of the jumps across the waves if there is more than one wave but for now, we just assume one.

part of the asymmetric (dissipative) flux. For Burgers equation, (5.27) becomes

$$\begin{aligned} 2[u]f^* &= [u^3] - \frac{u_R + u_L}{2}[u^2] \\ &= (u_R^2 + u_R u_L + u_L^2)[u] - \frac{(u_R + u_L)^2}{2}[u] \end{aligned} \quad (5.28)$$

Hence an entropy consistent flux for Burgers equation is

$$f^* = \frac{1}{4}(u_R^2 + u_L^2) \quad (5.29)$$

which is exactly the arithmetic averaging for the fluxes. This result however, is not surprising. Let us consider a stationary shock where there is zero contribution from the asymmetric flux $\frac{1}{2}\lambda^*[u]$ (since $\lambda^* = 0$). The exact Riemann solver (or Roe solver) $f^* = \bar{f} - \frac{1}{2}\lambda^*[u]$ solves the shock *exactly* hence generating the exact entropy production across the shock. This entropy production has to be from the symmetric part which is the arithmetic mean.

5.5.2 Achieving Entropy Consistency from $\bar{f} - f_C$

The above result can also be interpreted from another perspective. We know previously that the asymmetric part of the new flux function is identical to either the exact or Roe solvers. However, we have lost the entropy production in the symmetric portion by choosing the entropy conservative flux over the central differencing. Let the difference between the two symmetric fluxes be the entropy production required (in addition to the entropy production generated by the asymmetric flux) across

shocks

$$\begin{aligned}
D &= \bar{f} - f_C \\
&= \frac{1}{4}(u_R^2 + u_L^2) - \frac{1}{6}(u_R^2 + u_R u_L + u_L^2) \\
&= \frac{1}{12}(u_R^2 - 2u_R u_L + u_L^2) \\
&= \frac{1}{12}[u]^2 \\
&= \frac{1}{12}[\lambda][u]
\end{aligned} \tag{5.30}$$

Hence the entropy conservative flux function with Roe's entropy stable dissipation (EC-R) and entropy fix will be

$$f_I = f_C - \frac{1}{2}(\lambda_{Roe}^* + \frac{|f([\lambda])|}{6})[u] \tag{5.31}$$

and λ_{Roe}^* being the Roe's wave speed at interface * define in section 2. We have examined two options in determining the entropy fix $f([\lambda])$.

Entropy Fix 1

For the first method, the entropy fix is only applied in compressive regions.

$$f([\lambda]) = \begin{cases} 0 & \text{if } u_R - u_L \geq 0, \\ [u] & \text{if } u_R - u_L < 0. \end{cases} = \min(0, [u]) \tag{5.32}$$

This is the opposite to the entropy fix proposed for Roe solver capturing rarefaction fans. In addition, *note that with this fix we have recovered the original Roe-flux for compressive regions which includes shocks.*

Entropy Fix 2

For the second method, the entropy fix is applied to both compressive and expansive regions.

$$f([\lambda]) = [\lambda] = [u] \tag{5.33}$$

In other words, for compressive regions, the second method is identical to the first. We do not expect the entropy fix to strongly affect the expansive regions since the net entropy fix is proportional to the change in wave-speeds which is relatively smooth in expansive regions. However, we hope that the entropy fix will provide some smoothing mechanism to smooth out under-resolved expansive regions.

5.6 Numerical Examples

We want to see how the entropy conserving flux (EC) perform when tested with several problems satisfying Burgers equations. We will utilize Roe method for dissipation so our scheme will be denoted by EC-R. We will also include results of using entropy fix. *We will only compare the results of the two entropy fixes in Test 1 and for the rest of the numerical experiments, we have used entropy fix 2.*

We prescribe 40 cells within the computational domain with periodic boundary conditions. The Courant number is 0.8 for all cases and results from the exact Riemann solver and Roe-solver are also included. Note that the solid lines represent exact solutions and these solutions are analytically determined unless stated otherwise. Also, *it will be assumed that all of the numerical results are produced using a first order scheme (both time and space) unless stated otherwise.*

5.6.1 Test 1: Modelling Rarefaction with Stationary Shock

This problem is taken from [54]. We will compute the following square wave initial value problem to find $u(x, t)$ at $T=8$ (8 time-steps).

$$u(x, 0) = \begin{cases} -1 & \text{if } \frac{1}{3} \leq |x| \leq 1, \\ 1 & \text{if } |x| < \frac{1}{3}. \end{cases} \quad (5.34)$$

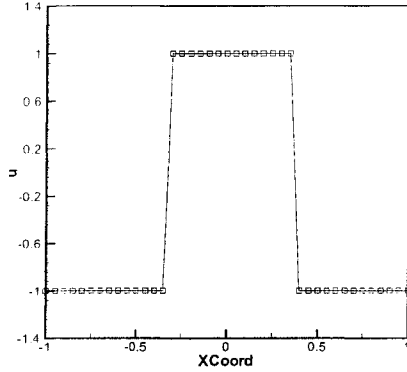


Figure 5.3: Test 1-IC Stationary Shock and Rarefaction

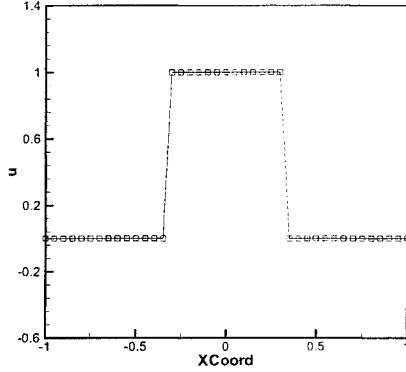


Figure 5.4: Test 2-IC Moving Shock and Rarefaction

The square wave will evolve into a rarefaction fan on the left while the right side will remain a stationary shock. Note that this problem will contain a sonic point rarefaction.

The exact solution to this initial value problem is

$$u(x, t) = \begin{cases} -1 & \text{if } -\infty < x < x_1, \\ -1 + 2\frac{x-x_1}{x_2-x_1} & \text{if } x_1 < x < x_2, \\ 1 & \text{if } x_2 < x < x_{shock}, \\ -1 & \text{if } x_{shock} < x < \infty. \end{cases} \quad (5.35)$$

where $x_1 = -\frac{1}{3} - t$, $x_2 = -\frac{1}{3} + t$ and $x_{shock} = \frac{1}{3}$. Figure (5.5)-(5.8) are results of various first order schemes. It shows the EC-R scheme does a decent job predicting the sonic point rarefaction wave compared to Roe solver¹⁰ although not as smooth as the exact Riemann solver. The smoothness can be improved with either using

¹⁰Recall Roe solver cannot detect sonic point because it only sees rarefactions as rarefaction shocks

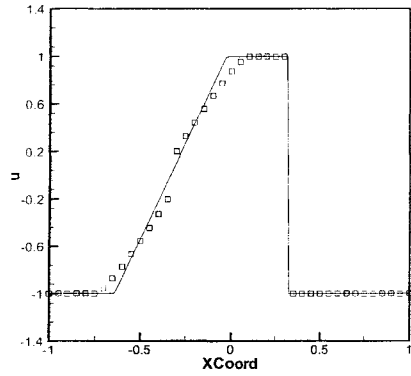


Figure 5.5: Test 1-Exact Riemann solver

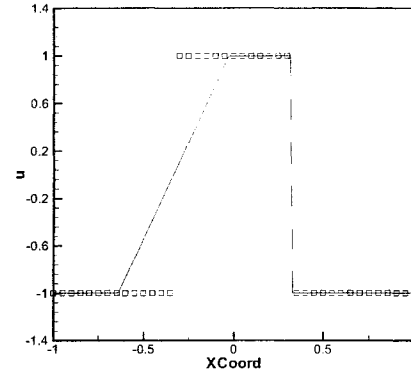


Figure 5.6: Test 1-Roe solver

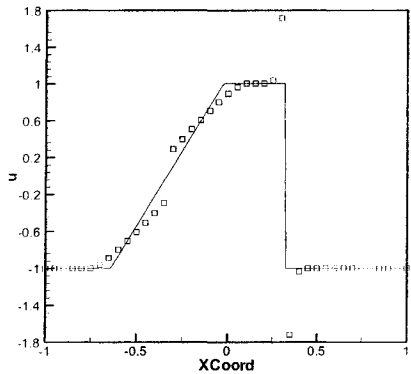


Figure 5.7: Test 1-EC-R solver

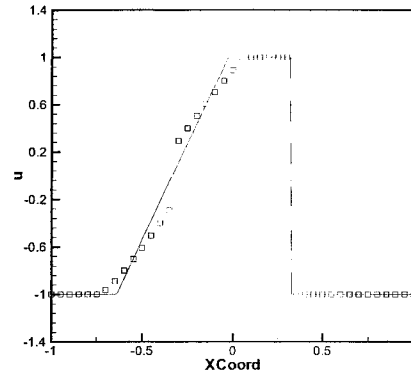


Figure 5.8: Test 1- EC-R solver with entropy fix 1

entropy fix 2 (Fig 5.11) or more successfully with a second order method (Fig 5.10). But across the shock, the EC-R scheme does not produce monotone solution even when a limiter is applied (Fig 5.9). However, this can be remedied with entropy fixes derived in section 5.5 giving entropy consistency. With either entropy fix 1 or 2, the EC-R flux produces shock solutions identical to those produced by the exact and Roe solver. This is to be expected since with the entropy fix, the EC-R scheme becomes the exact solver across a shock. However, the *results of rarefactions are slightly better*

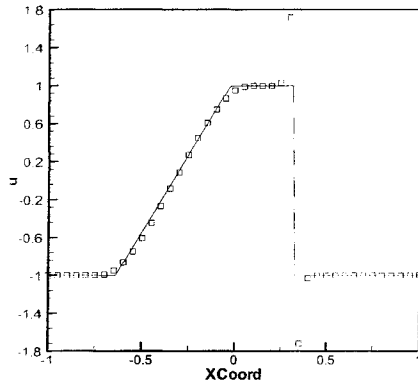


Figure 5.9: 2nd order EC-R solver using harmonic limiter (Test 1) with spurious over/undershoots present.

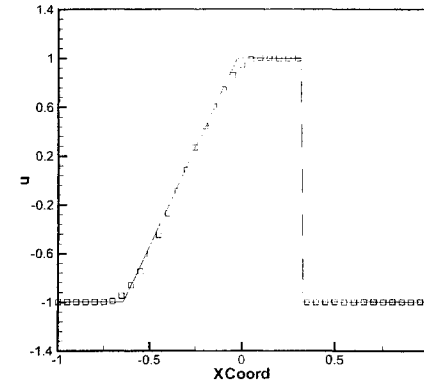


Figure 5.10: 2nd order EC-R solver (with entropy fix 1) using harmonic limiter for Test 1.

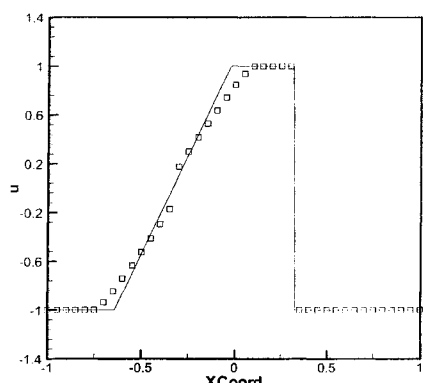


Figure 5.11: EC-R solver with entropy fix 2 (Test 1). Note that the rarefaction region is slightly smoother than the one produced with entropy fix 1.

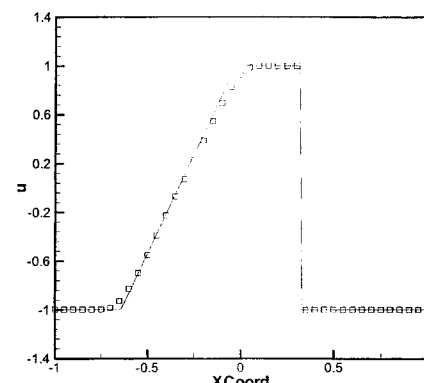


Figure 5.12: 2nd order EC-R solver (with entropy fix 2) using harmonic limiter for Test 1.

when using entropy fix 2 hence from now on, we will only deploy entropy fix 2 as the entropy fix in our computations.

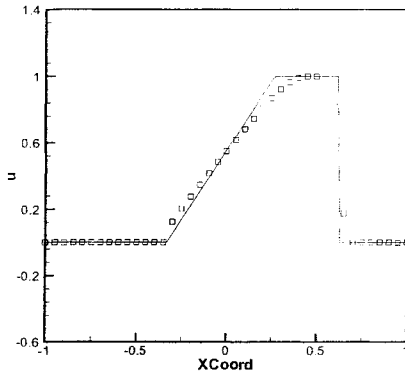


Figure 5.13: Test 2-Exact Riemann solver

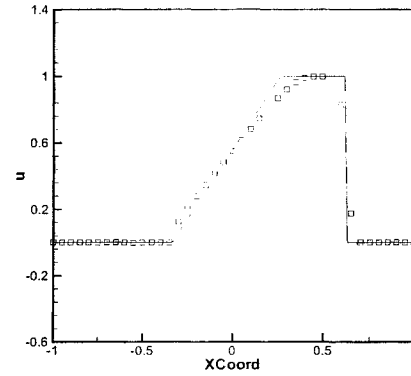


Figure 5.14: Test 2-Roe solver

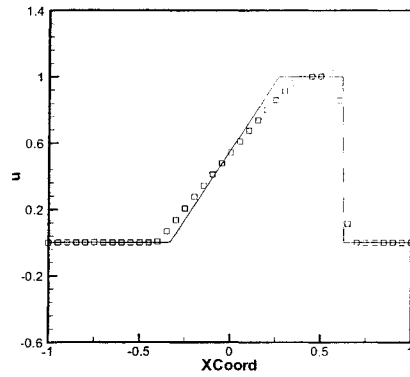


Figure 5.15: Test 2-EC-R solver

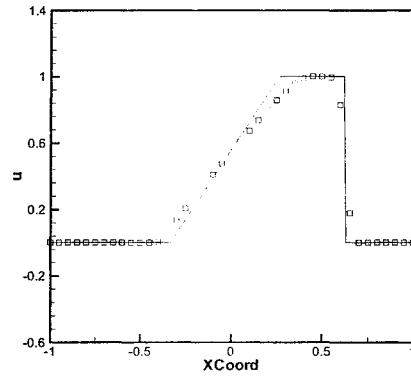


Figure 5.16: Test 2-EC-R solver with entropy fix

5.6.2 Test 2: Modelling Rarefaction with Moving Shock

This problem is also taken from [54]. We will compute the following square wave initial value problem to find $u(x, t)$ at $T=15$.

$$u(x, 0) = \begin{cases} 0 & \text{if } \frac{1}{3} \leq |x| \leq 1, \\ 1 & \text{if } |x| < \frac{1}{3}. \end{cases} \quad (5.36)$$

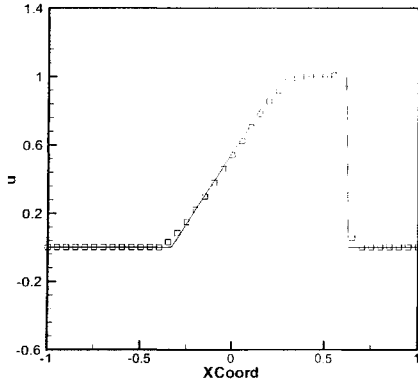


Figure 5.17: 2nd Order EC-R flux with harmonic limiter for Test 2. Note that there are small spurious over/undershoots even with a limiter being applied.

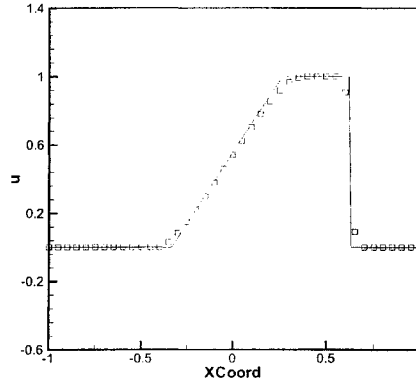


Figure 5.18: 2nd order EC-R solver (with entropy fix) using harmonic limiter

This problem is similar to the previous one except that the shock is moving and that there is no sonic point. The exact solution to this initial value problem is

$$u(x, t) = \begin{cases} 0 & \text{if } -\infty < x < x_1, \\ \frac{x-x_1}{x_2-x_1} & \text{if } x_1 < x < x_2, \\ 1 & \text{if } x_2 < x < x_{shock}, \\ 0 & \text{if } x_{shock} < x < \infty. \end{cases} \quad (5.37)$$

where $x_1 = -\frac{1}{3}$, $x_2 = -\frac{1}{3} + t$ and $x_{shock} = \frac{1}{3} + \frac{1}{2}t$. Figure (5.13)-(5.16) are the numerical results. Again, the EC-R scheme requires entropy fix for entropy consistency across the shock even when a second order scheme with limiter is applied (Fig 5.17).

5.6.3 Test 3: Modelling Compression Waves I

Note that the entropy fix is not able to distinguish between compression or shock waves. However, it remains to be seen if this actually matters in the context of Burgers equation. Before we continue any further, let us recall a few assumptions with regards to applying an entropy fix. One, entropy fix is an artificial method to generate ‘enough’ entropy so that the solution across a shock is monotone. Two, this entropy fix only needs to be enforced for shock waves and *not* for compression waves because in theory, entropy is conserved in compression waves.

Consider the following initial value problem.

$$u(x, 0) = \begin{cases} 0 & \text{if } |x| > 1, \\ -u_1 * \sin\pi x & \text{if } -1 \leq x \leq 1. \end{cases} \quad (5.38)$$

where the amplitude $u_1 = 5.0$ has been chosen. This is an initial value problem which consists of compression and expansion waves. The compression waves will then become a stationary shock and will interact with the expansion waves. The expansion waves will weaken the shock and eventually the shock will flatten out. We shall examine how the entropy conserving flux function (with and without entropy fix) will perform in this problem. The exact solution was numerically determined.

From the six figures (Figs. 5.19-5.24), we can see that there is not much difference between using entropy fix or not when predicting the compression waves. This result is not so surprising because the entropy fix is only a $\frac{1}{6}$ correction to the overall dissipation based on the difference of the left and right states hence for a smooth function, this is not a big deal. However, as soon as the shock forms, the difference between the left and right states are no longer marginal. As a result, the method without entropy fix generates spurious overshoots which is highly undesir-

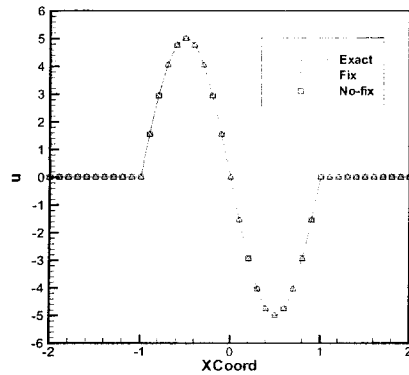


Figure 5.19: Test 3-T=0

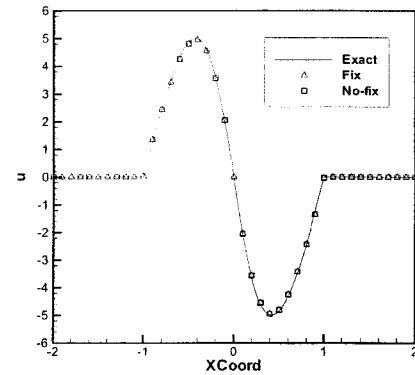


Figure 5.20: Test 3-Compression and Expansion waves at T=1.

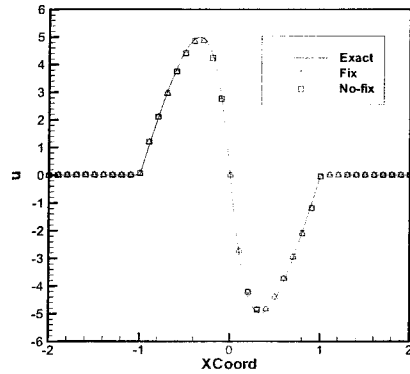


Figure 5.21: Test3-Compression and Expansion waves at T=2.

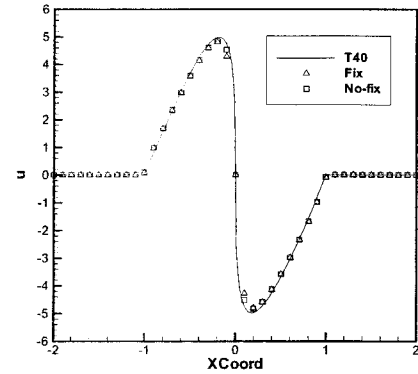


Figure 5.22: Slope of Compression begins to steepen at T=4 but there is only small differences between the 3 methods.

able. Including the entropy fix will remove this problem at the expense of a very little diffusion downstream of the shock.

We have also conducted tests for $u_o = 0.05, 500$ but their plots are not included since all of the results with and without entropy fix are of similar patterns to those

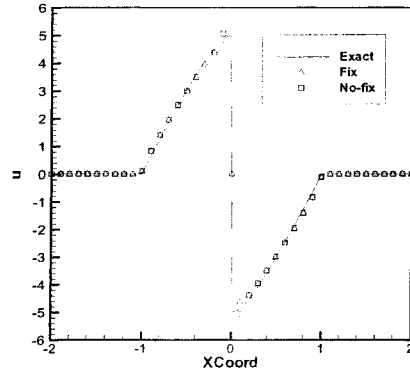


Figure 5.23: Test3-Shock forms at $T=6$. Note that there is spurious overshoot for the flux function without entropy fix.

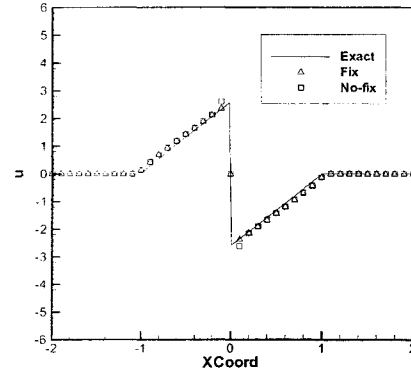


Figure 5.24: Test3-Decaying of shock $T=20$. There is still spurious overshoot for the flux function without entropy fix.

produced with $u_o = 5.0$. The only discrepancy lies in the magnitude difference.

Recall that the analytical solution of the Burgers equation is a solution of the nonlinear advection equation, $u(x, t) = f(x - ut)$. For this problem, the normalized solution is $\frac{u}{u_1} = -\sin(x - \frac{u}{u_1} u_1 t)$ which implies that the solution is dependent only on x and $u_1 t$. For constant Courant number, the solution is self-similar. To further justify this, we have plotted the normalized velocity difference between the scheme having entropy fix u_{fix} and the scheme without it u as a function of space and time.

$$\Delta u(x, t) = \frac{\sqrt{(u - u_{fix})^2}}{u_o} \quad (5.39)$$

The results of $\Delta u(x, t)$ for each case of u_o up until a shock appears are included in Figs. (5.25-5.28).

In addition, we have also included the results for the second order EC-R fluxes (with and without entropy fix) using the harmonic limiter (Fig 5.29). It seems that even with the limiter applied, spurious over/undershoots still are present near the

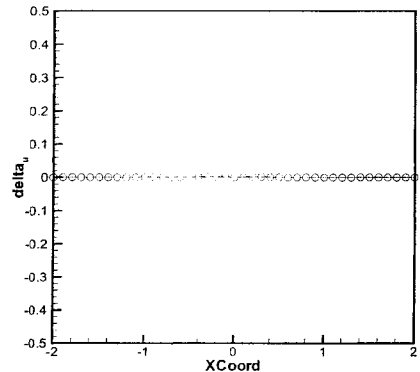


Figure 5.25: Test 3-The normalized difference between numerical velocities predicted with and without entropy fix at $T=1$.

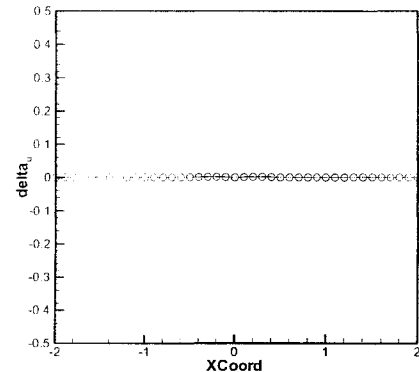


Figure 5.26: Test 3-The normalized difference between numerical velocities predicted with and without entropy fix at $T=2$.

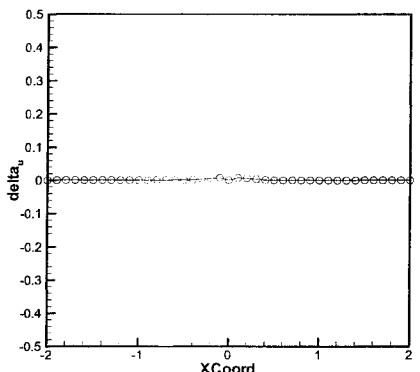


Figure 5.27: Test 3-The normalized difference between numerical velocities predicted with and without entropy fix at $T=4$.

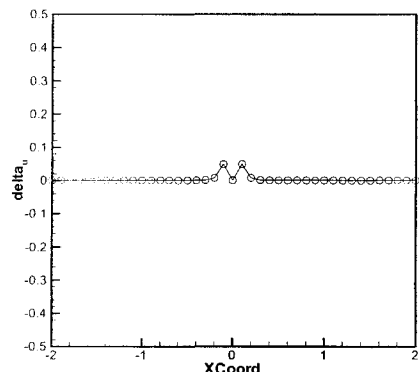


Figure 5.28: Test 3-The normalized difference between numerical velocities predicted with and without entropy fix at $T=5$ just before shock forms. Note there is at most 5-6 percent difference.

shock for the EC-R flux without the entropy fix. This further supports the argument that the entropy fix is required for genuine shock prediction.

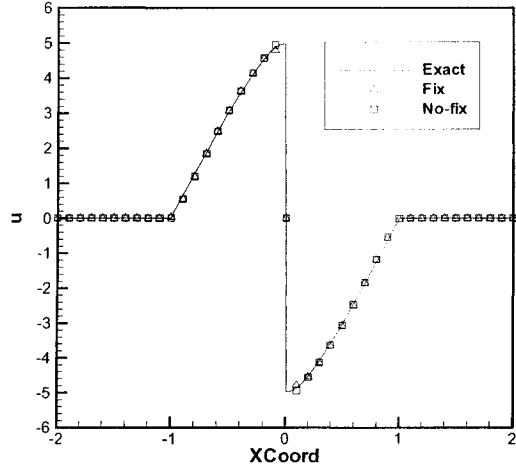


Figure 5.29: The second order results for Test 3 using the EC-R flux with harmonic limiter. Note that even with the limiter being applied, there are spurious overshoot and undershoots if the entropy fix is not used.

5.6.4 Test 4: Modelling Compression Waves II

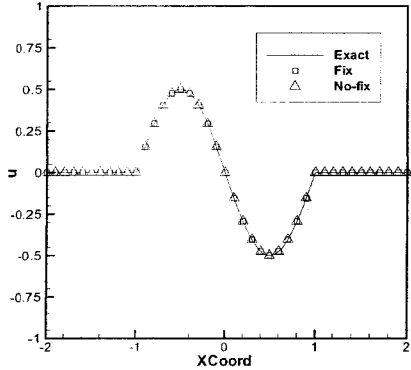
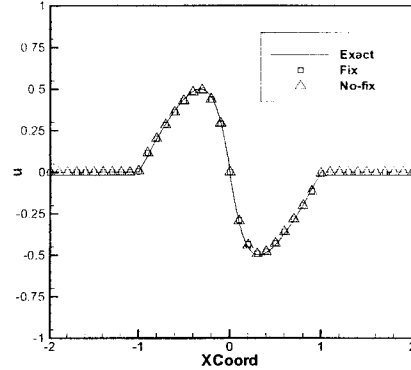
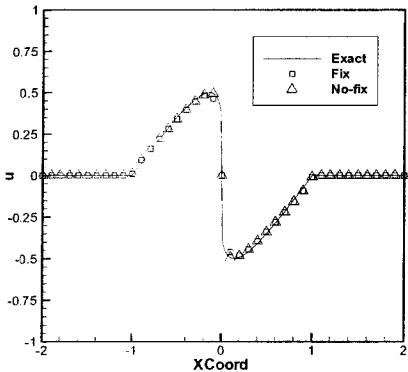
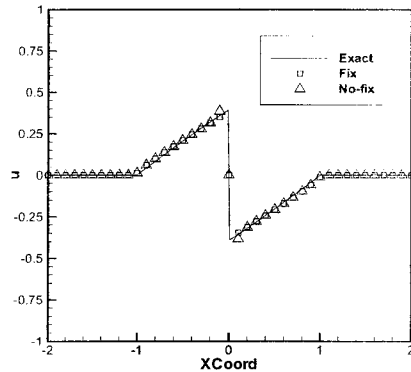
Consider the following initial value problem.

$$u(x, 0) = \begin{cases} u_0 & \text{if } |x| > 1, \\ u_0 - u_1 * \sin\pi x & \text{if } -1 \leq x \leq 1. \end{cases} \quad (5.40)$$

where the amplitude $u_1 = 0.5$ has been chosen. The background velocity u_0 are chosen to be 0.0, 1.0, 5.0. This is an initial value problem which also consists of compression and expansion waves. However, the normalized analytical solution will be in the form of

$$u(x, t) = \frac{u_0}{u_1} - \sin\left(x - \frac{u}{u_1}t\right) \quad (5.41)$$

This will be a test for slow moving strong shocks or fast moving weak shocks coupled with rarefactions. Results are included in Fig. 5.30-5.41. Note that the only visible difference of using the entropy fix or not is seen when the background velocity $u_0 =$

Figure 5.30: Test 4- $u_0 = 0.0$ at $T=0$ Figure 5.31: Test 4- $u_0 = 0.0$ at $T=2$.Figure 5.32: Test 4- $u_0 = 0.0$ at $T=6$.Figure 5.33: Test 4- $u_0 = 0.0$ at $T=10$.

0.0. The flux function without the fix generate spurious over/undershoots when the shock is formed unlike the flux function which includes entropy fix. This is consistent with the results produced in the previous test.

For finite background velocities, there are no spurious overshoots for either schemes. This is attributed mainly to the ‘extra’ dissipation mechanism¹¹ when u_0 is non-zero

¹¹For a stationary shock, $\lambda^* = 0$ thus the asymmetric flux produces less dissipation. However, when the shock is moving $\lambda^* \neq 0$ giving additional dissipation to the asymmetric flux.

and this dissipation is linearly proportional to the magnitude of $\frac{u_0}{u_1}$. The dissipation introduced by the entropy fix (factor $\frac{1}{6}$) is marginal compared to the dissipation produced by the background velocity hence the difference between using or not using the fix is hardly noticeable.

But the EC-R scheme is quite diffusive when predicting fast moving weak shocks (Fig. 5.41). Nonetheless, the results of the scheme with or without entropy fix are almost identical. This implies that the entropy fix does not compromise the quality of predicting fast moving shocks.

5.6.5 Test 5: Modelling Two Dimensional Problem

We will introduce a test case where a ray of compression waves meet and becomes a shock. This is also known as the two dimensional ‘tree-case’. The following partial differential equation is solved.

$$\partial_t u + \partial_x \frac{u^2}{2} + \partial_y u = 0 \quad (5.42)$$

where we have set the y-advection speed to a constant. The computational domain is a square domain with length of 1. We are interested to obtain the steady state solution with the following boundary conditions.

$$u(x, y) = \begin{cases} u(0, y) = 2.0 \\ u(x, 0) = 2.0 - 3.0x \\ u(1, 0) = -1.0 \end{cases} \quad (5.43)$$

Note that we have only specified three boundaries. The last one is the top boundary ($y = 1$) which is chosen to be non-reflecting. We have chosen 40 x 40 cells with $\nu = 0.1$. The results are included in Figs 5.42-5.50.

From the results of our test cases, we can justify that it is not critical if an entropy fix is used for compression waves or fast moving weak shocks when solving

the Burgers equation. However, *all* of our results indicate that it is imperative to include the entropy fix (hence EC-R is entropy-consistent) across shocks to ensure monotonicity. Without the entropy fix, we only have an entropy stable scheme but there is not enough entropy production to preserve monotonicity. By including the fix, we have reverted to the original Roe-flux in compressive regions and this is highly desirable for shock capturing (at least for Burgers equation) since the Roe-flux is an exact Riemann-solver when computing shocks.

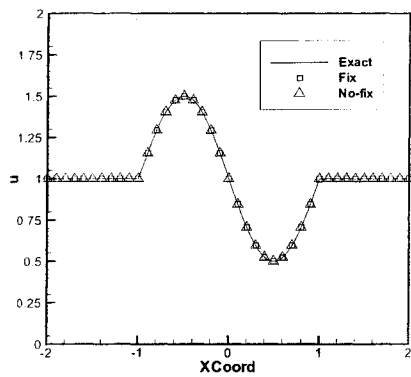
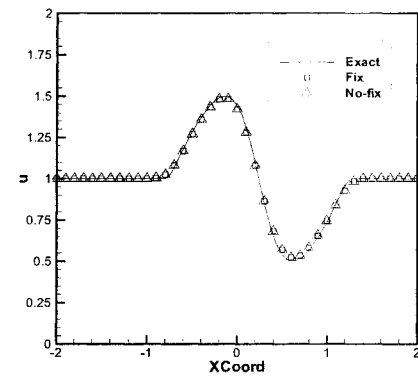
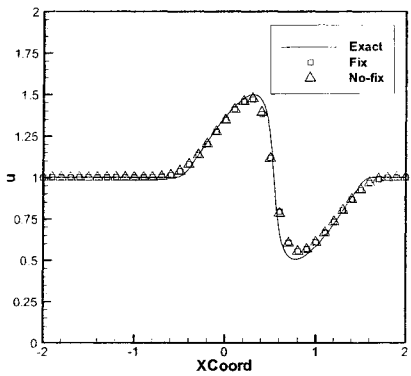
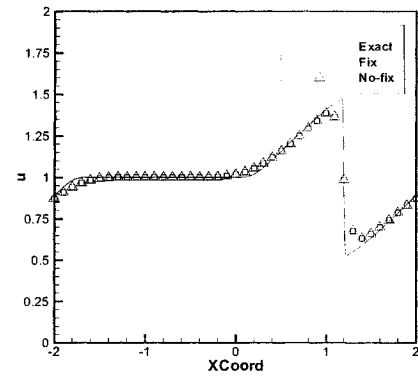
It must be noted that for the Burgers equation, the Roe-flux is an entropy-consistent flux when predicting shocks. However, for cases where there is a sonic point, the Roe flux is not entropy satisfying unlike the EC scheme. Combining these two features, we have the EC-R scheme which is entropy conserving for smooth functions and entropy consistent across shocks. This may suggest that we should use the Roe-flux as an entropy consistent flux function across a shock in Euler equations as well. However, this is not true since we have seen how Roe-flux suffers from shock instability in chapter 2 which is what we are trying to avoid.

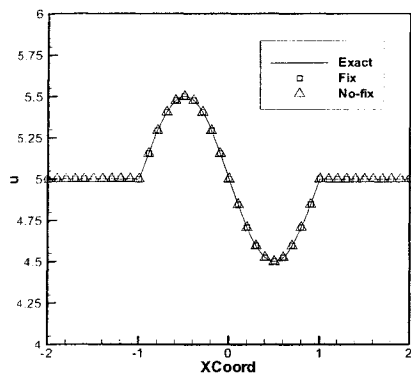
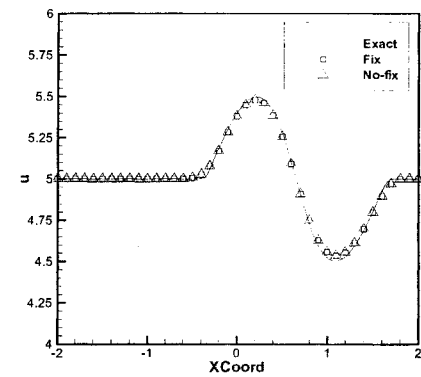
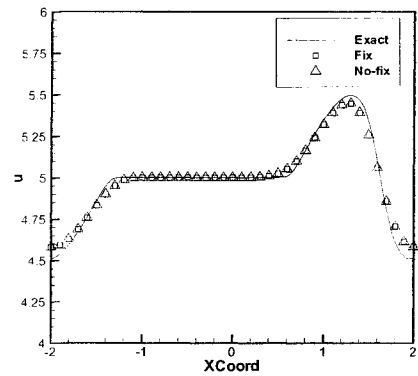
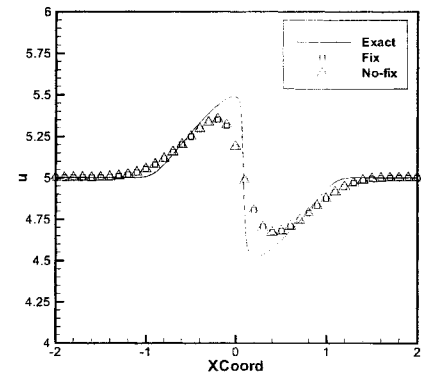
The final flux formula we choose to work with for Burgers equation is

$$f^* = \frac{1}{6}(u_L^2 + u_L u_R + u_R^2) - \frac{1}{4}|u_L + u_R|(u_R - u_L) - \frac{1}{12}|u_R - u_L|(u_R - u_L) \quad (5.44)$$

where the first term conserves entropy. The second terms is the upwinding required for linear stability, and produces entropy at a rate proportional to h^2 . The third term produces entropy at a rate proportional to h^3 . It removes spurious oscillations from captured shocks, and smoothes out under-resolved rarefactions.

We have said and shown enough on the principles of entropy conservation, stability and consistency for Burgers equation. Now we shall begin our journey of doing the same in the context of the Euler equations.

Figure 5.34: Test 4- $u_0 = 1.0$ at $T=0$ Figure 5.35: Test 4- $u_0 = 1.0$ at $T=4$ Figure 5.36: Test 4- $u_0 = 1.0$ at $T=9$.Figure 5.37: Test 4- $u_0 = 1.0$ at $T=20$.

Figure 5.38: Test 4- $u_0 = 5.0$ at $T=0$ Figure 5.39: Test 4- $u_0 = 5.0$ at $T=8$ Figure 5.40: Test 4- $u_0 = 5.0$ at $T=20$.Figure 5.41: Test 4- $u_0 = 5.0$ at $T=50$.

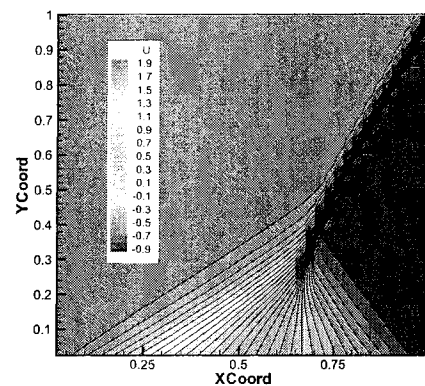


Figure 5.42: Test 5-Results for 1st order Roe and EC1-R (with entropy fix) fluxes.

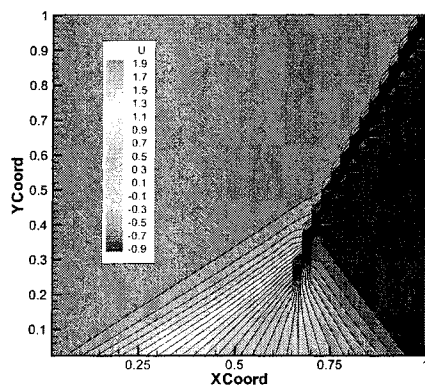


Figure 5.43: Test 5-EC1-R flux (no entropy fix) solution. Not much difference with the above contour plots.

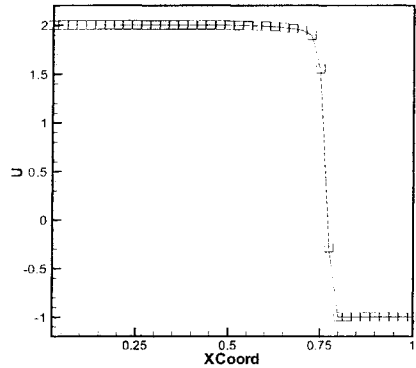


Figure 5.44: The cross sectional cut for Roe and EC1-R (fix) fluxes across the shock.

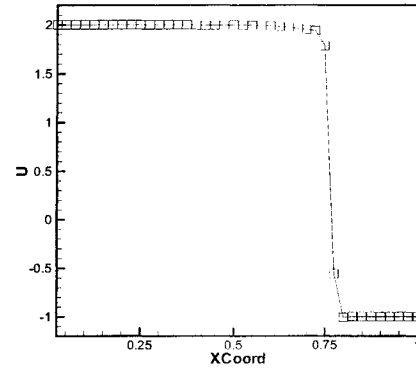


Figure 5.45: The EC1-R (no fix) flux across the shock. The solution is not monotone.

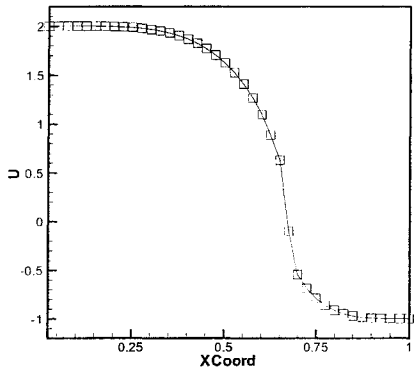


Figure 5.46: The cross sectional cut for Roe and EC1-R (fix) fluxes across the compression waves.

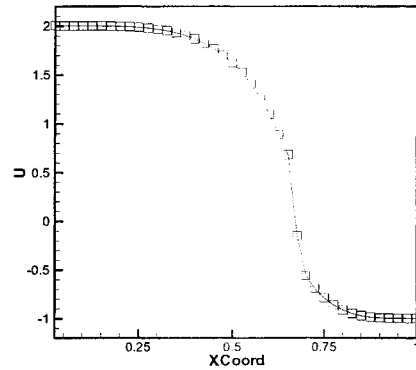


Figure 5.47: The EC1-R (no fix) flux across the compression waves.

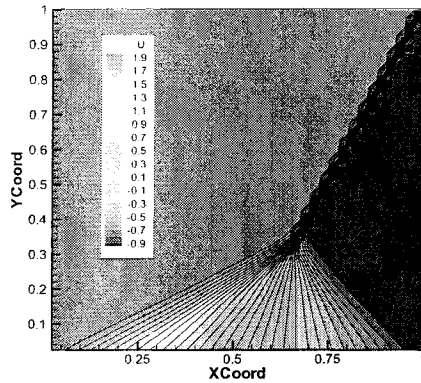


Figure 5.48: The second order EC-R (fix) flux with the Superbee limiter.

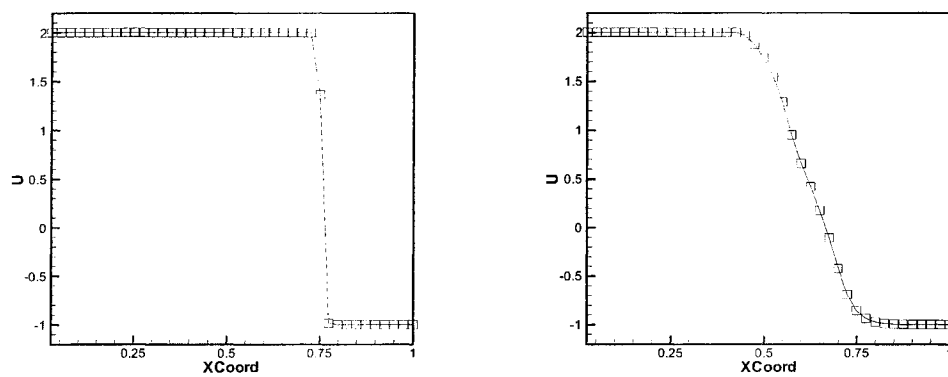


Figure 5.49: The cross sectional cut across the shock for the EC-R (fix) with Superbee.

Figure 5.50: The cross sectional cut across the compression wave for the EC-R (fix) with Superbee.

CHAPTER VI

ENTROPY CONSERVATION IN EULER EQUATIONS

In the context of the system of Euler equations, the entropy conservation law is a direct representation of the second law of thermodynamics. For inviscid flow, this law states that entropy should be conserved unless a shock is encountered. However, this law is not directly enforced in current compressible flow codes. These codes solve for conservation mass, momentum and energy with the assumption that entropy is conserved along the streamlines of inviscid flow until shocks appear. But nonetheless, without a precise mechanism to discretely control entropy, it is likely that spurious entropy is generated. This is somewhat accepted in practice and usually a good Euler code is the one that produces minimal spurious entropy [84].

The only form of entropy control enforced in practice is in the form of entropy condition used to recognize and keep physical shocks while destabilizing rarefaction shocks¹. This led to the developments of the entropy conditions which were discussed in chapter 2.

Nonetheless, in the same chapter we have pointed out that the commonly used entropy condition is imprecise and most likely to be the source of one dimensional

¹To destabilize rarefactions, usually artificial dissipation is added but in an imprecise manner.

shock instability. The most common fix to this is to add artificial dissipation in an ad hoc manner.

We strive to offer a better deal. Since we strongly suspect that imprecise entropy control is the root of the one dimensional shock instability, perhaps including the entropy conservation law more directly to the flux function is the way to prevent shock instability or at a larger scale, the carbuncle phenomenon.

Tadmor [95], [96] was the first to introduce the idea of directly including entropy conservation law solving for the system of Euler equations at a semi-discrete level. The underlying principle is that the discrete flux function not only satisfies discrete conservation laws of the conservative variables, but also satisfies the scalar conservation law for entropy in a discrete sense. Tadmor's flux function performs well for smooth data but will be unstable as soon as a shock is encountered². Moreover, the flux function is complicated and numerically expensive. Barth [7] derived another semi-discrete entropy conserving flux function which is also numerically expensive. Neither of these fluxes preserves isolated contact discontinuities, which is an important property for boundary layer computation. Tadmor [96] and Lefloch et. al [59] proposed a fully-discrete entropy conserving fluxes although it remains mostly of academic interest because of their extreme complexity and numerical cost. Roe [84] on the other hand, discovered a simple and numerically well-formed entropy conserving flux. This gives us hope in achieving our goal of controlling entropy.

We will first introduce the concept of entropy conservation for Euler equations and define our entropy variables. Next, we will include some numerical flux functions that

²This is expected since entropy is not physically conserved across a shock. Instead we want an entropy conserving scheme to be an entropy-stable or entropy consistent scheme across a shock so that entropy is appropriately produced.

conserve entropy and discussing briefly the features of each flux function. We will also introduce the concept of entropy stability and consistency for the Euler equations and how to numerically achieve them. Note that in this chapter, we will follow closely the work of Roe [84] but at the same time will add our own contributions specifically by presenting explicit averaged states for the dissipative flux and an entropy fix to achieve entropy consistency. Our analysis will be presented mostly in one dimension but the results can be extended straightforwardly to multi dimensions.

6.1 One Dimensional Entropy Conservation For Euler Equations

The system of hyperbolic conservation law in one dimension is given by

$$\partial_t \mathbf{u} + \partial_x \mathbf{f}(\mathbf{u}) = 0 \quad (6.1)$$

Our focus will be the Euler equations where mass, momentum and energy are conserved and written together with the conservative fluxes as

$$\mathbf{u} = [\rho, \rho u, \rho E]^T \quad (6.2)$$

$$\mathbf{f}(\mathbf{u}) = [\rho u, \rho u^2 + p, \rho u H]^T \quad (6.3)$$

The total energy is defined as $E = e + \frac{u^2}{2}$ and the total enthalpy $H = E + \frac{p}{\rho}$. The pressure is determined from the equation of state, $e = \frac{p(\gamma-1)}{\rho}$ which is assumed to be with an ideal gas constant γ . This system of equations is also known as the ideal-gas Euler equations.

For this set of equations, the entropy $S = \ln p - \gamma \ln \rho$ remains constant along the streamline path $\frac{dx}{dt} = u$ until a shock appears. This implies that besides conservation of F.1, we also have

$$\partial_t S + u \partial_x S = 0 \quad (6.4)$$

If we couple this equation with conservation of mass and let $U = \rho S$ and $F = \rho u S$, we have the entropy conservation law

$$\partial_t U + \partial_x F = 0 \quad (6.5)$$

In general, we define $U = -\rho g(S)$ and $F = -\rho u g(S)$ where $g(S)$ is some scalar function such that

$$g' > 0, \quad \frac{g''}{g'} < \frac{1}{\gamma}$$

so that $U = -\rho g(S)$ is a convex function. The negative sign is introduced for a mathematical convenience, specifically in proving stability conditions [84], [96]. Mathematically speaking, a function has to be bounded for it to be stable. For inviscid flow, the physical entropy S is constant for smooth flow but will increase when a shock is encountered. By inserting a negative sign, entropy will decrease across a shock implying that the following inequality

$$\partial_t U + \partial_x F \leq 0 \quad (6.6)$$

is satisfied. *This is the entropy stability condition* and states that the entropy function U is bounded by zero for a closed system³.

It is also important to define the entropy variables \mathbf{v} . These form a vector that provides an alternative description of the flow. Let us define the rate of change of the conservative variables as $\partial_t \mathbf{u}$, so that the rate of change entropy is $\partial_t U = \mathbf{v} \partial_t \mathbf{u}$ where $\mathbf{v} = \frac{\partial U}{\partial \mathbf{u}}$. In other words, the entropy variables are a transformation vector that maps the conservative variables into the entropy variable. It was shown by Harten [46] that this mapping is one-to-one under certain restrictions.

³A closed system is defined as a system where fluid does not enter or leave at the boundaries.

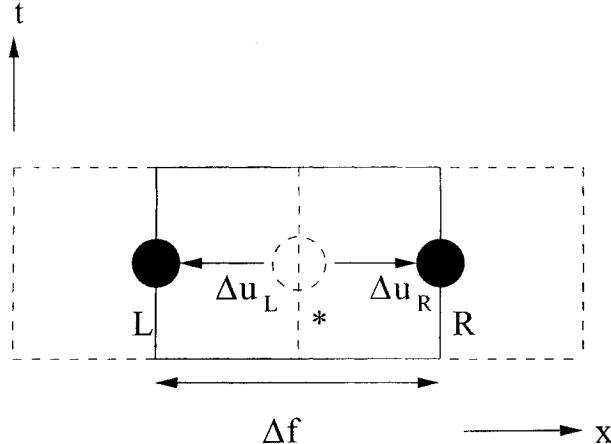


Figure 6.1: Dual interpretations of the updated scheme. The solid line represents residual distribution scheme. The dashed line represent finite volume scheme

There are many forms of entropy variables, \mathbf{v} since it depends on the choice of the entropy variables, U . In this thesis, we choose the physical entropy function, also selected by [7], [84], where

$$U = -\frac{\rho S}{\gamma - 1} \quad (6.7)$$

since it gives a simple form of the entropy variables

$$\mathbf{v} = \frac{\partial U}{\partial \mathbf{u}} = \left[\frac{\gamma - S}{\gamma - 1} - \frac{1}{2} \frac{\rho}{p} (u^2), \frac{\rho u}{p}, -\frac{\rho}{p} \right]^T \quad (6.8)$$

and is the only entropy function that can be used for the Navier-Stokes equations [49]. We are now ready to construct the discrete entropy conserving flux.

6.2 Discrete Entropy Conserving Fluxes For Euler Equations

In this section, we will introduce the concept of discrete entropy conservation and will closely follow the work of Roe [84]. Assume that we have two adjacent states (L, R) with dual cell area (h_L, h_R) , we discretize the Euler equations semi-discretely

as

$$\begin{aligned} h_L \partial_t \mathbf{u}_L &= \mathbf{f}_L - \mathbf{f} \\ h_R \partial_t \mathbf{u}_R &= \mathbf{f}^* - \mathbf{f}_R \end{aligned} \quad (6.9)$$

where $\mathbf{f}^* = \mathbf{f}_{sym}^* - \psi$ is a numerical flux at $*$ decomposed into symmetric and asymmetric parts⁴ yet to be determined. We can interpret the update as either a finite volume or residual distribution scheme as seen in Fig 6.1. The finite volume interpretation is where we have left and right cell-averaged values separated by a common flux interface $*$. In the residual distribution context, the left and right states are point values at vertices that surrounds a linear element centered at $*$. The residual $(\mathbf{f}_L - \mathbf{f}_R)$ is split as $(\mathbf{f}_L - \mathbf{f}^*) + (\mathbf{f}^* - \mathbf{f}_R)$ and distributed to the left and right states respectively.

Recall that $\partial_t U = \mathbf{v} \partial_t \mathbf{u}$, hence a semi-discrete entropy update is

$$\begin{aligned} h_L \partial_t U_L &= \mathbf{v}_L^T (\mathbf{f}_L - \mathbf{f}^*) \\ h_R \partial_t U_R &= \mathbf{v}_R^T (\mathbf{f}^* - \mathbf{f}_R) \end{aligned} \quad (6.10)$$

Assuming $[] = ()_R - ()_L$, the total element update will then be

$$\partial_t (h_L U_L + h_R U_R) = -[\mathbf{v} \cdot \mathbf{f}] + [\mathbf{v}]^T \mathbf{f}^* \quad (6.11)$$

We want the discrete entropy update to satisfy the discrete entropy conservation law.

To achieve this, we need to equate the RHS to their correct values thus select

$$[\mathbf{v} \cdot \mathbf{f}] - [\mathbf{v}]^T \mathbf{f}^* = [F] \quad (6.12)$$

⁴A simple example would be the Lax-Wendroff scheme in which the symmetric part is the pure central scheme and the asymmetric part is the numerical diffusion.

It can be shown by direct computation that

$$\mathbf{v} \cdot \mathbf{f} = \rho u + F \quad (6.13)$$

Combining this result with the linearity of the differencing operator \llbracket , 6.12 becomes

$$[\mathbf{v}]^T \mathbf{f}^* = [\rho u] \quad (6.14)$$

This constraint will be the discrete entropy conserving condition. However, this is a single condition on the vector \mathbf{f}^* so there will be many solutions for the entropy conserving flux \mathbf{f}^* . Let us now briefly introduce some of the entropy conserving fluxes.

6.2.1 Tadmor's Entropy Conserving Flux Function

Before we begin, we need to assert two important properties for an entropy conserving flux. One, it must be numerically consistent, that is $\mathbf{f}^*(\mathbf{u}_L, \mathbf{u}_R) = \mathbf{f}(\mathbf{u}^*)$ as the grid size approaches zero. Two, it has to satisfy 6.14.

Tadmor [95], [96] constructed the entropy flux function by connecting \mathbf{v}_L and \mathbf{v}_R by a straight path in \mathbf{v} space. Assuming this path is represented by ζ , we can compute $\mathbf{v}(\zeta)$ anywhere along this path

$$\mathbf{v}(\zeta) = \zeta \mathbf{v}_R + (1 - \zeta) \mathbf{v}_L \quad (6.15)$$

We then can compute \mathbf{f}^* along the path.

$$\mathbf{f}^* = \int_0^1 \mathbf{f}(\mathbf{v}(\zeta)) d\zeta \quad (6.16)$$

This numerical flux is consistent. To see that this is an entropy conserving flux, multiply the equation by $[\mathbf{v}]^T$ so that

$$[\mathbf{v}]^T \mathbf{f}^* = \int_0^1 [\mathbf{v}]^T \mathbf{f}(\mathbf{v}(\zeta)) d\zeta \quad (6.17)$$

It can be shown that $[\mathbf{v}]^T d\zeta = d\mathbf{v}$ and that $d\mathbf{v}^T \mathbf{f} = d(\rho u)$. Hence

$$[\mathbf{v}]^T \mathbf{f}^* = \int_0^1 d\mathbf{v}^T \mathbf{f} = \int_0^1 d(\rho u) \quad (6.18)$$

which completes the proof. However, it must be noted that the integrals of 6.16 are not in closed form and must be evaluated numerically which makes the flux function expensive.

6.2.2 Barth's Entropy Conserving Flux Function

Barth [7] provided an alternative to solving 6.16 by performing integration by parts.

$$\begin{aligned} \mathbf{f}^* &= [(\zeta - \frac{1}{2})\mathbf{f}(\mathbf{v}(\zeta))]_0^1 - \int_0^1 (\zeta - \frac{1}{2})\partial_\zeta \mathbf{f}(\mathbf{v}(\zeta))d\zeta \\ &= \frac{1}{2}(\mathbf{f}(\mathbf{v}(\zeta)_L) + \mathbf{f}(\mathbf{v}(\zeta)_R)) - \int_0^1 (\zeta - \frac{1}{2})\partial_\zeta \mathbf{f} \partial_\zeta \mathbf{v} d\zeta \\ &= \bar{\mathbf{f}} - \int_0^1 (\zeta - \frac{1}{2})\partial_\zeta \mathbf{f} d\zeta [\mathbf{v}] \\ &= \bar{\mathbf{f}} - \int_0^1 (\zeta - \frac{1}{2})\partial_u \mathbf{f} \partial_v \mathbf{u} d\zeta \end{aligned}$$

Barth showed that there exist scalings such that $\partial_u \mathbf{u} = \mathbf{R} \mathbf{R}^T$ and combined this with the fact that $\frac{\partial \mathbf{f}}{\partial \mathbf{u}} = \mathbf{R} \Lambda \mathbf{L}$ under these scalings, hence

$$\begin{aligned} \mathbf{f}^* &= \bar{\mathbf{f}} - \int_0^1 (\zeta - \frac{1}{2})(\mathbf{R} \Lambda \mathbf{L})(\mathbf{R} \mathbf{R}^T) d\zeta [\mathbf{v}] \\ &= \bar{\mathbf{f}} - \int_0^1 (\zeta - \frac{1}{2}) \mathbf{R} \Lambda \mathbf{R}^T d\zeta [\mathbf{v}] \quad (6.19) \end{aligned}$$

In this form, the fluxes can be constructed either to conserve or produce entropy [7]. However, this is also an expensive method since the integral requires some form of numerical quadrature for the matrix.

We have so far shown two entropy conserving methods of which neither one can be practically implemented for solving engineering problems. It is therefore not surprising that these fluxes and more generally the concept of conserving entropy, were mainly of academic interest. This perception should change since the discovery of the practical entropy conserving fluxes by Roe [84].

6.2.3 Roe's Entropy Conserving Flux Functions

Choose \mathbf{f}^* and such that

$$\mathbf{f}^* = \begin{bmatrix} \rho^* u^* \\ \rho^* u^{*2} + p_1^* \\ \frac{\gamma}{\gamma-1} p_2^* u^* + \frac{1}{2} \rho^* u^{*3} \end{bmatrix} \quad (6.20)$$

Our entropy conservation condition becomes

$$\begin{aligned} [\mathbf{v}]^T \mathbf{f}^* &= -\rho^* u^* \left(\frac{[S]}{\gamma-1} + \left[\frac{\rho u^2}{2p} \right] \right) \\ &\quad + (\rho^* u^{*2} + p_1^*) \left[\frac{\rho u}{p} \right] - \left(\frac{\gamma}{\gamma-1} p_2^* u^* + \frac{1}{2} \rho^* u^{*3} \right) \left[\frac{\rho}{p} \right] \\ &= [\rho u] \end{aligned} \quad (6.21)$$

Choose a parameter vector \mathbf{z} such that

$$z_1 = \sqrt{\frac{\rho}{p}}, \quad z_2 = \sqrt{\frac{\rho}{p}} u, \quad z_3 = \sqrt{\rho p} \quad (6.22)$$

with the identities

$$\begin{aligned} \frac{\rho}{p} &= z_1^2, & \frac{\rho u}{p} &= z_1 z_2 \\ \frac{\rho u^2}{p} &= z_2^2, & \rho u &= z_2 z_3 \\ S &= -(\gamma-1) \ln z_3 - (\gamma+1) \ln z_1 \end{aligned} \quad (6.23)$$

We employ the arithmetic mean (x, y) and the logarithmic mean $L(x, y)$ are defined as

$$(x, y) = \frac{1}{2}(x + y) \quad (6.24)$$

$$\frac{\ln(x) - \ln(y)}{x - y} = \frac{1}{L(x, y)} \quad (6.25)$$

so that we can rewrite

$$[S] = -(\gamma - 1) \frac{[z_3]}{z_3^{\ln}} - (\gamma + 1) \frac{[z_1]}{z_1^{\ln}} \quad (6.26)$$

where $z_{1,3}^{\ln} = L((z_{1,3})_L, (z_{1,3})_R)$ ⁵. Using identity $[ab] = \bar{a}[b] + \bar{b}[a]$, the entropy conserving condition becomes

$$\begin{aligned} & \rho^* u^* \left(\frac{[z_3]}{z_3^{\ln}} + \frac{\gamma + 1}{\gamma - 1} \frac{[z_1]}{z_1^{\ln}} - \bar{z}_2[z_2] \right) + (\rho^* u^{*2} + p_1^*) (\bar{z}_1[z_2] + \bar{z}_2[z_1]) \\ & - \left(\frac{\gamma}{\gamma - 1} p_2^* u^* + \frac{1}{2} \rho^* u^{*3} \right) 2\bar{z}_1[z_1] = \bar{z}_2[z_3] + \bar{z}_3[z_2] \end{aligned} \quad (6.27)$$

Recall that entropy-conserving condition is a single condition on a set of vectors so there will be more than one solution. If we choose

$$u^* = \frac{\bar{z}_2}{z_1} \quad (6.28)$$

and equating the terms $[z_3]$, $[z_2]$ and $[z_1]$ we get

$$\rho^* u^* = \bar{z}_2 z_3^{\ln} \Rightarrow \rho^* = \bar{z}_1 z_3^{\ln} \quad (6.29)$$

$$p_1^* = \frac{\bar{z}_3}{\bar{z}_1} \quad (6.30)$$

$$p_2^* = \frac{\gamma + 1}{2\gamma} \frac{z_3^{\ln}}{z_1^{\ln}} + \frac{\gamma - 1}{2\gamma} \frac{\bar{z}_3}{\bar{z}_1} \quad (6.31)$$

⁵The algorithm for computing logarithmic mean is included in appendix E.

Hence our entropy conserving interface fluxes are

$$\mathbf{f}^* = \begin{bmatrix} z_2 z_3^{ln} \\ \frac{z_3}{z_1} + u^* f_1 \\ \frac{u^*}{2} \left(\frac{\gamma+1}{\gamma-1} \frac{z_3^{ln}}{z_1^{ln}} + f_2 \right) \end{bmatrix} = \mathbf{f}_C \quad (6.32)$$

where an efficient computation of the logarithmic mean can be found in appendix E. These entropy conserving fluxes are not numerically expensive and are well-formed. We will only use this entropy conserving fluxes throughout the remainder of this thesis.

Of course, just as for Burgers equation, entropy is not conserved across a shock. As mentioned before, we need to obtain entropy stability across a shock. To achieve entropy stability, we need to produce proper entropy production which will be a part of the asymmetric dissipative flux. All of these will be the subject of the next section.

6.3 Including Dissipative Flux

Note that the entropy conserving fluxes \mathbf{f}_C in 6.32 are symmetric functions of the left and right input states. These fluxes are similar to central difference schemes and hence are numerically unstable by nature. To stabilize these fluxes, we need to include upwinded dissipative fluxes which are usually asymmetric. Recall that our definition of the numerical fluxes at interface is

$$\mathbf{f}^* = \mathbf{f}_{sym}^* - \psi \quad (6.33)$$

where we have decomposed the flux into its symmetric and asymmetric parts. If we select $\mathbf{f}_{sym}^* = \mathbf{f}_C$ and $\psi = \mathbf{0}$, we will obtain Roe's entropy conserving flux. We want to include an upwinded dissipation in the asymmetric part ψ .

A numerical flux function is usually viewed as a pure central difference scheme

subtracted by some form of numerical dissipation expressed in the form of

$$\mathbf{f}^* = \bar{\mathbf{f}} - \frac{1}{2}\mathbf{D}[\mathbf{u}] \quad (6.34)$$

where $\bar{\mathbf{f}}$ is the arithmetic mean of the left and right states and D is the dissipative matrix. Note that flux functions based on linearized Riemann solvers have the dissipative matrix expressed as $\mathbf{D} = \mathbf{R}|\Lambda|\mathbf{L}$ where \mathbf{R} is the right eigenvector matrix, Λ as the diagonal eigenvalue matrix and \mathbf{L} is the left eigenvector matrix satisfying $\mathbf{LR} = \mathbf{I}$. Usually it is too expensive to obtain the exact value of each component of the matrices so *averaged states* are normally used.

For a system of diagonalizable hyperbolic equations such as the Euler equations, we can write its conservation law of (F.1) in terms of

$$\partial_t \mathbf{u} + \mathbf{A} \partial_{\mathbf{x}} \mathbf{u} = \mathbf{0} \quad (6.35)$$

where the Jacobian matrix is $\mathbf{A} = \frac{\partial \mathbf{f}}{\partial \mathbf{u}} = \mathbf{R} \Lambda \mathbf{L}$ and that the right eigenvectors with their corresponding eigenvalues in diagonal form are given as

$$\mathbf{R} = \begin{bmatrix} 1 & 1 & 1 \\ u-a & u & u+a \\ H-ua & \frac{1}{2}(u^2+v^2) & H+ua \end{bmatrix} \quad (6.36)$$

$$\Lambda = \begin{bmatrix} u-a & 0 & 0 \\ 0 & u & 0 \\ 0 & 0 & u+a \end{bmatrix} \quad (6.37)$$

Note that the left eigenvector is the inverse of the right ($\mathbf{L} = \mathbf{R}^{-1}$).

The linearized Riemann solver based on Roe flux enforces the Rankine-Hugoniot jump relation

$$[\mathbf{f}] = \hat{\mathbf{A}}[\mathbf{u}] \quad (6.38)$$

where $\hat{\mathbf{A}} = \hat{\mathbf{R}}|\hat{\mathbf{A}}|\hat{\mathbf{L}}$ is the averaged state determined such that the flux function recognizes precisely isolated discontinuities of any strength. This is the property that makes the Roe-flux one of the best shock capturing methods. Combining this dissipative flux with the entropy conserving flux, our numerical flux function becomes

$$\mathbf{f}^* = \mathbf{f}_C - \frac{1}{2}\hat{\mathbf{A}}[\mathbf{u}] \quad (6.39)$$

However, we will see in the next section that the Roe dissipative flux is not necessarily ideal especially in the context of achieving entropy stability.

6.3.1 Enforcing Entropy Stability

Recall that entropy stability means that entropy within the system is a decreasing function and satisfies the following inequality.

$$\partial_t U + \partial_x F \leq 0 \quad (6.40)$$

From equation (6.11), the total entropy update within the element (now including an asymmetric part as the dissipation term $\psi = \frac{1}{2}\mathbf{R}|\mathbf{A}|\mathbf{L}[\mathbf{u}]$) is

$$\begin{aligned} \partial_t(h_L U_L + h_R U_R) &= -[\mathbf{v} \cdot \mathbf{f}] + [\mathbf{v}]^T \mathbf{f}^* \\ &= -[\mathbf{v} \cdot \mathbf{f}] + [\mathbf{v}]^T \mathbf{f}_{\text{sym}}^* - [\mathbf{v}]^T \psi \\ \Rightarrow \partial_t(h_L U_L + h_R U_R) + [F] &= -\frac{1}{2}[\mathbf{v}]^T \mathbf{R}|\mathbf{A}|\mathbf{L}[\mathbf{u}] \end{aligned} \quad (6.41)$$

if we select $\mathbf{f}_{\text{sym}}^* = \mathbf{f}_C$ since $[F] = [\mathbf{v} \cdot \mathbf{f}] - [\mathbf{v}]^T \mathbf{f}_{\text{sym}}^*$. To ensure entropy stability, we need the RHS term to be non-positive but this may not be the case thus compromising entropy stability. We will now introduce Roe's entropy stable dissipative flux.

Before we do this, recall that the wave strengths of the Euler equations in one dimension is given by $\mathbf{L}[\mathbf{u}] = [\alpha_1^x, \alpha_2^x, \alpha_3^x]^T$ where the first and last components represent acoustic waves and the second component represents entropy wave which can

be written in differential form as

$$\alpha_1^x = \frac{1}{2} \left(\frac{dp}{a^2} - \frac{\rho du}{a} \right), \quad \alpha_2^x = d\rho - \frac{\rho dp}{a^2}, \quad \alpha_3^x = \frac{1}{2} \left(\frac{dp}{a^2} + \frac{\rho du}{a} \right) \quad (6.42)$$

For *infinitesimal disturbances*, it can be shown by direct computation and also noted by [7] that⁶

$$\mathbf{L}[\mathbf{u}] = \mathbf{S}\mathbf{R}^T[\mathbf{v}] \quad (6.43)$$

where the diagonal scaling matrix is

$$\mathbf{S} = \begin{bmatrix} \frac{\rho}{2\gamma} & 0 & 0 \\ 0 & \frac{(\gamma-1)\rho}{\gamma} & 0 \\ 0 & 0 & \frac{\rho}{2\gamma} \end{bmatrix} \quad (6.44)$$

This was also proven by [84] using Merriam-Barth identity [71] but again only for *infinitesimal disturbances*. Roe proposed the following numerical flux function

$$\mathbf{f}^* = \mathbf{f}_C - \frac{1}{2} \mathbf{R}|\underline{\Lambda}| \mathbf{R}^T[\mathbf{v}] \quad (6.45)$$

where we have included the diagonal scaling matrix within the diagonal wave speeds, $\underline{\Lambda} = \mathbf{S}\Lambda$. Thus the total entropy update within the element is

$$\begin{aligned} \partial_t(h_L U_L + h_R U_R) &= -[\mathbf{v} \cdot \mathbf{f}] + [\mathbf{v}]^T \mathbf{f}^* \\ &= -[F] - \frac{1}{2} [\mathbf{v}]^T \mathbf{R}|\underline{\Lambda}| \mathbf{R}^T[\mathbf{v}] \end{aligned} \quad (6.46)$$

with the dissipative flux satisfying

$$-\frac{1}{2} [\mathbf{v}]^T \mathbf{R}|\underline{\Lambda}| \mathbf{R}^T[\mathbf{v}] \leq 0 \quad (6.47)$$

since the matrix $\mathbf{R}|\underline{\Lambda}| \mathbf{R}^T$ is positive definite. We now have an entropy stable flux function. The next question in mind is how do we determine the averaged states for this new dissipative flux.

⁶The results in three dimensions are included in appendix A

6.3.2 Determining Averaged State

Let $\mathbf{D} = \mathbf{R}|\underline{\Delta}|\mathbf{R}^T$ be the new dissipative matrix. We want to know what are the properties of the new dissipative flux. We know that $\mathbf{D}[\mathbf{v}]$ is an entropy stable dissipative flux. Also, it is easy to show that the dissipative matrix is consistent, i.e.

$$\mathbf{D}^*(\mathbf{v}, \mathbf{v}) = \mathbf{D}(\mathbf{v}^*) \quad (6.48)$$

Recall that the original Roe-flux dissipation is based on the Rankine-Hugoniot jump condition such that

$$[f] = \hat{\mathbf{A}}[\mathbf{u}] = \mathbf{R}|\underline{\Delta}|\mathbf{L}[\mathbf{u}] \quad (6.49)$$

which gives crisp capturing of discontinuities of any strength. For finite disturbances, Roe's new dissipative flux (also observed by Barth [6])

$$\mathbf{R}|\underline{\Delta}|\mathbf{R}^T[\mathbf{v}] \neq \mathbf{R}|\underline{\Delta}|\mathbf{L}[\mathbf{u}] \quad (6.50)$$

which implies that we have compromised the quality of capturing discontinuities for entropy stability. Moreover, it is not clear what is the precise physical meaning of $\mathbf{D}[\mathbf{v}]$. As a result, it is difficult to determine the averaged states of \mathbf{D} because at the moment, we are unclear on what general principle should $\hat{\mathbf{D}}$ be constructed.

However, Roe discovered that some averaging conditions need to be met in order to preserve stationary contact discontinuities [84]. The idea is to conserve entropy across contact discontinuities which requires two things. One, the density has to be averaged using a logarithmic mean $\hat{\rho} = \rho^{ln}$. Two, the averaged speed of sound must be computed from $\hat{a} = (\frac{\gamma \hat{\rho}}{\hat{\rho}})^{\frac{1}{2}}$. Unfortunately, we are still left to wonder how to average the velocities and pressure, specifically on what physical constraints should the two be averaged.

Until we shed more light to the current situation, we have determined the averaged dissipative matrix $\hat{\mathbf{D}}$ strongly based on numerical cost which satisfies the averaging constraints given by [84]. For computational economy, we propose the following averaged states for \mathbf{D} .

$$\hat{\rho} = \bar{z}_1 z_3^{ln} \quad (6.51)$$

$$\hat{u} = \frac{\bar{z}_2}{\bar{z}_1} \quad (6.52)$$

$$\hat{p} = \frac{\bar{z}_3}{\bar{z}_1} = \hat{p}_1 \quad (6.53)$$

$$\hat{a} = \left(\frac{\gamma \hat{p}}{\hat{\rho}} \right)^{\frac{1}{2}} \quad (6.54)$$

$$\hat{H} = \frac{1}{2}(\hat{u}^2) + \frac{\gamma}{\gamma - 1} \frac{\hat{p}_2}{\hat{\rho}} \quad (6.55)$$

where

$$z_1 = \sqrt{\frac{\rho}{p}}, \quad z_2 = \sqrt{\frac{\rho}{p}} u, \quad z_3 = \sqrt{\rho p} \quad (6.56)$$

with $\bar{\cdot}$ and ln being the arithmetic and logarithmic means defined earlier. We choose simply to employ the average states already used to compute \mathbf{f}_C .

6.3.3 Enforcing Entropy Consistency

As mentioned before in the previous chapter, producing too much entropy would lead to diffused shock profiles⁷. On the other hand, insufficient entropy production across shocks would yield spurious oscillations or sometimes, unstable solutions. The goal is to strike a balance between the two extremes and in the context of Euler equations, this is not straightforward.

We have learned that to achieve entropy consistency in the Burgers equation, we need to resolve to the original Roe-flux across a shock to obtain crisp and monotone

⁷An example of would be the Lax-Friedrich scheme

shock profiles. Unfortunately, we have seen that in chapter 2 that the original Roe-flux may not produce a genuine entropy-consistent solution when solving the Euler equations. Consider the one dimensional stationary shock with one intermediate cell within the shock⁸. In some circumstances (see section 2.3), when the intermediate state is perturbed, the original Roe-flux maintained sharp and monotone steady shock profiles. For these cases, this implies that the original Roe-flux produced just enough entropy production to achieve stability but not enough to smear the shock hence the term *entropy consistency* is appropriate here. However, in other circumstances, when the intermediate state is perturbed, the Roe-flux produces solutions which never converge due, even though the perturbed cell values are bounded by the left and right states. In multi dimensions, this instability leads to the carbuncle. This suggests that it may not be a good idea to use the original Roe-flux when capturing shocks in the Euler equations because it captures the shock more sharply than actually desired. Therefore, we have to come up with something better.

We have also learned from the Burgers equation that one way to achieve entropy consistency across a shock is to include a small dissipation to the numerical wave speeds. In the context of Burgers equation, by selecting the proper multiplication factor to this small dissipation, we obtained just enough entropy production so that the entropy stable flux function becomes the original Roe-flux across a shock. However, we can select another multiplication factor such that the entropy stable flux achieve monotonicity but at a less sharply captured shock than those produced with the original Roe-flux. This maybe the price that we have to pay in order to achieve

⁸This is a standard feature of the original Roe-flux capturing a discontinuity such as the shock with one intermediate cell. A slight perturbation to the values of this cell may result in shock instability and sometimes all it takes is just round off errors.

entropy consistency without suffering from any shock instability.

It must be emphasized that this entropy fix is only applied to the acoustic waves. This implies that the quality of the entropy wave which propagate contact discontinuities and in multi dimensions, shear waves which are important in boundary layers, are not compromised. Also, note that this dissipation is not used to stabilize shock instability but is utilized to ensure monotonicity. We present an entropy fix based on the change of *acoustic wave-speeds* across the interface. Our experience from the Burgers equation indicate that there is a greater need for entropy fix when dealing with stationary shocks. Hence we will develop the entropy fix for the Euler equations based on stationary shock formulation and hope that the formulation will still be accurate for moving shocks. We want the fix to be simple yet effective.

Our entropy-consistent-upwinded interface-flux is⁹

$$\mathbf{f}_I = \mathbf{f}_C - \frac{1}{2} \hat{\mathbf{R}} |\hat{\Lambda}_{\text{fix}}| \hat{\mathbf{S}} \hat{\mathbf{R}}^T [\mathbf{v}] \quad (6.57)$$

where $\hat{\mathbf{S}}$ is a diagonal scaling matrix to ensure $\hat{\mathbf{L}}[\mathbf{u}] = \hat{\mathbf{S}} \hat{\mathbf{R}}^T [\mathbf{v}]$ and $\hat{\cdot}$ is the averaged value at the cell interface.

We will only modify the averaged acoustic wave-speeds $\hat{\lambda}_1 = \hat{u} - \hat{a}$, $\hat{\lambda}_3 = \hat{u} + \hat{a}$ either individually or both depending on the change in the wave speeds across the cell interface. We propose the following entropy-fix¹⁰:

$$|\hat{\Lambda}_{\text{fix}}| = \begin{bmatrix} |\hat{\lambda}_1| + \alpha ||\hat{\lambda}_1|| & 0 & 0 \\ 0 & |\hat{\lambda}_2| & 0 \\ 0 & 0 & |\hat{\lambda}_3| + \alpha ||\hat{\lambda}_3|| \end{bmatrix} \quad (6.58)$$

⁹Note the square parenthesis denote the finite difference operator $[a] = \Delta a = a_R - a_L$.

¹⁰It can be shown in appendix F that our entropy fix always produces the correct sign of entropy for either compressive or expansive region if $\alpha \geq 0$.

where $\alpha = 0.2$ determined by numerical experiments which compares with the value $\alpha = 0.167$ obtained by simple theory for Burgers equation. Higher α means more dissipation to ensure monotonicity however, we have found that the choice of $\alpha = 0.2$ works well for almost all the cases that we have tested.

Note that the fix is also applied not only to compression or shock waves but also to rarefaction waves. However, we expect that the magnitude of the fix to be *proportional* to the difference between the left and right states of a cell and entropy is produced at a rate of only $O(h^3)$. This implies that for smooth data like the rarefaction region, the effects of the fix will be small, hence entropy will still be mostly conserved.

From the results of Burgers equation, even without entropy fix, the entropy conserving flux captures a rarefaction as an expansive region although first order solutions are not quite smooth. We expect the trend would be the same for the Euler equations and by either including the entropy fix and/or by using a second order method, we hope that we get a smoother profile when capturing rarefactions.

6.4 Extension to More Dimensions

For a finite volume method, all the analysis presented thus far carries over straightforwardly to any number of dimensions as long as the interface-flux is computed via a pairwise (normal) interaction of adjacent cells.

Define two adjacent cells, L and R with volume V_L and V_R as shown in Fig. 6.2. Let \vec{n}_{LR} be define as the normal direction along a common interface * pointing from

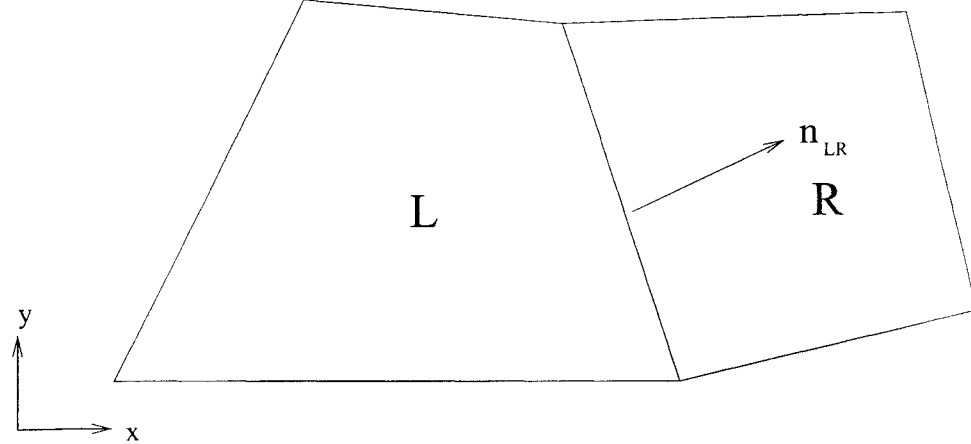


Figure 6.2: Two adjacent cells separated by a common interface with normal direction \vec{n}_{LR} .

L to R . Consider the same semi-discrete update for conservative variables

$$\begin{aligned} V_L \partial_t \mathbf{u}_L &= ((\mathbf{f}_L, \mathbf{g}_L, \mathbf{h}_L) - (\mathbf{f}^*, \mathbf{g}^*, \mathbf{h}^*)) \cdot \vec{n}_{LR} \\ V_R \partial_t \mathbf{u}_R &= ((\mathbf{f}^*, \mathbf{g}^*, \mathbf{h}^*) - (\mathbf{f}_R, \mathbf{g}_L, \mathbf{h}_L)) \cdot \vec{n}_{LR} \end{aligned} \quad (6.59)$$

In terms of entropy variables, this is

$$\begin{aligned} V_L \partial_t U_L &= \mathbf{v}_L^T ((\mathbf{f}_L, \mathbf{g}_L, \mathbf{h}_L) - (\mathbf{f}^*, \mathbf{g}^*, \mathbf{h}^*)) \cdot \vec{n}_{LR} \\ V_R \partial_t U_R &= \mathbf{v}_R^T ((\mathbf{f}^*, \mathbf{g}^*, \mathbf{h}^*) - (\mathbf{f}_R, \mathbf{g}_L, \mathbf{h}_L)) \cdot \vec{n}_{LR} \end{aligned} \quad (6.60)$$

The total change of entropy at the interface would be

$$\begin{aligned} V_L \partial_t U_L + V_R \partial_t U_R &= \mathbf{v}_L^T ((\mathbf{f}_L, \mathbf{g}_L, \mathbf{h}_L) - (\mathbf{f}^*, \mathbf{g}^*, \mathbf{h}^*)) \cdot \vec{n}_{LR} \\ &\quad + \mathbf{v}_R^T ((\mathbf{f}^*, \mathbf{g}^*, \mathbf{h}^*) - (\mathbf{f}_R, \mathbf{g}_L, \mathbf{h}_L)) \cdot \vec{n}_{LR} \\ &= -[\mathbf{v}]^T (\mathbf{f}^*, \mathbf{g}^*, \mathbf{h}^*) \cdot \vec{n}_{LR} + \mathbf{v}^T (\mathbf{f}, \mathbf{g}, \mathbf{h}) \cdot \vec{n}_{LR} \end{aligned}$$

Using the result of 6.13, it can be shown that

$$\begin{aligned} V_L \partial_t U_L + V_R \partial_t U_R &= -[\mathbf{v}]^T (\mathbf{f}^*, \mathbf{g}^*, \mathbf{h}^*) \cdot \vec{n}_{LR} + [\rho(u, v, w) \cdot \vec{n}_{LR}] + [(F, G, H) \cdot \vec{n}_{LR}] \\ & \quad (6.61) \end{aligned}$$

We want the RHS to be equal to the discrete entropy fluxes hence

$$[\mathbf{v}]^T(\mathbf{f}^*, \mathbf{g}^*, \mathbf{h}^*) \cdot \vec{n}_{LR} = [\rho(u, v, w) \cdot \vec{n}_{LR}] \quad (6.62)$$

or in another form

$$[\mathbf{v}]^T \mathbf{f}_n^* = [\rho u_n] \quad (6.63)$$

This is exactly the one dimensional constraint for entropy conservation but in a more general form. The entropy stable and entropy consistent fluxes are also easily extended to multi dimensions with minimal modifications which is included in the appendix C. However, the extension to a residual distribution scheme in fully multi dimensional form is not so straightforward although a beginning has been made [84].

6.5 One Dimensional Gas Dynamics Problems

We will now test the new flux function with several problems satisfying the one dimensional Euler equations. Recall that our definition of a numerical flux function is

$$\mathbf{f}^* = \mathbf{f}_{sym}^* - \psi \quad (6.64)$$

where we have decomposed the interface flux into its symmetric and asymmetric parts. From now on, we will refer to a numerical flux function by a short hand notation combining various options of the two parts. For example, A-R flux refers to the arithmetic mean for the symmetric part with the original Roe-dissipation for the asymmetric portion. Roe's entropy stable flux with Roe-averaging will be referred to as EC1-RV1 whereas EC1-RV2 is the same flux function with the newly proposed set of averaging. Note that it is also possible to have the new symmetric flux with the old asymmetric flux and vice-versa.

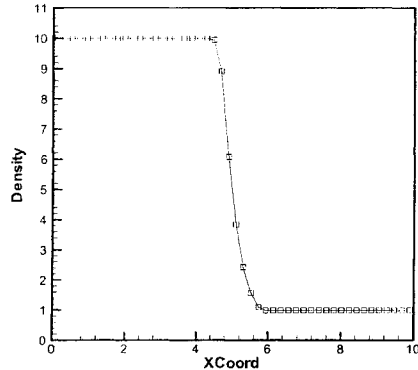


Figure 6.3: EC1-RV1 scheme (Roe averaging) at $T=1000$.

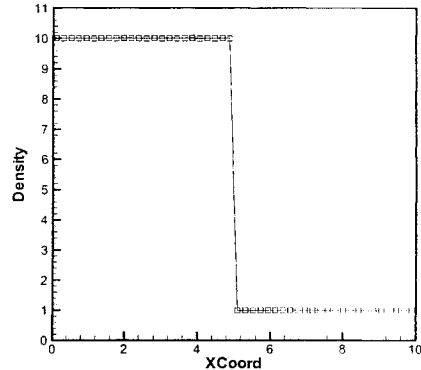


Figure 6.4: A-R and EC1-RV2 schemes at $T=1000$.

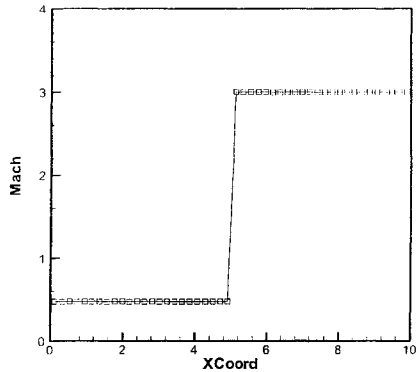
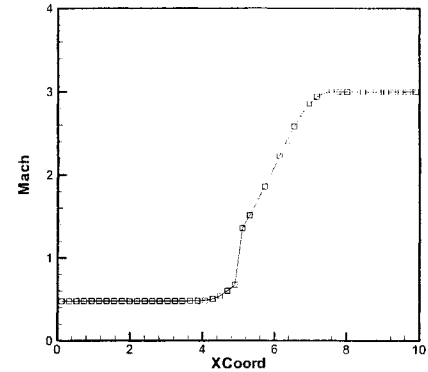
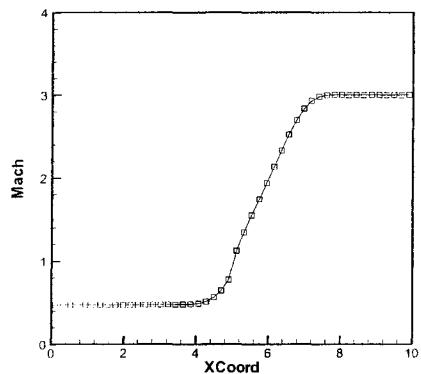
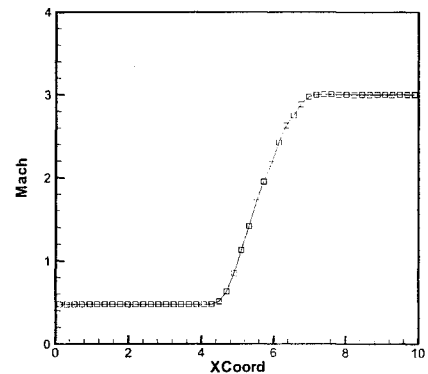
Note that our new flux formulation is only based on a *semi-discrete analysis* which means that strictly speaking, the flux function is stable only for very small Courant numbers ($\nu \rightarrow 0$). However, we shall see that for most cases, its solution is stable for $\nu \leq 0.8$ in one dimension and approximately half of that in two dimensions. It is known, [71], [96] that using a semi-discretely entropy conserving flux in an explicit fully discrete scheme results in a reduction of entropy which is destabilizing.

6.5.1 Modelling Stationary Contact Discontinuity

Although we expect this new flux function to prevent carbuncles from happening, it is also important that the flux function keeps most (if not all) of the good properties of current methods. For a start, let us observe if this new flux function is able to preserve a stationary contact discontinuity.

The following initial value problem is prescribed with zero slopes on the inflow and out flow boundaries and 50 computational cells with $\nu = 0.8$.

$$\rho_L = 10, \quad \rho_R = 1, \quad u_L = u_R = 0, \quad p_L = p_R = 1 \quad (6.65)$$

Figure 6.5: A-R scheme at $T=1000$.Figure 6.6: EC1-RV2 at $T=17$.Figure 6.7: EC1-RV2 with entropy fix at $T=17$.Figure 6.8: 2nd Order EC1-RV2 (Harmonic) at $T=17$.

Results are shown in Figs. (6.3-6.4) where clearly, Roe-averaging smears the contact discontinuity unlike the new averaging. This outcome agrees with the predictions from theory mentioned in 6.3.2. From now on, we will only use the newly proposed averaging for the EC1-RV2 flux function.

6.5.2 Omitting Rarefaction Shocks

This a one dimensional problem with an interface separated by a left and right state with M_0 is the upstream Mach number and $\gamma = 1.4$, the normalized upstream (state 0) and downstream (state 1) conditions are given by

$$\begin{aligned}\mathbf{U}_1 &= \left[\begin{array}{ccc} 1 & 1 & \frac{1}{\gamma(\gamma-1)M_0^2} + \frac{1}{2} \end{array} \right] \\ \mathbf{U}_0 &= \left[\begin{array}{ccc} f(M_0) & 1 & \frac{g(M_0)}{\gamma(\gamma-1)M_0^2} + \frac{1}{2f(M_0)} \end{array} \right]\end{aligned}\quad (6.66)$$

where $f(M_0)$ and $g(M_0)$ are the jump conditions of density and pressure across the shock given by

$$\begin{aligned}f(M_0) &= \left(\frac{2}{(\gamma+1)M_0^2} + \frac{\gamma-1}{\gamma+1} \right)^{-1} \\ g(M_0) &= \frac{2\gamma M_0^2}{(\gamma+1)} - \frac{\gamma-1}{\gamma+1}\end{aligned}\quad (6.67)$$

We have selected $\nu = 0.7$ with 50 computational cells and zero slopes at the boundaries. Except for the boundary conditions and having the upstream and downstream conditions flipped over, this is exactly the same initial value problem for the one dimensional carbuncle as described in chapter 2.

As expected, the first order Roe-scheme recognizes this as a rarefaction shock (Fig 6.5) which is totally unphysical. The EC1-RV2 scheme however, sees it as an expansion wave but exhibiting a dogleg pattern (Fig. 6.6). Including the entropy fix seems to smooth out the situation. Although using a second order method may seem to be a bit premature at this stage, nevertheless, we have used the EC1-RV2 flux with the second order Hancock scheme. The second order results also smooth out the dogleg.

The EC1-RV2 flux function is designed to capture only contact discontinuities as a single jump and other type of discontinuities will be smoothed out proportional to

M_0	ν_{max}
≤ 4	0.9
4-6	0.7
6-8	0.5
8-10	0.4
10-16	0.2
16-20	0.1

Table 6.1: Stability limit for various upstream conditions.

the change of the entropy variables. This explains why the rarefaction is diffused but the question remains whether this smoothing process will badly deteriorate shock profiles. We will obtain that information in the next section.

6.5.3 Modelling Stationary Shock

This is similar to the initial value problem introduced in the previous section except that the upstream and downstream conditions are switched. Also, the left boundary is fixed to the upstream Rankine Hugoniot conditions with non reflecting boundary conditions on the right. The initial value problem is run until the solution residual is $O(10^{-13})$. *Note that the A-R scheme would maintain the initial value data for all Mach numbers and so their stationary shock results are omitted¹¹.* We would like to see how the EC1-RV2 would measure up against the A-R scheme. To avoid the solution from blowing out of proportion, the Courant number must be restricted to a smaller value for high upstream Mach number. Although we have not performed any rigorous mathematical proof for stability, Table 6.1 summarizes our findings based on numerical experience in one dimension.

The EC1-RV2 flux produces shock solution with intermediate cells with the number cells being introduced is proportional to the magnitude of the shock. This implies

¹¹For this special case, having this property is desirable but we have seen before this may lead to shock instability.

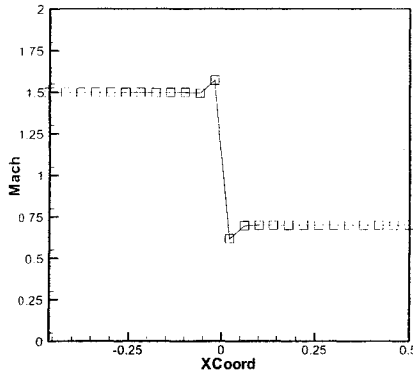


Figure 6.9: EC1-RV2 for $M_0 = 1.5$.
Note there are spurious overshoot and undershoot near the shock.

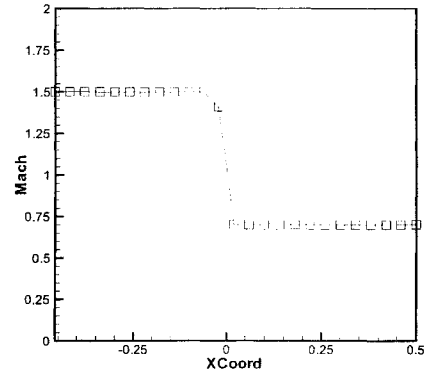


Figure 6.10: EC1-RV2 (with entropy fix) at $M_0 = 1.5$.

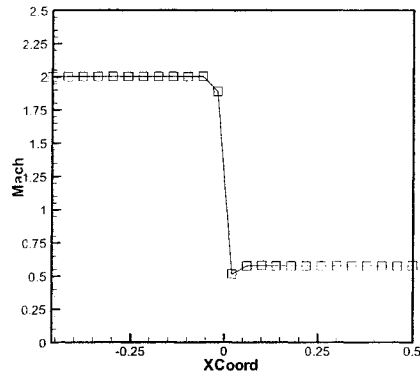


Figure 6.11: EC1-RV2 at $M_0 = 2.0$.

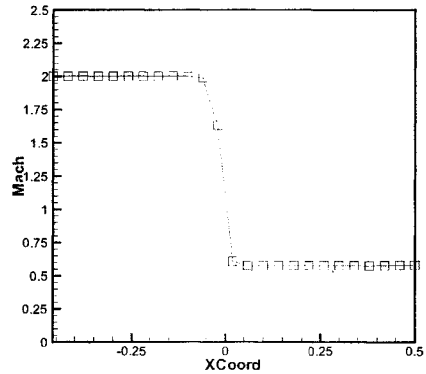
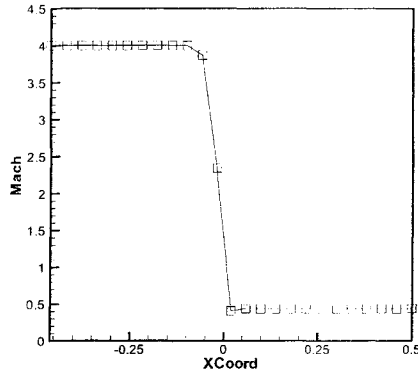
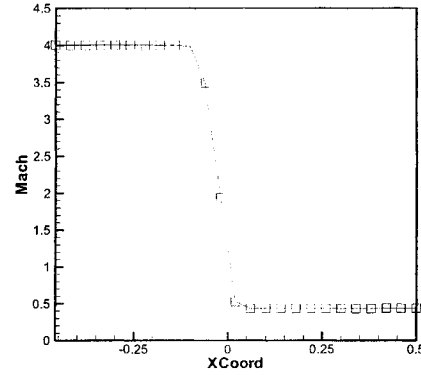
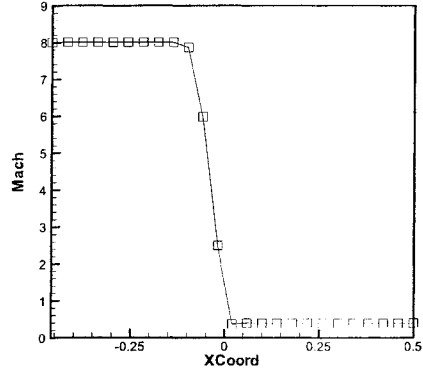
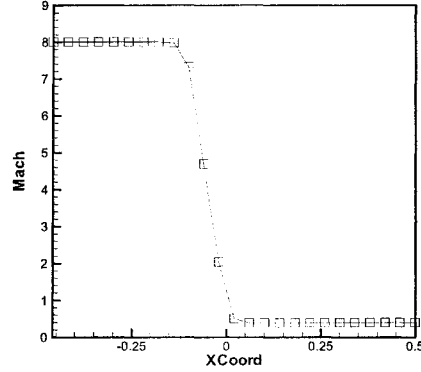


Figure 6.12: EC1-RV2 (with entropy fix) at $M_0 = 2.0$.

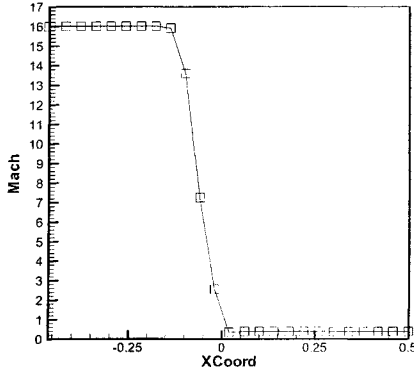
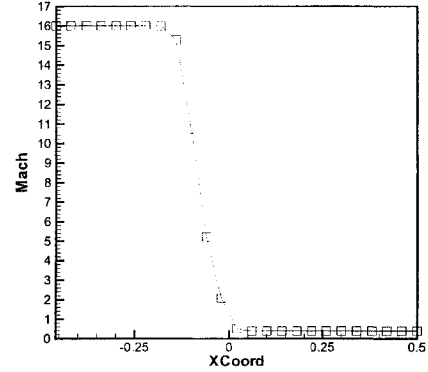
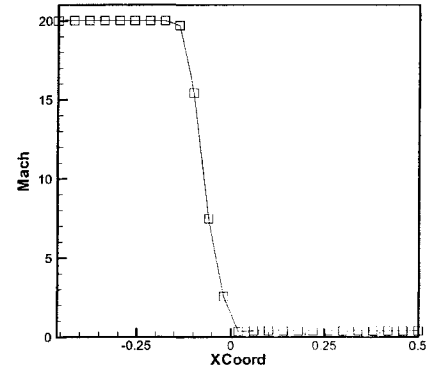
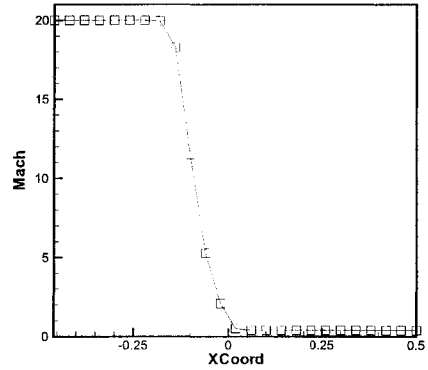
that we would expect more intermediate cells for higher upstream Mach numbers, roughly about 2 cells for $M_0 \leq 8$ and 3 cells for $M_0 \leq 20$. Although we no longer have shock captured as a single jump, however, we also have not completely diffused the shock like we have diffused the rarefaction shocks indicated in the previous section. We will further test the new flux function with some standard benchmark problems

Figure 6.13: EC1-RV2 at $M_0 = 4.0$.Figure 6.14: EC1-RV2 (with entropy fix) at $M_0 = 4.0$.Figure 6.15: EC1-RV2 for $M_0 = 8$. Note there is a small undershoot downstream of the shock.Figure 6.16: EC1-RV2 (with entropy fix) at $M_0 = 8.0$. Shock is slightly smeared.

in one dimensional gas dynamics.

6.5.4 Sod's Shock Tube Problem

We have seen that the EC1-RV2 flux function performs well in capturing rarefactions and stationary (steady state) discontinuities. Now we want to check if the scheme can do the same for unsteady problems which consist of moving discontinu-

Figure 6.17: EC1-RV2 at $M_0 = 16.0$.Figure 6.18: EC1-RV2 (with entropy fix) at $M_0 = 16.0$.Figure 6.19: EC1-RV2 at $M_0 = 20.0$.Figure 6.20: EC1-RV2 (with entropy fix) at $M_0 = 20.0$. The shock is more diffused when compared with no entropy fix. The smearing can be improved using a second order scheme.

ties and rarefactions. We refer to Sod's problem [110] where

$$p_L = 10^5, \quad \rho_L = 1.0, \quad u_L = 0.0 \quad (6.68)$$

$$p_R = 10^4, \quad \rho_R = 0.125, \quad u_R = 0.0 \quad (6.69)$$

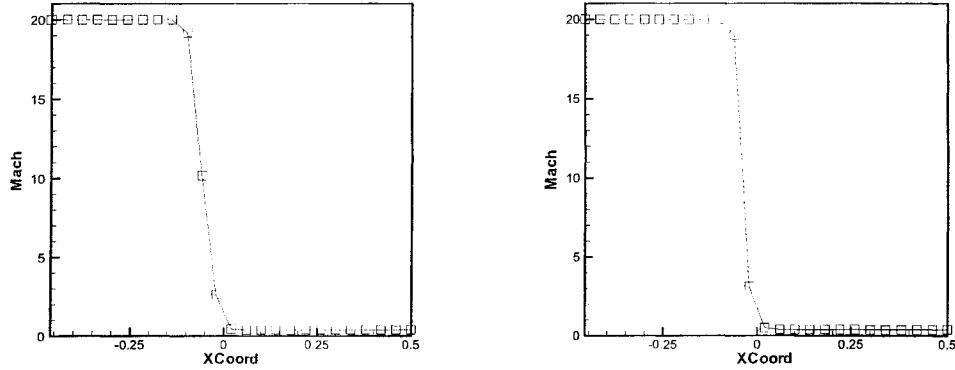


Figure 6.21: Second order EC1-RV2 (fix) at $M_0 = 20.0$ using Minmod limiter.

Figure 6.22: Second order EC1-RV2 (fix) at $M_0 = 20.0$ using Harmonic limiter. The shock profile is much 'tighter'.

utilizing 100 computational cells. We have tested the EC1-RV2 flux (with entropy fix) and their results are almost identical to those produced by the original Roe (A-R) flux Figs. (6.23-6.26). The discontinuity on right represents a moving shock in which the first order EC1-RV2 (fix) flux captures the shock with 3 intermediate cells compared to 2 cells captured via the original Roe-flux. The middle discontinuity represents a moving contact discontinuity which is more difficult to capture. First order results of both A-R and EC1-RV2 fluxes capture the contact discontinuity with 8 intermediate cells. Second order solutions of both fluxes however, capture the contact discontinuity with only 4 intermediate cells. The point here is that, the new EC1-RV2 flux function is able to matched up against the A-R flux which is a Godunov-type flux, and perceived by most in the CFD community as the best numerical discontinuity capturing method [109], [18], [78], [25], [112], [40].

Note that *we have used $\nu = 0.7$ for all cases* which implies that the semi-discrete

formulation goes far beyond what it was expected to do. However, for $\nu > 0.8$, we have spurious overshoots for first order EC1-RV2 flux even with entropy fix. Without entropy fix, the EC1-RV2 flux can only be monotonicity preserving for $\nu \leq 0.6$.

6.5.5 Woodward and Collela's Double Blast Problem

This test case is taken from [114] where we have a shock tube of length one with reflecting walls at $x = 0$ and $x = 1$. The initial values are given as

$$\begin{cases} p = 10^3, \rho = 1.0, u = 0.0 & \text{if } 0 \leq x < 0.1 \\ p = 10^{-2}, \rho = 1.0, u = 0.0 & \text{if } 0.1 \leq x < 0.9 \\ p = 10^2, \rho = 1.0, u = 0.0 & \text{if } 0.9 \leq x \leq 1.0 \end{cases} \quad (6.70)$$

We have chosen 1200 cells to be consistent with the choice of Woodward and Collela. The exact solutions are computed via a second order Hancock scheme with the Harmonic limiter using 4800 computational cells.

This is a gas dynamic problem where the gases will be compressed by the high pressures at both ends of the tube and then collide with each other. [114] computed this problem with a *third* order scheme but we have only computed the problem with a first order method. Clearly, our numerical results will not be satisfactory compared to the exact or even their third order solutions but again the point is to demonstrate that the EC1-RV2 flux produce results which are almost identical to those produced by the original Roe flux. Figs 6.27-6.30 will justify this.

Overall, from our numerical experiments thus far, we can conclude that by directly including the physics of entropy, we can better predict rarefactions and still able to capture crisp contact discontinuities. However, we have compromised a little bit on capturing shocks due to the inclusion of intermediate states within the shock. This is maybe the price that we have to pay in order to prevent the carbuncle.

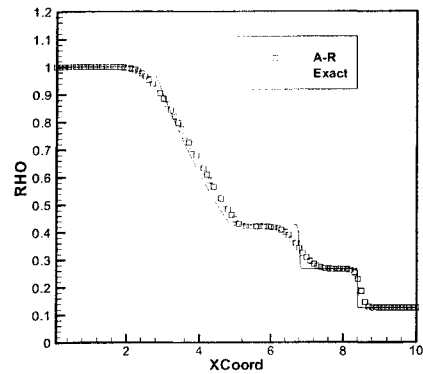


Figure 6.23: Density plot of Sod's problem for A-R flux.

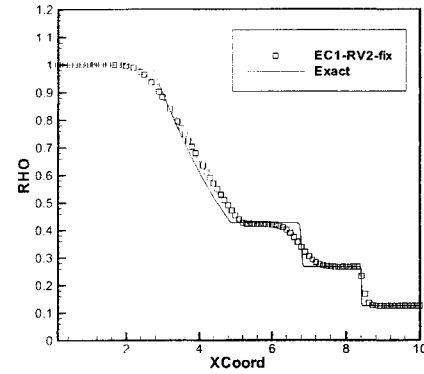


Figure 6.24: EC1-RV2 flux with fix. Note how its solution is comparable to A-R's.

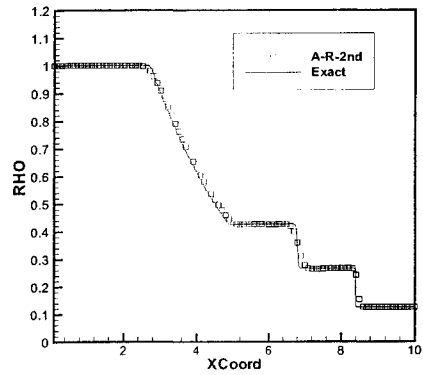


Figure 6.25: Second order A-R flux with harmonic limiter. The contact is now captured with only 4 intermediate cells.

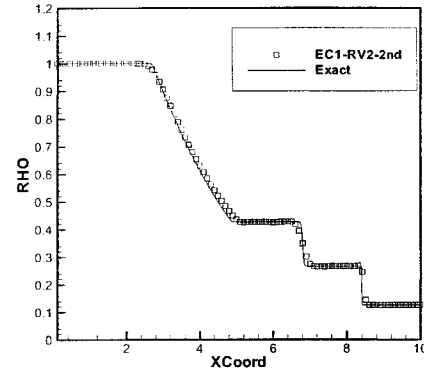


Figure 6.26: Second order EC1-RV2 flux (fix) with harmonic limiter. Almost identical to the second order A-R flux.

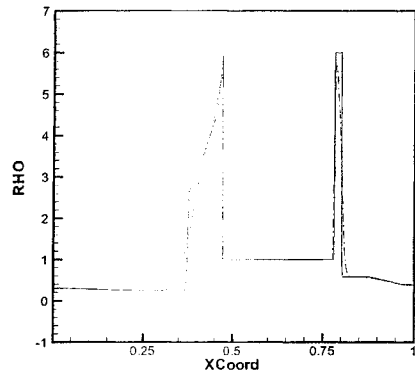


Figure 6.27: Density plot for A-R flux before collision of the waves with solid lines representing exact solution.

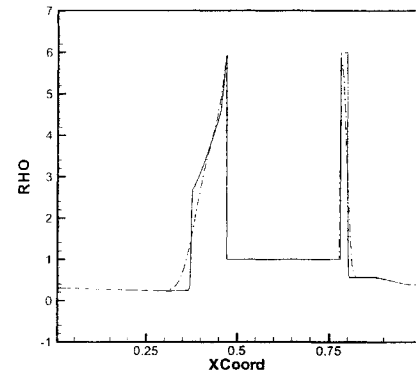


Figure 6.28: Density plot of the EC1-RV2 (fix) before collision of the waves.

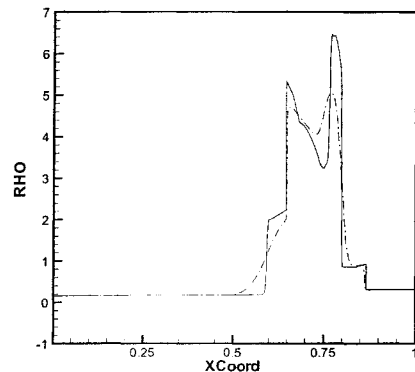


Figure 6.29: Density plot for A-R flux after the collision of the waves.

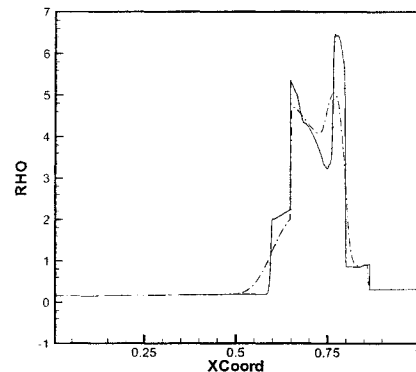


Figure 6.30: EC1-RV2 flux with fix. Although the solution is not as sharp as the exact solution, it is comparable to A-R's..

6.6 A New Method of Controlling the Carbuncle II: Controlling Entropy

We will now attempt to cure the carbuncle phenomenon with the new flux function. Except for the two dimensional carbuncle, the set up and nature of the other carbuncle problems were presented in details in chapter 2 thus we will only focus on the results using the new flux function.

6.6.1 The 1 dimensional carbuncle

From Figs. 6.31-6.36, the EC1-RV2 flux does not suffer from the carbuncle phenomenon for *all* upstream Mach numbers $1.5 \leq M_0 \leq 20.0$, for various specific heat ratios $\gamma = 1.1, 1.2, \dots, 1.4, 1.5, 1.67$ and for all $\epsilon = 0.0, 0.1, \dots, 0.9, 1.0$. The steady-state solutions are stable and converged to residual of $O(10^{-13})$. However, the solutions are not monotone across the shock unless we include the entropy fix. Larger values of α are needed for larger mass flux deviations of the intermediate cell (corresponding to $\epsilon = 0.6, 0.7, 0.8$) . For conciseness, we will only include results of the EC1-RV2 flux without entropy fix for the 1 dimensional carbuncle. The results of EC1-RV2 with entropy fix can be inferred from the one dimensional solutions of the same flux function in the 1 1/2 dimensional carbuncle problem¹².

For brevity, we have only included the results for $M_0 = 8.0$ and $\gamma = 1.4$. For this set of upstream Mach number and specific heat ratio, the maximum mass-flux deviation for the intermediate cell occurs when $\epsilon = 0.7$. From our numerical experience, this maximum mass flux deviation corresponds to the most unstable configuration hence will be chosen as an example to demonstrate the effectiveness

¹²For the same upstream Mach number, sometimes the 1 dimensional carbuncle requires a much higher coefficient for entropy fix (up to $\alpha = 0.6$) when $\epsilon = 0.6, 0.7$.

of the EC1-RV2 flux. Results of the A-R flux are also included for comparison purposes. It must be emphasized that the A-R solution oscillates due to shock instability. Although it is almost impossible to verify this from a still picture but this can be inferred from the log plot of residual (Fig 6.35). Oscillations in the residual corresponds to oscillations occurring within the shock profile. Note that for all cases, we have chosen $\nu = 0.1$ with 25 computational cells.

6.6.2 The 1 1/2 dimensional carbuncle

The EC1-RV2 flux function is also tested with the 1 1/2 dimensional carbuncle. We chose $\nu = 0.1$ use 25×25 computational cells. The carbuncle is seeded with a point perturbation of $O(10^{-14})$. We have tested the scheme for the range of Mach numbers and γ given in the 1 dimensional carbuncle. We found that the EC1-RV2 scheme is also carbuncle-free in 1 1/2 dimensions.

Since 1 1/2 dimensional carbuncle is just stacks of the 1 dimensional carbuncle problem in y-direction, we expect that the cross-sectional solution across any y-plane of the former will be identical to the solution of the later if the prescribed conditions are the same. Hence for brevity, we will not include the cross-sectional solution if it has already been presented in the one dimensional carbuncle. Results of the 1 1/2 dimensional carbuncle are included in Figs. 6.37-6.51.

Note how monotonicity is achieved when the entropy fix of section 6.3.3 is applied. In addition, using a second order limited Hancock scheme with the new flux function give a tighter shock profile. For $M_0 = 20.0$, we are able to capture the shock with only 3 intermediate cells using Minmod limiter (Fig. 6.50) without suffering any shock instability.

Moreover, from this exercise we can conclude that by directly including the en-

tropy conservation law in the numerical flux function, we have not only prevented the generation of spurious vorticity (Fig. 6.51) but more importantly, we have prevented the carbuncle and any other form of shock instability from occurring.

6.6.3 The 2 dimensional carbuncle

This is a steady state numerical simulation of a blunt body subjected to a high Mach number flow in two dimensions. Genuine prediction of the flow requires capturing of a smooth bow shock profile upstream of the body. Unfortunately, most schemes with minimal artificial dissipation¹³ are unable to achieve this [78], [81], [40], [89] because they produce shock anomalies around the stagnation region. This steady state hypersonic blunt body simulation will be the ultimate test for the EC1-RV2 flux function.

We have chosen a cylinder as the blunt body which is subjected to a fixed free-stream Mach number M_0 of diatomic gas $\gamma = 1.4$ or mono atomic gas $\gamma = 1.67$. We will utilize quadrilateral cells with solid wall boundary conditions for the cylinder and on-reflecting for the outflow.

Our numerical experiment is conducted for Mach numbers ranging from $2.0 \leq M_0 \leq 30.0$ and for both mono atomic and diatomic gases. However, we will only include the results for $M_0 = 20.0$ and $\gamma = 1.4$ using first order A-R, EC1-RV2 and EC1-RV2 (fix) flux functions. Note that the iteration is performed until a residual of $O(10^{-12})$ is achieved.

As expected, the A-R flux suffers from the carbuncle phenomenon but *the EC1-RV2 flux does not exhibit any form of shock instability or carbuncle for the range of*

¹³Minimal dissipation in the sense that the scheme can capture crisp shocks and contact discontinuities and preserve boundary layers.

Mach numbers specified above and for either mono atomic or diatomic gases.. The results for $M_0 = 20.0$ with $\gamma = 1.4$ are included in Figs. 6.54,6.66. In addition, the EC1-RV2 flux predicts the stagnation region much more accurately than the A-R flux (Figs 6.67-6.68). However, the EC1-RV2 without entropy fix generate spurious oscillations in its shock profile (Figs 6.57-6.63) but this is easily remedied with the proposed entropy fix (Figs 6.69-6.72). The choice of $\alpha = 0.2$ seems to be sufficient to maintain monotone shock profiles for almost all the cases that we have tested. For most test cases, we have restricted ourselves in using a Courant number $\nu = 0.2$ but for some cases, we were able to achieve stability even up to $\nu \leq 0.8$. To further demonstrate and convince the reader of the capability of the EC1-RV2 flux, we have also included its results for $M_0 = 30.0$ (Figs. 6.73-6.78) in which is still carbuncle-free.

Prediction of Stagnation Conditions at the Body Surface ($y=0$)

From Fig 6.79-6.80, it is clear that the EC1-RV2 (with entropy fix) flux predicts the stagnation pressure and temperature much more accurately than those produced by the AR flux. When it comes to predicting stagnation temperature at the body, the AR flux is off by about 20 percent than the analytical prediction. The prediction of stagnation pressure is even worse for the AR flux, deviating from the analytical solution by an average of 50 percent. However, the EC1-RV2 flux produces at most 2 percent error when predicting either the stagnation pressure or temperatures.

Varying Aspect Ratio of Grid

It is known in the literature that the carbuncle is more prone to occur when the grid is finer along the captured the shock [78], [25]. In two dimensional cylinder problem, this means that we have a finer mesh and hence less damping in the

azimuthal direction. To perform this test, we have chosen a very coarse mesh in the radial direction (20 cells) but with varying mesh size in the azimuthal direction (200,400 and 600 cells). Our computational results indicate that the EC1-RV2 flux (with and without entropy fix) is carbuncle free for all of the grid configurations and for various Mach numbers $2.0 \leq M_0 \leq 20.0$. However, we have only included the results for $M_0 = 20.0$ for brevity (Figs 6.81-6.86). Note that the shock is slightly thicker than those produced with 80×160 cells merely because we have utilized a very coarse mesh in the radial direction.

To conclude, the EC1-RV2 flux is carbuncle-free when tested with the 1, 1 1/2 and 2 dimensional carbuncle problems. However, the EC1-RV2 flux requires the entropy fix proposed in section 6.3.3 to achieve monotone shock profiles. It must be emphasized that when simulating these shocks, for upstream conditions $M_0 \geq 6$, we need to include the physics of chemistry and real gas in order for the numerical simulation to be truly valid. However, we did not do so in this thesis since our goal was to design a carbuncle-free algorithm for pure inviscid hypersonic flow with perfect gas and no chemistry assumptions and we were able to achieve that with the EC1-RV2 flux function. We hope that the success of EC1-RV2 flux will carry over not only to three dimensional viscous computations but also to simulation that includes chemistry and real gas effects¹⁴ and in any arbitrary body or domain configuration. All of these will subjects of future research.

¹⁴Since the carbuncle phenomenon is independent of the real gas and chemistry effects [40].

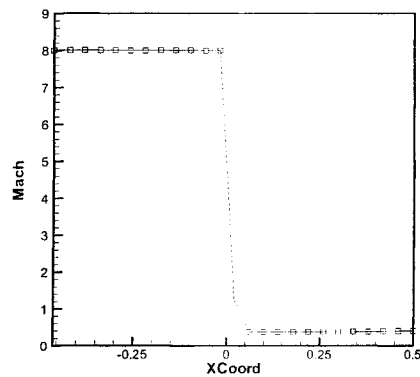


Figure 6.31: Mach profile of 1D car-bunble using A-R flux at $T=10000$.

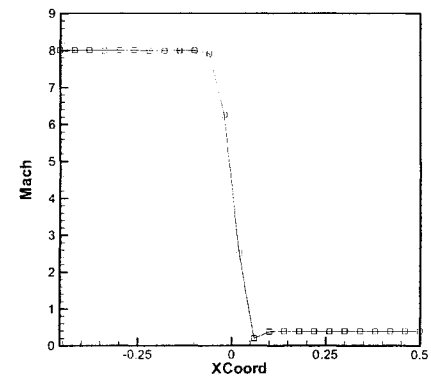


Figure 6.32: Mach profile of EC1-RV2 flux at $T=10000$.

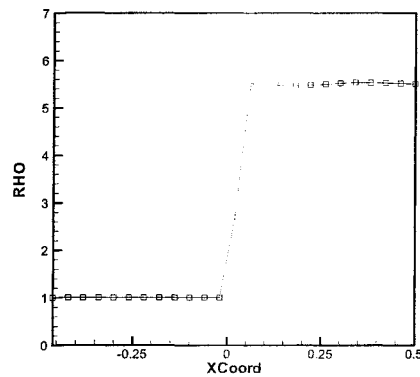


Figure 6.33: Density profile of A-R flux at $T=10000$.

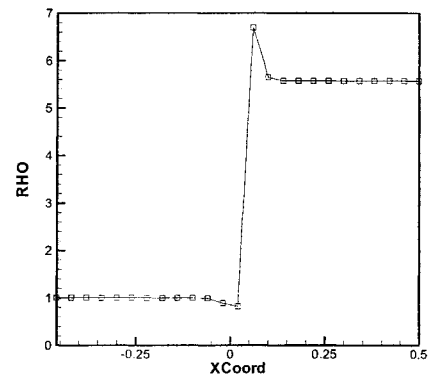


Figure 6.34: Density profile of EC1-RV2 flux at $T=10000$.

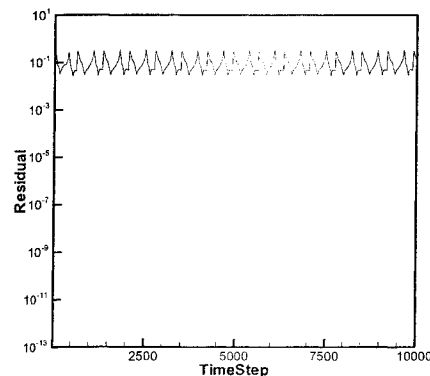


Figure 6.35: Residual plot of A-R flux.

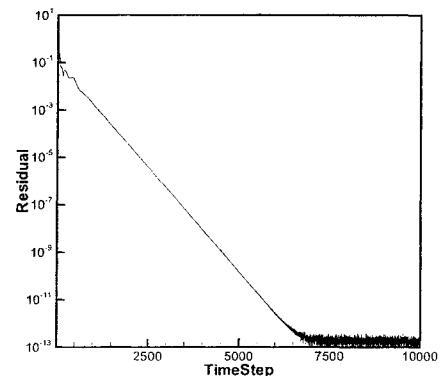


Figure 6.36: Residual plot of EC1-RV2.

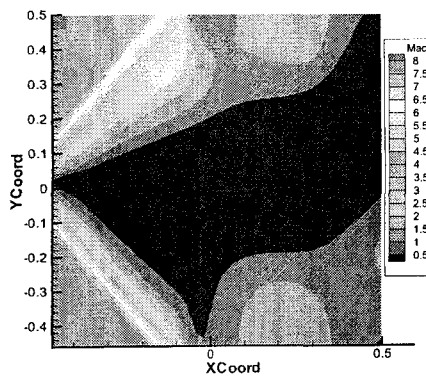


Figure 6.37: A-R flux Mach contours of the 1 1/2 dimensional carbuncle ($M_0 = 8.0$) at $T=10000$.

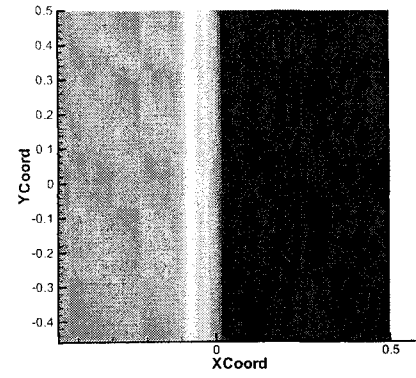


Figure 6.38: EC1-RV2 flux Mach contours at $M_0 = 8.0$. Note the cross-sectional solution are identical to Fig. 6.32.

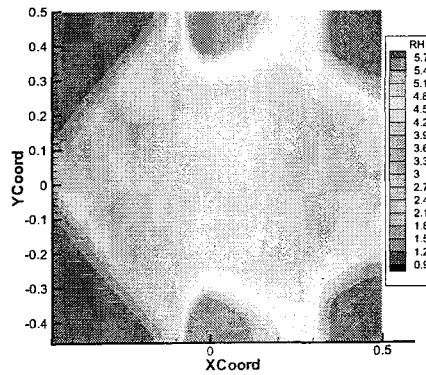


Figure 6.39: A-R flux density contours at $T=10000$ with $M_0 = 8.0$.

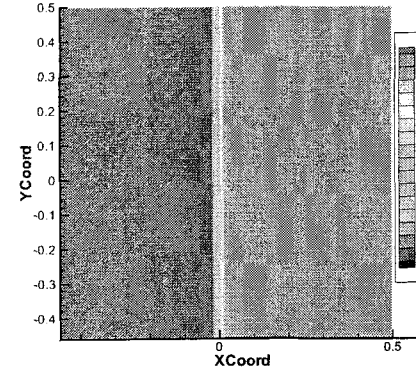


Figure 6.40: EC1-RV2 flux density contours with $M_0 = 8.0$.

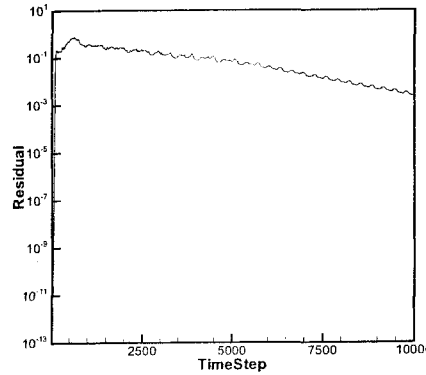


Figure 6.41: Residual plot of A-R flux.

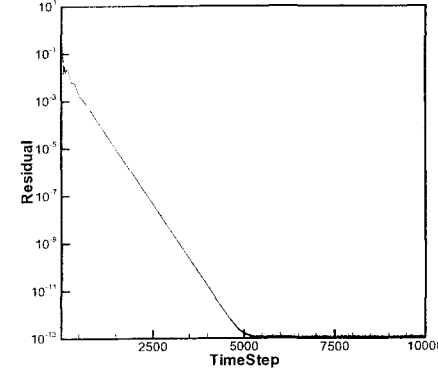


Figure 6.42: Residual plot of EC1-RV2.

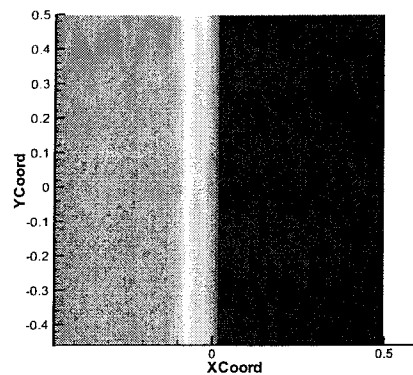


Figure 6.43: EC1-RV2 flux with entropy fix Mach contours with $M_0 = 8.0$.

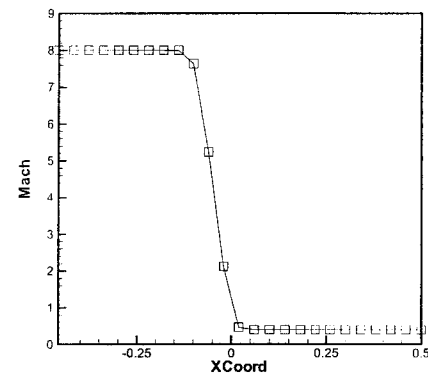


Figure 6.44: The cross-sectional solution of EC1-RV2 (fix) flux in which monotonicity is achieved.

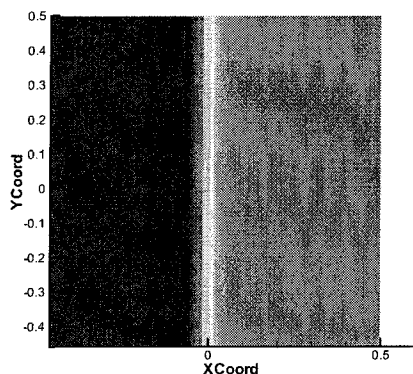


Figure 6.45: Density contours of the EC1-RV2 flux with entropy fix.

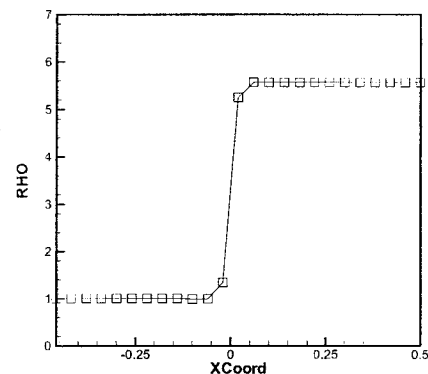


Figure 6.46: The cross-sectional density solution of EC1-RV2 (fix).

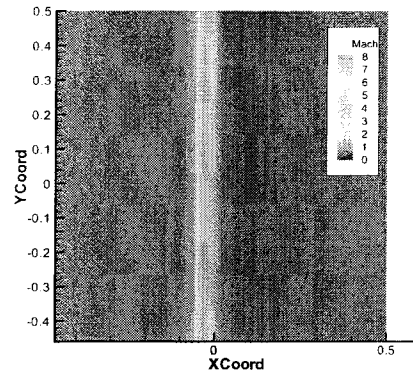


Figure 6.47: 2nd order EC1-RV2 (fix) with Minmod at $M_0 = 8.0$.

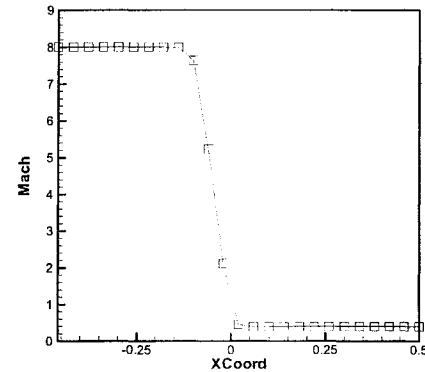


Figure 6.48: The cross-sectional solution of 2nd order EC1-RV2 (fix) having a tighter shock.

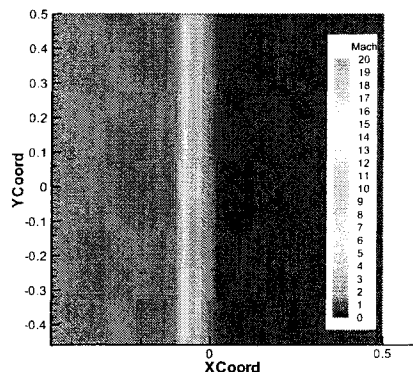


Figure 6.49: 2nd order EC1-RV2 (fix) with Minmod at $M_0 = 20.0$.

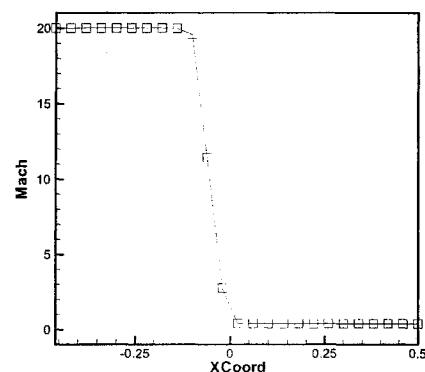


Figure 6.50: The cross-sectional 2nd order solution at $M_0 = 20.0$.

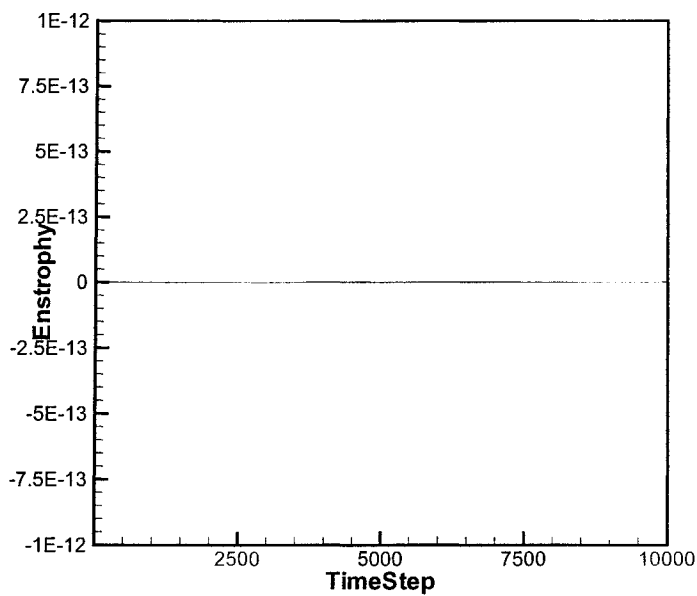


Figure 6.51: The total enstrophy (vorticity squared) within the computational domain for each time-step for the EC1-RV2 flux when solving the 1 1/2 dimensional carbuncle. Since total enstrophy is machine zero, we can conclude that by controlling entropy we have prevented the generation of spurious vorticity and shock instability all together.

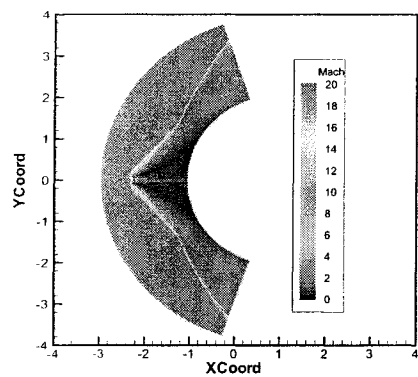


Figure 6.52: A-R flux at $M_0 = 20.0$. A typical carbuncle profile.

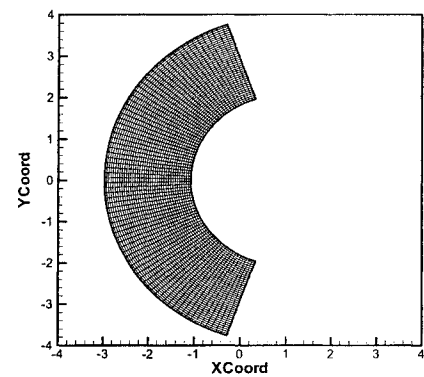


Figure 6.53: The quadrilateral 80 x 160 cells.

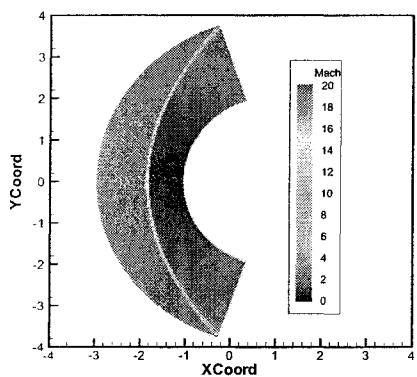


Figure 6.54: EC1-RV2 flux at $M_0 = 20.0$ with no carbuncle.

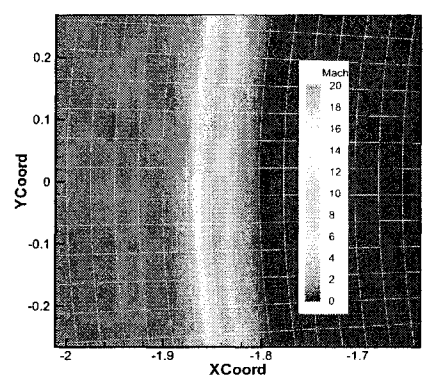


Figure 6.55: EC1-RV2 captures shock with only 3 intermediate cells.

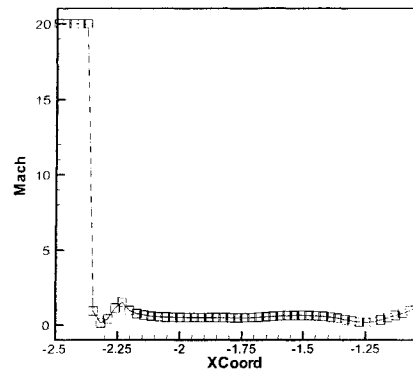


Figure 6.56: Mach profile along $y = 0$ (stagnation region) for A-R flux. Note how the shock profile exhibit violent spurious oscillations in the stagnation region.

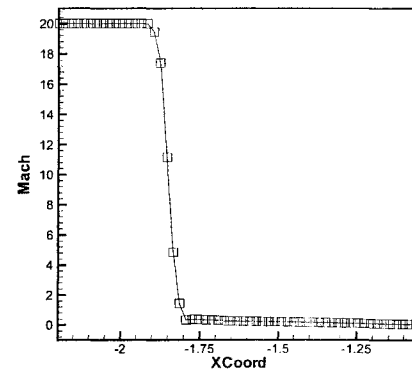


Figure 6.57: EC1-RV2 flux without entropy fix. A much better shock profile, with 3 intermediate cells but the solution is not monotone.

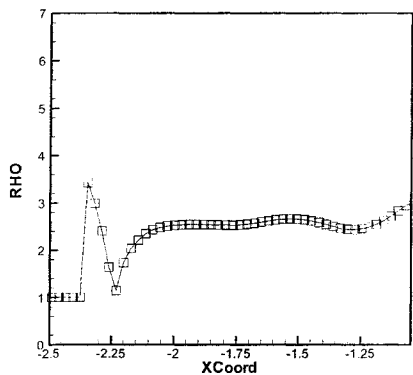


Figure 6.58: Density profile along $y = 0$ (stagnation region) for A-R flux. The solution is completely off.

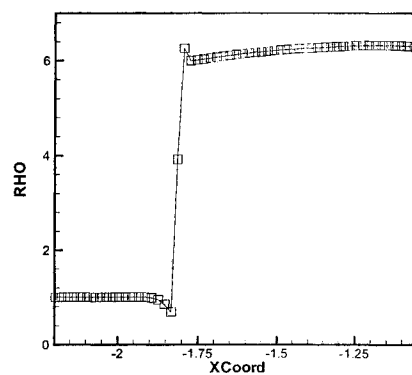


Figure 6.59: EC1-RV2 flux without entropy fix. A much better solution compared to A-R flux but spurious overshoots are present.

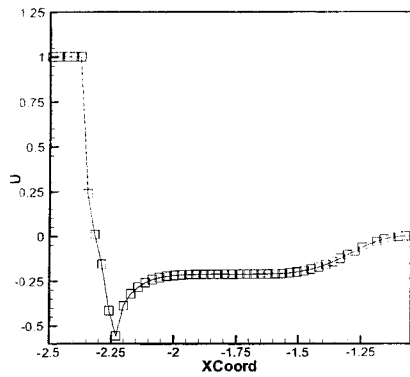


Figure 6.60: U profile along $y = 0$ (stagnation region) for A-R flux. The negative velocity represents reverse flow within the stagnation region.

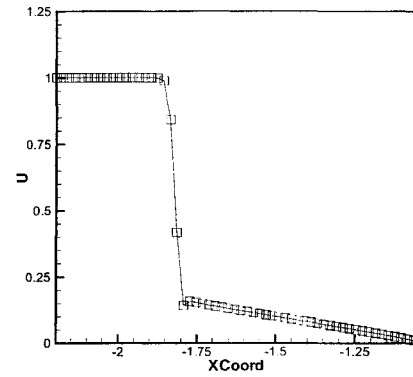


Figure 6.61: EC1-RV2 flux without entropy fix. By far, a much better solution at the stagnation region in which the velocity drops rapidly after crossing the shock and slowly decreases to zero as the fluid approaches the stagnation point .

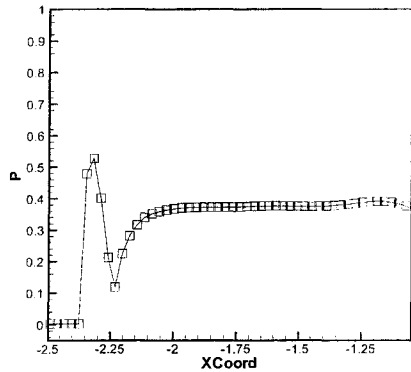


Figure 6.62: Pressusre profile along $y = 0$ (stagnation region) for A-R flux. The solution is completely off.

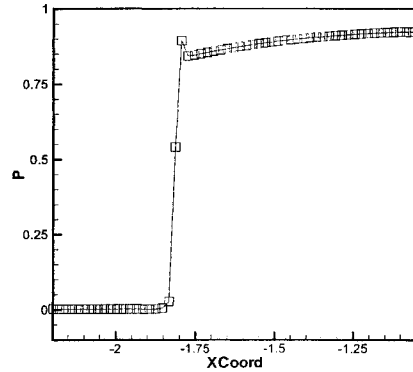


Figure 6.63: EC1-RV2 flux without entropy fix. A much more reasonable solution although not monotone.

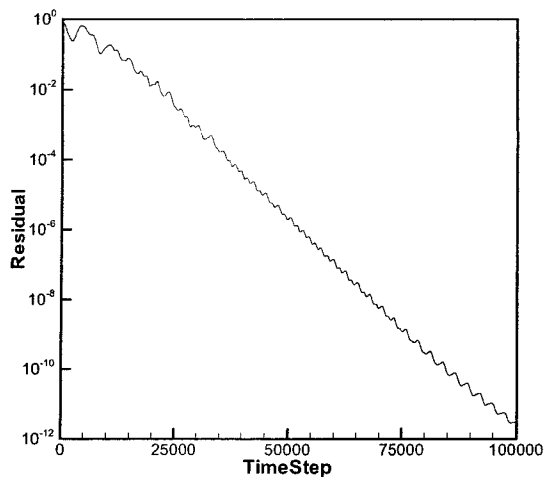


Figure 6.64: The residual (in absolute value) plot for the A-R flux for Mach 20 flow past a two-dimensional cylinder. Note the oscillations depict shock instability. By the time the solution goes to steady-state, it would have produced a spurious but weakly consistent solution of the Euler equations.

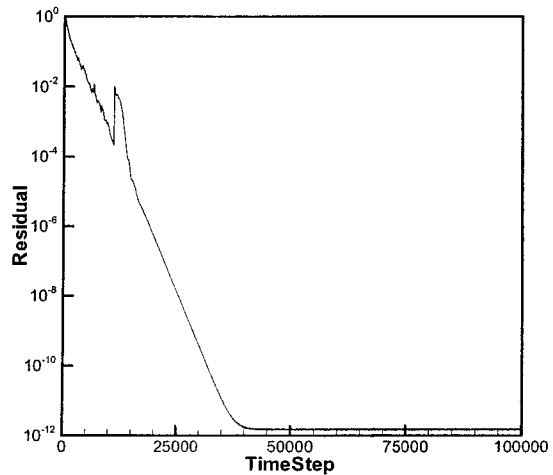


Figure 6.65: The residual (in absolute value) plot for the new flux function EC1-RV2 predicting the Mach 20 flow past a two dimensional cylinder. The residual goes to machine zero smoothly for the most part.

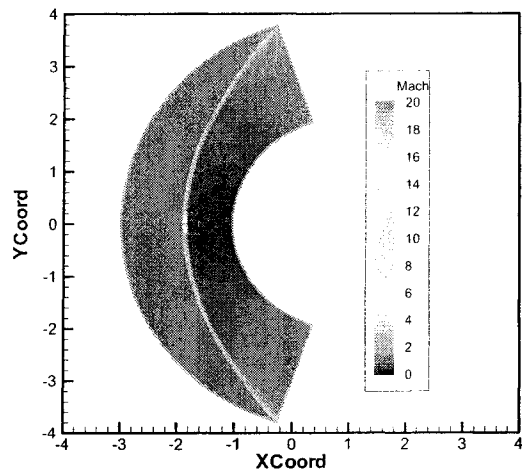


Figure 6.66: EC1-RV2 flux with entropy fix at $M_0 = 20.0$ with no carbuncle.

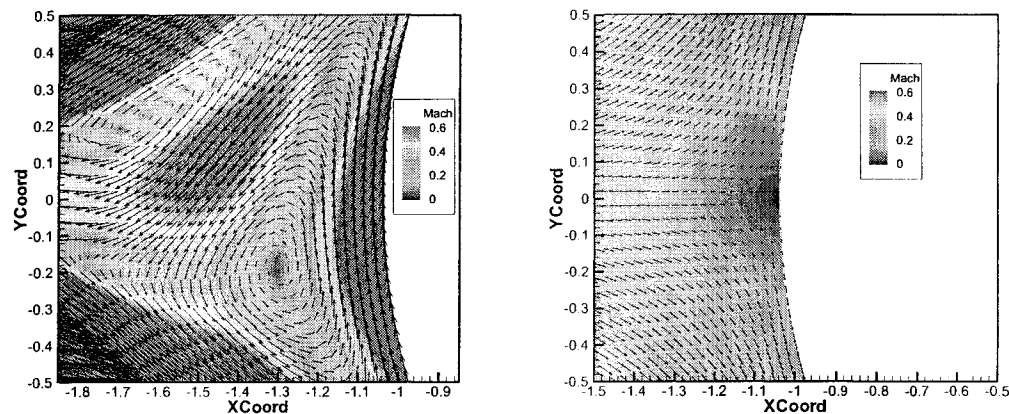


Figure 6.67: Stagnation point predicted by AR flux at $M_0 = 20.0$. Note how its location is completely off.

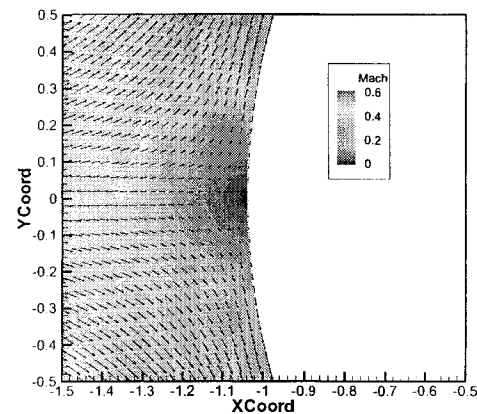


Figure 6.68: Stagnation point predicted by EC1-RV2 flux with entropy fix at $M_0 = 20.0$.

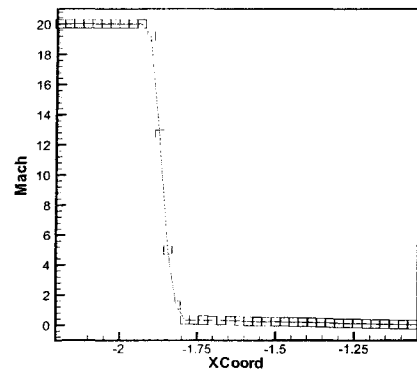


Figure 6.69: The Mach profile of EC1-RV2 flux with entropy fix at $M_0 = 20.0$. Monotonicity is achieved.

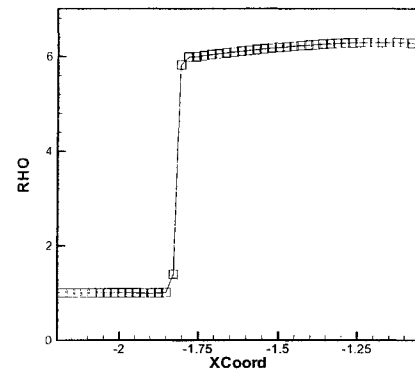


Figure 6.70: Density profile along $y = 0$ (stagnation region) for EC1-RV (fix) flux at $M_0 = 20.0$. A much improved solution compared to solution without entropy fix.

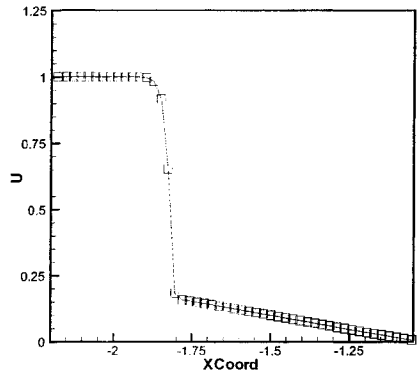


Figure 6.71: U-velocity profile for EC1-RV2 flux with entropy fix at $M_0 = 20.0$.

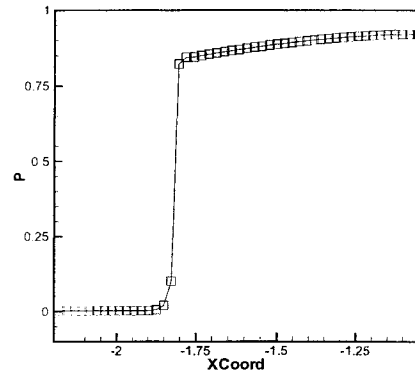


Figure 6.72: Pressure profile for EC1-RV2 flux with entropy fix at $M_0 = 20.0$.

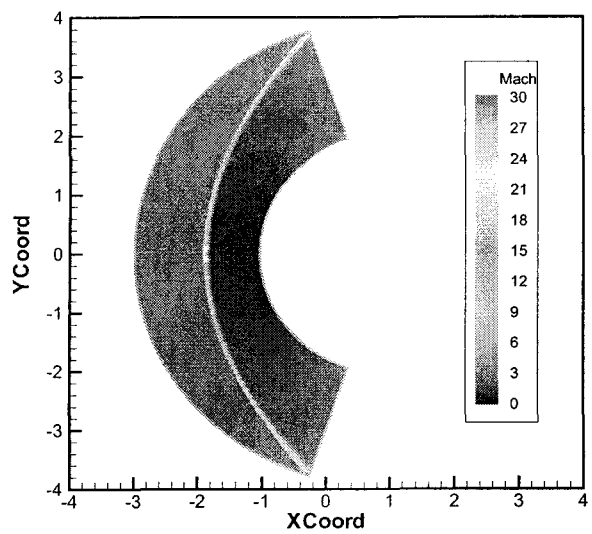


Figure 6.73: EC1-RV2 flux with entropy fix at $M_0 = 30.0$ with no carbuncle.

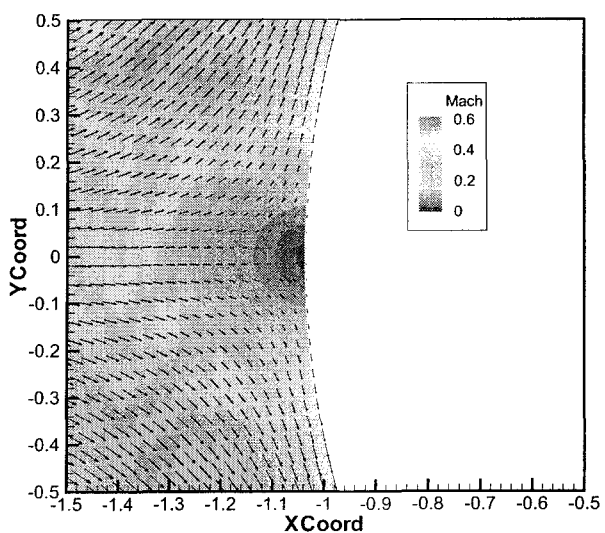


Figure 6.74: Stagnation point predicted by EC1-RV2 flux with entropy fix at $M_0 = 30.0$.

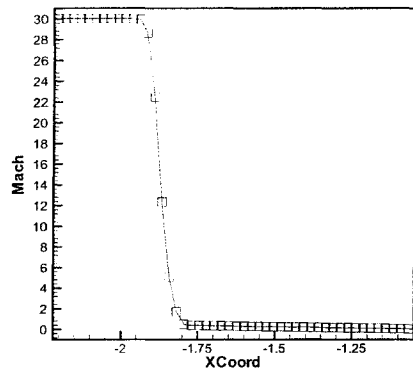


Figure 6.75: The Mach profile of EC1-RV2 flux with entropy fix at $M_0 = 30.0$. Monotonicity is still achieved but the shock profile is slightly broader than those produced with $M_0 = 20.0$.

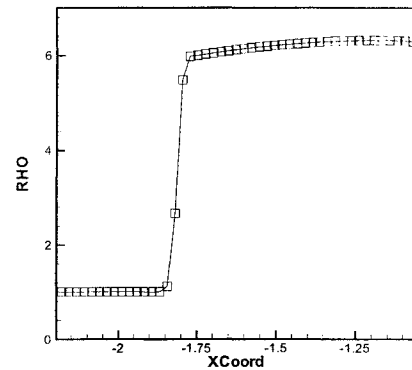


Figure 6.76: Density profile along $y = 0$ (stagnation region) for EC1-RV (fix) flux at $M_0 = 30.0$.

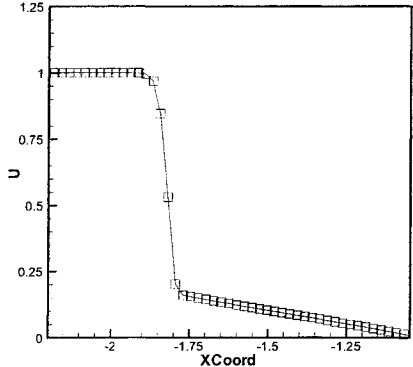


Figure 6.77: U-velocity profile for EC1-RV2 flux with entropy fix at $M_0 = 30.0$.

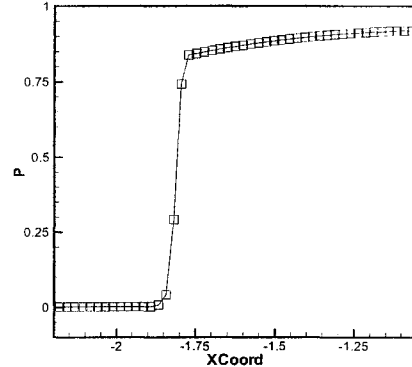


Figure 6.78: Pressure profile for EC1-RV2 flux with entropy fix at $M_0 = 30.0$.

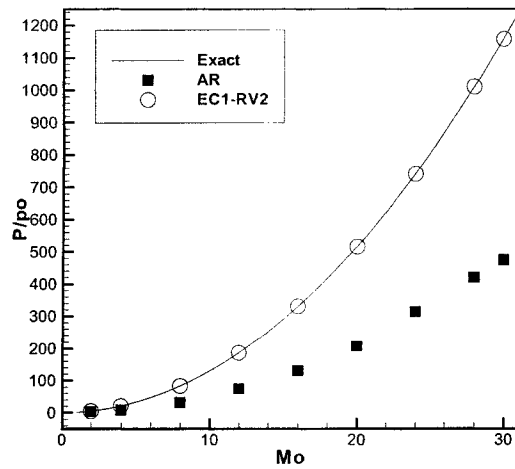


Figure 6.79: The normalized stagnation pressures (P_s/p_0) at the cylinder surface ($y=0$) for various upstream Mach numbers M_0 . Note the AR flux produces stagnation pressure that deviates more than 50 percent than the exact stagnation pressure. The EC1-RV2 flux only produces at most 2 percent error.

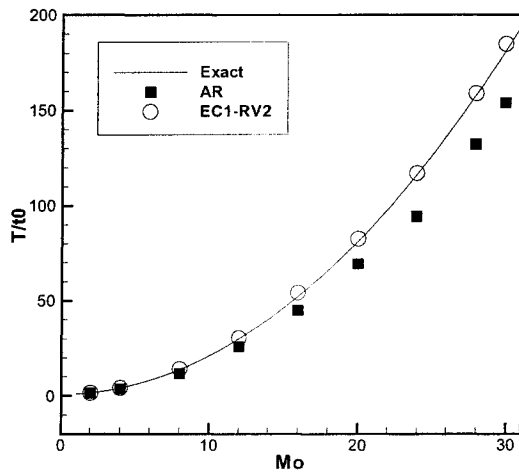


Figure 6.80: The normalized stagnation temperatures (T_s/t_0) at the cylinder surface ($y=0$) for various upstream Mach numbers M_0 . The EC1-RV2 flux only produces about 2 percent error compared to the exact stagnation temperature as opposed to 20 percent error produced by the AR flux.

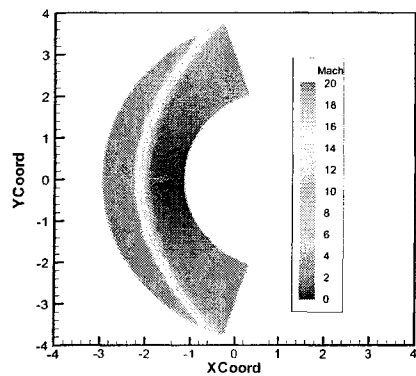


Figure 6.81: EC1-RV2 (fix) with 20 x 200 cells.

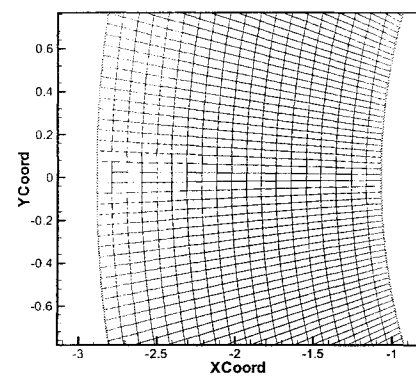


Figure 6.82: Zooming into the mesh of 20 x 200 cells.

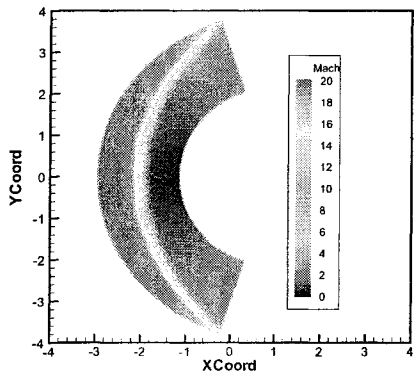


Figure 6.83: EC1-RV2 (fix) with 20 x 400 cells.

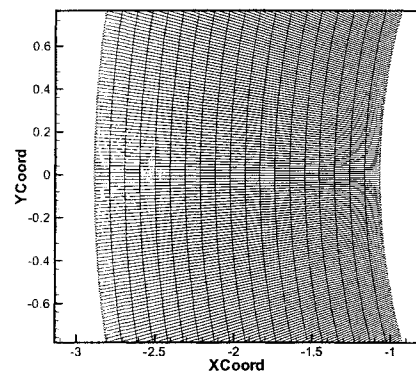


Figure 6.84: Zooming into the mesh of 20 x 400 cells.

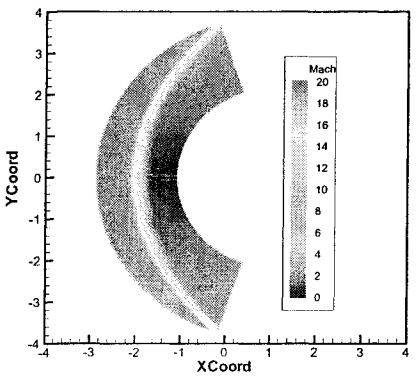


Figure 6.85: EC1-RV2 (fix) with 20 x 600 cells.

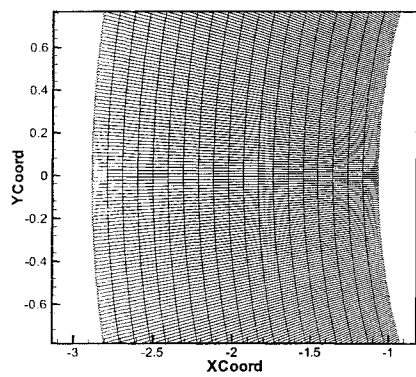


Figure 6.86: Zooming into mesh of 20 x 600 cells.

CHAPTER VII

CONCLUSION AND FUTURE WORK

7.1 Conclusion

In this thesis, we have conducted a systematic series of investigation to understand the nature of the carbuncle problem in order to determine its root and provide a solution to completely eliminate the problem. To simplify our investigation, we have examined the model carbuncle problem, specifically the 1 and $1\frac{1}{2}$ dimensional steady shocks. Major results include the following:

- Results from our numerical experiments coupled with analytical and numerical results of others led us to believe that the carbuncle problem is universal and can be described by 3 distinct stages: “Pimples”, where initial shock instability occurs along the shock; “Bleeding”, where the pimples are propagated or ‘bleed’ downstream of the shock; “Carbuncle”, where the shock instability goes into reverse flow and penetrate upstream of the shock.
- In $1\frac{1}{2}$ dimensional carbuncle, spurious vorticity is generated along and downstream of the shock, which we initially thought was the reason behind the carbuncle. However, the shock instability still persists when solving the $1\frac{1}{2}$ dimensional planar shock with a vorticity capturing scheme, thus we have con-

cluded that spurious vorticity is just a symptom but not the cause of the carbuncle.

- By analyzing the 1 dimensional steady shock, based on the results of Barth [6] and ours, we made a conjecture stating that the *imprecise enforcement of entropy* or the Second Law of Thermodynamics in the Godunov-type flux is the *root of shock instability*. In multi dimensions, this shock instability is in the form of “pimples” which may “bleed” and generate spurious vorticity before finally it becomes a carbuncle.
- In order to improve current technology of numerical entropy control, we have developed a new conservative, upwinded and entropy-consistent flux function (EC1-RV2 flux). The flux function is a coupling of Roe’s practical and relatively inexpensive entropy conserving flux [84] with his entropy stable dissipative flux but using our proposed averaged formulation for the latter. In addition, we have semi-empirically determined an entropy fix to generate enough entropy production across a shock ensuring monotonicity of the solution.
- We have tested the EC1-RV2 flux function with various numerical problems in 1, 1 1/2 and 2 dimensions. The results are very much comparable to those produced by the original Roe method with these exceptions. One, *the new flux function does not produce any carbuncle or any form of shock instability when capturing weak, moderate or strong shocks*¹. Two, the new flux function does not capture the unphysical rarefaction shock, capturing it instead as a reasonably smooth expansion region as it should be. Three, the EC1-RV2 flux

¹By weak, we mean transonic flow; Moderate means supersonic flow; Strong means hypersonic flow.

predicts more accurate stagnation conditions at the body surface deviating by only 2 percent from the exact inviscid solution compared to more than 20 percent error predicted by the original Roe-flux (Fig 6.79-6.80).

- *The EC1-RV2 flux function totally eliminates the carbuncle phenomenon without sacrificing the ability to capture crisp contact discontinuities.* For years, many have believed [81], [52], [83] and even claimed to have, mathematically proven [45] that the two properties cannot co-exist but we have presented several numerical counter examples in chapter 6 to disprove the theory.
- The EC1-RV2 flux function is developed based on one dimensional principles hence it should be readily extended to multi dimensional finite volume methods based on one dimensional fluxes in any grid formulation and either structured or unstructured. Moreover, the formulation of entropy conservation is of a general fluctuation splitting technique so the physics of directly including entropy in the numerics is not limited only to a finite volume scheme but can be of a finite element nature.

In addition, we have also developed a novel continuum approach for vorticity capturing. The method is truly an unsteady, upwinded and conservative vorticity capturing scheme (VC) for solving the two dimensional system of Euler equations. The following will highlight the motivation for developing the method and some of the features and achievements of the method.

- We have mathematically proven that the vorticity preserving Lax-Wendroff type scheme developed by Morton and Roe [73] is not vorticity preserving when solving the two dimensional linear wave equations with constant advection if the process of nonlinear limiting is included.

- In order to circumvent this severe restriction, we have developed a vorticity correctional algorithm which makes small adjustments to the flux evaluation at each cell interface to ensure vorticity is physically conserved. By being conserved, we mean that the computed vorticity obeys the discrete vorticity transport equations. When computing the Euler equations, the vorticity transport equations are based on the curl of momentum to ensure conservation of the primary Euler variables.
- This vorticity correctional algorithm solves a Poisson equation at each time step which is dependent on the numerical computation of the discrete vorticity transport equations. We have formulated a conservative and upwinded numerical method to predict the discrete vorticity transport equations in two dimensions based on the technology of incompressible CFD.
- Our vorticity capturing method is fundamentally based on conservatively modifying (minutely) the flux at the cell interface hence can be used with *any good flux function*. For this thesis, we have employed the original Roe-flux combined with second order (limited) Hancock time integration scheme.
- The second order vorticity capturing scheme (VC-2) accurately captures the features of an inviscid travelling vortex with less than 2 percent error than the exact solution in terms of total enstrophy measurement. The first order Roe flux dissipated almost 60 percent of enstrophy while the second order Roe-flux generated more than 20 percent of spurious enstrophy for the same amount of time.
- Our error analysis indicate that by combining the new vorticity capturing method with the second order Hancock scheme, the order of accuracy in pre-

dicting the conservative Euler variables does not deteriorate. In fact, the accuracy of predicting vorticity is doubled when the vorticity capturing method is included in the Hancock scheme.

7.2 Future Work On Vorticity Capturing

In this thesis, our vorticity capturing formulation is restricted to uniform Cartesian grids in two dimensions. There is still a need to extend the current work to arbitrary grid formulations although a beginning has been made in the context of linear wave equations [73]. In addition, the sub-iterations performed for the vorticity corrections (Poisson equation) in this thesis are based on the Gauss-Seidel method which is not the most efficient method solving the Poisson equation. To speed up the sub-iterations, we propose the multigrid method. Since the multigrid is usually employed as a 'black box' method, we believe it can be easily implemented to solve our Poisson equation and that will be one of our immediate plans for future work.

As mentioned before, vorticity capturing depends on vorticity discretization. In other words, vorticity is only captured at a specific grid location where it was designed to be captured. In two dimensions, we have several options to capture discrete vorticity which is either at the cell center, cell-edge or cell vertices. In this thesis, even though the main variables are conserved at the cell centers, vorticity is captured at the cell vertices as to minimize the spurious modes. In three dimensions however, we have more degrees of freedom in choosing where vorticity should be captured.

However, we choose to capture vorticity at the midpoint² of the cell edges as shown in Fig. 7.1. It was chosen because by doing so, we would still produce the minimum number of spurious modes and use the minimum amount of discrete

²This is to also minimize the spurious modes.

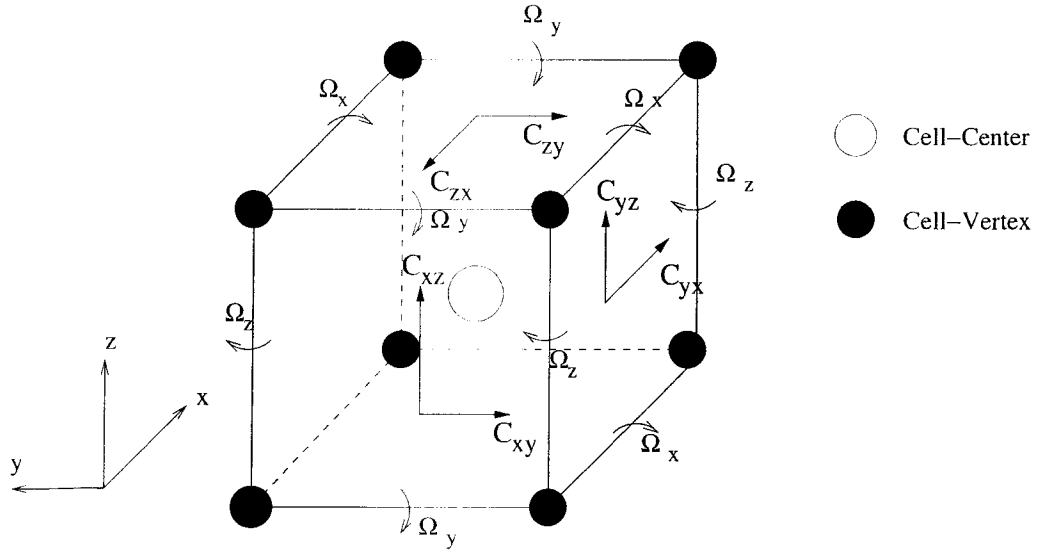


Figure 7.1: A three dimensional cell with vorticity location and flux corrections.

operators in three dimensions. In short, edges that are parallel to the x-direction are chosen to be the location of vorticity pointing in that direction Ω_x . Similarly, Ω_y and Ω_z are located at the midpoint of cell edges that are parallel in the y and z-directions respectively. We are now ready to construct the vorticity corrections in three dimensions.

7.2.1 Vorticity Corrections in Three Dimensions

We will assume that we have a uniform Cartesian mesh in three dimensions and the formulation is restricted to solving a three dimensional system of Euler equations. Let any 'good'³ one dimensional based flux function solving the fluxes along the x,y and z-directions be defined as f , g and h . Hence the modified fluxes at the cell

³Good here means a numerically convergent flux.

interfaces will be

$$\tilde{\mathbf{f}} = \mathbf{f} - \mathbf{C}_x \quad (7.1)$$

$$\tilde{\mathbf{g}} = \mathbf{g} - \mathbf{C}_y \quad (7.2)$$

$$\tilde{\mathbf{h}} = \mathbf{h} - \mathbf{C}_z \quad (7.3)$$

where $(\mathbf{C}_x, \mathbf{C}_y, \mathbf{C}_z)$ are flux corrections located at the center of the cell-faces with normal pointing in the (x, y, z) directions. Note that each flux corrections alters the respective momentum equations at the cell interface in the tangential directions⁴ as indicated in Fig. 7.1 and can be written as

$$\mathbf{C}_x = [0, 0, c_{xy}, c_{xz}, 0]^T \quad (7.4)$$

$$\mathbf{C}_y = [0, c_{yx}, 0, c_{yz}, 0]^T \quad (7.5)$$

$$\mathbf{C}_z = [0, c_{zx}, c_{zy}, 0, 0]^T \quad (7.6)$$

By discretizing the three dimensional Euler equations (refer to appendix A) using the standard and modified fluxes, we have

$$\mathbf{u}_{i,j,k}^{n+1} = \mathbf{u}_{i,j,k}^n - \frac{\Delta t}{h^2} [\mathbf{f}_{i+\frac{1}{2},j,k}^n - \mathbf{f}_{i-\frac{1}{2},j,k}^n + \mathbf{g}_{i,j+\frac{1}{2},k}^n - \mathbf{g}_{i,j-\frac{1}{2},k}^n + \mathbf{h}_{i,j,k+\frac{1}{2}}^n - \mathbf{h}_{i,j,k-\frac{1}{2}}^n] \quad (7.7)$$

$$\tilde{\mathbf{u}}_{i,j,k}^{n+1} = \tilde{\mathbf{u}}_{i,j,k}^n - \frac{\Delta t}{h^2} [\tilde{\mathbf{f}}_{i+\frac{1}{2},j,k}^n - \tilde{\mathbf{f}}_{i-\frac{1}{2},j,k}^n + \tilde{\mathbf{g}}_{i,j+\frac{1}{2},k}^n - \tilde{\mathbf{g}}_{i,j-\frac{1}{2},k}^n + \tilde{\mathbf{h}}_{i,j,k+\frac{1}{2}}^n - \tilde{\mathbf{h}}_{i,j,k-\frac{1}{2}}^n] \quad (7.8)$$

where $\mathbf{u}_{i,j,k}^n$ and $\tilde{\mathbf{u}}_{i,j,k}^n$ are the standard and modified cell averages of the conservative variables at coordinate (i,j,k) and time level n . We define pseudo-vorticity $\Omega_x, \Omega_y, \Omega_z$ as shown in Fig 7.1 through the compact difference of four neighboring cell-center

⁴The flux corrections are now second order tensors. For example, c_{xy} is a flux correction located at the center of cell-interface normal in x-direction and alters the y-momentum.

momenta ($\rho\vec{u}$) hence the corrected and uncorrected vortices are related by

$$\tilde{\Omega}_x^{n+1} = \Omega_x^{n+1} + \frac{\Delta t}{h^3} [\mu_z \delta_y^2 c_{yz} - \mu_y \delta_z^2 c_{zy} + \mu_z \delta_x \delta_y c_{xz} - \mu_y \delta_x \delta_z c_{xy}]^n \quad (7.9)$$

$$\tilde{\Omega}_y^{n+1} = \Omega_y^{n+1} + \frac{\Delta t}{h^3} [\mu_x \delta_z^2 c_{zx} - \mu_z \delta_x^2 c_{xz} + \mu_x \delta_y \delta_z c_{yx} - \mu_z \delta_x \delta_y c_{yz}]^n \quad (7.10)$$

$$\tilde{\Omega}_z^{n+1} = \Omega_z^{n+1} + \frac{\Delta t}{h^3} [\mu_y \delta_x^2 c_{xy} - \mu_y \delta_y^2 c_{yx} + \mu_y \delta_x \delta_z c_{zy} - \mu_x \delta_y \delta_z c_{zx}]^n \quad (7.11)$$

where now we have the correctional dependence in the third dimension. Again we insist that the corrected vorticity be identical to some independent numerical estimate such that

$$\tilde{\Omega}_x^{n+1} = \Omega_{IND,x}^{n+1} \quad (7.12)$$

$$\tilde{\Omega}_y^{n+1} = \Omega_{IND,y}^{n+1} \quad (7.13)$$

$$\tilde{\Omega}_z^{n+1} = \Omega_{IND,z}^{n+1} \quad (7.14)$$

and to achieve this we will use subiterations within the timestep. Denote conditions after the k th subiteration by $(\cdot)^k$ and conditions after the subiterations have converged by $(\cdot)^\infty$. The problem that we wish to solve is

$$\Omega_x^\infty = \Omega_{IND,x}^{n+1} = \Omega_x^{n+1} + \frac{\Delta t}{h^3} [\mu_z \delta_y^2 c_{yz}^\infty - \mu_y \delta_z^2 c_{zy}^\infty + \mu_z \delta_x \delta_y c_{xz}^\infty - \mu_y \delta_x \delta_z c_{xy}^\infty] \quad (7.15)$$

$$\Omega_y^\infty = \Omega_{IND,y}^{n+1} = \Omega_y^{n+1} + \frac{\Delta t}{h^3} [\mu_x \delta_z^2 c_{zx}^\infty - \mu_z \delta_x^2 c_{xz}^\infty + \mu_x \delta_y \delta_z c_{yx}^\infty - \mu_z \delta_x \delta_y c_{yz}^\infty] \quad (7.16)$$

$$\Omega_z^\infty = \Omega_{IND,z}^{n+1} = \Omega_z^{n+1} + \frac{\Delta t}{h^3} [\mu_y \delta_x^2 c_{xy}^\infty - \mu_y \delta_y^2 c_{yx}^\infty + \mu_y \delta_x \delta_z c_{zy}^\infty - \mu_x \delta_y \delta_z c_{zx}^\infty] \quad (7.17)$$

where $c_{xy}^\infty, c_{yx}^\infty, c_{xz}^\infty, c_{zx}^\infty, c_{yz}^\infty, c_{zy}^\infty$ are the corrections that need to be determined. The sub-iterations that bring this about are

$$\Omega_x^{k+1} = \Omega_x^k + \frac{\Delta t}{h^3} [\mu_z \delta_y^2 (c_{yz}^{k+1} - c_{yz}^k) - \mu_y \delta_z^2 (c_{zy}^{k+1} - c_{zy}^k) + \mu_z \delta_x \delta_y (c_{xz}^{k+1} - c_{xz}^k) - \mu_y \delta_x \delta_z (c_{xy}^{k+1} - c_{xy}^k)] \quad (7.18)$$

$$\Omega_y^{k+1} = \Omega_y^k + \frac{\Delta t}{h^3} [\mu_x \delta_z^2 (c_{zx}^{k+1} - c_{zx}^k) - \mu_z \delta_x^2 (c_{xz}^{k+1} - c_{xz}^k) + \mu_x \delta_y \delta_z (c_{yx}^{k+1} - c_{yx}^k) - \mu_z \delta_x \delta_y (c_{yz}^{k+1} - c_{yz}^k)] \quad (7.19)$$

$$\Omega_z^{k+1} = \Omega_z^k + \frac{\Delta t}{h^3} [\mu_y \delta_x^2 (c_{xy}^{k+1} - c_{xy}^k) - \mu_y \delta_y^2 (c_{yx}^{k+1} - c_{yx}^k) + \mu_y \delta_x \delta_z (c_{zy}^{k+1} - c_{zy}^k) - \mu_x \delta_y \delta_z (c_{zx}^{k+1} - c_{zx}^k)] \quad (7.20)$$

where we assume $\Omega_x^{n+1}, \Omega_y^{n+1}, \Omega_z^{n+1}$ as the initial values for the sub-iterations. The particular choices

$$c_{xy}^{k+1} - c_{xy}^k = \zeta \mu_y (\Omega_z^k - \Omega_{IND,z}^{n+1})$$

$$c_{zx}^{k+1} - c_{zx}^k = -\zeta \mu_x (\Omega_z^k - \Omega_{IND,z}^{n+1})$$

$$c_{xz}^{k+1} - c_{xz}^k = \zeta \mu_x (\Omega_y^k - \Omega_{IND,y}^{n+1})$$

$$c_{yx}^{k+1} - c_{yx}^k = -\zeta \mu_z (\Omega_y^k - \Omega_{IND,y}^{n+1})$$

$$c_{zy}^{k+1} - c_{zy}^k = -\zeta \mu_y (\Omega_x^k - \Omega_{IND,x}^{n+1})$$

$$c_{yz}^{k+1} - c_{yz}^k = \zeta \mu_z (\Omega_x^k - \Omega_{IND,x}^{n+1})$$

with ζ as a parameter that restricts the iteration step will lead to

$$\Omega_x^{k+1} = \Omega_x^k + \kappa [(\mu_z^2 \delta_y^2 + \mu_y^2 \delta_z^2) \Delta \Omega_x^k - (\mu_z^2 \delta_x \delta_y \Delta \Omega_y^k + \mu_y^2 \delta_x \delta_z \Delta \Omega_z^k)] \quad (7.21)$$

$$\Omega_y^{k+1} = \Omega_y^k + \kappa [(\mu_x^2 \delta_z^2 + \mu_z^2 \delta_x^2) \Delta \Omega_y^k - (\mu_x^2 \delta_y \delta_z \Delta \Omega_z^k + \mu_z^2 \delta_x \delta_y \Delta \Omega_x^k)] \quad (7.22)$$

$$\Omega_z^{k+1} = \Omega_z^k + \kappa [(\mu_y^2 \delta_x^2 + \mu_x^2 \delta_y^2) \Delta \Omega_z^k - (\mu_y^2 \delta_x \delta_z \Delta \Omega_x^k + \mu_x^2 \delta_y \delta_z \Delta \Omega_y^k)] \quad (7.23)$$

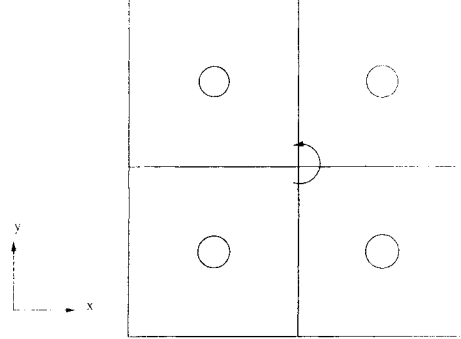


Figure 7.2: A planar view of computing vorticity using four neighboring cells.

where $\kappa = \zeta \frac{\Delta t}{h^3}$ is the sub-iterative step with vorticity discrepancies

$$\Delta\Omega_x^k = \Omega_x^k - \Omega_{IND,x}^{n+1} \quad (7.24)$$

$$\Delta\Omega_y^k = \Omega_y^k - \Omega_{IND,y}^{n+1} \quad (7.25)$$

$$\Delta\Omega_z^k = \Omega_z^k - \Omega_{IND,z}^{n+1} \quad (7.26)$$

so that we arrive to a similar Poisson equation as in two dimensions but with extra terms that governs a three dimensional nature. For example, if we look at Ω_z , the corrections depend on $\Delta\Omega_z$ or (c_{xy}, c_{yx}) (cell-interfaces normal in (x, y) directions) and on the interfaces normal in the z directions, (c_{zx}, c_{zy}) .

7.2.2 The Independent Inviscid Vorticity Estimate in Three Dimensions

In three dimensions, we have the vortex stretching as source terms in the vorticity transport equation, hence the equation is no longer a pure hyperbolic conservation law. Recall that the vorticity transport equations based on the curl of momentum written in vector form

$$\iiint_V \left[\frac{\partial \vec{\Omega}}{\partial t} + \nabla \cdot (\vec{\Omega} \circ \vec{U}) + \nabla \times [\vec{U}(\Phi)] \right] dV = \iiint_V [(\vec{\Omega} \cdot \nabla) \vec{U}] dV \quad (7.27)$$

The terms on the left hand side correspond to unsteady vorticity, vorticity advection and compressibility effects and the last two terms can be rewritten in conservative-

flux form by the Divergence Theorem. By adding another dimension, these terms can be discretized straightforwardly using the same conservative techniques in two dimensional discretization given in chapter 4.

On the other hand, the right hand side represents vortex stretching and is a non-conservative nonlinear source term which can be evaluated using a numerical quadrature techniques. We will not go into the details of evaluating the source term. However, it must be emphasized that there is much success in numerically predicting conservation laws with nonlinear source terms and would refer to the interested reader to some excellent sources [61], [10], [43].

7.3 Future Work On the Entropy-Consistent Flux

In this thesis, we have presented a semi-discrete entropy conserving flux beginning from a fluctuation splitting ideology in one dimension and by a different interpretation, converting it to a finite volume (FV) formulation in one dimension. From the FV context, we are able to easily extend the results to multi dimensions. However, the same cannot be said when extending the fluctuation splitting method even to higher dimensions although [84] has made a start.

In addition, we would like to investigate the if the EC1-RV2 flux function can predict boundary layers with minimal smearing when coupled with an accurate diffusion method. If successful, the EC1-RV2 flux function will possibly be the new methodology in predicting shock-boundary layer interactions.

The results of this thesis, when viewed as a whole, represents a significant advancement toward a reliable numerical prediction of hypersonic flow, holding the promise of making computational methods a practical and reliable tool in designing hypersonic vehicles.

APPENDICES

APPENDIX A

Scaling Matrix for the Dissipative Flux

The three dimensional Euler equations can be written in conservative form.

$$\partial_t \mathbf{u} + \partial_x \mathbf{f}(\mathbf{u}) + \partial_y \mathbf{g}(\mathbf{u}) + \partial_z \mathbf{h}(\mathbf{u}) = 0 \quad (\text{A.1})$$

where the conservative variables are mass, momentum and energy $\mathbf{u} = [\rho, \rho u, \rho v, \rho w, \rho E]^T$

and their conservative fluxes are given as

$$\mathbf{f}(\mathbf{u}) = \begin{bmatrix} \rho u \\ \rho u^2 + p \\ \rho uv \\ \rho uw \\ \rho uH \end{bmatrix}, \quad \mathbf{g}(\mathbf{u}) = \begin{bmatrix} \rho v \\ \rho uv \\ \rho v^2 + p \\ \rho vw \\ \rho vH \end{bmatrix}, \quad \mathbf{h}(\mathbf{u}) = \begin{bmatrix} \rho w \\ \rho uw \\ \rho vw \\ \rho w^2 + p \\ \rho wH \end{bmatrix} \quad (\text{A.2})$$

where the total energy and total enthalpy are defined as $E = e + \frac{u^2 + v^2 + w^2}{2}$ and $H = E + \frac{P}{\rho}$. The compatibility relation between pressure and internal energy e is used for closure, $p = \rho e(\gamma - 1)$ and γ is the fluids ratio of specific heats.

The Euler equations can be cast into a non-conservative formulation written as

$$\partial_t \mathbf{u} + A \partial_x \mathbf{u} + B \partial_y \mathbf{u} + C \partial_z \mathbf{u} = 0 \quad (\text{A.3})$$

where the Jacobian matrices are defined as

$$A = \frac{\partial \mathbf{f}}{\partial \mathbf{u}}, \quad B = \frac{\partial \mathbf{g}}{\partial \mathbf{u}}, \quad C = \frac{\partial \mathbf{h}}{\partial \mathbf{u}} \quad (\text{A.4})$$

in which each Jacobian matrix is explicitly written as

$$A = \begin{bmatrix} 0 & 1 & 0 & 0 & 0 \\ (\gamma - 1)H - u^2 - a^2 & (3 - \gamma)u & -(\gamma - 1)v & -(\gamma - 1)w & \gamma - 1 \\ -uv & v & u & 0 & 0 \\ -uw & w & 0 & u & 0 \\ \frac{u}{2}((\gamma - 3)H - a^2) & H - (\gamma - 1)u^2 & -(\gamma - 1)uv & -(\gamma - 1)uw & \gamma u \end{bmatrix} \quad (\text{A.5})$$

$$B = \begin{bmatrix} 0 & 0 & 1 & 0 & 0 \\ -uv & v & u & 0 & 0 \\ (\gamma - 1)H - v^2 - a^2 & -(\gamma - 1)u & (3 - \gamma)v & -(\gamma - 1)w & \gamma - 1 \\ -vw & 0 & w & v & 0 \\ \frac{v}{2}((\gamma - 3)H - a^2) & -(\gamma - 1)uv & H - (\gamma - 1)v^2 & -(\gamma - 1)vw & \gamma v \end{bmatrix} \quad (\text{A.6})$$

$$C = \begin{bmatrix} 0 & 0 & 0 & 1 & 0 \\ -uw & w & 0 & u & 0 \\ -vw & 0 & w & v & 0 \\ (\gamma - 1)H - w^2 - a^2 & -(\gamma - 1)u & -(\gamma - 1)v & (3 - \gamma)w & \gamma - 1 \\ \frac{w}{2}((\gamma - 3)H - a^2) & -(\gamma - 1)uw & -(\gamma - 1)vw & H - (\gamma - 1)w^2 & \gamma w \end{bmatrix} \quad (\text{A.7})$$

These matrices have real eigenvalues with linearly independent eigenvectors hence can be diagonalized. For example, we can write $A = R_u \Lambda_u L_u$ where R_u is the matrix which contains the right eigenvectors of A and Λ_u is the matrix of the diagonalized eigenvalues and the left eigenvector is defined as $L_u = R_u^{-1}$. It can be shown by

direct computation that

$$R_u = \begin{bmatrix} 1 & 1 & 0 & 0 & 1 \\ u-a & u & 0 & 0 & u+a \\ v & v & 1 & 0 & v \\ w & w & 0 & 1 & w \\ H-ua & \frac{u^2+v^2+w^2}{2} & v & w & H+ua \end{bmatrix} \quad (\text{A.8})$$

$$\Lambda_u = \begin{bmatrix} u-a & 0 & 0 & 0 & 0 \\ 0 & u & 0 & 0 & 0 \\ 0 & 0 & u & 0 & 0 \\ 0 & 0 & 0 & u & 0 \\ 0 & 0 & 0 & 0 & u+a \end{bmatrix} \quad (\text{A.9})$$

$$L_u = \begin{bmatrix} H + \frac{a}{\gamma-1}(u-a) & -(u + \frac{a}{\gamma-1}) & -v & -w & 1 \\ -2H + \frac{4a^2}{\gamma-1} & 2u & 2v & 2 & -2 \\ -\frac{2va^2}{\gamma-1} & 0 & \frac{2a^2}{\gamma-1} & 0 & 0 \\ -\frac{2va^2}{\gamma-1} & 0 & 0 & \frac{2a^2}{\gamma-1} & 0 \\ H + \frac{a}{\gamma-1}(u+a) & -u + \frac{a}{\gamma-1} & -v & -w & 1 \end{bmatrix} \quad (\text{A.10})$$

Hence the wave-strengths can be written as

$$L_u d\mathbf{u} = \begin{bmatrix} \frac{1}{2}(\frac{dp}{a^2} - \frac{\rho du}{a}) \\ d\rho - \frac{\rho dp}{a^2} \\ \rho dv \\ \rho dw \\ \frac{1}{2}(\frac{dp}{a^2} + \frac{\rho du}{a}) \end{bmatrix} \quad (\text{A.11})$$

Recall that physical entropy is defined as $S = \ln p - \gamma \ln \rho$ and that our conserved

entropy is defined as $U = -\frac{\rho S}{\gamma-1}$. Hence the entropy variables

$$\mathbf{v} = \frac{\partial U}{\partial \mathbf{u}} = \begin{bmatrix} \frac{\gamma-S}{\gamma-1} - \frac{\rho}{2p}(u^2 + v^2 + w^2) \\ \frac{\rho u}{p} \\ \frac{\rho v}{p} \\ \frac{\rho w}{p} \\ \frac{-\rho}{p} \end{bmatrix} \quad (\text{A.12})$$

It can be shown by direct computation that there exists a diagonal matrix

$$\mathbf{S} = \begin{bmatrix} \frac{\rho}{2\gamma} & 0 & 0 & 0 & 0 \\ 0 & \frac{(\gamma-1)\rho}{\gamma} & 0 & 0 & 0 \\ 0 & 0 & p & 0 & 0 \\ 0 & 0 & 0 & p & 0 \\ 0 & 0 & 0 & 0 & \frac{\rho}{2\gamma} \end{bmatrix} \quad (\text{A.13})$$

such that

$$\mathbf{L}_u d\mathbf{u} = \mathbf{S} \mathbf{R}_u^T d\mathbf{v}^T \quad (\text{A.14})$$

Moreover, if we decompose $B = R_v \Lambda_v L_v$ and $C = R_w \Lambda_w L_w$, it also can be shown that the same matrix \mathbf{S} satisfies the following.

$$\mathbf{L}_v d\mathbf{u} = \mathbf{S} \mathbf{R}_v^T d\mathbf{v}^T \quad (\text{A.15})$$

$$\mathbf{L}_w d\mathbf{u} = \mathbf{S} \mathbf{R}_w^T d\mathbf{v}^T \quad (\text{A.16})$$

The matrix \mathbf{S} is the scaling matrix required for the new dissipative flux $\mathbf{R}|\boldsymbol{\Lambda}| \mathbf{S} \mathbf{R}[\mathbf{v}]$ given in chapter 6.

APPENDIX B

Two Dimensional Hancock Scheme

The Hancock scheme[110], [97] is a MUSCL type finite volume scheme [107] enforced in a predictor-corrector fashion, much like the Richtmayer scheme of the Lax-Wendroff family. The scheme is a second order accurate in both time and space discretizations. At the predictor level, it performs a limited half-step in time, utilizing the primitive Euler variables¹ providing provisional solutions within the cells. We use these provisional solutions to determine the fluxes at the cell interfaces. Finally, at the corrector level (full step), the scheme conservatively updates the each cell quantities using these fluxes. Before we explicitly introduce the scheme, recall that the two dimensional primitive Euler equations can be written as

$$\partial_t \mathbf{w} + \mathbf{A}_w \partial_x \mathbf{w} + \mathbf{B}_w \partial_y \mathbf{w} = 0 \quad (\text{B.1})$$

where the matrices \mathbf{A}_w and \mathbf{B}_w are given as

$$\mathbf{A}_w = \begin{bmatrix} u & \rho & 0 & 0 \\ 0 & u & 0 & \frac{1}{\rho} \\ 0 & 0 & u & 0 \\ 0 & \rho a^2 & 0 & u \end{bmatrix}, \quad \mathbf{B}_w = \begin{bmatrix} v & 0 & \rho & 0 \\ 0 & v & 0 & 0 \\ 0 & 0 & v & \frac{1}{\rho} \\ 0 & 0 & \rho a^2 & v \end{bmatrix} \quad (\text{B.2})$$

¹Although the conservative variables can also be used[97].

The Hancock scheme carried out on a Cartesian grid with cell center located at (i, j) can be expressed as the following. The half-step formulation is

$$\tilde{\mathbf{w}}_{i,j} = \mathbf{w}_{i,j}^n - \frac{\Delta t}{2} (\mathbf{A}_w \frac{\delta_x \mathbf{w}_{i,j}}{\Delta x} + \mathbf{B}_w \frac{\delta_y \mathbf{w}_{i,j}}{\Delta y})^n \quad (\text{B.3})$$

giving the provisional solution to solve for the fluxes at the interfaces² i.e.

$$\tilde{\mathbf{f}}_{i+\frac{1}{2},j} = \mathbf{f}(\tilde{\mathbf{w}}_{i+\frac{1}{2}L,j}, \tilde{\mathbf{w}}_{i-\frac{1}{2}R,j}) \quad (\text{B.4})$$

$$\tilde{\mathbf{g}}_{i,j+\frac{1}{2}} = \mathbf{g}(\tilde{\mathbf{w}}_{i,j+\frac{1}{2}L}, \tilde{\mathbf{w}}_{i,j-\frac{1}{2}R}) \quad (\text{B.5})$$

where the fluxes can evaluated using the original Roe flux (appendix D) or the EC1-RV2 flux(appendix C) with the time centered interface values given as

$$\tilde{\mathbf{w}}_{i+\frac{1}{2}L,j} = \tilde{\mathbf{w}}_{i,j} + \frac{\delta_x \mathbf{w}_{i,j}}{2} \quad (\text{B.6})$$

$$\tilde{\mathbf{w}}_{i-\frac{1}{2}R,j} = \tilde{\mathbf{w}}_{i,j} - \frac{\delta_x \mathbf{w}_{i,j}}{2} \quad (\text{B.7})$$

The limited slopes are computed by comparing the two neighboring slopes at (i, j) dimension by dimension i.e.

$$\delta_x \mathbf{w}_{i,j} = \phi(\mathbf{w}_{i,j} - \mathbf{w}_{i-1,j}, \mathbf{w}_{i+1,j} - \mathbf{w}_{i,j}) \quad (\text{B.8})$$

with similar approach in the y-direction. The limiter function ϕ can be any of the conventional one dimensional limiter [94] which can be written as

$$\phi(a, b) = \begin{cases} \minmod(\frac{a+b}{2}, 2a, 2b), & \text{if } ab > 0, \\ 0, & \text{if } ab \leq 0 \end{cases} \quad (\text{B.9})$$

which is the double minmod limiter and the superbee limiter

$$\phi(a, b) = \begin{cases} \minmod(\maxmod(a, b), \minmod(2a, 2b)), & \text{if } ab > 0. \\ 0, & \text{if } ab \leq 0 \end{cases} \quad (\text{B.10})$$

²We have only provided flux interface evaluations at $(i + \frac{1}{2}, j)$ and $(i, j + \frac{1}{2})$ but similar methods can be used applied to solve for the fluxes at $(i - \frac{1}{2}, j)$ and $(i, j - \frac{1}{2})$ interfaces

and finally the harmonic limiter

$$\phi(a, b) = \begin{cases} \frac{2 * \max \operatorname{mod}(a, b)}{a + b}, & \text{if } ab > 0, \\ 0, & \text{if } ab \leq 0 \end{cases} \quad (\text{B.11})$$

Finally the corrector (full step) for the Hancock scheme updates the conservative cell values at time level $n + 1$

$$\mathbf{u}_{i,j}^{n+1} = \mathbf{u}_{i,j}^n - \Delta t \left(\frac{\tilde{\mathbf{f}}_{i+\frac{1}{2},j} - \tilde{\mathbf{f}}_{i-\frac{1}{2},j}}{\Delta x} + \frac{\tilde{\mathbf{g}}_{i,j+\frac{1}{2},j} - \tilde{\mathbf{g}}_{i,j-\frac{1}{2},j}}{\Delta y} \right) \quad (\text{B.12})$$

Note that if $\delta_x \mathbf{w}_{i,j} = 0$, the Hancock scheme becomes a first order forward Euler method. Hence for an arbitrary grid formulation in two dimensions, the first order Hancock scheme can be written as

$$\mathbf{u}_{i,j}^{n+1} = \mathbf{u}_{i,j}^n - \frac{\Delta t}{A_{ij}} \left(\sum_{\text{faces}} (\mathbf{f} \Delta y - \mathbf{g} \Delta x) \right)_{ij} \quad (\text{B.13})$$

where A_{ij} is the volume of cell with centers (i, j) .

APPENDIX C

Two Dimensional Finite Volume Discretization of the EC1-RV2 Flux

From the notes of [110], the Euler equations can be semi-discretized on arbitrary grids in two dimensions via a finite volume formulation.

$$\partial_t \mathbf{u}_{ij} = -\frac{1}{A_{ij}} \left(\sum_{faces} (\mathbf{f} \Delta y - \mathbf{g} \Delta x) \right)_{ij} \quad (C.1)$$

where i, j represent the center-coordinates of a particular cell with the area of the cell denoted by A_{ij} . We compute the fluxes across each cell interface and obtain the total net flux within the cell as the sum of all the interface-fluxes¹. Define the length of a particular cell-face f as $\Delta l_f = \sqrt{(\Delta x)_f^2 + (\Delta y)_f^2}$ as shown in Fig. C.1, the normal and tangential velocities at f are given by

$$\begin{aligned} q_f &= \frac{u \Delta y - v \Delta x}{\Delta l_f} \\ r_f &= \frac{u \Delta x + v \Delta y}{\Delta l_f} \end{aligned} \quad (C.2)$$

Combining these results with the information from appendix A, we have the normal

¹For triangular grids, we take the sum of three interfaces. For quadrilateral grids, it will be four interfaces.

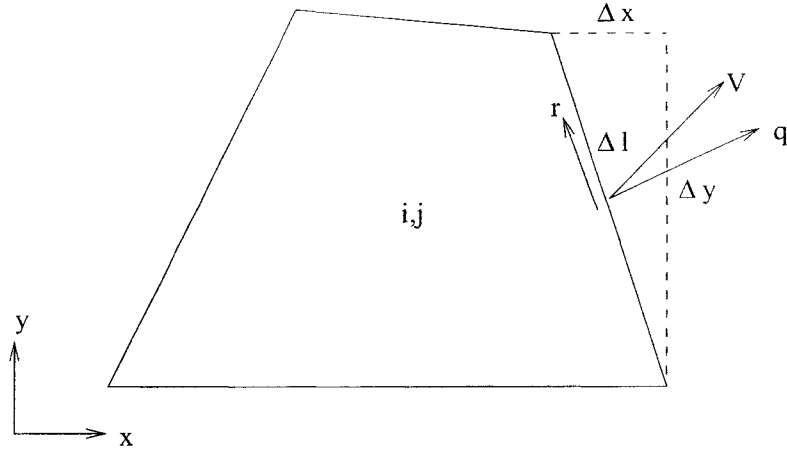


Figure C.1: A sample arbitrary cell with normal and tangential velocities (q, r) w.r.t to a particular interface.

flux through the cell-face f as

$$\mathbf{f}\Delta y - \mathbf{g}\Delta x = \begin{bmatrix} \rho q \\ \rho u q + p_1 \frac{\Delta y}{\Delta l} \\ \rho v q - p_1 \frac{\Delta x}{\Delta l} \\ \rho q H \end{bmatrix} \Delta l_f = \mathbf{F}_f \Delta l_f \quad (\text{C.3})$$

with the total enthalpy $H = \frac{1}{2}(u^2 + v^2) + \frac{\gamma}{\gamma-1} \frac{p_2}{\rho}$. Note that we have defined two pressures p_1, p_2 and each pressure will be computed differently.

Define two neighboring cell states as L and R which is separated by a common cell-face f . The net flux across cell-face f is obtained by adding the symmetric entropy conserving flux with an entropy stable (or consistent) dissipative flux given by²

$$\begin{aligned} \mathbf{F}_f(\mathbf{u}_L, \mathbf{u}_R) &= \mathbf{F}_C(\mathbf{u}_L, \mathbf{u}_R) - \frac{1}{2} \hat{\mathbf{R}} |\hat{\Lambda} \hat{\mathbf{S}}| \hat{\mathbf{R}}^T [\mathbf{v}] \\ &= \mathbf{F}_C(\mathbf{u}_L, \mathbf{u}_R) - \frac{1}{2} \sum_{k=1}^4 |\hat{\lambda}_k \hat{S}_k| [V_k] \hat{\mathbf{r}}_k \end{aligned} \quad (\text{C.4})$$

²Recall that $[a] = a_R - a_L$.

The entropy conserving flux is computed as averaged quantities written as

$$\mathbf{F}_C(\mathbf{u}_L, \mathbf{u}_R) = \begin{bmatrix} \hat{\rho}\hat{q} \\ \hat{\rho}\hat{u}\hat{q} + \hat{p}_1 \frac{\Delta y}{\Delta t} \\ \hat{\rho}\hat{v}\hat{q} - \hat{p}_1 \frac{\Delta x}{\Delta t} \\ \hat{\rho}\hat{q}\hat{H} \end{bmatrix} \quad (\text{C.5})$$

Define parameter vectors

$$z_1 = \sqrt{\frac{\rho}{p}}, \quad z_2 = \sqrt{\frac{\rho}{p}}u, \quad z_3 = \sqrt{\frac{\rho}{p}}v, \quad z_4 = \sqrt{\rho p} \quad (\text{C.6})$$

so that the averaged quantities are computed as functions of arithmetic ($\bar{a} = \frac{a_L + a_R}{2}$)

and logarithmic mean (defined in appendix E)

$$\hat{\rho} = \bar{z}_1 z_4^{ln} \quad (\text{C.7})$$

$$\hat{u} = \frac{\bar{z}_2}{\bar{z}_1} \quad (\text{C.8})$$

$$\hat{v} = \frac{\bar{z}_3}{\bar{z}_1} \quad (\text{C.9})$$

$$\hat{p}_1 = \frac{\bar{z}_4}{\bar{z}_1} \quad (\text{C.10})$$

$$\hat{p}_2 = \frac{\gamma + 1}{2\gamma} \frac{z_4^{ln}}{z_1^{ln}} + \frac{\gamma - 1}{2\gamma} \frac{\bar{z}_4}{\bar{z}_1} \quad (\text{C.11})$$

$$\hat{a} = \left(\frac{\gamma \hat{p}_1}{\hat{\rho}} \right)^{\frac{1}{2}} \quad (\text{C.12})$$

$$\hat{H} = \frac{1}{2}(\hat{u}^2 + \hat{v}^2) + \frac{\gamma}{\gamma - 1} \frac{\hat{p}_2}{\hat{\rho}} \quad (\text{C.13})$$

and \hat{q} and \hat{r} are determined via equations in (C.2) using averaged velocities.

The dissipative flux has averaged wave-speeds given by $\hat{\lambda}_k = [\hat{q} - \hat{a}, \hat{q}, \hat{q}, \hat{q} + \hat{a}]$ with the $\hat{\mathbf{S}}$ as the averaged scaling matrix (obtained from appendix A) and $\hat{\mathbf{r}}_k$ as the

columns of the averaged right eigenvectors

$$\hat{\mathbf{R}} = \begin{bmatrix} 1 & 1 & 0 & 1 \\ \hat{u} - \hat{a} \frac{\Delta y}{\Delta l} & \hat{u} & \frac{\Delta x}{\Delta l} & \hat{u} + \hat{a} \frac{\Delta y}{\Delta l} \\ \hat{v} + \hat{a} \frac{\Delta x}{\Delta l} & \hat{v} & \frac{\Delta y}{\Delta l} & \hat{v} - \hat{a} \frac{\Delta x}{\Delta l} \\ \hat{H} - \hat{q}\hat{a} & \frac{\hat{u}^2 + \hat{v}^2}{2} & \hat{r} & \hat{H} + \hat{q}\hat{a} \end{bmatrix} \quad (\text{C.14})$$

and the new averaged wave-strengths are given as

$$\begin{aligned} [V_k] &= \hat{\mathbf{R}}^T [\mathbf{v}] \\ &= \begin{bmatrix} [v_1] + (\hat{u} - \hat{a} \frac{\Delta y}{\Delta l})[v_2] + (\hat{v} + \hat{a} \frac{\Delta x}{\Delta l})[v_3] + (\hat{H} - \hat{q}\hat{a})[v_4] \\ [v_1] + \hat{u}[v_2] + \hat{v}[v_3] + \frac{\hat{u}^2 + \hat{v}^2}{2}[v_4] \\ \frac{\Delta x}{\Delta l}[v_2] + \frac{\Delta y}{\Delta l}[v_3] + \hat{r}[v_4] \\ [v_1] + (\hat{u} + \hat{a} \frac{\Delta y}{\Delta l})[v_2] + (\hat{v} - \hat{a} \frac{\Delta x}{\Delta l})[v_3] + (\hat{H} + \hat{q}\hat{a})[v_4] \end{bmatrix} \end{aligned} \quad (\text{C.15})$$

with $[v_k]$ defined as the change in the entropy variables between the left and right states across a particular cell-face

$$[\mathbf{v}] = \begin{bmatrix} \left[\frac{\gamma-S}{\gamma-1} - \frac{\rho(u^2+v^2)}{2p} \right] \\ \left[\frac{\rho u}{p} \right] \\ \left[\frac{\rho v}{p} \right] \\ -\left[\frac{\rho}{p} \right] \end{bmatrix} \quad (\text{C.16})$$

Note that the dissipative flux also uses the *same* averaging as the entropy-conserving flux. Although there are two choices for pressure for the averaging the speed of sound and within the scaling matrix \mathbf{S} , we chose \hat{p}_1 .

We have only presented an entropy-stable flux function. To achieve entropy-consistency, we need to modify the acoustic wave-speeds ($k = 1, 4$) as explained in

chapter 6 section 3.3 given as

$$|\hat{\Lambda}_{\text{fix}}| = \begin{bmatrix} |\hat{\lambda}_1| + \alpha|\hat{\lambda}_1| & 0 & 0 & 0 \\ 0 & |\hat{\lambda}_2| & 0 & 0 \\ 0 & 0 & |\hat{\lambda}_3| & 0 \\ 0 & 0 & 0 & |\hat{\lambda}_4| + \alpha|\hat{\lambda}_4| \end{bmatrix} \quad (\text{C.17})$$

However, from our numerical experience, the selection of $\alpha = 0.2$ works well for almost all cases that we have tested.

APPENDIX D

Two Dimensional Finite Volume Discretization of the Roe Flux

We have the same arbitrary two dimensional grid formulation as given in appendix C except that now, the interface flux is computed as

$$\mathbf{F}_f(\mathbf{u}_L, \mathbf{u}_R) = \frac{1}{2}(\mathbf{F}(\mathbf{u}_L) + \mathbf{F}(\mathbf{u}_R)) - \frac{1}{2} \sum_{k=1}^4 |\hat{\lambda}_k| [V_k] \hat{\mathbf{r}}_k \quad (\text{D.1})$$

in which the wavespeeds (eigenvalues) and column right eigenvectors are given in C (but averaged differently) and the wave strengths are

$$[V_k] = \begin{bmatrix} \frac{[p] - \hat{\rho}\hat{a}[q]}{2\hat{a}^2} \\ \frac{-([p] - \hat{a}^2[\rho])}{\hat{a}^2} \\ \hat{\rho}[r] \\ \frac{[p] + \hat{\rho}\hat{a}[q]}{2\hat{a}^2} \end{bmatrix} \quad (\text{D.2})$$

with (q, r) given in appendix C. The hat quantities represent Roe-averaged values

$$\hat{\rho} = W\rho_L \quad (\text{D.3})$$

$$\hat{u} = \frac{u_L + Wu_R}{1 + W} \quad (\text{D.4})$$

$$\hat{v} = \frac{v_L + Wv_R}{1 + W} \quad (\text{D.5})$$

$$\hat{H} = \frac{H_L + WH_R}{1 + W} \quad (\text{D.6})$$

where $W = \sqrt{\rho_R/\rho_L}$ and the averaged sound speed $\hat{a} = \sqrt{(\gamma - 1)(\hat{H} - \frac{\hat{u}^2 + \hat{v}^2}{2})}$.

APPENDIX E

The Logarithmic Mean

Let a be some quantity of interest which has a left and right state. The logarithmic mean of a is defined as

$$a^{\ln}(L, R) = \frac{a_L - a_R}{\ln(a_L) - \ln(a_R)} \quad (\text{E.1})$$

However, this is not numerically well-posed when $(a_L) \rightarrow (a_R)$. To overcome this, let us write the logarithmic mean in another form. Let $\zeta = \frac{a_L}{a_R}$, so that

$$a^{\ln}(L, R) = \frac{a_L + a_R \zeta - 1}{\ln \zeta} \frac{\zeta - 1}{\zeta + 1} \quad (\text{E.2})$$

where $\ln(\zeta) = 2\left(\frac{1-\zeta}{1+\zeta} + \frac{1}{3}\frac{(1-\zeta)^3}{(1+\zeta)^3} + \frac{1}{5}\frac{(1-\zeta)^5}{(1+\zeta)^5} + \frac{1}{7}\frac{(1-\zeta)^7}{(1+\zeta)^7} + O(\zeta^9)\right)$

to obtain a numerically well-formed logarithmic mean. The subroutine for computing the logarithmic mean is the following. Let

$$\zeta = \frac{a_L}{a_R}, \quad f = \frac{(\zeta - 1)}{(\zeta + 1)}, \quad u = f * f$$

1. if $(u < \epsilon)$

$$F = 1.0 + u/3.0 + u * u/5.0 + u * u * u/7.0$$

2. else

$$F = \ln(\zeta)/2.0/(f)$$

so that $a^{\ln}(L, R) = \frac{a_L + a_R}{2F}$ with $\epsilon = 10^{-2}$

APPENDIX F

Entropy Fix for EC1-RV2 Flux: Generating the "Correct" Sign of Entropy Production

We want to show that as long as $\alpha \geq 0$, the entropy fix will generate positive entropy production regardless if we have an expansive or compressive region. Define the system of conservation laws for the inviscid fluid dynamics to be

$$\partial_t \mathbf{u} + \partial_x \mathbf{f}(\mathbf{u}) = 0 \quad (\text{F.1})$$

where $\mathbf{u} = [\rho, \rho u, \rho E]^T$ and $\mathbf{f}(\mathbf{u}) = [\rho u, \rho u^2 + p, \rho u H]^T$. Recall that the entropy function $U = \frac{-\rho S}{\gamma - 1}$ where S is the physical entropy hence the entropy variables

$$\mathbf{v} = \frac{\partial U}{\partial \mathbf{u}} = \left[\frac{\gamma - S}{\gamma - 1} - \frac{1}{2} \frac{\rho}{p} (u^2), \frac{\rho u}{p}, -\frac{\rho}{p} \right]^T \quad (\text{F.2})$$

Now let us discretize (F.1) semi-discretely in one dimension within an element $*$ with nodes (L, R) .

$$h_L \partial_t \mathbf{u}_L = \mathbf{f}_L - \mathbf{f}^*, \quad h_R \partial_t \mathbf{u}_R = \mathbf{f}^* - \mathbf{f}_R \quad (\text{F.3})$$

Multiplying the last equation by \mathbf{v} will give

$$h_L \partial_t U_L = \mathbf{v}_L (\mathbf{f}_L - \mathbf{f}^*), \quad h_R \partial_t U_R = \mathbf{v}_R (\mathbf{f}^* - \mathbf{f}_R) \quad (\text{F.4})$$

so that the total entropy update within the element $*$ is

$$\partial_t (h_L U_L + h_R U_R) = -[\mathbf{v} \cdot \mathbf{f}] + [\mathbf{v}]^T \mathbf{f}^* \quad (\text{F.5})$$

Recall that interface flux consists of the symmetric entropy conserving flux subtracted by the asymmetric upwinded-entropy-consistent flux $\mathbf{f}^* = \mathbf{f}_C - \frac{1}{2}\hat{\mathbf{R}}|\hat{\Lambda}_{\text{fix}}|\hat{\mathbf{S}}\hat{\mathbf{R}}^T[\mathbf{v}]$, hence

$$\partial_t(h_L U_L + h_R U_R) = [\mathbf{v} \cdot \mathbf{f}] + [\mathbf{v}]^T \mathbf{f}_C - \frac{1}{2}[\mathbf{v}]^T \hat{\mathbf{R}} |\hat{\Lambda}_{\text{fix}}| \hat{\mathbf{S}} \hat{\mathbf{R}}^T [\mathbf{v}]$$

The first two terms on the RHS are equal to $[F]$ by definition of entropy conservation thus

$$h\partial_t U + [F] = -\frac{1}{2}(\hat{\mathbf{R}}^T[\mathbf{v}])^T \hat{\mathbf{S}} |\hat{\Lambda}_{\text{fix}}| (\hat{\mathbf{R}}^T[\mathbf{v}]) = -\frac{1}{2}\hat{\mathbf{W}}^T \hat{\mathbf{S}} |\hat{\Lambda}_{\text{fix}}| \hat{\mathbf{W}} \quad (\text{F.6})$$

is the semi-discrete entropy conservation law with a production term and $\hat{\mathbf{S}} \geq \mathbf{0}$ is the diagonal scaling matrix satisfying $\hat{\mathbf{L}}[\mathbf{u}] = \hat{\mathbf{S}}\hat{\mathbf{R}}^T[\mathbf{v}]$. Recall that

$$|\hat{\Lambda}_{\text{fix}}| = \begin{bmatrix} |\hat{\lambda}_1| + \alpha|[\hat{\lambda}_1]| & 0 & 0 \\ 0 & |\hat{\lambda}_2| & 0 \\ 0 & 0 & |\hat{\lambda}_3| + \alpha|[\hat{\lambda}_3]| \end{bmatrix} \quad (\text{F.7})$$

which implies that as long as $\alpha \geq 0$, the entropy production generated by the entropy fix will be positive regardless if we have expansive or compressive region.

APPENDIX G

Discrete Operators

We will focus on simple finite difference formulations on two dimensional uniform grids. Define h and Δt to be the discretized grid space in x, y directions while Δt is the time step. Let $u_{i,j}^n$ be a discrete approximation located at cell-center $(x, y, t) = (ih, jh, n\Delta t)$. The discrete differencing and averaging operators are defined by

$$\delta_x(\cdot)_{..} = (\cdot)_{+\frac{1}{2}, ..} - (\cdot)_{-\frac{1}{2}, ..} \quad (G.1)$$

$$\delta_y(\cdot)_{..} = (\cdot)_{.. + \frac{1}{2}} - (\cdot)_{.. - \frac{1}{2}} \quad (G.2)$$

$$\mu_x(\cdot)_{..} = \frac{1}{2}[(\cdot)_{+\frac{1}{2}, ..} + (\cdot)_{-\frac{1}{2}, ..}] \quad (G.3)$$

$$\mu_y(\cdot)_{..} = \frac{1}{2}[(\cdot)_{.. + \frac{1}{2}} - (\cdot)_{.. - \frac{1}{2}}] \quad (G.4)$$

The result of any above operator will lie half-way between the two inputs. We may also utilize the product of two operators. For example, $\mu_x \delta_x(\cdot)_{i,j}$ is a *central difference* of $\frac{1}{2}[(\cdot)_{i+1,j} - (\cdot)_{i-1,j}]$ in the x -direction located at grid point i, j . Another example is the *compact difference* $\mu_y \delta_x(\cdot)_{i,j}$, which involves four points $(i \pm \frac{1}{2}, j \pm \frac{1}{2})$ of a square centered at grid i, j Fig G.1. Assume prime and non-prime variables to be quantities located at the vertices and cell-center respectively. Capitalized variables define edge values in two dimensions. Cells are points with all integer coordinates while vertices are points with all half integer coordinates. On the other hand, points with one

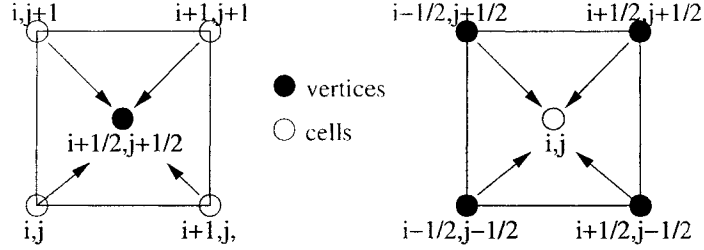


Figure G.1: Product of two operators on cells and vertices

integer and one half integer coordinate define an edge. The following product of operators will describe some of the the discretized notations used in the thesis.

$$\mu_x \mu_y(u) = \frac{1}{4}[(u)_{i+1,j+1} + (u)_{i,j+1} + (u)_{i,j} + (u)_{i+1,j}] \quad (\text{G.5})$$

$$\mu_y \delta_x(u) = \frac{1}{2}[(u)_{i+1,j+1} + (u)_{i+1,j} - (u)_{i,j+1} - (u)_{i,j}] \quad (\text{G.6})$$

$$\mu_x \delta_y(u) = \frac{1}{2}[(u)_{i+1,j+1} + (u)_{i,j+1} - (u)_{i+1,j} - (u)_{i,j}] \quad (\text{G.7})$$

where it is understood that the product of the above operators will lie on a vertex with coordinates $(i + \frac{1}{2}, j + \frac{1}{2})$. Likewise, applying these operators on the vertex quantities gives us the following.

$$\mu_x \mu_y(u') = \frac{1}{4}[(u')_{i+\frac{1}{2},j+\frac{1}{2}} + (u')_{i-\frac{1}{2},j+\frac{1}{2}} + (u')_{i-\frac{1}{2},j-\frac{1}{2}} - (u')_{i+\frac{1}{2},j-\frac{1}{2}}] \quad (\text{G.8})$$

$$\mu_y \delta_x(u') = \frac{1}{2}[(u')_{i+\frac{1}{2},j+\frac{1}{2}} + (u')_{i+\frac{1}{2},j-\frac{1}{2}} - (u')_{i-\frac{1}{2},j+\frac{1}{2}} - (u')_{i-\frac{1}{2},j-\frac{1}{2}}] \quad (\text{G.9})$$

$$\mu_x \delta_y(u') = \frac{1}{2}[(u')_{i+\frac{1}{2},j+\frac{1}{2}} + (u')_{i-\frac{1}{2},j+\frac{1}{2}} - (u')_{i+\frac{1}{2},j-\frac{1}{2},k-\frac{1}{2}} - (u')_{i-\frac{1}{2},j-\frac{1}{2},k-\frac{1}{2}}] \quad (\text{G.10})$$

in which the resulting products live in a cell with coordinate (i, j) . Note that in this thesis, we only use compact vorticity defined as $\omega = \mu_y \delta_x(v) - \mu_x \delta_y(u)$, where cell variables are utilized to compute vorticity at the vertices.

APPENDIX H

Jump Conditions

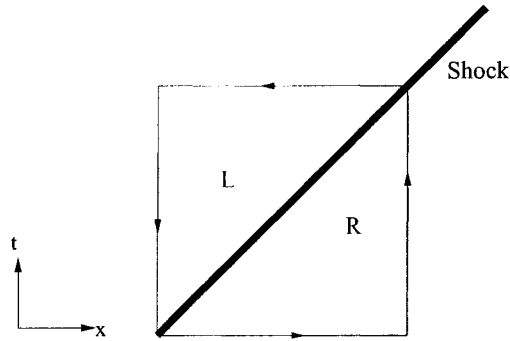


Figure H.1: A sample control volume with a right running shock. Assume that the shock has thickness $\rightarrow 0$.

We will perform a closed integral around the space-time control volume containing a left u_L and right u_R states separated by a shock moving at speed $\Lambda = \frac{\Delta x}{\Delta t}$,

$$\begin{aligned}
 \oint (udx - fdt) &= u_R \Delta x - f_R \Delta t - u_L \Delta x + f_L \Delta t \\
 &= (\Lambda(u_R - u_L) - (f_R - f_L)) \Delta t \\
 &= 0 \Rightarrow [f] = \Lambda[u]
 \end{aligned} \tag{H.1}$$

if we have conservation across the shock. However, if we do not have conservation, there will be a production term such that

$$\oint (udx - fdt) = P \Rightarrow [f] = \Lambda[u] + P \tag{H.2}$$

BIBLIOGRAPHY

BIBLIOGRAPHY

- [1] ALMGREN, A., BUTTKE, T., AND COLLELA, P. A fast adaptive vortex method in three dimensions. *J. Comp. Physics* 113 (1994).
- [2] ANDERSON, J. *Introduction to Flight*, reprint ed. McGraw-Hill, 1989.
- [3] ANDERSON, J. *Hypersonic and High Temperature Gas Dynamics*, first ed. Reprint AIAA, 2000.
- [4] ANDERSON, J. *Modern Compressible Flow with Historical Perspective*, second ed. Springer, 2004.
- [5] BALSARA, D., AND SPICER, D. A staggered mesh algorithm using high order godunov fluxes to ensure solenoidal magnetic fields in magnetohydrodynamic simulations. *J. Comp. Physics* 149 (1999), 270.
- [6] BARTH, T. Some notes on shock-resolving flux functions part i, stationary characteristics. NASA TM-101087, Ames Research Center, 1989.
- [7] BARTH, T. An introduction to recent developments in theory and numerics of conservation laws. In *Numerical Methods for Gasdynamic Systems On Unstructured Meshes*. 1999.
- [8] BATCHELOR, G. *An Introduction to Fluid Dynamics*, reprinted ed. 2001.
- [9] BELL, J., COLLELA, P., AND GLAZ, H. A second order projection method for the incompressible navier-stokes equations. *J. Comp. Phys.* 85 (1989), 257.
- [10] BERMUDEZ, A., AND VAZQUEZ, M. Upwind methods for hyperbolic problems with source terms. *Comp. and Fluids* 23 (1994), 1049–1071.
- [11] BERTIN, J. *Hypersonic Aerodynamics*, third ed. AIAA, 1994.
- [12] BOGDONOFF, S., AND VAS, I. Preliminary investigation of spiked bodies at supersonic speeds. *J. Aero. Sci* 26 (1959), 584.
- [13] BORIS, B., AND BOOK, D. Flux corrected transport i, shasta, a fluid transport algorithm that works. *J. Comp. Physics* 11 (1973), 38–69.

- [14] BRACKBILL, J., AND BARNES, D. The effect of nonzero $\nabla \cdot B$ on the numerical solution of magnetohydrodynamics equations. *J. Comp. Physics* 35 (1980), 426.
- [15] BRANDT, A. Multigrid techniques. In *VKI Lecture Series on Computational Fluid Dynamics 1984-04*. 1984.
- [16] BRIGGS, W., HENSON, V., AND MCCORMICK, S. *A multigrid tutorial*, second ed. SIAM, 2000.
- [17] BURTON, G. *A multifractal subgrid scale model for the large eddy simulation of turbulent flows*. PhD thesis, The University of Michigan, 2003.
- [18] CHARLTON, E. *An Octree Solution to Conservation laws over Arbitrary Regions (OSCAR) with applications to aircraft aerodynamics*. PhD thesis, The University of Michigan, 1997.
- [19] CHORIN, A. Numerical solution of the navier-stokes equations. *Math. Comp.* 22 (1968), 745.
- [20] COLLELA, P. Multidimensional upwind methods for hyperbolic conservation laws. LBL-17023, Lawrence Berkeley Lab Report, 1984.
- [21] COLOMBO, R. A 2 x 2 hyperbolic traffic flow model. *Math. Comput. Modelling* 35 (2002), 683–688.
- [22] COURANT, R., FRIEDRICH, K., , AND LEWY, H. On the partial difference equations of mathematical physics. *IBM Journal* 11 (1967), 215–234.
- [23] COURANT, R., ISAACSON, E., AND REESE, M. On the solution of nonlinear hyperbolic differential equations by finite differences. *Comm. Pure and Applied Mathematics* 5 (1952), 243–255.
- [24] CRANDALL, M., AND MAJDA, A. The method of fractional steps for conservation laws. *Math. Comp.* 34 (1980), 285–314.
- [25] DUMBSER, M., MOSCHETTA, J., AND GRESSION, J. A matrix stability analysis of the carbuncle phenomenon. *J. Comp. Physics* 197 (2004), 647.
- [26] DYAKOV, S. *Z. Ekspres. Teort. Fiz.* 27 (1954), 288.
- [27] EDWARDS, J. Towards unified cfd simulation of real fluid flows. In *CFD Conference* (2001), no. A01-31131, AIAA Conference.
- [28] EINFELDT, B. On godunov type methods for gas dynamics. *J. Comp. Physics* 25 (1988), 294–318.
- [29] ELLING, V. Carbuncles as self-similar entropy solutions. *unpublished*.

- [30] ELLING, V. A possible counterexample to wellposedness of entropy solutions and to godunov scheme convergence. *Mathematics of Computation*.
- [31] ELLING, V. Nonuniqueness of entropy solutions and the carbuncle phenomenon. 10th Conference on Hyperbolic Problems, Osaka Japan.
- [32] EVANS, C., AND HAWLEY, J. Simulation of magnetohydrodynamic flows: A constrained transport method. *Astrophys. J.* 332 (1988), 659.
- [33] FEY, M., AND TORIHILLON, M. A vorticity preserving finite volume method for the wave equation. 10 thInternational Conference on Hyperbolic Problems.
- [34] GEORGE, D. A high resolution godunov method for the shallow water equations with topography and evolving dry regions. www.amath.washington.edu/~dgeorge/documents/fieldposter.pdf.
- [35] GIBBS-SMITH, C. The wright brothers. Booklets Prepared for British Science Museum, 1963.
- [36] GIBBS-SMITH, C. A brief history of flying. Booklets Prepared for British Science Museum, 1967.
- [37] GIBBS-SMITH, C. Aviation: A historical survey from its origins to the end of world war ii. Booklets Prepared for British Science Museum, 1970.
- [38] GIBBS-SMITH, C. Flight through the ages. Booklets Prepared for British Science Museum, 1974.
- [39] GNOFFO, P., WEILMUENSTER, K., OLYNICK, D., AND VENKATAPATHY, E. Computational aerothermodynamic design issues for hypersonic vehicles. *Ann. Rev. Fluid Mech.* 31 (1999), 459–494.
- [40] GNOFFO, P., AND WHITE, A. Computational aerothermodynamic simulation issues on unstructured grids. No. 2004-2371, AIAA Thermophysics Conference.
- [41] GODUNOV, S. Finite difference method for numerical computation of discontinuous solutions of the equations of fluid dynamics. *Math Sb.* 47 (1959), 271–306.
- [42] GOMBOSI, T., POWELL, K., AND DE ZEEUW, D. Axisymmetric modelling of cometary mass loading on an adaptively refined grid: Mhd results. *J. Geophys. Res.* 99 (1994), 21.
- [43] GOSSE, L. A well balanced scheme using non-conservative products designed for hyperbolic system with source terms. *Math. Mod. Meth. Appl. Sci* 11 (2001), 339–365.
- [44] GREENBERG, M. *Advanced Engineering Mathematics*. 1988.

- [45] GRESSIER, J., AND MOSCHETTA, J. On the pathological behavior of upwind schemes. No. 1998-0110, AIAA Conference.
- [46] HARTEN, A. High resolution schemes for hyperbolic conservation laws. *J. Comp. Physics* 49 (1983), 357–393.
- [47] HARTEN, A. Eno schemes with subcell resolutions. *J. Comp. Physics* 83 (1987), 148–184.
- [48] HIRSCH, C. *Numerical Computation of internal and external flows, Vol 1 and 2*, reprint ed. Wiley, 2000.
- [49] HUGHES, T., FRANCA, L., AND MALLET, M. A new finite element formulation for compressible fluid dynamics: I. symmetric forms of the compressible euler and navier stokes equations and the second law of thermodynamics. *Comp. Meth. App. Mech. Eng.* 54 (1986).
- [50] HUSSAINI, M., VAN LEER, B., AND ROSENDALE, J. In *Upwind and High Resolutions Schemes*. 1997.
- [51] ISMAIL, F., AND ROE, P. Toward a vorticity preserving second order finite volume scheme solving the euler equations. In *17th CFD Conference* (Toronto, 2005), no. 2005-5235, AIAA Conference.
- [52] KIM, S.-S., KIM, C., RHO, O.-H., AND HONG, S. Cures for the shock instability, development of a shock-stable roe scheme. *J. Comp. Physics* 186 (2003), 342.
- [53] LANDAU, L., AND LIVSCHITZ, E. *Fluid Mechanics*. Pergamon, 1959.
- [54] LANEY, C. *Computational Gasdynamics*. 1998.
- [55] LAX, P. Weak solutions of nonlinear hyperbolic equations and their numerical computation. *Comm. Pure and Applied Mathematics* 7 (1954), 159–193.
- [56] LAX, P. Hyperbolic systems of conservation laws ii. *Comm. Pure and Applied Mathematics* 10 (1957), 537–566.
- [57] LAX, P., AND RICHTMAYER, R. Survey of the stability of linear finite difference equations. *Comm. Pure and Applied Mathematics* 11 (1956), 267–293.
- [58] LAX, P., AND WENDROFF, B. System of conservation laws. *Comm. Pure Applied Math* 13 (1960), 217–.
- [59] LEFLOCH, P., MERCIER, J., AND ROHDE, C. Full discrete entropy conservative schemes of arbitrary order. *SIAM J. Num. Anal.* 40 (2002), 1968–1992.
- [60] LEVEQUE, R. *Numerical Methods for Conservation Laws*, reprinted ed. Birkhauser, 1999.

- [61] LEVEQUE, R. *Finite Volume Methods for Hyperbolic Problems*, first ed. Cambridge Text in Applied Mathematics, 2002.
- [62] LEVEQUE, R., AND LANGSETH, J. Three dimensional euler computations using clawpack. Conference on Num. Meth. for Euler and Navier-Stokes Equations.
- [63] LIN, H.-C. Dissipative additions to flux-difference splitting. *J. Comp. Physics* 117 (1995), 20–27.
- [64] LINDE, T. *A three dimensional adaptive multifluid MHD model of the heliosphere*. PhD thesis, The University of Michigan, 1998.
- [65] LINDSAY, K., AND KRASNY, R. A particle method and adaptive treecode for vortex sheet motion in three dimensional flow. *J. Comp. Physics* 172 (2001), 879–907.
- [66] LIOU, M. Mass flux schemes and connections to shock instability. *J. Comp. Physics* 160 (2000), 623–648.
- [67] LIOU, M. Ten years in the making-ausm-family. In *CFD Conference* (2001), no. 2001-2521, AIAA Conference.
- [68] LOWRIE, R. *Compact Higher Order Numerical Methods for Hyperbolic Conservation Laws*. PhD thesis, The University of Michigan, 1996.
- [69] LUKACOVA-MEDVID'JOVA, M., MORTON, K., AND WARNECKE, G. Evolution galerkin methods for hyperbolic systems in two space dimension. *Math Comp.* 69 (2000), 1355–1384.
- [70] MACCORMACK, R. The effects of viscosity in hypervelocity impact cratering. No. 69-354, AIAA Conference.
- [71] MERRIAM, M. An entropy based approach to nonlinear stability. NASA TM-101086, Ames Research Center, 1989.
- [72] MORETTI, G. On the matter of shock fitting. In *Lecture Notes in Physics* 35:287-292. 1974.
- [73] MORTON, K., AND ROE, P. Vorticity-preserving lax-wendroff type schemes for the system wave equation. *SIAM* 23 (2001), 170–192.
- [74] NEUMANN, J., AND RICHTMAYER, R. A method for numerical calculation of hydrodynamic shocks. *J. Appl Phys.* 21 (1950), 232–237.
- [75] NISHIKAWA, H., AND ROE, P. Adaptive quadrature fluctuation splitting schemes solving the euler equations. In *17th CFD Conference* (Toronto, 2005), AIAA Conference.

- [76] OH, W., KIM, J., AND KWON, O. Numerical simulation of two dimensional blade vortex interactions using unstructured adaptive meshes. *AIAA Journal* 40 (2002), 474–480.
- [77] OSHER, S. Riemann solvers, entropy conditions and difference approximations. *SIAM J. Num. Anal.* 21 (1984), 217–235.
- [78] PANDOLFI, M., AND D'AMBROSIO. Numerical instabilities in upwind methods. *J. Comp. Physics* 166 (2001), 271–301.
- [79] PEERY, K., AND IMLAY, S. Blunt body flow simulations. No. 88-2924, AIAA Conference.
- [80] POWELL, K. An approximate riemann solver for magnetohydrodynamics (that works in more than one dimension). 94-24, ICASE Report, 1994.
- [81] QUIRK, J. A contribution to the great riemann solver debate. *Int. J. Num. Meth. Fluids* 18 (1994), 555–574.
- [82] RICHTMAYER, R., AND MORTON, K. *Difference Methods for Initial-value Problems*, first ed. Wiley-Interscience, 1967.
- [83] ROBINET, J., GRESSIER, J., CASSALIS, G., AND MOSCHETTA, J. Shock wave instability and carbuncle phenomenon; same intrinsic origin. *J. Fluid. Mechanics* 417 (2000), 237–263.
- [84] ROE, P. Affordable, entropy-consistent, euler flux functions i. analytical results. *J. Comp. Physics*.
- [85] ROE, P. Approximate riemann solvers, parameter vectors and difference schemes. *J. Comp. Physics* 43 (1981), 357–372.
- [86] ROE, P. Numerical algorithms for the linear wave equations. 81047, Royal Aircraft Establishment, 1981.
- [87] ROE, P. *Principles of Computational Fluid Dynamics*. Introduction to CFD, University of Michigan, 2000.
- [88] ROE, P. Vorticity capturing. In *15th CFD Conference* (Anaheim, 2001), no. 2001-2523, AIAA Conference.
- [89] ROE, P., NISHIKAWA, H., ISMAIL, F., AND SCALABRIN, L. On carbuncles and other excrescences. No. 2005-4872, AIAA Conference.
- [90] SALAS, M. Shock fitting method for complicated two dimensional supersonic flows. *AIAA Journal* 14 (1976), 583–588.
- [91] SANDERS, R., MORANO, E., AND DRUGUET, M. Multidimensional dissipation for upwind schemes: Stability and applications to gas dynamics. *J. Comp. Physics* 54 (1994).

- [92] STEGER, J., AND WARMING, R. Flux vector splitting of the inviscid gas dynamics equations with application to finite difference methods. *J. Comp. Physics* 40 (1981), 263–293.
- [93] STEINHOFF, J. Vorticity confinement: a new technique for computing vortex dominated flow. In *Frontiers of Computational Fluid Dynamics*. 1994.
- [94] SWEBY, P. High resolution schemes using flux limiters for hyperbolic conservation laws. *SIAM J. Num. Anal.* 21 (1984), 995–1011.
- [95] TADMOR, E. The numerical viscosity of entropy stable schemes for systems of conservation laws. *Math. Comp.* 49 (1987).
- [96] TADMOR, E. Entropy stability theory for difference approximations of nonlinear conservation laws and related time dependent problems. In *Acta Numerica*. 2002.
- [97] TORO, E. *Riemann Solvers and Numerical Methods for Fluid Dynamics*, second ed. Springer, 1999.
- [98] TOTH, G. The $\nabla \cdot B = 0$ constraint in shock-capturing magnetohydrodynamics codes. *J. Comp. Physics* 161 (2000), 605–652.
- [99] TOTH, G., AND ODSRCIL, D. Comparison of some flux corrected transport and total variation diminishing numerical schemes for hydrodynamic and magnetohydrodynamic problems. *J. Comp. Phys.* 128 (1996), 82.
- [100] TREFETHEN, L., AND BAU, D. *Numerical Linear Algebra*, first ed. SIAM, 1997.
- [101] TSINOBER, A., SHTILMAN, L., AND VAISBURD, H. A study of properties of vortex stretching and enstrophy generation in numerical and laboratory turbulence. *Fluid Dyn. Res.* 21 (1998), 477–494.
- [102] VAN DYKE, M. *An Album of Fluid Motion Plate*. Parabolic Press, 1982.
- [103] VAN LEER, B. Toward the ultimate conservative difference scheme i. the quest of monotonicity. In *Lecture Notes in Physics* 18:173–178. 1973.
- [104] VAN LEER, B. Toward the ultimate conservative difference scheme ii. monotonicity and conservation combined in a second order scheme. *J. Comp. Physics* 14 (1974), 361–370.
- [105] VAN LEER, B. Toward the ultimate conservative difference scheme iii. upstream-centered finite difference schemes for ideal compressible flow. *J. Comp. Physics* 23 (1977), 263–275.
- [106] VAN LEER, B. Toward the ultimate conservative difference scheme iv. a new approach to numerical convection. *J. Comp. Physics* 23 (1977), 276–299.

- [107] VAN LEER, B. Toward the ultimate conservative difference scheme v. a second order sequel to godunov's method. *J. Comp. Physics* 32 (1979), 101–136.
- [108] VAN LEER, B. Flux-vector splitting for the euler equations. In *Lecture Notes in Physics* 170:507-512. 1982.
- [109] VAN LEER, B. On the relations between the upwind differencing schemes of godunov, enquist-oshier and roe. *SIAM J. Sci. Stat. Comput.* 5 (1984), 1–20.
- [110] VAN LEER, B. Aero 623-computational fluid dynamics project 2 winter 2003. Class Project, 2003.
- [111] VAN LEER, B., AND NOMURA, S. A new diffusion approach for discontinuous galerkin method. No. 2005-4872, AIAA Conference.
- [112] VIDOVIC, D. *Superlinearly convergent unstructured staggered schemes for compressible and incompressible flows*. PhD thesis, The University of Delft, 2005.
- [113] WATKINS, D. *Fundamentals of Matrix Computations*, first ed. SIAM, 1997.
- [114] WOODWARD, P., AND COLELLA, P. The numerical simulation of two-dimensional fluid flow with strong shocks. *J. Comp. Physics* 166 (1984), 271–301.
- [115] XU, K. Gas kinetic schemes for unsteady compressible flow simulations. In *VKI Lecture Series 1998-03*. 1998.